Theoretical modelling of electrons and holes in semiconductor nanostructures

Modelatge teòric d'electrons i forats en nanoestructures semiconductores

PER

MIQUEL ROYO VALLS

TESI

PRESENTADA EN COMPLIMENT PARCIAL DELS REQUERIMENTS
PER OPTAR AL TÍTOL DE
DOCTOR PER LA UNIVERSITAT JAUME I

Setembre de 2010

Departament de Química Física i Analítica
Universitat Jaume I
Castelló de la Plana, España, 2010

Els Doctors Josep Planelles Fuster i Joan Ignasi Climente Plasencia, del Departament de Química Física i Analítica de la Universitat Jaume I,

CERTIFIQUEN:

Que la memòria presentada pel llicenciat Miquel Royo Valls amb títol "Theoretical modelling of electrons and holes in semiconductor nanostructures" ha estat realitzada sota la nostra direcció i constitueix la Tesi Doctoral de l'esmentat llicenciat. Autoritze la presentació d'aquesta mitjançant el present escrit.

Castelló de la Plana, Novembre de 2010.

Josep Planelles Fuster   Joan Ignasi Climente Plasencia

ii

Agraïments

En primer lloc, voldria expressar el meu agraïment a Josep Planelles i Joan Ignasi Climente per oferir-me la possibilitat de realitzar aquests estudis de doctorat sota la seua direcció. A tots dos els agraeixo la seua dedicació i recolzament en tot moment sense els quals aquestes pàgines no s'hagueren mai imprès.

Per una altra banda i a pesar de que aquesta tesi doctoral ha requerit un gran esforç per part de l'autor i dels seus directors, la seua realització no hagués estat possible sense la participació desinteressada de moltes altres persones. En aquest sentit, agraeixo als professors Martí Pi i Manuel Barranco la seua col·laboració científica i sobretot la seua hospitalitat. Menció especial mereix el professor Enrico Lipparini qui hem va fer sentir com a casa durant els tres mesos que vaig passar en Trento sota la seua tutela. Als meus companys Fernado Rajadell, Jose Luis Movilla (Movi) i Ana Ballester els voldria agrair no sols la seua col·laboració científica, si no la seua amistat i la tasca fosca d'aguantar-me dia a dia, i a Jose Maria Mengíbar (Txema) el disseny de la portada d'aquesta memòria.

Finalment, voldria agrair al meu pare i a la meua germana l'afecte i la total confiança que he rebut durant tota la meua vida, i a Assun l'haver-me estimat des del dia en que ens vam conèixer. A ells que són el que més m'importa els dedique aquesta tesi.

iv

Introducció

Molts dels esforços realitzats durant les darreres dècades en la industria dels semiconductors han estat dirigits cap a la miniaturització de dispositius electrònics que permeta incorporar més i més elements lògics en un xip. Els continus avanços en aquesta direcció són els responsables de que la denominada llei de Moore es segueixi acomplint hui en dia. Enunciada en 1965 pel cofundador de l'empresa *Intel*, Gordon E. Moore, aquesta llei estableix que la velocitat dels nostres ordenadors es dobla cada dos anys aproximadament [1]. No obstant, fou el mateix Moore qui recentment va posar el sostre a aquesta tendència al afirmar que cap al 2020 ens trobaríem amb un obstacle insalvable que aturaria el creixement de la capacitat dels ordinadors convencionals: les lleis de la física.

Certament, a mesura que la mida d'un semiconductor es redueix des d'un cristall continu (*bulk*) fins un règim molecular, moltes de les seues propietats observables es veuen alterades. Així, per exemple, la separació energètica entre l'estat electrònic ocupat de més alta energia i l'estat buit de més baixa energia (l'anomenat *band gap*) es pot arribar a incrementar fins en un parell d'electronvolts, i el temps de vida mitja de l'excitació permesa de més baixa energia es redueix entre dos i tres ordres de magnitud [2]. L'evolució, però, no és continua, i aquest és el fet al qual Moore feia referència. Quan les dimensions d'un semiconductor s'aproximen a una escala nanoscòpica, el moviment dels seus electrons de conducció es troba confinat en un espai suficientment menut per què entren en joc efectes quàntics. En aquestes condicions, els dispositius han de ser tractats com sistemes quàntics que sovint no segueixen les lleis físiques a partir de les quals s'ha construït tota la tecnologia i els algorismes de la informàtica convencional. Aquest representa, per tant, el límit físic dels ordinadors conforme els coneixem hui en dia. En canvi, hi ha moltes esperances posades en l'aparició d'una nova generació d'ordinadors quàntics que vindrà a suplir i millorar els actuals ordinadors digitals [3].

El de la computació quàntica és un exemple més entre les nombroses promeses tecnològiques responsables de que la recerca i desenvolupament de materials a escala nanoscòpica haja sigut l'activitat més important en el camp dels semiconductors durant els últims trenta anys. Aquesta tesi està dedicada a l'estudi teòric d'un tipus de nanoestructures que es troben en el centre d'aquest vast creixement tecnològic, els punts quàntics.

Un punt quàntic (en anglès, *quantum dot*) és una estructura zerodimensional en la qual el moviment dels portadors de càrrega d'excés (tant electrons de conducció com forats de valència) està confinat a escala nanoscòpica en les tres direccions espacials. Com a conseqüència d'aquest confinament quàntic l'espectre d'energies esdevé discret, i les degeneracions i separacions entre nivells depenen de la grandària, forma i composició del punt quàntic. Aquesta és, de fet, una de les propietats més interessants dels punts quàntics, ja que ofereix la possibilitat de dissenyar el seu espectre d'energies en el procés de fabricació.

En aquest sentit, grans avanços han tingut lloc des que els primers punts quàntics foren obtinguts via mètodes de tipus *top-down* basats en l'ús de tècniques litogràfiques i atacs amb agents corrosius [4]. No obstant, aquests primers punts quàntics tenien més bé una mida mesoscòpica i les seues propietats òptiques es veien fortament degradades per l'agressivitat de les tècniques litogràfiques. Uns resultats més prometedors ofereixen les denominades metodologies *bottom-up*, les quals permeten la síntesi de punts quàntics a escala nanoscòpica mitjançant un control a nivell atòmic dels processos de creixement i nucleació. Així per exemple, tècniques de creixement autoordenat aconsegueixen la formació de punts quàntics en forma de discs [5], lents [6], o fins i tot anells (*quantum rings*) [7] disposats sobre una matriu d'un altre material semiconductor. Mentre que les denominades tècniques de química humida permeten la síntesi dels punts quàntics més menuts (sovint anomenats nanocristalls) de diverses formes geomètriques, com ara esferes i varetes, dispersats en suspensions col·loïdals [8].

A banda de les potencials aplicacions tecnològiques d'aquestes nanoestructures, que s'inclouen en camps de tant ressò com l'anomenada computació quàntica [9], la criptografia quàntica [10], la fotovoltaica [11] o la lluita contra el càncer [12], els punts quàntics són l'escenari ideal on observar i manipular efectes quàntics. El motiu resideix en que a diferència del que ocorre en àtoms i molècules, els portadors de càrrega d'excés d'un punt quàntic no

estan sotmesos a la intensa atracció Coulómbica dels nuclis, sinó que es troben deslocalitzats per tota la nanoestructura. Per tant, aquestos portadors de càrrega són molt més sensibles a pertorbacions externes, fet que permet estudiar en un laboratori alts règims de correlació electrònica o confinament magnètic difícilment observables en àtoms i molècules.

Probablement, les tècniques més emprades per estudiar experimentalment els punts quàntics siguen aquelles basades en espectroscòpia òptica [13, 14], bé mesurant transicions entre les bandes de valència i conducció (interbanda), o entre els estats d'una mateixa banda (intrabanda). A part, l'espectroscòpia d'efecte túnel (*scanning tunneling spectroscopy*) s'ha convertit en una tècnica vital en l'estudi dels punts quàntics [15]. En aquest tipus d'experiments es mesura el transport d'electrons a través d'un punt quàntic feblement acoblat a dos elèctrodes metàl·lics, de manera que controlant la velocitat en que els electrons són transferits i extrets del semiconductor es pot estudiar no sols l'espectre monoelectrònic, sinó també estats multielectrònics. En aquest últim cas l'espectroscòpia d'efecte túnel permet observar un dels fenòmens més importants de la física dels sistemes nanoscòpics, el denominat bloqueig de Coulomb (*Coulomb blockade*) [16–18]. Aquest consisteix bàsicament en la supressió del transport a través d'un punt quàntic degut a que, per afegir un nou electró al sistema, es requereix una aportació d'energia que compense la interacció electrostàtica d'aquest electró amb els que ja es troben en el punt quàntic.

Des d'un punt de vista teòric, alguns del conceptes bàsics del comportament dels materials semiconductors nanoscòpics s'han pogut derivar a partir d'estudis previs en cristalls macroscòpics. En canvi, algunes observacions experimentals, moltes de les quals han resultat ser d'un alt interès científic i tecnològic, han requerit la formulació de nous models teòrics que permetin la seua interpretació. En aquest sentit, una de les majors complicacions que presenta l'estudi teòric dels punts quàntics resideix en que es troben a mig camí entre el món molecular i el macroscòpic. Açò implica, per una banda, que no es poden considerar com sistemes infinits on aplicar condicions de contorn periòdiques, ja que es ben sabut que moltes de les seues propietats deriven concretament del seua mida finita. Per una altra banda, un punt quàntic convencional està format per uns quants milers d'àtoms, cosa que invalida els mètodes atomístics *ab initio* emprats en simulacions moleculars, ja que aquestos donarien lloc a càlculs computacionalment intractables. Per aquests motius es habitual l'ús de metodologies empíriques més senzilles i computacionalment més tractables, com ara l'aproximació de massa efectiva

(EMA) i mètodes k·p. Aquests mètodes que en un principi foren pensats per estudiar sistemes macroscòpics, s'adapten a l'estudi d'heteroestructures nanoscòpiques gràcies a l'aproximació de funció envolupant (EFA).

En aquesta tesi s'estudien diversos aspectes de la física dels punts quàntics semiconductors fent ús de simulacions teòriques basades en l'aproximació de massa efectiva i funció envolupant. Els estudis realitzats pretenen anar més enllà dels efectes derivats directament de confinar portadors de càrrega en unes dimensions nanoscòpiques, de manera que incorporen l'acció de factors addicionals en el tractament teòric. Es considera l'acció de camps externs magnètics i elèctrics, així com l'anomenat confinament dielèctric, el qual sorgeix a causa de la diferent constant dielèctrica entre els materials que conformen els punts quàntics i les matrius en les que es solen dispersar. Paral·lelament, en ocasions també es considera l'efecte de les interaccions Coulòmbiques que tenen lloc quan més d'un portador de càrrega d'excés resideix en el sistema. En concret considerarem sistemes poblats amb un alt nombre d'electrons en la banda de conducció, i també estats excitònics. formats per parells electró de conducció i forat de valència.

La present memòria està estructurada de la següent manera:

En el capítol 1 es fa un breu repàs sobre alguns aspectes teòrics de la física dels semiconductors amb la intenció d'introduir al lector en el marc teòric on es desenvolupen els treballs exposats en aquesta memòria. Així, es parteix d'una descripció qualitativa de la formació de les bandes d'energia que conformen l'estructura electrònica d'un cristall, per posteriorment introduir els formalismes de massa efectiva i funció envolupant. Finalment, es revisen les tècniques emprades per tractar els sistemes multipartícula, posant especial esment en el formalisme seguit per descriure els complexes excitònics. [1]

En el capítol 2 s'estudia la resposta a camps magnètics externs per part de diversos sistemes formats per anells quàntics: dos anells acoblats lateralment, una xarxa periòdica bidimensional d'antianells quàntics i dos anells acoblats verticalment. Prèviament, es realitza una petita introducció teòrica sobre com considerar l'efecte d'un camp magnètic extern en el formalisme

---

[1]Altres consideracions teòriques addicionals s'aniran exposant al llarg de la memòria per ser més específiques de cada capítol, o perquè meresquen major atenció degut a la pròpia contribució del nostre grup de recerca en el seu desenvolupament.

EMA-EFA, el qual es resumeix en fer ús de l'operador de moment canònic conjugat on s'inclou el potencial vector del camp. Mentre que els dos primers estudis es centren en l'evolució magnètica de l'espectre monoelectrònic, en l'últim cas es considera que el sistema d'anells acoblats verticalment està poblat amb un elevat nombre d'electrons, fins 40. Per avaluar les energies i densitats electròniques d'aquest sistema es realitzen càlculs basats en la teoria del funcional de la densitat (DFT) en aproximació de densitat local d'espín (LSDA).

En el capítol 3 s'estudia l'efecte del confinament dielèctric sobre les propietats electroòptiques de nanocristalls semiconductors típicament fabricats mitjançant tècniques de síntesi col·loidal. Com a punt de partida s'exposen les contribucions a l'energia dels portadors de càrrega que sorgeixen a conseqüència del desajust de constant dielèctrica entre els nanocristalls i les matrius on aquests es troben immersos. A continuació el capítol està estructurat en tres parts. En la primera s'estudien nanocristalls esfèrics poblats amb un elevat nombre d'electrons de conducció. Per a dur a terme aquesta tasca, es desenvolupa un mètode DFT-LSDA que considera una constant dielèctrica i una massa efectiva dependents de la posició, així com els efectes derivats d'una dispersió no parabòlica de la banda de conducció. Posteriorment es realitza un estudi de l'efecte del confinament dielèctric sobre les propietats òptiques de nanocristalls esfèrics. Concretament, s'investiga la possibilitat de formar estats excitònics superficials on els portadors de càrrega es veuen atrapats en el denominat pou d'autopolarització dielèctrica. Finalment, en l'última part del capítol es fa un salt cap a l'estudi de nanoestructures de simetria més baixa que l'esfèrica, els denominats *nanorods*. Primer es realitza un estudi comparatiu de l'efecte del medi dielèctric extern sobre nanocristalls esfèrics i *nanorods*, on s'observa una resposta molt més acusada per part dels segons amb importants conseqüències en les seues propietats observables. Aquesta tendència es confirma en l'última part del capítol, on es realitza un estudi exhaustiu dels efectes del confinament dielèctric sobre excitons confinats en *nanorods* homogenis, així com heterogenis on electrons i forats es localitzen preferentment en parts diferents de la nanoestructura.

En el capítol 4 es realitza un estudi DFT-LSDA de l'estructura electrònica de *nanorods* poblats fins amb 20 electrons. En primer lloc, es calculen els espectres d'energies d'addició al llarg d'un procés en el que un nanocristall esfèric es va transformant en un *nanorod* fins arribar a formar un sistema quasi unidimensional. En segon lloc, s'estudien les transicions de fase que

x

experimenta la densitat electrònica de l'estat fonamental a mesura que els *nanorods* esdevenen més i més anisotròpics i s'assoleix un major règim de correlació electrònica.

Finalment, en el capítol 5 es realitza un breu resum de la present memòria de tesi on també s'enumeren les majors conclusions dels treballs presentats.

El llistat que s'enumera a continuació conforma la col·lecció d'articles publicats (o enviats a publicar) en revistes científiques de caràcter internacional fruit de la tasca investigadora desenvolupada al llarg d'aquest projecte de tesi doctoral. Al final d'aquesta memòria s'adjunta una còpia de cada un d'ells.

1. J. Planelles i M. Royo, *Magnetic-field control of ground-state transition from delocalized-to-localized electronic density in antiring superlattices*, Physical Review B **73**, 113306 (2006). [2]

2. M. Pi, M. Royo i J. Planelles, *A consistent extension of the local spin density approximation to account for quantum dot mass and dielectric mismatches*, Journal of Applied Physics **100**, 073712 (2006).

3. M. Royo, J. Planelles i M. Pi, *Effective mass and dielectric constant mismatch effects in spherical multishell quantum dots*, Physical Review B **75**, 033302 (2007).

4. F. Rajadell, J.L. Movilla, M. Royo i J. Planelles, *Theory of dielectrically induced surface excitonic states in spherical quantum dots*, Physical Review B **76**, 115312 (2007). [3]

5. J. Planelles, M. Royo i M. Pi, *Nonparabolicity and dielectric effects on addition energy spectra of spherical nanocrystals*, Journal of Applied Physics **102**, 094304 (2007). [4]

6. J. Planelles, F. Rajadell, J.I. Climente, M. Royo i J.L. Movilla, *Electronic states of laterally coupled quantum rings*, Journal of Physics: Conference Series **61**, 936 (2007).

---

[2]Selected for the March 20, 2006 issue of Virtual Journal of Nanoscale Science & Technology, Volume 13, Issue 11.

[3]Selected for the September 24, 2007 issue of Virtual Journal of Nanoscale Science & Technology, Volume 16, Issue 13.

[4]Selected for the November 19, 2007 issue of Virtual Journal of Nanoscale Science & Technology, Volume 16, Issue 21.

7. J. Planelles, F. Rajadell i M. Royo, *Dielectric control of spin in semiconductor spherical quantum dots*, Journal of Applied Physics **104**, 014313 (2008). [5]

8. M. Royo, F. Malet, M. Barranco, M. Pi i J. Planelles, *Isospin phases of vertically coupled double quantum rings under the influence of perpendicular magnetic fields*, Physical Review B **78**, 165308 (2008).

9. J.I. Climente, M. Royo, J.L. Movilla i J. Planelles, *Strong configuration mixing due to dielectric confinement in semiconductor nanorods*, Physical Review B **79**, 161301(R) (2009).

10. J. Planelles, J.I. Climente, M. Royo i J.L Movilla, *Correlation in narrow nanorods: a variational potential–configuration interaction scheme*, Journal of Physics: Condensed Matter **21**, 215801 (2009).

11. J. Planelles, M. Royo, A. Ballester i M. Pi, *From quantum dots to quantum wires: Electronic structure of semiconductor nanorods*, Physical Review B **80**, 045324 (2009). [6]

12. M. Royo, J.I. Climente, J.L. Movilla i J. Planelles, *Dielectric confinement of excitons in type-I and type-II semiconductor nanorods*, enviat a publicar.

---

[5]Selected for the July 28, 2008 issue of Virtual Journal of Nanoscale Science & Technology, Volume 18, Issue 4.

[6]Selected for the August 10, 2009 issue of Virtual Journal of Nanoscale Science & Technology, Volume 20, Issue 6.

Contents

Chapter 1

Introductory theoretical aspects

The aim of this chapter is to perform a brief description of the theoretical frame in which the works presented throughout this thesis are developed. Further specific details that can be found in books or reference papers are skipped. Others, however, will be introduced in subsequent chapters when necessary.

Crystal electronic structure

An ideal crystal is a solid material in which the constituent atoms present an spatial ordering periodic in the three spatial directions. This crystalline structure is held together through the chemical bonds formed by the valence electrons of the constituent atoms. The remaining core electrons are, in turn, strongly attracted by the atomic centers forming closed shell electronic configurations, and therefore do not participate in the bond charge distribution nor contribute to the electronic properties investigated here.

Let us consider the case of III-V binary compounds like GaAs which crystallize in a zinc-blende structure where the elementary unit cell contains an atom of each type. In these systems, there are 8 outer electrons per unit cell which contribute to the chemical bonds. These electrons hybridize to form molecular orbitals to bind an atom of one type (say Ga) and its four nearest neighbors (As). As usual, bonding and antibonding orbitals are formed in this hybridization process, and the valence electrons are distributed in some of them, leaving others unoccupied, in the most stable configuration.

Because there is a large number of unit cells, due to the crystal periodicity, these molecular orbitals broaden into continuous energy bands which form the crystal energy spectrum.

Then, the ground state of an ideal semiconductor crystal is formed by a set of fully occupied bands (valence bands) that are energetically separated by the band gap (E_g) from a set of unoccupied bands (conduction bands). For the case of direct gap semiconductors, as the ones studied here, the most interesting region of the band structure, namely, the energy top and bottom of the valence and conduction bands respectively, occurs at the center of the Brillouin zone (the so-called Γ point). Figure 1.1 shows the energy dispersion vs. the wave vector k around this region. As illustrated in the figure, four energy bands, one conduction band and three valence bands, appear near the band edge. These bands are well separated from the so-called remote bands, which is why the electro-optical properties of most direct semiconductors are mainly determined by the physics of these four bands.
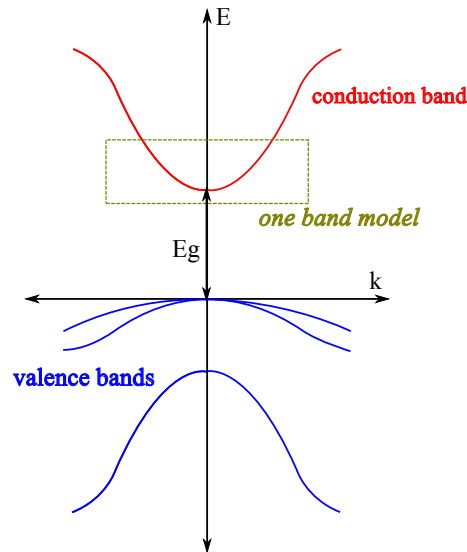
Figure 1.1: Schematic representation of the energy band structure of a direct gap semiconductor around the center of the Brillouin region.

In this thesis, interest is paid in studying excited states of the crystal in which one or more electrons are promoted to the lowest conduction band

(excess electrons). Such excited configuration can be experimentally performed in semiconductor nanostructures by means of methodologies such as single-electron charging from metallic reservoirs, doping or optical excitation of electrons from the valence to the conduction band. In the latter case, empty levels (holes) are also generated in the valence band so that electron-hole pairs are created. Due to their mutual Coulomb attraction, the electron-hole pairs can form bound states known as excitons. Thus, the theoretical treatments carried out along this text are mainly devoted to describe electrons in the lowest conduction band and occasionally holes in the highest valence band.

The effective mass approximation

Neglecting spin-orbit coupling and relativistic effects, the electronic states of an ideal crystal may be obtained from the eigenstates of the following Hamiltonian:

$$
\hat{\mathcal{H}} = \sum_i \frac{\hat{p}_i^2}{2m_i} + \sum_I \frac{\hat{p}_I^2}{2m_I} + \sum_{i<j} \frac{e^2}{4\pi\varepsilon_0|\mathbf{r}_i - \mathbf{r}_j|} + \sum_{I<J} \frac{Z_I Z_J e^2}{4\pi\varepsilon_0|\mathbf{R}_I - \mathbf{R}_J|}
$$
$$
- \sum_{i,I} \frac{Z_I e^2}{4\pi\varepsilon_0|\mathbf{R}_I - \mathbf{r}_i|}. \quad (1.1)
$$

In this expression, the different terms are respectively, the kinetic energy of electrons and nuclei, and the electron-electron, nucleus-nucleus, and electron-nucleus Coulomb interactions. As can be easily deduced, finding the exact solution to the corresponding eigenvalue equation is not possible and therefore a set of physically acceptable approximations have to be introduced in order to simplify the problem.

As a first approximation, due to the higher electron velocity, it can be considered that the nuclei are at rest, and hence, that the electronic motion can be evaluated for a static nuclear arrangement[1]. Secondly, it can be considered that each electron moves under the influence of an averaged electrostatic potential $V_{cr}(\mathbf{r})$ which describes interactions with the other electrons in the crystal and with the static nuclei. Such a potential can be viewed

---

[1]Electronic and nuclear motions are coupled through the so-called electron-phonon interaction, which will not be considered here.

as a three-dimensional lattice of spherically symmetric ionic core potentials screened by the inner shell electrons, which are further surrounded by the covalent bond charge distributions. The motion of an electron will be then given by:

$$\left[\frac{\hat{p}^2}{2m_0} + V_{cr}(\mathbf{r})\right]\psi_{n,k}(\mathbf{r}) = E_{n,k}\,\psi_{n,k}(\mathbf{r}). \tag{1.2}$$

Due to the periodicity of the effective potential $V_{cr}(\mathbf{r})$, the Bloch theorem enables to write the electron wave function as

$$\psi_{n,k}(\mathbf{r}) = e^{i\mathbf{k}\mathbf{r}}u_{n,k}(\mathbf{r}), \tag{1.3}$$

here, $e^{i\mathbf{k}\mathbf{r}}$ is a plane wave slowly varying along the crystal, and $u_{n,k}(\mathbf{r})$ is a Bloch function which has the periodicity of the crystal and describes variations of the wave function within an elementary unit cell. It is labeled by the wave vector k but also by the set of quantum numbers n corresponding to the point symmetry of the crystal.

By introducing this $\psi_{n,k}(\mathbf{r})$ in the wave equation 1.2 and after some algebra, one obtains

$$\underbrace{\left(-\frac{\hbar}{2m_0}\nabla^2 + V_{cr}(\mathbf{r}) + \frac{\hbar^2 k^2}{2m_0} + \frac{\hbar}{m_0}k\,\hat{p}\right)}_{\hat{\mathcal{H}}_{kp}}u_{nk}(\mathbf{r}) = E_{nk}u_{nk}(\mathbf{r}), \tag{1.4}$$

where the terms in brackets constitute the so-called $k\cdot p$ Hamiltonian. When $k = 0$, i.e., the center of the Brillouin zone or Γ point, the solutions of equation 1.4 form a complete set of functions $\{u_{n,0},\ n = 1, 2, 3, \dots\}$, that allows one to construct the wave function for any $k \neq 0$ as a linear combination of these Bloch functions as follows,

$$u_{nk}(\mathbf{r}) = \sum_{n'}^{\infty} u_{n'0}(\mathbf{r})c_{n\,n'}. \tag{1.5}$$

In the above expression, the coefficients $c_{n\,n'}$ are known as envelope functions, and are given as the eigenfunctions of an effective Hamiltonian that is fixed by the details of the band structure of the crystal.

Since interest is here focused on electrons in the conduction band, which is normally well separated from the valence bands (except in narrow gap

semiconductors), one can adopt the simplification of studying this energy band independently (one band model). Thereby, the wave function of an excited state consisting of an electron in the conduction band is just formed from a Bloch function and the corresponding envelope function. In other words, the $k \cdot p$ Hamiltonian is only expanded in an element of the basis 1.5, which yields

$$\langle u_{n0} \mid \hat{\mathcal{H}}_{kp} \mid u_{n0} \rangle = E_{n0} + \frac{k^2}{2m_0}. \tag{1.6}$$

This simplified model leads to a parabolic energy dispersion equivalent to the one of a freely moving electron ($E(k) = \frac{\hbar k^2}{2 m_0}$). Actually, as illustrated in figure 1.1, the region of the conduction band near the $k = 0$ point has a roughly parabolic shape. However, the curvature of this parabola differs from the free electron one and depends on the specific composition and crystalline structure of the semiconductor crystal. In the effective mass approximation (EMA) this different curvature is introduced by means of an empirical parameter called effective mass (m_e^*), which is obtained from a perturbative treatment of the $k \cdot p$ Hamiltonian. Therein, the unperturbed Hamiltonian and the perturbation are defined as

$$\hat{\mathcal{H}}_0 = -\frac{\hbar}{2m_0}\nabla^2 + V_{cr}(\mathbf{r}), \tag{1.7}$$

$$\hat{\mathcal{H}}' = \frac{\hbar^2 k^2}{2m_0} + \frac{\hbar}{m_0}k\,\hat{p}, \tag{1.8}$$

and the energy E_{nk} up to second order of perturbation is

$$E_{nk} = E_{n0} + \sum_{\alpha=x,y,z} \frac{k_\alpha^2}{2} \underbrace{\left[\frac{1}{m_0} + \frac{2}{m_0^2} \sum_{n'} \frac{\mid \mathbf{P}_{nn'}^\alpha \mid^2}{E_{n0} - E_{n'0}} \right]}_{\frac{1}{m_e^*}}. \tag{1.9}$$

In the above expression, the terms in brackets are identified as the inverse of the electron effective mass (m_e^*), where $\mathbf{P}_{nn'}^\alpha$ is an empirical parameter determined through experimental measurements or atomistic calculations. Therefore, within the EMA formalism the conduction band dispersion is given by

$$E(k) = E_{n0} + \frac{\hbar k^2}{2 m_e^*}, \tag{1.10}$$

and the effective Hamiltonian yielding the above energy is

$$\hat{\mathcal{H}} = \frac{\hat{p}^2}{2\,m_e^*}. \tag{1.11}$$

It is therefore easy to conclude that for the case of an infinite periodic crystal (so-called bulk) the envelope function of the conduction band is a plane wave, as indicated by the Bloch theorem (equation 1.3).

In summary, within the EMA the electrons in the conduction band of a crystal are thought of as freely moving particles where the influence of the crystal electrostatic potential and the interactions with the other electrons are taken into account by the introduction of the effective mass. The latter depends on material-specific parameters such as the type of crystal structure, chemical composition and bonding energies.

Nanoscopic heterostructures: the envelope function approximation

The theoretical review performed above has been done under the assumption of an infinite crystal. Nevertheless, the present thesis is devoted to semiconductor heterostructures with nanoscopic sizes. In such systems, the electron motion is confined inside the nanostructure boundaries, which is why the energy spectrum becomes quantized into discrete levels and the ground state is lifted from the bottom of the bulk conduction band.

This spatial confinement is here interpreted as a step-like potential $V(\mathbf{r})$ whose height is set to mimic the band mismatch (band offset) that takes place when two materials of different band gap are placed adjacent to each other and form an heterojunction (see figure 1.2). Then, in order to obtain the envelope function of an electron in the conduction band states of a nanostructure the effective Hamiltonian to solve is:

$$\hat{\mathcal{H}} = \frac{\hat{p}^2}{2\,m_e^*} + V(\mathbf{r}) \tag{1.12}$$

The envelope function approximation (EFA) is the name given to the mathematical justification of a series of arguments which enable to use the EMA formalism to study heterostructured nanoscopic materials by means of Hamiltonians like 1.12 (see for example references [19] and [20]). Among other premises, the EFA considers that all materials forming the heterostructure present the same lattice structure and similar lattice constants, which
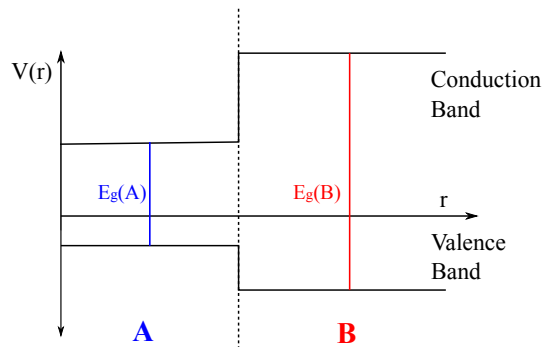
Figure 1.2: One-dimensional representation of the spatial potentials $V(r)$ in the conduction and valence bands that occur at a heterojunction between two dissimilar materials

enables to assign the same Bloch function for the whole system. On the other hand, due to slower variation of the envelope function with respect to the Bloch function, the first one can be evaluated independently of the second one.

One of the strengths of the EMA-EFA formalism is the relative simplicity to include the effect of additional confinements, such as electric or magnetic fields, in the theoretical description of the electron motion. As will be shown in subsequent chapters, this task is often reduced to introducing one-body potentials in Hamiltonian 1.12. In such cases, the single-particle energies and envelope functions of the systems under study are here achieved by numerical integration of the corresponding effective Hamiltonian following a finite differences scheme.

Many-particle systems

Frequently throughout this thesis, systems hosting more than one conduction band electron or an electron-hole pair are studied. The theoretical modeling of such systems involves the introduction in the effective Hamiltonian of a Coulomb term of type $1/\mathbf{r}_{i,j}$. As it is well known, this term greatly hinders the solution of the corresponding eigenvalue equation, this being more problematic with increasing the number of interacting particles. In the works reviewed here two methodologies arisen from different foundations have been used to tackle the problem of interacting particle systems.

On the one hand, configuration interaction (CI) calculations have been carried out when the number of conduction band electrons is small. Within this technique, the full interacting Hamiltonian including the Coulomb interaction term,

$$\hat{\mathcal{H}} = \sum_i \frac{\hat{p}^2}{2\,m_e^*} + \sum_i V(\mathbf{r}) + \sum_{i<j} \frac{e^2}{4\pi\varepsilon_0|\mathbf{r}_i - \mathbf{r}_j|}, \qquad (1.13)$$

is expanded in a basis of Slater determinants built up from single-particle functions. Such treatment renders the closest energies and wave functions to the exact solution. Nonetheless, it becomes computationally intractable in many-electron regimes. In those cases, density functional theory (DFT) calculations within the self-consistent formulation of Kohn-Sham have been carried out to obtain the ground state energy and electron charge density. A detailed description of these methods to deal with electronic correlations is not given here since both CI and DFT methodologies are well known and documented (see for example references [21, 22]).

The formalism followed to describe excitonic states is worth to be outlined, though. As briefly mentioned, excitons are formed when photons of energy comparable to the band gap promote electrons from the valence band, thus creating holes in this band, to the conduction band. Then, the Coulomb attraction between opposite charges leads to formation of bound electron-hole pairs. In order to theoretically model excitons, in this thesis both the electron and the hole have been studied with a one band model, so that the exciton Hamiltonian can be written as

$$\hat{\mathcal{H}} = \frac{\hat{p}^2}{2\,m_e^*} + \frac{\hat{p}^2}{2\,m_h^*} + V^e(\mathbf{r}_e) + V^h(\mathbf{r}_h) - \frac{e^2}{4\pi\varepsilon_0|\mathbf{r}_e - \mathbf{r}_h|}, \qquad (1.14)$$

the last term being the attractive Coulomb interaction. Since just two particles come into play, the exciton energy and wave functions are obtained in this thesis exclusively by means of CI calculations. In this case, however, the Hamiltonians are expanded in a basis of Hartree products since they deal with distinguishable particles not requiring an antisymmetric wave function.

To define the exciton energy, the convention is to put the zero of the energy at the top of the valence band. Thus, as illustrated in figure 1.3, in bulk, the total energy of the exciton is simply the energy of the free

electron-free hole pair (i.e., the band gap) minus the electron-hole Coulomb attraction (E_{eh}). However, in a heterostructure the single particle states are shifted from the bands bottoms due to quantum confinement, so that two additional components, namely, the electron and hole confinement energies, have to be included in the exciton energy. Actually, the exciton energy data presented throughout this text are expressed relative to the bulk band gap, i.e., E_g has been subtracted to the total exciton energy.
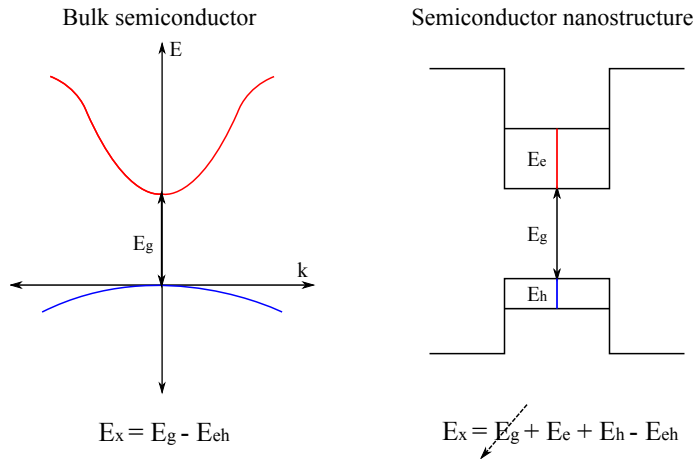
Figure 1.3: Schematic diagrams showing the different contributions to the exciton energy (E_X) in bulk semiconductors and nanostructures.

Another interesting magnitude in the exciton physics is the binding energy (E_b). This refers to the electron-hole bond degree and is calculated as

$$E_b = E_e + E_h - E_X, \tag{1.15}$$

where $E_{e,h}$ are the electron and hole confinement energies and E_X is the exciton energy relative to the bulk band gap. In other words, the binding energy represents the Coulombic correction of a single-particle exciton energy calculation.

Chapter 2

Quantum ring complexes in magnetic fields

Quantum rings (QRs) are semiconductor nanostructures with toroidal, doubly connected, topology which provides them with special quantum properties, particularly interesting are those related with their response to magnetic fields. When a QR is populated with excess carriers and is pierced by an external magnetic field perpendicular to the ring plane, the carriers orbit a magnetic flux in a closed trajectory, which offers the opportunity to observe so-called Aharonov-Bohm effects, such as energy oscillations (see, e.g., figure 2.2(b)) [23, 24] or persistent currents in the ring [25–27]. This pure topological quantum effect, which was theoretically predicted in 1959 [23] and experimentally confirmed in mesoscopic QRs many years later [28, 29], has fascinated the physics community over the last two decades [30–32]. The interest arises, partly, from theoretical motivations, but also from its potential applications in quantum information systems [33, 34].

Nowadays, the advances in experimental synthesis by means of lithographic [35], self-assembly [7,36] or droplet-epitaxy techniques [37,38] enable the formation of QRs with nanoscale sizes, i.e., in the true quantum limit, populated with a small number of electrons (see, e.g, the pictures shown in figure 2.1). This development in growth techniques has been paralleled by new experimental demonstrations of the Aharonov-Bohm effect by means of far infrared and capacitance spectroscopy [39], as well as magnetization measurements [27]. Likewise, although at one time it was thought that Aharonov-Bohm effect was strictly linked to the presence of a net charge in the ring, the effect has been predicted [40, 41] and experimentally observed
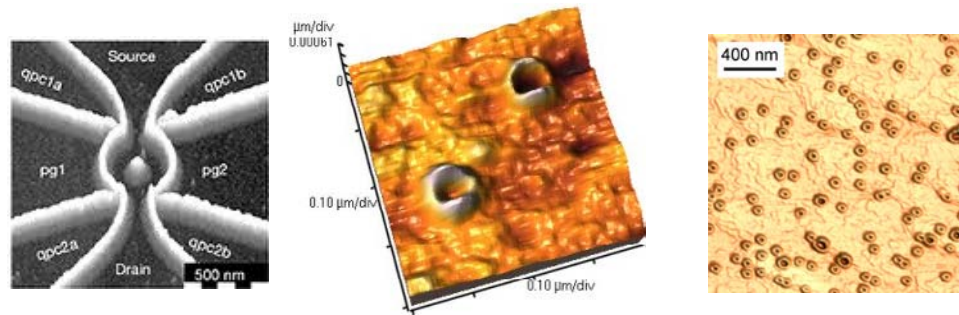
Figure 2.1: Atomic force microscopy images of a lithographed QR (left) and self-assembled QRs (center and right).

through the magneto-photoluminescence spectrum of neutral excitons in QRs [35] and in type-II QDs [42, 43]. This "optical" Aharonov-Bohm effect originates in the non-zero exciton electric dipole momentum caused by the different spatial distribution of the electron and the hole.

Given that the fundamental properties of single QRs are now reasonably well understood, in the last years the aims of theoretical and experimental researchers have started focusing on the study of coupled QR entities and their ability to form molecular states (QR molecules). The present chapter reviews three studies on the electronic spectrum and magnetic field response of different QR complexes: two laterally coupled QRs, two vertically stacked QRs and a QR superlattice. Apart from the magnetic field effect, the chapter stresses the point and translational symmetry properties of the systems under study as well as the role of the electronic correlation on the ground state of QR systems populated with many electrons. Previously, a brief introduction on EMA Hamiltonians accounting for magnetic fields is given in order to set the theoretical treatment employed to model charged nanostructures under the effect of external magnetic fields.
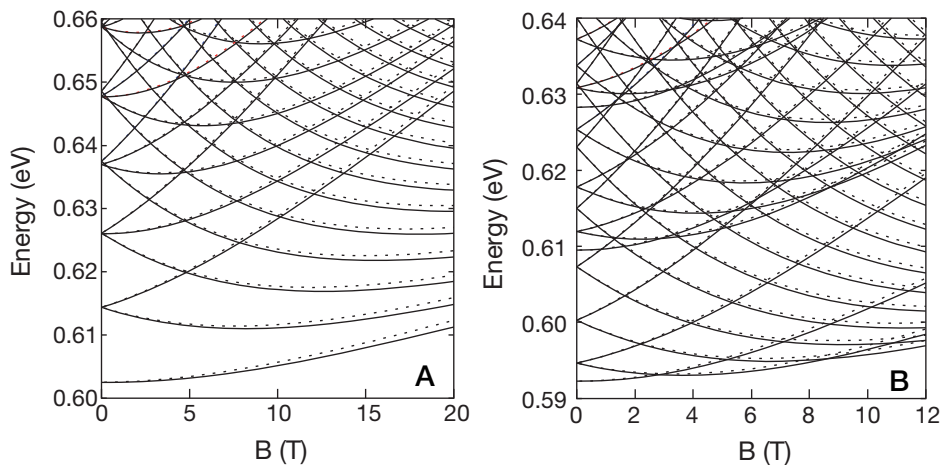
Figure 2.2: Magnetic field evolution of the single-particle spectra of a disk-shaped QD (left panel) and a QR (right panel). Solid and dashed lines represent the spin up and down levels. While in the QD the levels forming the first Landau band do not cross each other, the QR spectrum displays many quasi-periodic crossings between states with different angular momentum. *Taken from Phys. Rev. B 70, 081301 (2004)*

2.1 EMA Hamiltonian in presence of magnetic fields

When a charged particle is under the influence of an external magnetic field **B** the common momentum operator $\hat{p}$ no longer describes properly the kinetics of the system. Instead, the Hamiltonian must be rewritten using the conjugated canonic momentum $(\hat{p} - e\mathbf{A})$. In this expression e stands for the electric charge while **A** is the potential vector which depends on the direction of the magnetic field and accomplishes $\mathbf{B} = \nabla \wedge \mathbf{A}$ [44]. Thus, the EMA Hamiltonian of a single electron confined by a spatial potential $V(\mathbf{r})$ in presence of a magnetic field is

$$\hat{\mathcal{H}} = \frac{1}{2m^*} (\hat{p} - e\mathbf{A})^2 + V(\mathbf{r}), \qquad (2.1)$$

which after expanding the squared term, assuming a gauge $\nabla\mathbf{A} = 0$, reads

$$\hat{\mathcal{H}} = \frac{\hat{p}^2}{2m^*} - \frac{e}{m^*}\mathbf{A}\hat{p} + \frac{e^2}{2m^*}\mathbf{A}^2 + V(\mathbf{r}). \qquad (2.2)$$

The works presented in this chapter are mainly devoted to study the effects of magnetic fields applied perpendicular to the ring plane, namely the z direction. In such cases, it is usual to take the potential vector $\mathbf{A} =$

$\frac{\mathbf{B}}{2}(-y, x, 0)$ (symmetric gauge) which fulfills the gauge condition $\nabla\mathbf{A} = 0$. Bringing this potential vector into Hamiltonian 2.2 and operating leads to the following expression (written in Cartesian coordinates),

$$\hat{\mathcal{H}} = -\frac{\hbar^2}{2m^*}\nabla^2 + \frac{e^2\mathbf{B}^2}{8m^*}\underbrace{(x^2 + y^2)}_{\rho} - \frac{e\mathbf{B}}{2m^*}\underbrace{i\hbar\left(x\frac{\partial}{\partial y} - y\frac{\partial}{\partial x}\right)}_{\hat{L}_z} + V(x, y, z). \quad (2.3)$$

Finally, rewriting equation 2.3 in terms of the z component of the angular momentum operator $\hat{L}_z$ and the cyclotron frequency $\omega_c = -\frac{e\mathbf{B}}{m^*}$ yields

$$\hat{\mathcal{H}} = -\frac{\hbar^2}{2m^*}\nabla^2 + \frac{1}{8}m\omega_c^2\rho + \frac{1}{2}\omega_c\hat{L}_z + V(x, y, z). \quad (2.4)$$

Hence, the inclusion of the magnetic field causes the appearance of two new terms in the EMA Hamiltonian. The linear term has predominant effects at low-intensity fields or strongly confined systems (e.g., atoms). On the other hand, the quadratic term has the form of a harmonic potential, and it will produce noticeable effects when it overtakes the spatial confining potential V. This condition will be favored at strong fields and weakly confined systems (e.g., electron gases).

The inclusion of the electronic spin [1] entails two additional terms, namely, the Zeeman effect term $g\mu_B\sigma\mathbf{B}$ (here g is the Landé factor, μ_B is the Bohr magneton and σ is the electronic spin) and the spin-orbit coupling term. The latter is normally neglected in studies of electrons in the conduction band because this band is mainly formed from s-type orbitals so that the spin-orbit coupling is very weak [45]. Consequently, the spin-orbit contributions have not been regarded in the works reviewed along the present chapter.

---

[1] In this chapter the electronic spin only plays a role in the DFT calculations of section 2.4.

2.2 Laterally coupled quantum rings under the effect of magnetic fields

One of the most appealing properties of semiconductor QDs is their ability to form coupled entities. When two QDs are close enough they can become tunnel-coupled, and in the ideal case of two identical dots their individual energy levels will be in resonance. When this occurs, the states localized in the individual dots hybridize forming molecular-like states, in good analogy with atomic molecular bonds [46–48]. However, today is almost inconceivable to experimentally grow two identical QDs, which is why the resonance condition is set normally by means of external electric and magnetic fields [49,50]. Unlike atomic molecules, these "artificial molecules" offer the interesting possibility to engineer some of their properties, such as the bond length, the material, shape and size of the individual components or the number and nature of carriers, during and after the process of fabrication. Consequently, semiconductor artificial molecules have become the ideal scenario to learn basic physics of molecular systems [51–53].

Vertically and laterally coupled QDs approximately disc-shaped have been extensively studied since they were proposed as entangled photon emitters [48], and candidate building blocks for the development of scalable two-qubit logic gates, entering the challenging area of the quantum computation [9]. However, the appearance of QR systems capable to undergo molecular coupling took place later than their QD counterparts, which is why the first works focusing on systems of coupled QRs were carried out in the recent years. Works on complexes formed of vertically coupled [54–65] and concentric QRs [37,66–72] have been reported, but at the moment of realization of the work exposed here, little attention had been yet paid on systems of laterally coupled quantum rings (LCQRs). This is nonetheless an interesting problem since LCQRs constitute artificial molecules with unique topology (two LCQRs may be multiply-connected), what should be reflected in unique energy structures. Besides, as can be observed in the right picture of figure 2.1, the formation of pairs of LCQRs in the synthesis of self-assembled QRs is apparent [73,74].

This section reviews a study of the magnetic field effect on the low-lying energy levels and wave functions of a single-electron located in two identical GaAs LCQRs [75]. This kind of self-assembled QRs normally present much stronger spatial confinement in the axial direction than in the equato-
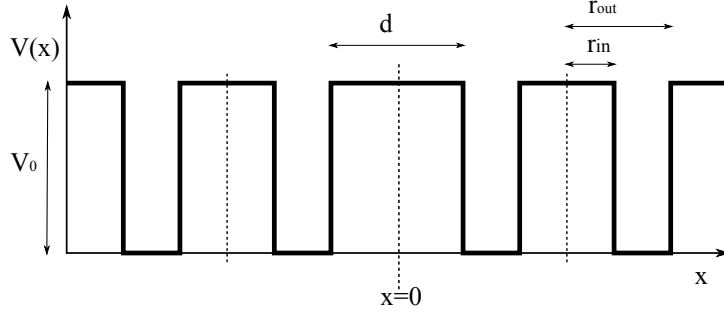
Figure 2.3: Confining potential profile in the direction of molecular coupling

rial plane. As a consequence, one can assume the adiabatic approximation in which the electron motion in the in-plane and vertical directions is decoupled. Therein, the bottom of the energy spectrum is formed from the lowest vertical state and many in-plane states. By this reason, and following a common modus operandi [35,39,76], a two-dimensional EMA and EFA Hamiltonian describing the in-plane confinement is employed to study the low-lying states of the system of two LCQRs:

$$\hat{\mathcal{H}} = \frac{1}{2m^*}(\hat{p} + \mathbf{A})^2 + V(x, y). \tag{2.5}$$

Where $V(x, y)$ is the step-like potential that confines the electron within the lateral limits of the double ring heterostructure (see figure 2.3). The x direction is taken as the direction of molecular coupling. The external magnetic field is applied parallel to the axial and the two in-plane axes. Hence, three different potential vectors have to be employed. Actually, the choice of $\mathbf{A}$ is limited by the requirement that it should make it possible to separate x-y coordinates from z in the Hamiltonian [77]. The following potential vectors fulfill this condition for each direction of the applied magnetic field B: $A_{B_z} = \frac{B}{2}(-y, x, 0)$, $A_{B_x} = B(0, 0, y)$ and $A_{B_y} = B(0, 0, -x)$. Replacing these potential vectors in equation 2.5 yields the Hamiltonian whose eigenvalues and eigenvectors are analyzed below:

$$\hat{\mathcal{H}}(B_z) = \frac{\hat{p}_\parallel^2}{2m^*} + \frac{B_z^2}{8\,m^*}(x^2 + y^2) - i\frac{B_z}{2\,m^*}\left(x\frac{\partial}{\partial y} - y\frac{\partial}{\partial x}\right) + V(x, y), \tag{2.6}$$

$$\hat{\mathcal{H}}(B_x) = \frac{\hat{p}_\parallel^2}{2m^*} + \frac{B_x^2}{2\,m^*}y^2 + V(x, y), \tag{2.7}$$

$$\hat{\mathcal{H}}(B_y) = \frac{\hat{p}_{\parallel}^2}{2m^*} + \frac{B_y^2}{2\,m^*}x^2 + V(x,y). \tag{2.8}$$

Two identical QRs are considered, with an inner radius $r_{in} = 12$ nm and outer radius $r_{out} = 16$ nm. A constant effective mass of $m^* = 0.067$ is employed. In turn, the confining potential is zero inside the QRs (GaAs) and $V_0 = 0.262$ eV outside (AlGaAs) [78]. The above Hamiltonians are numerically integrated on a two-dimensional grid (x, y) for growing inter-ring distances d, thus simulating a process of dissociation of the QR molecule.
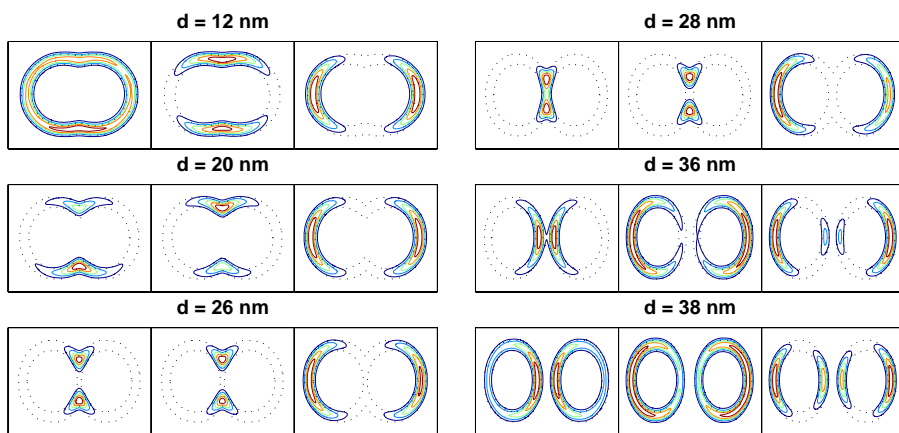
Figure 2.4: Contours of the charge densities corresponding to the three lowest-lying electron states (from left to right) of LCQRs with different inter-ring distance d at $B = 0$. Dotted lines denote the confinement potential profile.

Let us start by studying the wave function localization in absence of external fields throughout the dissociation process of the molecule. This will be useful later to analyze the magnetic response of the system. Particularly, when the magnetic field is applied along the vertical direction, in which case the field barely squeezes the wave functions. Figure 2.4 illustrates the charge density of the three lowest-lying electron states for increasing values of the inter-ring distance d. The dotted lines represent the corresponding profiles of the confining potential barrier. When the QRs are strongly coupled ($d = 12$ nm) the system resembles a single elliptical QR. Consequently one can clearly identify an *s*-like ground state and two *p*-like excited states. As can be seen in the figures, some excess of charge density is placed in the roomy regions where the two QRs overlap. The available space in these

regions first increases as the rings are separated which tends to localize the ground and first excited states in such regions ($d = 20$ nm) until they eventually become the even and odd solutions of a double quantum well ($d \sim 26$ nm). For further increased inter-ring distance, an inner arm of the LCQRs is formed. The ground state tends to localize along it ($d = 28$ nm), thus benefiting from a reduced centrifugal energy. Meanwhile, the excited states, which are not so prone to minimize centrifugal forces due to their p-like symmetry, prefer to spread along the external arms of the rings. Finally, when the rings begin to be detached ($d = 36$ nm) the tunneling between both structures tends to localize the ground state mostly in the middle of the LCQRs, an effect that vanishes as the rings are further separated ($d = 38$ nm) evolving into the ground state of single QRs. All along the dissociation process, the second and higher excited states remain relatively insensitive to changes in the inter-ring distance due to their larger kinetic energy.
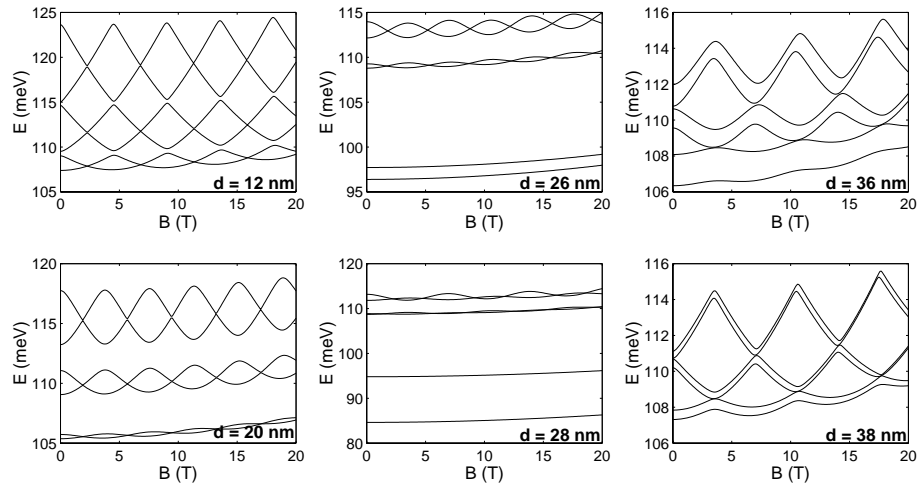
Figure 2.5: Low-lying electron energy levels vs axial magnetic field in LCQRs with different inter-ring distances.

Figure 2.5 plots the evolution of the low-lying energy levels with an axial magnetic field B_z for several inter-ring distances. As can be observed, when the rings are strongly coupled ($d = 12$ nm) the spectrum displays the usual Aharonov-Bohm oscillations of a single QR (see, e.g., figure 2.2(b)) [32, 77], except for the anticrossings appearing between sets of two consecutive energy levels. These anticrossings are a consequence of the lack of perfect circular symmetry (C_∞ point group) of the electron states. As stated ear-

lier, in this coupling regime the system has a rather elliptical symmetry (unlike single QRs). Therefore, the pairs of eigenvalues which cross one another correspond to the two irreducible representations of the C_2 symmetry group. As the inter-ring distance increases, the ellipsoid formed by the rings has a larger eccentricity resulting in larger anticrossings gaps. Furthermore, the above mentioned trend of the two lowest-lying states to become the even and odd solutions of a double quantum well, reduces the amplitude of their oscillations due to a reduced efficiency to trap magnetic flux (see, e.g., the $d = 20$ nm panel in figure 2.5). Eventually, when the ground state entirely localizes along the inner arm of the LCQRs the limit behavior of a QD is retrieved, as displayed in figure 2.5 for $d = 26$ nm and $d = 28$ nm. Finally, when the rings are detached the spectra resemble that of isolated QRs with a vanishing disturbance arising from the tunneling between the rings. Note that in this weak-coupling limit, the period of the Aharonov-Bohm oscillations is larger than in the strongly coupled limit. This is due to the smaller area of the inner holes of the individual rings as compared to the elliptical-like structure.
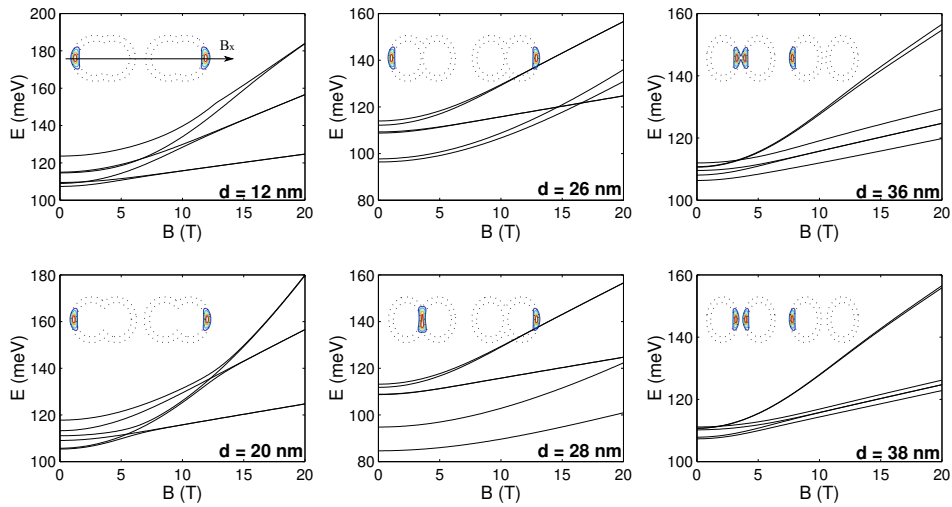
Figure 2.6: Low-lying electron energy levels vs in-plane magnetic field in LCQRs with different inter-ring distances. The field is applied parallel to the dissociation axis. The insets show the charge densities of the two lowest-lying electron states (from left to right) at $B = 20$ T.

The effect of external magnetic fields applied along the in-plane directions produces a less regular response in the energy spectra of the system

because, in this case, the field reshapes the wave functions. Specifically, fields applied along the dissociation axis B_x tend to squeeze the electron wave function in the y direction, whereas the opposite holds for B_y. Figures 2.6 and 2.7 show the energy levels against magnetic fields applied along the x and y directions for the same inter-ring distances discussed earlier. When the rings are strongly coupled ($d = 12 - 20$ nm) a common trend to form pairs of degenerate states is observed as the intensity of both fields is increased. These are the even and odd solutions of double quantum wells built up in the longitudinal (B_x) and transversal (B_y) edges of the ring structure, whose formation is a direct consequence of the mentioned wave function modeling by the in-plane fields. The formation of these double-well solutions, which are illustrated in the insets of figures 2.6 and 2.7 for the first pair of states, was also predicted for single QRs [77]. However, an additional feature is present in a pair of LCQRs: the anisotropic spatial confinement leads to an anisotropic response to magnetic fields applied along the x and y directions. An example is the field at which the double well solutions are formed. Whereas the two lowest-lying states at $d = 12$ nm become degenerate at $B \sim 5$ T for B_y, they do so at $B \sim 8$ T for B_x. In intermediate regimes (see, e.g., $d = 26$ nm), the states which in absence of external fields have singly-connected wave functions show a QD-like magnetic response, i.e., they depend weakly on the external field. Conversely, the doubly-connected states keep on behaving as in a QR, forming double-well solutions. Finally, for weakly coupled QRs ($d \sim 38$ nm), different limits are reached depending on the in-plane magnetic field direction. While B_y tends to localize the charge density in the vicinity of the inter-ring region, thus favoring tunneling phenomena, for B_x the states are alternatively localized in the inner or in the outer edges of the QRs.

To summarize, the electron states of nanoscopic LCQRs have been studied as a function of the inter-ring distance and external magnetic fields. In absence of external fields the wave function localization changes dramatically with the inter-ring distance which gives rise to characteristic magnetic response for different coupling regimes. Moreover, a clearly anisotropic response is found for in-plane fields applied parallel or perpendicular to the LCQRs dissociation direction. These results suggest that magneto-optic experiments on LCQRs may provide valuable information on the strength of coupling and the orientation of the QR molecule.
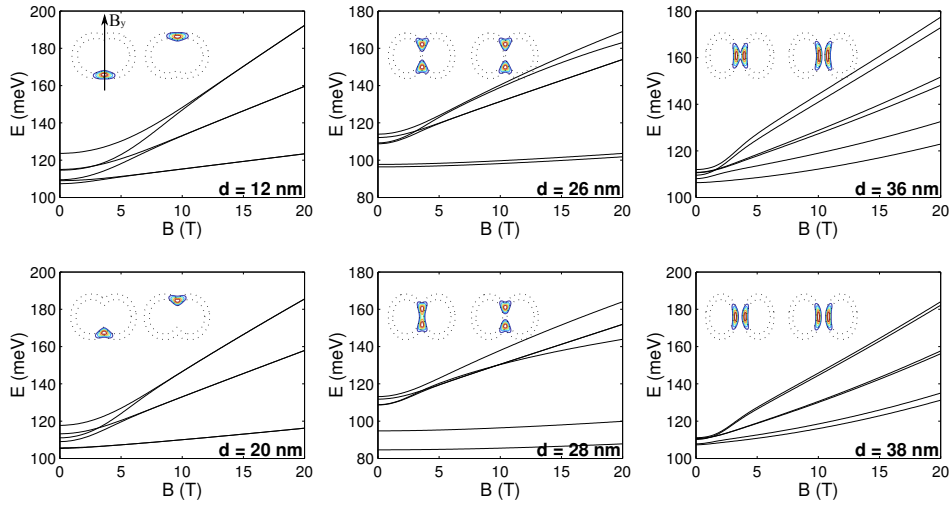
Figure 2.7: The same as figure 2.6 but the field is now applied perpendicular to the dissociation axis

2.3 Magnetic modulation of two-dimensional superlattices

The study of two-dimensional electron systems, often referred to as two-dimensional electron gases (2DEGs), affected by magnetic and periodic spatial confinements has long fascinated the theoretical physics community [79–87]. The bewitching features of these systems proceed from the competition of two characteristic length scales: the lattice constant, which determines the periodicity of the lattice potential, and the Landau length, which characterizes the semi-classical magnetic electron orbits. Thereby, when a 2DEG is pierced by a perpendicular magnetic field, the magnetic confinement quantizes the system into the well known Landau bands [88]. The interesting point for the present section appears though, when periodic repulsive islands are grown over the two-dimensional plane. This periodic spatial confinement splits the Landau bands into subbands, resulting in the celebrated Hofstadter-Butterfly spectrum [89], a fractal magnetic dispersion of the electronic spectrum first observed in tight-binding calculations on 2DEGs.

Semiconductor superlattices formed from arrays of QDs, which act as potential wells for electrons, and antidots (ADs), which act as potential
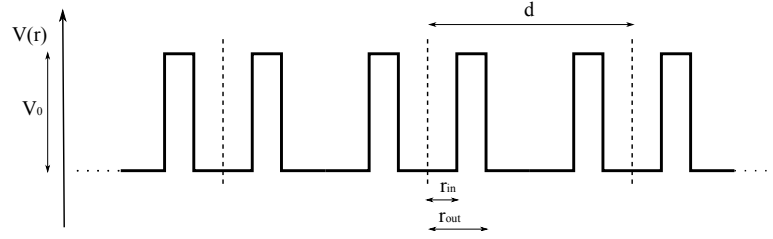
Figure 2.8: Confining potential profile along a lattice direction passing through the ARs centers. Three neighbor spatial unit cells are represented.

barriers (see figure 2.9), have been widely studied [15]. Apart from the mentioned butterfly-like spectrum, applying perpendicular magnetic fields on these periodic systems produces various interesting phenomena, including the quenching of the Hall effect [90] or the appearance of periodic energy oscillations versus the magnetic field B (Aharonov-Bohm type) and versus $1/B$ (Subnikov-de Has type) [91, 92]. Periodic systems formed from QRs or antirings (ARs) remain almost unexplored despite the interesting magnetic response of these ring-shaped nanostructures. The present section reviews a study on the electronic properties of AR superlattices under the influence of perpendicular magnetic fields [93]. The choice of ARs as building constituents of the supperlattice is made with the intention of finding a spatial confinement regime where an external magnetic field could induce ground state transitions between states localized in the inner holes of the rings and states delocalized over the outer region. Such a result would suggest the possibility of employing self-assembled arrays of ARs as the building blocks of magnetic field-controlled electron transport devices.

To theoretically model the system of an electron in the two-dimensional (x, y) plane in presence of a perpendicular magnetic field, a single-particle Hamiltonian similar to that presented in the previous section (equation 2.5) is employed. Now, however, $V(x, y)$ represents the periodic potential of the lattice which is step-like: it has a constant value V_0 in the potential barrier regions and it is set to zero in the potential well regions (see figure 2.8). The eigenvalue equation of the Hamiltonian is numerically solved on a two-dimensional grid which defines the spatial unit cell with an AR located in the center. To this end, proper boundary conditions should be employed that simulate the magnetic and periodic features of the system. Here, the main difficulty lies in the fact that while the superlattice is periodic, the Hamiltonian (including the magnetic potential vector) is not. As

a consequence, common spatial translation operators ($\hat{T}(\mathbf{R}) = e^{-i\mathbf{R}\cdot\mathbf{p}}$) do not commute with the Hamiltonian and usual periodic boundary conditions cannot be employed. The proper symmetry operations that fulfill the real symmetry of the present system and, hence, commute with the Hamiltonian are known as magnetotranslations [94]:

$$\hat{T}_A(\mathbf{R}) = e^{-i\mathbf{R}\cdot(\mathbf{p}-\mathbf{A})}. \tag{2.9}$$

Here $\mathbf{R}$ stands for the translation vector, $\mathbf{p}$ is the momentum and $\mathbf{A}$ the potential vector. To find the useful boundary conditions, $\hat{T}_A(\mathbf{R})f(\mathbf{r})$ should yield the function $f(\mathbf{r})$ up to a phase factor $e^{i\phi}$,

$$\hat{T}_A(\mathbf{R})f(\mathbf{r}) = e^{i\mathbf{R}\cdot\mathbf{A}} \underbrace{e^{-i\mathbf{R}\cdot\mathbf{p}}}_{\hat{T}(\mathbf{R})} f(\mathbf{r}) = e^{i\mathbf{R}\cdot\mathbf{A}} f(\mathbf{r}-\mathbf{R}) = e^{i\phi} f(\mathbf{r}), \tag{2.10}$$

then, regrouping the last two terms leads to

$$f(\mathbf{r}) = e^{-i\phi} e^{i\mathbf{R}\cdot\mathbf{A}} f(\mathbf{r}-\mathbf{R}), \tag{2.11}$$

which are the practical boundary conditions to impose on the eigenfunctions. Considering that to describe the uniform perpendicular magnetic field $B = (0,0,B)$ the Landau gauge is employed $A = B(0,x,0)$, the specific boundary conditions used in the calculations in both in-plane directions are:

$$f(\mathbf{r}) = e^{-i\phi} f(\mathbf{r}-\mathbf{R_x}), \tag{2.12}$$

$$f(\mathbf{r}) = e^{-i\mathbf{R_y}B\,x} e^{-i\phi} f(\mathbf{r}-\mathbf{R_y}). \tag{2.13}$$

Where it can be observed that the Landau gauge preserves the translational symmetry of the periodic potential along the vector $\mathbf{R_x} = (d,0,0)$ (with d being the lattice constant) so that x-magnetotranslations are just spatial translations.

By means of this outlined numerical procedure an InGaAs AR superlattice is studied. The rings have inner radii $r_{in} = 10$ nm and outer radii $r_{out} = 13$ nm, and are embedded in an InAs matrix forming a square lattice of constant $d = 45$ nm. Thus, the ARs have a radial section of 3 nm acting as a barrier for the electrons in the InAs matrix due to a conduction band offset between materials of $V_0 = 0.3$ eV [95, 96]. Also, since the electrons are placed in the InAs regions, the InAs electron effective mass has been
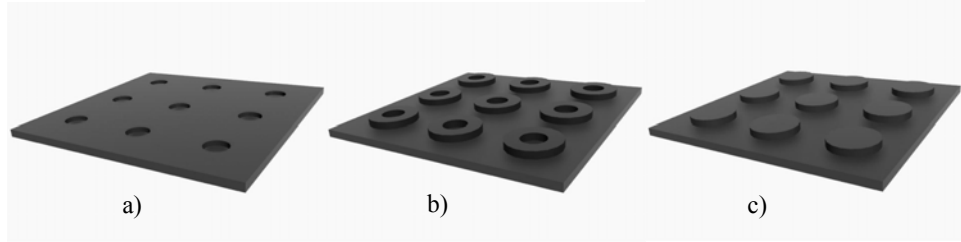
Figure 2.9: The three studied superlattices, formed from a) QDs, b) ARs and c) ADs. Nine spatial unit cells are represented.

employed, $m^* = 0.03$ [97, 98]. As discussed below, the electronic spectrum of AR superlattices can be interpreted as a superposition of localized states trapped in the inner AR cores (which act as a QD) and delocalized states which do not penetrate into the AR regions (the ARs acting as ADs for these states). By this reason, two additional superlattices are also studied for the sake of comparison, namely, a superlattice of $r = 10$ nm InAs QDs (i.e., with the same radius as r_{in} in the ARs superlattice) embedded in InGaAs, and another of $r = 13$ nm InGaAs ADs (i.e., with radius equal to r_{out} in the ARs superlattice) embedded in InAs, both with the same lattice constant $d = 45$ nm.

The results corresponding to the low-lying states at the Γ point of the reciprocal lattices are shown in figure 2.10. The superlattice of QDs (panel (a) in figure 2.10) shows the simplest magnetic dispersion of the energy levels. These evolve as states of small isolated QDs, i.e., the field dependence is almost exclusively linear. [2] What is more, even though the lattice has C_{4v} symmetry which reduces to C_4 in presence of the magnetic field, the calculated electron charge densities display axial symmetry with a value nearly zero at the unit cell border (not shown). This fact reveals that the QD system does not feel the lattice point nor the translational symmetry and behaves as a set of isolated circular QDs.

The opposite situation can be found in figure 2.10(c) for the AD superlattice spectrum. In this case, the electronic charge density is spread over the InAs matrix with finite values at the cell border, thus the energy spec-

---

[2]Remember from section 2.1 that the quadratic term of the magnetic field has significant effects when it takes over the spatial confinement which does not hold for the present case.
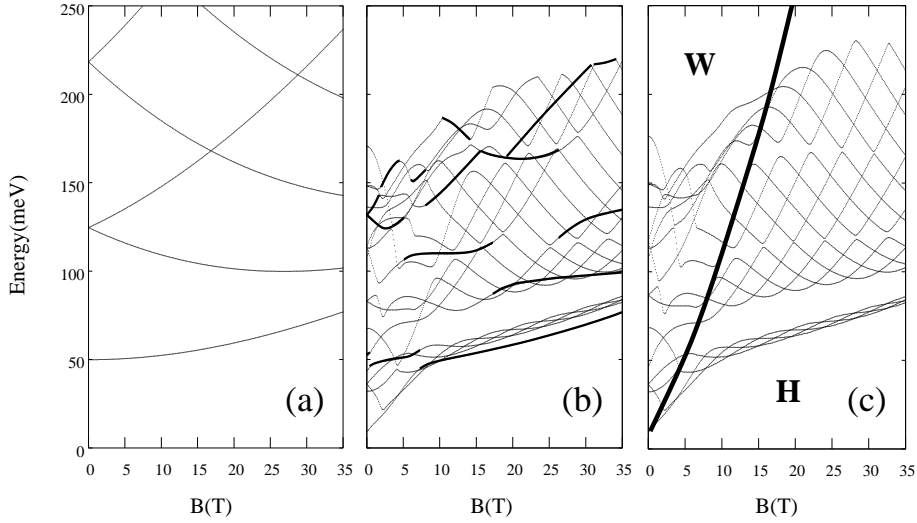
Figure 2.10: Energy spectra of two-dimensional superlattices ($d = 45$ nm) for three different potential profiles as a function of the magnetic field (a) QD, (b) AR and (c) AD. Solid lines in (b) correspond to states localized within the AR core, and thin lines to states delocalized over the outer region. The thick solid line in (c) is the border between the weak field (**W**) and the high field (**H**) regimes.

trum reveals the symmetry of the lattice. In the plot, the spectrum has been divided in two regions by a solid thick line. The region labeled with **W** corresponds to the weak magnetic field regime. In this area the periodic spatial confinement dominates over the magnetic confinement, which is why the spectrum does not show regularities. On the other hand, in the high magnetic field regime (the region labeled with **H**) the magnetic confinement predominates. Consequently, at first glance this part of the spectrum resembles that of a single QR with the typical Aharonov-Bohm oscillations due to the non-simply connected topology of the electron domain. However, some new features appear illustrating the symmetry of the system. As can be observed, the spectrum forms sets of four levels which cross as B increases, but at the same time anticross with the other sets of states. Every set contains one instance of each of the four C_4 symmetries, namely, A, B, E_+ and E_- whose crossings are allowed by symmetry rules. The anticrossings consequently appear when one of these levels approach its similar from the next set, in such a case crossings are not allowed by symmetry rules.

The spectrum of figure 2.10(b) can be viewed as a superposition of the QD and AD spectra. The solid lines in the plot represent states completely

localized within the ARs cores while the thin lines correspond to states delocalized over the outer InAs matrix. This spectrum provides evidence for the sought property. At low magnetic fields, the ground state, which belongs to the totally symmetric irreducible representation A of C_4, is a delocalized state. It becomes strongly destabilized by increasing the magnetic field due to the diamagnetic term in the Hamiltonian which has an important effect on this weakly confined states. On the other hand, the second A-symmetry state is completely localized within the AR core (lowest solid line in figure 2.10(b)) and it is almost unaffected by the magnetic field (it behaves like the $M = 0$ state of a QD). As a consequence, an anticrossing between the two A states occurs and leads the ground state to become localized for magnetic fields higher than 9 T. Therefore, the desired transition from delocalized to localized electronic states has been proved. To illustrate it, figure 2.11 shows the electron charge density of the ground state at $B = 0$ T and $B = 15$ T.

(a)   (b)
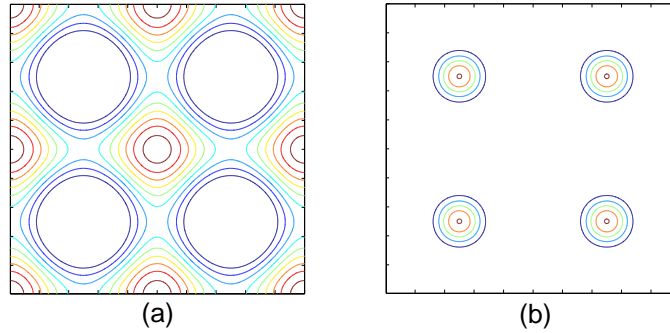
Figure 2.11: Contours of the ground state electronic density at (a) $B = 0$ T and (b) $B = 15$ T corresponding to the AR superlattice. Four neighbor spatial unit cells are represented.

In summary, the study of AR superlattices pierced by perpendicular magnetic fields has demonstrated that the magnetic dispersion of the energy spectrum can be viewed as a superposition of localized states trapped in the AR cores and delocalized states which do not penetrate into the AR regions. Besides, it has been proved that by choosing the appropriate AR geometry and spacing, a transition from a delocalized to a localized ground state can be externally controlled by the applied magnetic field. This suggest the possibility of employing self-assembled arrays of ARs as the building blocks of magnetic field-controlled transport nanodevices.

2.4 Many-electron states of vertically coupled quantum rings under perpendicular magnetic fields

Artificial molecules based on two vertically coupled QDs (QDMs) are probably the type of complexes consisting of coupled zero-dimensional nanostructures that has generated most research interest hitherto. One of the main reasons for this is their aforementioned potential applications in solid state-based quantum computation. To date, several models have been proposed which make use of the charge and spin degrees of freedom of a small number of carriers confined in QDMs to develop logical quantum gates (e.g., two electrons [9, 99], an exciton [48] or a positively charged exciton [100]). In parallel with this justified interest on the few-body physics of QDMs, during the last decade a remarkable variety of works have focused their attention on the study of many-electron states of two vertically coupled QDs. This interest arose as a consequence of the realization of single-electron tunneling experiments on vertically coupled QDs which allowed to populate the dots with a high number of electrons [50, 51, 101–103], thus revealing new molecular-type phases that were highly sensitive to the inter-dot separation (molecular coupling), the number of electrons and external magnetic fields. The fact that these new phases can be monitored in the electron addition energies has motivated a considerable number of theoretical works that seek to reproduce addition energy spectra of QDMs as well as to identify the many-electron configurations as a function of the molecular coupling [51, 104–106] and external magnetic fields [102, 103, 107–109].

Recently, molecular-beam epitaxy techniques have enabled the synthesis of quantum ring molecules (QRMs) in form of vertically stacked layers of self-assembled QRs [54, 55], where the strain fields favor the nucleation of upper rings right on top of bottom rings, so that the circular symmetry of the QR systems is preserved. This achievement, has sparked theoretical studies on the structure and optical response of vertically coupled QRs of different complexity and scope, revealing properties different from those of their QD counterparts [56, 57, 61, 64, 65, 110, 111]. For instance, studies on the single-electron states of vertical QRMs have shown that the electronic spectrum of these systems is expected to be more sensitive to the inter-ring distance than that of coupled QDs [57]. This is because the coupling-induced energy splitting is as large as that of self-assembled dots, but the energy spacing between consecutive states in typical self-assembled rings is smaller than that in dots, the ring-like morphology favoring the stabilization

of azimuthal states. On the other hand, unlike the QDM case, there exists a gap in the bibliography concerning the realization of any kind of single-electron transport experiment capable of achieving the addition energies of vertical QRMs; this has been carried out for a single QR [112], though. Very recently, vertically coupled QRs populated with few tens of electrons have been theoretically studied at zero magnetic field [58, 60], and the electron addition spectra have been obtained for different coupling regimes and sizes of the constituents rings.

The work reviewed in this section studies the ground state of two verti-cally coupled identical QRs forming "homonuclear" QRMs populated with up to 40 electrons and pierced by a perpendicularly applied magnetic field [59]. This work extends and complements a previous work carried out at zero magnetic field [58], and addresses the appearance and physical interplay be-tween the spin and isospin (an analogous magnitude to the bond order in molecular physics) degrees of freedom as functions of the variation in both the intensity of the magnetic field and the inter-ring separation.

Modeling systems charged with large number of electrons, as in the present case, requires the employment of methodologies that minimize the computational cost such as mean field methods. The numerical results presented in this section have been obtained by means of density func-tional theory (DFT) calculations within the local spin density approxima-tion (LSDA) [22, 113]. The accuracy of the numerical code employed to carry out these calculations has been assessed for the considered values of the magnetic field by comparing results with those given by the current spin density functional theory (CSDFT) [114], which is in principle better suited for high magnetic fields, and also with benchmark configuration interaction (CI) methods [106]. The numerical procedure follows the self-consistent formulation of Kohn-Sham [115] and the single-particle aspects of the elec-tronic spectrum are modeled within the framework of the effective mass and envelope function approximations. In this way, the Kohn-Sham equations written in cylindrical coordinates and atomic units read

$$
\left[-\frac{1}{2m^*} \left(\frac{\partial^2}{\partial r^2} + \frac{1}{r}\frac{\partial}{\partial r} - \frac{l^2}{r^2} + \frac{\partial^2}{\partial z^2} \right) - \frac{\omega_c}{2} l + \frac{1}{8}\omega_c^2 r^2 + V_{cf}(r,z) \right.
$$

$$
\left. + \Phi + V_{xc} + \left(W_{xc} + \frac{1}{2}g^*\mu_B B \right) \eta_\sigma \right] u_{nl\sigma}(r,z) = \varepsilon_{nl\sigma} u_{nl\sigma}(r,z) \; .
$$

(2.14)

Here, the Hamiltonian has been integrated over the azimuthal angle θ and the electron spin σ. In turn, the single-particle wave functions have been factorized in the form $\phi_{nl\sigma}(r, z, \theta, \sigma) = u_{nl\sigma}(r, z)e^{-il\theta}\chi_\sigma$, where $n = 0, 1, 2, \ldots$ is the main quantum number, $l = 0, \pm 1, \pm 2, \ldots$ represents the projection of the angular momentum on the symmetry axis (actually, due to the convention commonly adopted for the single-particle wave functions [104] the projection of the angular momentum is $-l$) and $\sigma = \uparrow(\downarrow)$ represents spin-up (-down) states. To include the effect of an external perpendicular magnetic field the vector potential has been chosen in the symmetric gauge, namely, $A = B(-y, x, 0)/2$. Additionally, the magnetic Zeeman term has been also regarded, with g being the gyromagnetic factor, $\mu_B = \hbar e/(2m_e c)$ the Bohr magneton, $\omega_c = eB/cm^*$ the cyclotron frequency and $\eta_\sigma = +1(-1)$ for $\sigma = \uparrow(\downarrow)$. $V_{cf}(r, z)$ is the spatial confining potential which confines the electrons inside the double ring structure. This potential has been taken parabolic in the (x, y) plane with a repulsive step-like core of radius R_0 around the origin [3], plus a double quantum well in the z direction:

$$V_{cf}(r, z) = V_{cf}(r) + V(z), \tag{2.15}$$

$$V_{cf}(r) = \begin{cases} V_0 & \text{if } r_0, \\ 1/2\, m\, \omega_0^2\, (r - R_0)^2 & \text{if } r > R_0. \end{cases} \tag{2.16}$$

Representations of the transversal and longitudinal profiles of the aforementioned confining potential are illustrated in figure 2.12. All the material parameters specified in the picture remain constant, only the inter-ring distance d is varied to study QRMs with different molecular coupling.

The remaining terms in equation 2.14 correspond to many-body interaction contributions. Thus, Φ is the Coulomb potential which is obtained by solving the Poisson equation, whereas V_{xc} and W_{xc} are the exchange-correlation potentials in terms of the ground state electronic density $\rho(r, z)$ and the spin magnetization $\zeta(r, z) \equiv \rho^\uparrow(r, z) - \rho^\downarrow(r, z)$:

$$V_{xc} = \frac{\partial \mathcal{E}_{xc}(\rho, \zeta)}{\partial \rho}\Big|_{gs} \ ; \ \ W_{xc} = \frac{\partial \mathcal{E}_{xc}(\rho, \zeta)}{\partial \zeta}\Big|_{gs}. \tag{2.17}$$

According to LSDA the exchange-correlation functional can be expressed as sum of two local contributions, i.e., $\mathcal{E}_{xc}(\rho, \zeta) \equiv \mathcal{E}_x(\rho, \zeta) + \mathcal{E}_c(\rho, \zeta)$. The

---

[3]The convenience of this hard-wall inner potential is endorsed by several works in the literature [57, 116, 117].
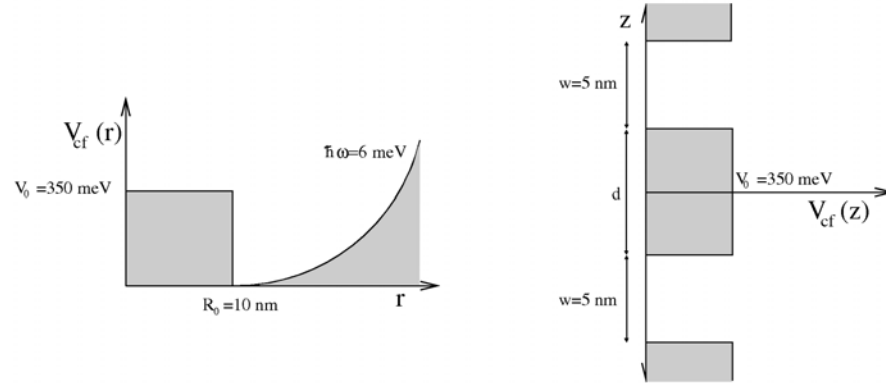
Figure 2.12: Radial and longitudinal profiles of the confining potential employed in the calculations

Dirac exchange functional $\mathcal{E}_x(\rho, \zeta)$ is employed, which corresponds to a three-dimensional homogeneous electron gas [118]. Finally, the parametrization proposed by Perdew and Zunger has been used for the correlation term [119]. To compute the ground state energy and electronic density, the Kohn-Sham and Poisson equations are iteratively solved in a multi-grid discretization scheme and using imaginary time methods to speed the convergence process up (further computational details can be found in Ref. [104]).

The numerical calculations are carried for GaAs coupled QRs considering different inter-ring distances, $d = 2, 4$ and 6 nm, with the aim of simulating different molecular coupling regimes. The GaAs material parameters are employed, namely, dielectric constant $\varepsilon = 12.4$, effective mass $m^* = 0.067$ and effective gyromagnetic factor $g^* = -0.44$. For the sake of comparison, the case of a single QR with the same shape and size as the individual components of the QRMs is also addressed.

A good way to tackle the magnetic field response of highly populated systems is to look at the evolution of the Kohn-Sham orbitals. To this end, figure 2.13 shows the Kohn-Sham levels for a single ring hosting N=40 electrons as a function of the orbital quantum number l for different values of the applied magnetic field. The horizontal line in the plots represents the energy of the highest occupied single-particle orbital (also referred to as the chemical potential or Fermi level). Thus, the levels lying under this line conform the electronic configuration of the system. At zero magnetic field,
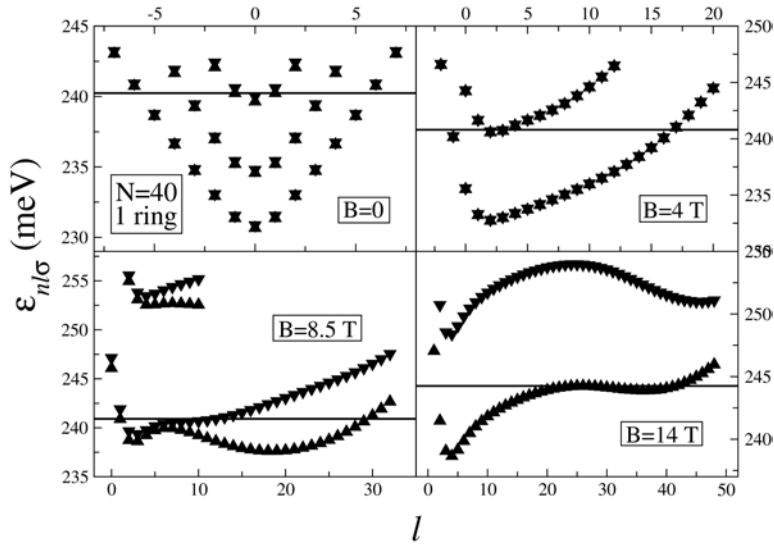
Figure 2.13: Kohn-Sham orbitals energies as functions of l for a N=40 single QR. Upward (downward) triangles denote up (down) spin states. The horizontal lines represent the Fermi levels. The value of the magnetic field is indicated in each panel.

the levels with $\pm l$ are degenerate and the ground state of the system is made up of states with up to n=3. In this case, all the plotted levels correspond to symmetric states (hereafter referred to as bonding states) with respect the $z = 0$ plane (the antisymmetric states will be represented by empty triangles). Hence, the labels $n = 2$ and $n = 3$ imply that these states develop nodal surfaces along the radial direction but not yet in the vertical direction. This fact is a direct consequence of the stronger confinement in the longitudinal direction as compared to that in the radial one.

When the magnetic field is switched on the $\pm l$ degeneracy is lifted. As the intensity of the field is increased the $-l$ states become destabilized and depopulated in favor of the l states which are stabilized by the field. At the same time, the states with $n \neq 1$ become depopulated too, reaching a situation where only $l > 0$ states from the first Landau band are occupied. From here on, the main features caused by increasing the external field are related with the different Zeeman and exchange potentials experienced by states with different spin quantum number σ, thus breaking the spin-up spin-down degeneracy. Finally, as can be observed in the $B = 14$ T case, the system becomes fully spin-polarized. This peculiar electronic configuration

is known as maximum density droplet (MDD) and has been experimentally observed in a QD under the influence of intense magnetic fields [120].
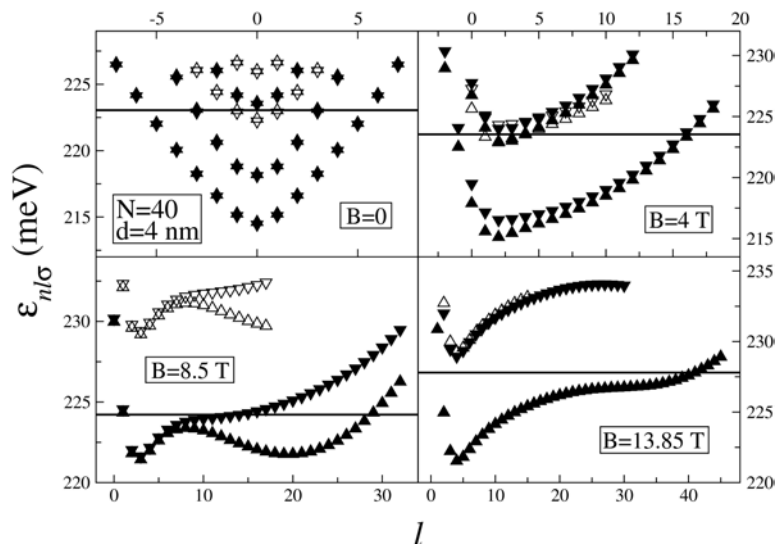
Figure 2.14: Same as figure 2.13 for a QRM with $N = 40$ electrons and $d = 4$ nm. Bonding and antibonding states are indicated by solid and open triangles respectively.

The electron occupation of the Kohn-Sham orbitals for the case of the QRMs will obviously be marked by the relative stabilization of the anti-symmetric (antibonding) orbitals. These will become lower in energy as the rings are separated, but the extent of this stabilization is strongly dependent on the axial and longitudinal confinements. For the present study, inter-ring distances of $d = 2$ and 4 nm have proven systems showing strong coupling regime signatures as will be promptly shown. The evolution of the Kohn-Sham orbitals for the $d = 2$ nm molecule is qualitatively identical to the single ring case with only bonding states occupied (results not shown here). As d is increased until 4 nm a few antibonding orbitals become populated at small fields (see the top panels of figure 2.14). However, the magnetic field favors the occupation of higher orbital momentum bonding states and eventually the system becomes again completely formed from bonding states.

The scenario is quite different for the largest ring separation considered, namely, $d = 6$ nm. As illustrated in figure 2.15, a large amount of anti-bonding orbitals take part in the electronic configuration, which has some consequences on the magnetic field response of the QRM. The most relevant
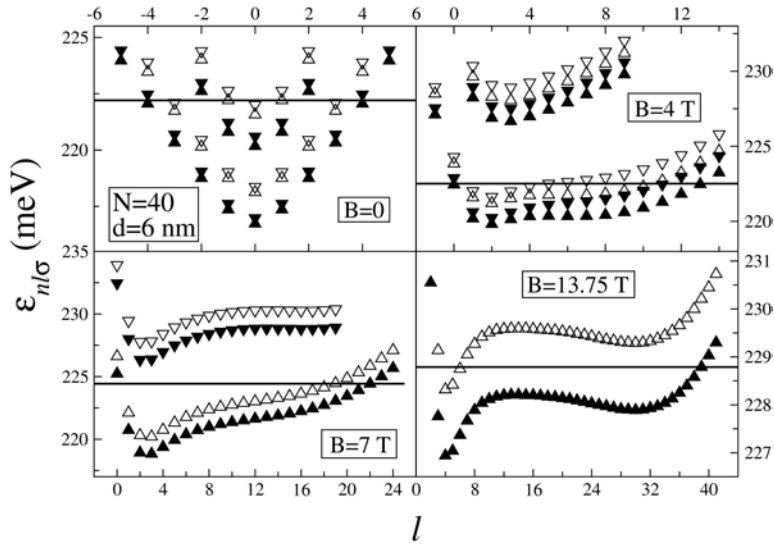
Figure 2.15: Same as figure 2.14 for $d = 6$ nm

one is the appearance of the fully spin-polarized state at smaller fields: it is attained at $B \sim 7$ T whereas for $d = 2$ and 4 nm it appears near $B \sim 14$ T. This is a consequence of the energetic proximity between the first bonding and antibonding bands, which enables formation of a mixed spin-polarized phase by populating spin-up orbitals of each band.

When antibonding orbitals are populated, the variation of the magnetic field yields numerous transitions between molecular phases with different number of electrons in bonding and antibonding states. To label these phases and quantify the bound strength, the "isospin" quantum number I_z (bound order in molecular physics) is defined as $I_z = (N_B - N_{AB})/2$, with $N_{B(AB)}$ being the number of occupied bonding (antibonding) states. The total spin (S_z) and isospin phases as functions of the magnetic field are shown in figure 2.16 for $d = 6$ nm and $N = 8$, 16 and 24 electrons. The visible transitions are more complex than those observed in vertically coupled QDs [102–104], which is due to the periodic destabilization experienced by the lowest-l occupied orbitals induced by the magnetic field. This direct consequence of the Aharonov-Bohm effect makes it rather difficult to find a pattern among the observed evolutions for the different electronic populations, unlike it was done for the case of molecules formed from QDs [102–104]. Nevertheless, two facts also present in QDMs are worth to be stressed: on the one
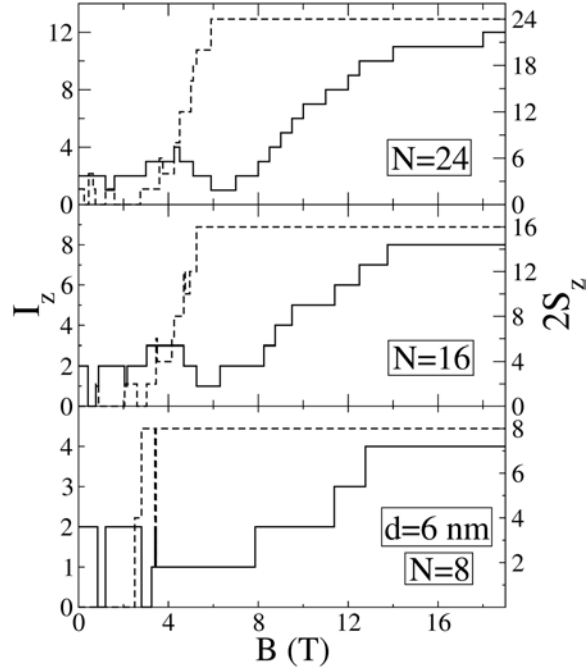
Figure 2.16: Isospin (solid line, left scale) and spin (dashed line, right scale) values as functions of B for QRMs with $d = 6$ nm and $N = 8$, 16, and 24.

hand, molecular phase transitions involving changes from ground states with odd (even) to even (odd) number of electrons in antibonding states involve $\Delta I_z = +1(-1)$ flips; on the other hand, quite often the transitions in S_z and I_z take place simultaneously except obviously when the full spin-polarized point is reached, from which on the isospin increases in one-unit jumps until the system is made up of bonding states only.

The electron addition energies (Δ_2 or E_{add}) have also been studied. These magnitudes can be obtained as

$$\Delta_2(N) = \mu(N) - \mu(N-1). \tag{2.18}$$

Here, $\mu(N)$ is the chemical potential of the N-electron system computed as follows,

$$\mu(N) = E(N+1) - E(N) \tag{2.19}$$

where E(N) is the ground state energy of the N-electron system. Hence, the
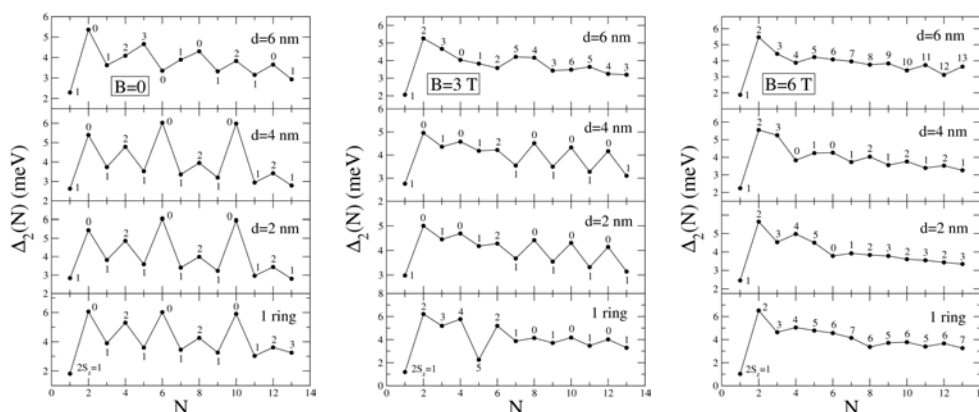
Figure 2.17: Addition energy spectra for QRMs at different magnetic fields and inter-ring distances $d =2$, 4 and 6 nm and for a single QR. The value of $2S_z$ is indicated for each N number of electrons.

chemical potential is an analogous magnitude to the atomic electron affinity, while the addition energies mimics differences in electron affinities. The panels in figure 2.17 represent the addition energy spectra for the above studied QRMs populated with up to 14 electrons under magnetic fields of 0, 3 and 6 T. The case of a single QR is also shown for the sake of comparison. In the left panels ($B = 0$ T) one can see that, once more, the spectra of QRMs with inter-ring distances 2 and 4 nm are qualitatively identical to the single ring one, showing the usual intense peaks denoting closed shells at $N = 2$, 6 and 10, and the peaks at $N = 4$ and 8 corresponding to half-filled shells. The spectrum for the molecule with $d = 6$ nm is shown in the top left panel of the same figure. One can see that, although some of the pronounced peaks are preserved (in particular those at $N = 2$ and 8), the ones at $N = 4$ and 6 no longer exist due to the filling of the first antibonding orbitals. Despite these differences with the single ring case, the addition spectrum evidences that 6 nm is not a separation large enough for the QRMs to be in the weak coupling limit. In such a case, one would expect to find peaks at the same N values as for the single QR multiplied by 2, i.e., $N = 4$, 12 and 20, indicating that the rings are so apart that they behave as isolated entities.

When the magnetic field is tuned in to $B = 3$ T, the spectra of the single QR and that of the molecules with $d = 2$ and 4 nm evolve in a rather similar way, still showing a shell-like structure. The main difference appears for small number of electrons (see the peaks of $N \leq 5$ in the bottom center panel of figure 2.17) since the single ring system develops spin-polarized con-

figurations. This striking phase is attributed to the combined effect of the magnetic field and a relative strong exchange-correlation interaction characteristic of few-electron QR systems. In turn, for larger inter-ring distances ($d = 6$ nm), the occupancy of the first antibonding orbitals washes out the shell structure and the spectrum becomes flatter and irregular.

As can be observed in the right panels of the same figure, when the magnetic field is $B = 6$ T, the only marked peak is the one at $N = 2$, with the rest of the spectra being rather flat as a consequence of the Landau bands flattening that takes place at high fields (see the previous figures showing the Kohn-Sham levels). Also, as commented earlier, the occupation of the antibonding orbitals leads to the fully spin-polarized phase at smaller fields, which is why the spectrum corresponding to $d = 6$ nm shows sequential unit-jumps in $2S_z$ every time an electron is added to the system.

To summarize, the DFT-LSDA results reported here for vertical QRMs have shown that in the strong coupling regime the magnetic response of the Kohn-Sham levels and the addition energies is similar to that of a single QR. However, when the rings are moved apart and the first antibonding orbitals are populated, the addition spectra become flatter and irregular and the system reaches the fully spin-polarized electronic configuration at relatively low magnetic fields.

Finally, it is worth noting that the reviewed results may be helpful in the analysis of future tunneling or capacitance spectroscopy measures on vertically coupled QRs. In such experiments, the evolution of the chemical potential $\mu(N)$ with the magnetic field can be experimentally identified as the variation in the position of the current peaks as a function of the magnetic field, showing irregularities arising from phase transitions [102, 103].

Chapter 3

Dielectric confinement of semiconductor nanocrystals

The beginnings of the 21st century have witnessed significant advances in the chemical synthesis of nanostructures [8, 121–123]. Such procedures enable the synthesis of a wide range of semiconductor nanocrystals (NCs) in form of colloidal suspension (see, e.g., figure 3.1), where the NCs ensembles normally present very low defects density and size dispersion. Since the QDs obtained through these colloidal protocols present the smallest sizes that can be obtained nowadays, the size-dependent spectrum of carriers in these nanosystems is one of the most identifiable manifestation of quantum confinement [14, 124]. Furthermore, the fact that the NCs size and shape, and hence the electro-optical properties, are easily controlled during the process of fabrication, confers promising applications to NCs as building blocks of novel optoelectronic devices. These range from lasers [125] or light-emitting-diodes (LEDs) [126] to solar cells [127]. Also, the NCs fluorescence emission is employed in biolabelling due to their superior photostability compared with the majority of organic dyes [128, 129]. What is more, very recently, one of the main drawbacks of the optical behavior of colloidal NCs, their randomly intermittent fluorescence emission (blinking) [130], has been overcome [131, 132], thus boosting their technological prospects [133].

From a purely physical point of view, the research in the field of semiconductor NCs has been mainly focused on quantifying the size- and shape-dependence of their electro-optical properties. With this aim, considerable work has been carried out probing the electronic states both by optical spectroscopy [134, 135], as well as by single electron tunneling [136]. How-
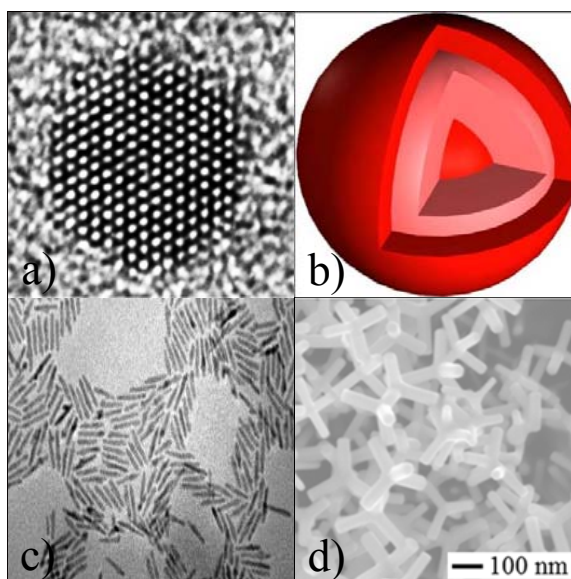
Figure 3.1: Images of several nanosctructures that can be synthesized by means of colloidal chemistry: a) spherical NC, b) multishell NC, c) nanorods, and d) nanotetrapods.

ever, spatial confinement is not the only source of quantum confinement in these structures. All the aforementioned technological applications require the NCs to be buried in matrices like organic solvents, glasses, polymers or even biological media, which present the common property of having a much smaller dielectric constant than semiconductor materials. The dielectric constant mismatch between the NC and the environment is the source of the so-called dielectric confinement.

According to the electrodynamics of continuous media, the carriers confined in a system which includes dielectric mismatches induce the appearance of polarization charges at the dielectric interfaces [88]. These induced charges have the same (opposite) sign as the source charges when the material hosting the carriers has a higher (lower) dielectric constant than the adjacent material. A schematic representation of the surface charges formation is shown in figure 3.2. As a consequence of the interaction with these polarization charges, two new contributions to the energy of carriers arise. On the one hand, there is a single-particle contribution coming from the interaction of the carriers with their own induced charges (self-polarization energy). On the other hand, there are many-particle contributions coming

from the interaction of a carrier with the charges induced by the other ones (polarization of the Coulomb interaction).
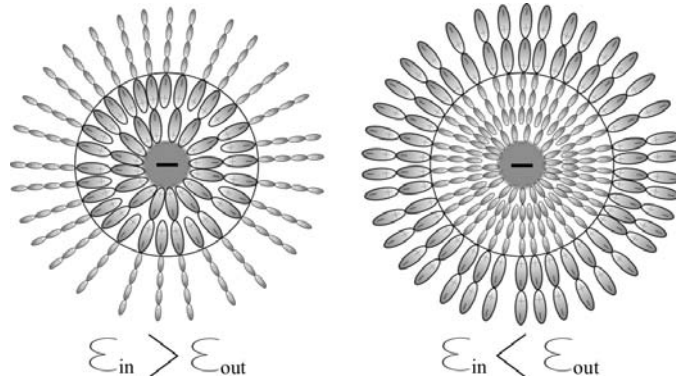
Figure 3.2: Schematics of the formation of polarization charges induced by a negative charge distribution located inside a spherical NC. The different sizes of the represented dipoles mimic the different material polarizability, which is directly related with the dielectric constant. As can be seen, the different polarizability of the NC and the environment leads to charge accumulation at the NC surface. When $\varepsilon_{in} > \varepsilon_{out}$ the surface charge has a predominant negative sign while it is positive when $\varepsilon_{in} < \varepsilon_{out}$

The impact of the system-environment dielectric mismatch on the electronic states of carriers in semiconductor QDs was first studied by L.E. Brus [137, 138]. In his works, he adapted a set of analytical expressions from classic electrodynamics to model ideal spherical systems with carriers confined by infinite barriers, so that, the wave function extension outside the QD region was zero. This simplification is not always good and over the years more sophisticated treatments of the dielectric confinement have been developed to consider non-infinite confining systems and different nanostructure shapes [139–145]. The results reported have demonstrated that the dielectric confinement can have a strong influence on the properties of QDs, often suggesting an alternative Coulomb interaction engineering by controlling the dielectric character of the environment.

Given the electrostatic nature of the energetic contributions introduced by the dielectric confinement, the kind and magnitude of its effects are not the same when a QD is optically excited (forming electron-hole pairs) than when the dot is populated with several electrons through, for example, single-electron tunneling techniques:

- When a QD is populated with an electron-hole pair (exciton), the self-polarization energy and the polarization of the Coulomb interaction have opposite signs. As a result, both terms tend to cancel each other and the effect of the dielectric confinement is minimized. Even so, a relevant implication of the dielectric mismatch observed in some nanosystems is the enhancement of the exciton binding energy [138, 146,147]. This effect, which was first pointed by L.V. Keldysh [148] and later on experimentally confirmed [149,150], has been often suggested as a way of increasing the binding energy above the thermal (kT) energy, which is an essential condition to exploit exciton states in optical devices. On the other hand, several experimental works have recently suggested that the dielectric confinement plays an important role in the formation of QD clusters in high-density QD arrays [151–153].

- When the carriers inside the QDs have the same sign, both dielectric contributions act in the same direction, consequently the dielectric confinement effect is more relevant and can even compete with the spatial confinement in large dielectric constant mismatch regimes. The first consequence of this high influence is a considerable dependence of the electronic spectrum with the dielectric constant of the environment [138]. Additionally, the dielectric modulation of the electron-electron interactions can affect a magnitude as important in the physics of QDs as the Coulomb blockade, yielding quantitative and qualitative reconstructions in the addition energy spectra [154–157]. Transport properties can also be altered by the dielectric confinement. Thus, it has been reported that the electron mobility in nanostructures can be drastically improved by coating them with high dielectric constant materials on account of the screening of the Coulomb interactions induced by these environments [158].

The present chapter reviews a set of seven papers concerning dielectric confinement effects on many-electron spectra and optical properties of semiconductor NCs. After a brief theoretical introduction on EMA-EFA formalisms accounting for dielectric mismatch effects, the first part of the chapter focuses on spherical QDs, either homogeneous or multi-layered, populated with many electrons. To study such systems with a high number of correlated electrons, an extension of the DFT and LSDA is developed which accounts for dielectric constant and effective mass discontinuities in a consistent way [159]. The model is subsequently adapted to include the

non-parabolic dispersion of the conduction band in narrow gap semiconductors [160].

In second place, the excitonic states of dielectrically mismatched spherical NCs are studied. Special attention is paid to the possible formation of surface states in which one or both carriers can be localized in the self-polarization potential well. The transition from volumetric to surface states is found to bring about implications in the NCs luminescence [161].

Finally, the study of the dielectric confinement is extended to the case of elongated NCs also known as quantum rods or nanorods (NRs). The reduced symmetry of these colloidal nanostructures seriously hampers the resolution of the Poisson equation (see eq. 3.8 in the next section), to the point that up to the publication of the papers reviewed here, very few theoretical works are found in the literature tackling the dielectric confinement effect on these quasi-1D systems [162, 163]. By this reason, a detailed description of the methodology employed to compute the dielectric confinement contributions in axial symmetry systems will be given [145]. To conclude the chapter, the effects of the dielectric environment on the electro-optical properties of semiconductor NRs will be reviewed. The results will reveal how the anisotropic shape of these systems has implications on the appearance of responses to the environment hitherto not observed in spherical NCs [164, 165].

3.1   Dielectric confinement in the EMA-EFA formalism

When there is more than one electron (or hole) confined in a QD, Coulomb interaction arises. Macroscopically, the interaction between charges in a dielectric medium is screened by its dielectric constant. However, from a microscopic point of view, conduction band electrons, together with core electrons and nuclei, are located in a vacuum, so that no homogeneous screening dielectric medium is seen by them. Nevertheless, as far as EMA and EFA are concerned, where the microscopic details of the unit cell are integrated, the interaction of conduction band electrons with core electrons and nuclei is averaged as an interaction with a continuous medium able to be polarized. In other words, EMA recovers for the Coulomb interaction the macroscopic-like view.

Within the framework of classical electrodynamics, in the simplest case of two point-charges q_1, q_2 at $\mathbf{r_1}$, $\mathbf{r_2}$ in the crystal bulk, the electrostatic (or Coulomb) potential $\Phi(\mathbf{r})$ generated by one charge and the electrostatic energy W of the system can be obtained as,

$$\Phi(\mathbf{r}) = \frac{q_1}{\varepsilon|\mathbf{r} - \mathbf{r_1}|}, \tag{3.1}$$

$$W = \frac{q_1 \, q_2}{\varepsilon|\mathbf{r_1} - \mathbf{r_2}|}, \tag{3.2}$$

where the background dielectric constant ε accounts for the screening of the bare Coulomb interaction through the macroscopic polarization of the medium. The equivalent equations for the case of a continuous charge distribution, as the ones studied here, are

$$\Phi(\mathbf{r}) = \int \frac{\rho(\mathbf{r_1})}{\varepsilon|\mathbf{r} - \mathbf{r_1}|} d\mathbf{r_1}, \tag{3.3}$$

$$W = \frac{1}{2} \int \int \frac{\rho(\mathbf{r_1})\rho(\mathbf{r_2})}{\varepsilon|\mathbf{r_1} - \mathbf{r_2}|} d\mathbf{r_1} \, d\mathbf{r_2}. \tag{3.4}$$

In general, the methodologies followed in this thesis to deal with Coulomb interactions require numerical discretization of the charge distributions. In this process, the continuous charge can be viewed as a distribution of point charges q_k located at the k points of the discretization grid, and then it can be written as $\rho(\mathbf{r}) = \sum_k q_k \, \delta(\mathbf{r} - \mathbf{r}_k)$, where $\delta(\mathbf{r} - \mathbf{r}_k)$ is a Dirac delta

centered at point k. In this way, the corresponding equations to compute the Coulomb potential and energy can be expressed as

$$\Phi(\mathbf{r}) = \sum_i \frac{q_i}{\varepsilon |\mathbf{r} - \mathbf{r}_i|}, \tag{3.5}$$

$$W = \frac{1}{2} \sum_{i,j} \frac{q_i \, q_j}{\varepsilon |\mathbf{r}_i - \mathbf{r}_j|}. \tag{3.6}$$

The factor $1/2$ appearing in equations 3.4 and 3.6 is included in order to avoid considering twice the interaction between pairs of differential or point charges respectively. Likewise, it is also necessary to subtract the infinite-valued self-interaction terms,

$$\lim_{r \to 0} \frac{q_i^2}{\varepsilon \, r}, \tag{3.7}$$

to avoid the interaction of a charge with itself.

The equations introduced above are valid as long as a continuous medium is considered. However, in the presence of interfaces between media with different dielectric constants, additional effects of surface polarization on the effective Coulomb interaction should be also included, and equations like 3.3 and 3.4 are no longer proper. Instead, the electrostatic potential and energy must be inferred from the Poisson equation:

$$\nabla_r(\varepsilon(\mathbf{r}) \, \nabla_r \Phi(\mathbf{r}', \mathbf{r})) = -4\pi \rho(\mathbf{r}'). \tag{3.8}$$

Here, $\Phi(\mathbf{r}', \mathbf{r})$ is the electrostatic potential generated by a charge distribution $\rho(\mathbf{r}')$ in the $\mathbf{r}$ points of a system with a position dependent dielectric constant $\varepsilon(\mathbf{r})$. This potential includes the contribution of both the bare Coulomb and the dielectric polarization of the Coulomb interaction. Equation 3.8 can be analytically solved for certain simple cases, however, other less symmetric problems only admit a numerical solution of the Poisson equation, with appropriate boundary conditions.

On the other hand, in the presence of dielectric surface polarization, an additional self-interaction energy appears. It comes from the interaction of a charge with its own induced charges. Schematically speaking, the calculation of this self-energy requires, firstly, the numerical solution of the Poisson equation (eq. 3.8) for a point charge located at an arbitrary position $\mathbf{r}'$.

Then, after subtracting the bare Coulomb terms and dividing by two, as in equations 3.4 and 3.6, one should take the limit

$$V_s(\mathbf{r}) = \frac{1}{2} \lim_{\mathbf{r} \to \mathbf{r}'} \Phi(\mathbf{r}, \mathbf{r}'). \tag{3.9}$$

In the above equation, $V_s(\mathbf{r})$ is the self-polarization potential which can be described as the electrostatic potential generated in the point $\mathbf{r}$ by the surface image charges induced by a point charge located in the same position $\mathbf{r}$. For practical purposes, the self-polarization potential is incorporated in the Hamiltonian as a single-particle potential whose main features are (see figure 3.3): i) a constant shift of the energy bottom in the region of higher dielectric constant, ii) the appearance of a soft repulsive barrier in the regions of the higher dielectric constant closer to the interface, and iii) a deep narrow attractive potential well in the lower dielectric constant region just attached to the interface. The depth of this self-energy potential well is proportional to the dielectric mismatch, to the point that in strong mismatch regimes carriers can be trapped in this well, as will be shown in section 3.3, forming surface states.
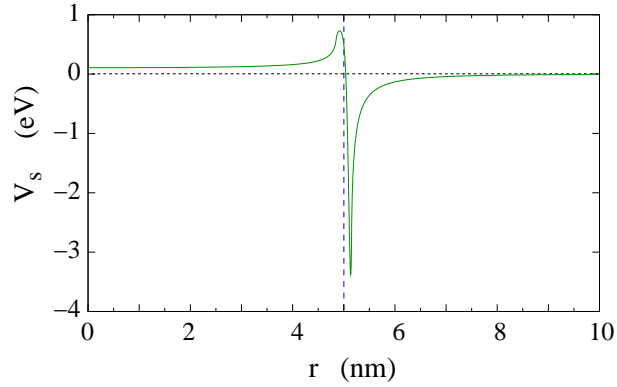
Figure 3.3: Radial profile of the self-polarization potential for a QD of radius $R = 5$ nm and a dielectric constant $\varepsilon_{QD} = 4$ in air or vacuum ($\varepsilon_{out} = 1$)

3.2 Dielectric confinement of many-electron colloidal nanocrystals

Semiconductor QDs are well known to exhibit a set of discrete energy levels, which is why they are often considered as artificial atoms [2]. Special mention deserve the chemically synthesized NCs. Unlike self-assembled or lithographic QDs, these NCs have a nearly spherical shape leading to atom-like symmetries and degeneracies for the electronic states. This issue has been experimentally probed, clearly showing s- and p-like sets of states [166–169]. To this end, one of the most employed techniques is scanning-tunneling-spectroscopy (STS) [170]. In such experiments, a metallic tip is positioned on top of a specific NC, and tunneling current voltage spectrum is acquired by applying a bias between the tip and the substrate where the dot is placed. The conductance dI/dV shows, as a function of the voltage, a series of sharp peaks which correspond to the N_{th} electron (hole) charging energies $\mu_{(N)}$ (or chemical potentials). In turn, the voltage spacings between these conductance peaks are related to differences of chemical potentials $\mu_{(N)} - \mu_{(N-1)}$ and, therefore, correspond to addition energies. Accordingly, from tunneling conductance measures one can obtain the addition energy spectra which is, actually, a usual procedure [171].

Most STS experiments that employ metallic electrodes can resolve the spectra up to a relatively small number of electrons, so that the d-like shell is hardly ever observed [166, 167]. However, very recently a new kind of transport experiment has been reported which employs a carbon nanotube as the only electrode [172]. The authors of this experiment claim they are able to monitor the sequential charge of a CdSe NCs with as much as 200 electrons, thus opening the door of the many-electron physics in semiconductor colloidal NCs.

Following these trends, the present section is devoted to study the electronic and addition energy spectra of spherical NCs populated with a large number of electrons. The ground state energy is obtained by solving the Kohn-Sham equations where the exchange correlation contributions are evaluated within the local spin density approximation (LSDA). The effects of dielectric constant and effective mass discontinuities, as well as an energy dependent effective mass (to account for conduction band non-parabolicity effects) are under consideration. To this end, the different contributions to the energy functional, as well as their corresponding potentials entering the

Kohn-Sham equations are properly modified [159] as shown in the incoming section.

3.2.1 Consistent extension of the LSDA to account for mass and dielectric mismatches

In multilayered QDs (as the one in figure 3.1(b)) and also in homogeneous QDs with finite potential barriers, where the wave function penetrates in the surroundings, carriers experience different effective masses in different materials. To compute the kinetic energy of such particles taking into account the position dependent mass, the most accepted hermitian operator is the one suggested by BenDaniel and Duke [173]:

$$\hat{T} = -\frac{\hbar^2}{2} \nabla \left(\frac{1}{m^*(\mathbf{r})} \nabla \right). \tag{3.10}$$

From this operator, the kinetic energy functional of the ideal system of N non-interacting electrons adopted in the Kohn-Sham formalism is

$$T_s[\rho] = \sum_i^N -\frac{\hbar^2}{2} \int \psi_i(\mathbf{r})^* \nabla \left(\frac{1}{m^*(\mathbf{r})} \nabla \psi_i(\mathbf{r}) \right) d\mathbf{r}. \tag{3.11}$$

However, for the case of bounded systems, i.e., systems with zero electronic density at the boundaries, the kinetic functional can be rewritten as

$$T_s[\rho] = \sum_i^N \int \frac{\hbar^2}{2m^*(\mathbf{r})} |\nabla \psi_i(\mathbf{r})|^2 \, d\mathbf{r}. \tag{3.12}$$

The classic part of the electron-electron interaction enters the effective Kohn-Sham potential through the Coulomb potential generated by an electronic charge density. In homogeneous media this potential is calculated as

$$\Phi(\mathbf{r}, \mathbf{r}') = \int \frac{\rho(\mathbf{r}')}{\varepsilon |\mathbf{r} - \mathbf{r}'|} d\mathbf{r}'. \tag{3.13}$$

Nevertheless, as stated earlier, obtaining this potential for systems with an inhomogeneous dielectric constant requires to solve the Poisson equation:

$$\nabla [\varepsilon(\mathbf{r}) \nabla \Phi(\mathbf{r}, \mathbf{r}')] = -4\pi \rho(\mathbf{r}'). \tag{3.14}$$

The corresponding functional is thus given by the expression

$$J[\rho] = \frac{1}{2} \int \Phi(\mathbf{r}, \mathbf{r}') \, \rho(\mathbf{r}) \, d(\mathbf{r}). \tag{3.15}$$

Within the LSDA, the exchange-correlation functional is separated in two terms. On the one hand, the exchange contribution is taken from the Dirac expression for an homogeneous electron gas:

$$E_x^{LSDA}[\rho, \zeta] = \frac{3}{8} \left(\frac{3}{\pi} \right)^{\frac{1}{3}} \int \rho(\mathbf{r})^{\frac{4}{3}} \left\{ [1 + \zeta(\mathbf{r})]^{\frac{4}{3}} + [1 - \zeta(\mathbf{r})]^{\frac{4}{3}} \right\} d\mathbf{r}, \tag{3.16}$$

where $\zeta(\mathbf{r})$ is the spin magnetization, i.e., $\zeta(\mathbf{r}) = |\rho^\uparrow(\mathbf{r}) - \rho^\downarrow(\mathbf{r})|$ with $\rho^{\uparrow\downarrow}(\mathbf{r})$ being the spin-up and spin-down densities. However, as in the case of the Coulomb interaction, this formula does not account for position dependent dielectric constant. In this regard, no specific formula has been suggested hitherto to deal with this problem. A way to overcome this drawback is proposed here. It consists in defining an effective dielectric constant from the employed Coulomb functional. To this end, a scaling parameter k is defined as

$$k = \frac{\int \int \frac{\rho(\mathbf{r}) \, \rho(\mathbf{r}')}{\varepsilon(\mathbf{r})|\mathbf{r}-\mathbf{r}'|} d\mathbf{r} \, d\mathbf{r}'}{\int \Phi(\mathbf{r}, \mathbf{r}') \, \rho(\mathbf{r}) \, d(\mathbf{r})}. \tag{3.17}$$

Here, the denominator is the Coulomb functional properly obtained by solving the Poisson equation (equations 3.14 and 3.15), while the expression in the numerator is a sort of Coulomb functional with a position dependent dielectric constant. The effective dielectric constant is then obtained as $\widetilde{\varepsilon}(\mathbf{r}) = k \, \varepsilon(\mathbf{r})$ so that it allows to write the next identity:

$$\int \Phi(\mathbf{r}, \mathbf{r}') \, \rho(\mathbf{r}) \, d(\mathbf{r}) = \int \int \frac{\rho(\mathbf{r}) \, \rho(\mathbf{r}')}{\widetilde{\varepsilon}(\mathbf{r})|\mathbf{r} - \mathbf{r}'|} d\mathbf{r} \, d\mathbf{r}'. \tag{3.18}$$

In other words, an effective Coulomb functional for a dielectrically mismatched system is obtained by introducing $\widetilde{\varepsilon}(\mathbf{r})$ in the denominator of the corresponding expression for an homogeneous system. Similarly, this effective dielectric constant is introduced in equation 3.16, thus obtaining an expression for the exchange functional which is globally consistent with the employed Coulomb functional.

On the other hand, the correlation contribution is calculated with the parametrization proposed by Perdew and Zunger [119] of the Ceperley and

Alder functional [174]. Therein, the correlation energy $E_{corr}(\zeta, r_s)$ is obtained in terms of the spin magnetization (ζ) and the Wigner-Seitz radius (r_s), i.e., the radius of the sphere occupied by one electron ($1/\rho = 4/3\,\pi r_s^3$). The functional is written in atomic units, namely, E_{corr} is obtained in Hartree and r_s should be injected in Bohr radii (a_0), and a free mass m_0 is implicit for electrons. Hence, to use this same functional for electrons with masses different than m_0 located in media with $\varepsilon \neq 1$, effective atomic units should be employed. For this purpose, the Wigner-Seitz radius is first scaled by $m^*(\mathbf{r})/\widetilde{\varepsilon}(\mathbf{r})$ and injected into the functional. Then, the computed correlation potential and energy, which are obtained in effective Hartree, are rescaled by $m^*(\mathbf{r})/\widetilde{\varepsilon}(\mathbf{r})^2$ in order to get back true atomic units.

To complete the energetic contributions that conform the energy functional, the dielectric self-polarization interaction potential is obtained as explained in reference [143] and is added to the spatial confining potential, which, in turn, is defined by the band offset between adjacent materials.

The ground state charge density and energy are obtained by means of an iterative process in which the scaling parameter k is self-consistently calculated. In each step of the process, the Kohn-Sham and Poisson equations are solved exploiting the spherical symmetry of the systems under study. Thus, the equations are numerically discretized in a one-dimensional grid extended far beyond the NC radius. To avoid numerical problems concerning the discretization of mathematical surfaces presenting abrupt mismatches, in the computational implementation of the present approach these mismatches are replaced by continuous variations within an extremely thin layer at the interface (a monolayer).

The present extension of LSDA is, on the one hand, local in the sense that the electronic density feels locally the physical properties of the medium, but, on the other hand, it is consistent with a rigorous non-local calculation of Coulomb energy in an inhomogeneous medium.

3.2.2 Benchmarking the method

As discussed in the previous section, the way of treating the variable effective mass does not introduce any approximation on top of the LSDA (as far as the system is bound, which will always be the case). Therefore, this section is devoted to check the robustness of the proposed approach to deal

with the variable dielectric constant. With this aim, addition energies of electrons and holes in InAs and CdSe QDs are computed simulating embedding media of different dielectric constant. The benchmark to compare with is a set of configuration interaction (CI) calculations carried out by Orlandi et al. [155]. These calculations employed a basis set including 1s, 1p, 1d and 2s single-particle orbitals and were exact up to 7 carriers. Larger QD populations were calculated within a Hubbard-like approximation, i.e., only semidiagonal elements of the Hamiltonian were retained.
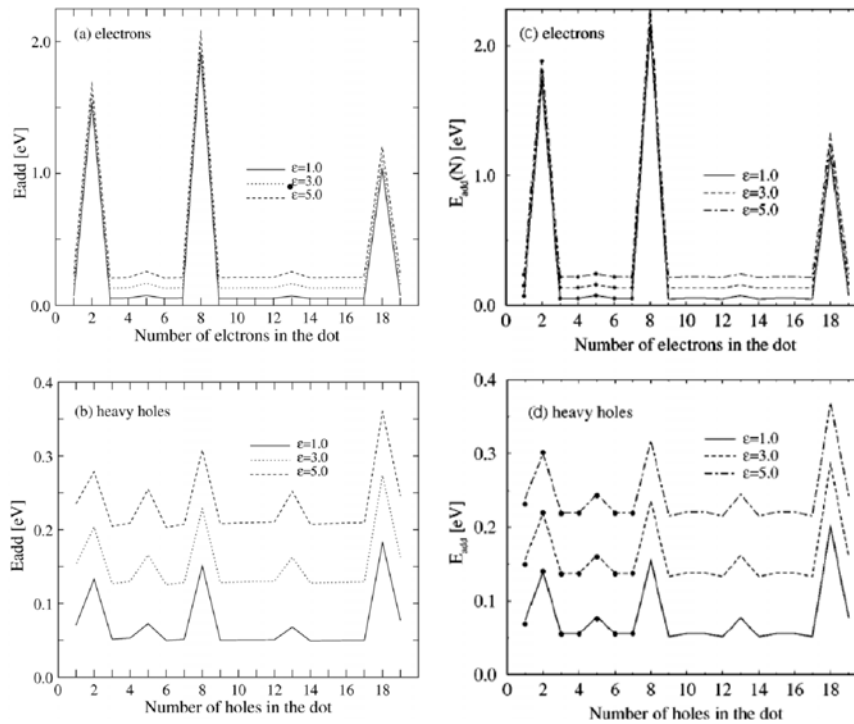
Figure 3.4: Calculated addition energies for electrons in panels (a) and (c), and holes in panels (b) and (d) as a function of the number of carriers in a 3.2 nm radius InAs QD. Results in the left panels correspond to LSDA calculations while the right ones correspond to CI calculations. The latter have been taken from Orlandi et al. *Phys. Rev. B* **63**, 045310 (2001).

The electron and hole addition energies obtained from LSDA and CI calculations are shown in left and right panels respectively of figure 3.4 for an InAs QD. In both calculations carriers are subjected to an infinite confinement, which, as stated earlier, is a rough approximation that here is adopted to mimic the benchmark CI calculations as far as possible. Likewise, the

same basis functions are employed in both calculations. Different dielectric matrices are considered which are defined by $\varepsilon = \varepsilon_{QD}/\varepsilon_{ext} = 1$, 3, 5. As can be observed in the addition energy spectra obtained from different methods, both qualitative and quantitative agreements are extremely good. Furthermore, by means of LSDA calculations with a larger basis set it was observed that the basis set employed in the CI calculations falls short to study the QD populated with holes. The obtained results revealed that the 19_{th} and 20_{th} holes come to fill 1f orbitals instead of 2s ones. It is worth noting that, unlike in CI methods, increasing the basis set in LSDA calculations do not entails an appreciable computational cost.
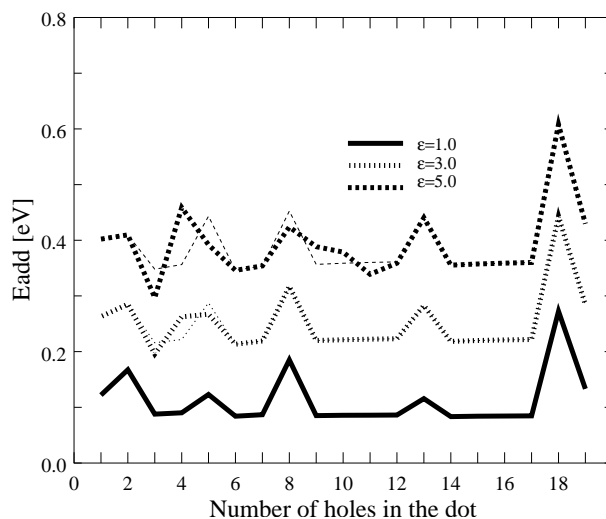
Figure 3.5: Comparison of addition spectra for holes in a 2 nm radius CdSe QD computed using LSDA absolute energy minimum configurations (thick lines) and forcing the dominant CI configurations (thin lines).

On the other hand, a few reconstructions with respect the CI ground state configurations are obtained by LSDA calculations when dealing with holes in CdSe QDs. These reconstructions, which are illustrated in the addition spectra of figure 3.5, occasionally appear when the CI electronic configurations are not imposed, and always entail an increment in the total spin (S_z) of the system. In this regard, it is relevant to notice the large effective mass employed in the calculations for CdSe holes $(m_h^* = 1)$, which brings the system into a strong correlation regime. In such regimes the LSDA is known to over-stabilize spin polarized states. Then, it is difficult

to assign this small disagreement with CI results either to the own LSDA or to the scaling approximation employed.

In summary, the proposed extension of the LSDA incorporates in an exact way the presence of position dependent effective masses. Illustrative calculations have shown that the approach is also very reliable accounting for dielectric mismatches. Finally, it is important to reiterate that the method is extremely fast and computationally very little demanding (as much as LSDA) in comparison with sophisticated CI calculations. Therefore, one can deal with large many-particle systems in inhomogeneous media without much effort.

3.2.3 Dielectric control of spin

The determination of the electronic configuration and the total spin of interacting multielectron QDs constitute an attractive and challenging theoretical problem. The interest arises from the great number of experimental publications exploring electron and spin transport in semiconductor QDs [15], and from the current perspectives of spintronics (short for spin-based electronics) to play a relevant role in future solid state-based technologies [175, 176].

The electronic configuration of an atom or a QD is determined by the balance of two factors, namely, the energy between consecutive levels and the pairing energy. In general, the Aufbau principle of sequential filling and Hund's rule of largest spin multiplicity in a shell are followed. However, QDs present a wide range of externally tunable parameters that can influence the orbital levels and hence, the electronic configuration and total spin, often leading to unfulfillments of the Aufbau and Hund rules [177–179]. This kind of orbital manipulation may start during the fabrication process, by tailoring the size and shape of the QDs, or later, normally by means of external magnetic fields [180]. Furthermore, since the electrons strongly interact with each other inside a dot, adding or subtracting extra electrons to the system may lead to an unexpected electronic configuration and total spin, in the sense that it is not predicted by the Aufbau and Hund rules. A clear signature of this system spin dependence on the number of carriers is the spin-blockade effect, which was theoretically predicted by Weinmann et al. [181, 182] and later on experimentally observed [183–185]. The effect is the occasional suppression of the conductance through a QD because the addition of an extra electron would reconstruct the electronic configuration

in such a way that it would change the total spin of the system by more than 1/2, which would be the usual case, thus violating a spin selection rule.

On the other hand, the correlation regime of a QD is an available degree of freedom to manipulate spin. Since one of the most relevant effects of the dielectric confinement is precisely to modulate the electron-electron interactions, one may wonder to which extent it is capable to affect the electronic configuration and total spin of a QD. The present section studies the effect of the system-environment dielectric mismatch on QD spin transitions. To this end, the ground state spin phase diagrams are analyzed versus the QD radius and the dielectric constant of the surrounding medium.
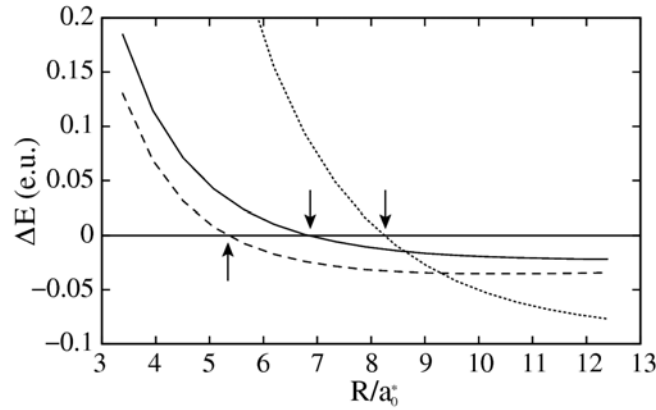
Figure 3.6: Energy difference ΔE ($Hartree^*$) between spin polarized minus spin least-polarized electronic configurations vs. QD radius R (a_0^*) corresponding to a QD populated with tree (solid line), four (dashed line) and nine (dotted line) excess electrons. Arrows indicate the phase transition.

Before delving into the dielectric confinement effect on the QD electronic configurations, it is worth studying the bare effect of modifying the radius of a QD. It is well known that as the size of a confining system is increased the energy spacing between consecutive levels is reduced and, eventually, this spacing becomes comparable to the energy required to place two electrons with anti-parallel spin in the same orbital [1]. At this point, the system is ex-

---

[1]This is a consequence of the different scaling of the quantization and Coulomb energies with the QD size. Whereas the quantization energy scales as $\sim 1/R^2$, the Coulomb energy does it as $\sim 1/R$. Therefore, large QDs are mainly governed by Coulomb interactions

pected to experience transitions from electronic configurations with paired electrons to unpaired ones presenting larger spins.

In a first set of calculations, this transition process is here reproduced for a QD populated with 3, 4 and 9 electrons. The dielectric constant and the effective mass of the electrons are taken constant, namely, the same for the system and the surroundings. One can then work in effective atomic units, thus reaching universal results that can be extrapolated to any semiconductor material. The only parameter introduced in these calculations is the large height of the confining barrier which is fixed to 14 $Hartree^*$ (effective Hartree) [2]. For the electronic populations considered, only two configurations, namely, least-polarized and fully polarized, become the ground state. Figure 3.6 shows the energy difference between these two configurations as a function of the radius of the QD. [3] Thus, for N=3 the configuration $1s^2\ 1p$ is the lowest lying for $R < 7a_0^*$ (a_0^* being the effective Bohr radii) and $1s\ 1p^2$ otherwise. For N=4 it is $1s^2\ 1p^2$ up to $R \sim 5.5a_0^*$ and then $1s\ 1p^3$. Finally, when N=9, $1s^2\ 1p^6\ 1d$ is the ground state if $R < 8.3a_0^*$ and $1s\ 1p^3\ 1d^5$ if R is larger. It is worth noting that, despite the higher correlation regime of the system with 3 electrons, the phase transition to the spin polarized state takes place at smaller radii for the case of N=4 electrons. The reason comes from the half-filled shell structure of the fully polarized state of N=4 electrons, which entails extra stabilization of this phase .

From figure 3.6 it can be deduced that semiconductor materials with small Bohr radii are the best candidates to externally control QD spin transitions, given that the phase transition takes place at smaller QD radii and, as a consequence, the resulting energetic change from external manipulation is larger. Then, in order to show the dielectric modulation of spin, ZnS QDs are now studied. This wide band gap semiconductor has an electron effective mass of $m_{ZnS}^* = 0.34m_0$ and a dielectric constant $\varepsilon_{ZnS} = 5.7$ which lead to an effective Bohr radius of $a_0^* \sim 17a_0$. The electron effective mass outside the QDs is now taken as $m_{ext}^* = 1$ and the carriers are confined by a typical potential barrier of 4 eV (14 $Hartree^*$). The panels of figures 3.7 and 3.8 depict the ground state phase diagrams of ZnS QDs, for the same electronic populations above studied, as a function of the QDs radii (R)

---

[2]14 $Hartree^*$ correspond to 4 eV for the ZnS QDs studied below.

[3]Although the proofs of the Hohenberg and Kohn theorems apply to the ground state [186], it can be generalized to the energetically lowest state of each symmetry [187]. Then, the LSDA scheme introduced in section 3.2.1 allows to study several low-lying electronic configurations with different spin S_z.
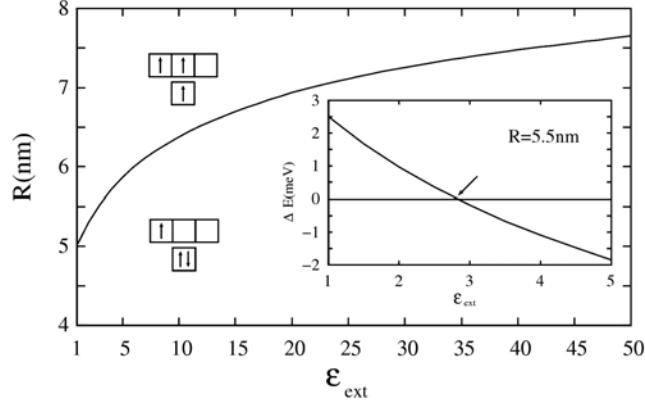
Figure 3.7: Ground state phase diagram of a ZnS QD populated with three electrons vs. the QD radius R (nm) and the external dielectric constant ε_{ext}. The schematic boxes diagrams indicate the electronic configuration in the different regions of the plot. Inset: Energy difference ΔE (meV) of the spin least-polarized minus the spin polarized configuration vs. the external dielectric constant ε_{ext} for a fixed value of the QD radius R.

and the dielectric constant of the surrounding medium (ε_{ext}). The range of studied radii has been selected from the proximity with the transition radius in absence of mass and dielectric mismatch (figure 3.6). The line represented in each panel corresponds to the (R, ε_{ext}) conditions leading to a phase transition. Above the line the ground state is spin polarized, while below it corresponds to the least polarized configuration. These representations show that, as announced, phase transitions can be dielectrically induced for a fixed QD radius, this can be tested by choosing any point of the transition line and moving horizontally. Such process is illustrated in the insets of the figures. For instance, the inset of figure 3.7 plots the energy difference between the least- and fully polarized configurations versus ε_{ext} for the case of a 5.5 nm radius QD populated with 3 electrons. On the one hand, the plot reveals that whereas a freestanding ($\varepsilon_{ext} = 1$) QD has a fully polarized ground state ($S_z = 3/2$), if the same dot is immersed in a solvent like chloroform with a dielectric constant $\varepsilon_{ext} \sim 4$ a transition toward the least-polarized ($S_z = 1/2$) configuration occurs. On the other hand, a solution with a dielectric constant of about $\varepsilon_{ext} = 2.8$ would be able to tune degeneracy between both electronic configurations. The obtained results for

N=4 and N=9 electrons (figure 3.8) are qualitatively the same as the case of N=3, but the changes in spin and/or energy are larger.
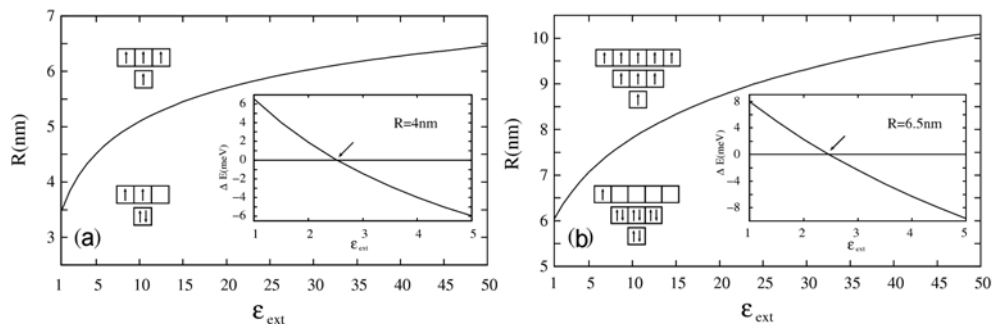
Figure 3.8: The same as figure 3.7 but for N=4 (a) and N=9 (b) excess electrons in the QD.

In summary, the ground state phase diagrams presented in this section have shown that it is possible to switch between high/low spin configurations by means of an appropriate QD environment. This suggest the use of QD spin as a sensor of the dielectric response of a given medium.

3.2.4 Many-electron multishell quantum dots

Colloidal procedures of NC synthesis offer the interesting possibility of fabricating multishell QDs, i.e., built of concentric layers (shells) of different materials [188–192]. The relevance of this growth of external shells around a NC core arises chiefly from what is known as passivation [193, 194]. At the surface of a semiconductor NC substantial reconstructions in the atomic positions occur, leading to the appearance of surface states with energies lying within the forbidden gap of the crystal bulk. These states can trap electrons and holes, and degrade the electrical and optical properties of the material. Passivation is the chemical process by which the surface atoms of a NC are bonded to another material of a larger band gap, eliminating in great measure the energy levels inside the gap [2].

More than a decade ago, Eychmüller and coworkers synthesized a remarkable NC heterostructure, a quantum dot quantum well (QDQW) [188, 189]. It was composed of a central CdS core surrounded by a HgS shell and

capped with an additional CdS shell. Subsequently, more complex onion-like NCs have been synthesized by means of alternative precipitation of HgS and CdS on a CdS central core [190]. The peculiar physics of this kind of NCs derives from the different band gap of neighboring materials. As illustrated in figure 3.9, in CdS/HgS systems, the band alignment yields a potential well in the HgS regions and a barrier in the CdS layers. Thus, in a CdS/HgS/CdS QDQW the electronic density, coming from either optical excitation or tunneling from metallic electrodes, is largely confined in a narrow well which is embedded inside of a NC [195–197]. The relative easy control of the size and composition of these structures, and therefore, the possibility of modifying the charge density localization, grants a high degree of flexibility in tailoring their discrete energy spectra [198–200].
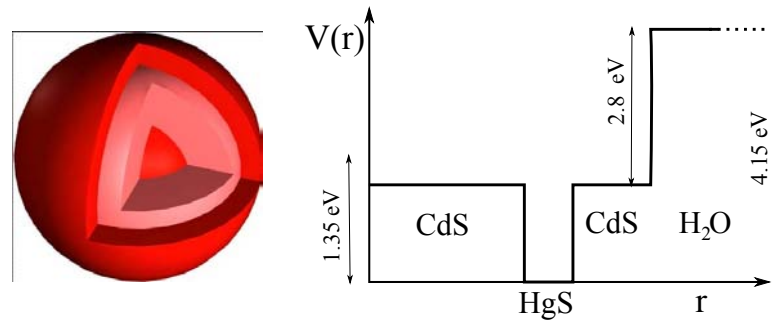
Figure 3.9: 3D representation of a QDQW (left) and the corresponding radial confining potential profile (right).

Concerning the theoretical modeling of such heterostructures, given that the electronic density is mainly localized in regions composed by the smaller band gap material (HgS), one could think that it is safe to employ the effective mass and the dielectric constant of this material for the whole multishell QD. Such a presumption is refuted in the present section. To this end, several CdS/HgS-based spherical multishell QDs are studied in the regime of many-electron population. The LSDA methodology introduced in section 3.2.1 is employed to calculate the ground state properties of the NCs. The obtained results prove that a correct description of multishell QDs requires consideration of variable, i.e., position-dependent, effective mass and dielectric constant. Otherwise, results can even lead one to mistake the number of electrons that fit in the dots.

Material	m_0^*	ε	Eg (eV)	Δ (eV)
HgS	0.04	11.4	0.5	0.08
CdS	0.15	5.5	2.5	0.08
H_2O	1.	1.78	8	0.08
		HgS/H_2O	CdS/H_2O	HgS/CdS
V (eV)		4.15	2.8	1.35

Table 3.1: Parameters employed in this section (taken from references [201–203]). Namely, effective mass (m_0^*), dielectric constant (ε) and spatial confining potential barrier (V). The band gap (E_g), and split off (Δ) are parameters used in section 3.2.5.

The studied QDs are formed from CdS and HgS, and are always surrounded by water. The material parameters employed in the calculations are indicated in table 3.1. To simplify the system description, the notation $A/B/A/\ldots x/y/z/\ldots$ will be employed hereafter. Here $A/B/\ldots$ are the materials forming the QD, from the inner to the outer shell, and $x/y/\ldots$ are the corresponding shell thickness in nm. Results are obtained by means of three different LSDA calculations, namely, one which employs the effective mass and dielectric constant of the HgS shells for the whole system (hereafter referred to as *unpolarized* calculation), another which employs variable material parameters but neglects the self-energy (*polarized* calculation), and finally the polarized calculation including the self-energy (see section 3.1). The bottom of the HgS conduction band is assumed to be the origin of energies in all cases.

The first system under study is a QDQW with structure CdS/HgS/CdS 3/2/1. Figure 3.10 shows the chemical potentials $\mu(N)$ and electron addition energies $E_{add}(N)$ of this NC (equations 2.18 and 2.19 respectively). As evidenced by panel 3.10(a), chemical potentials obtained from polarized calculations, either including self-energy or not, are considerably larger than those obtained from the unpolarized calculation, which leads to disagreement in the number of electrons that can be hosted by the system. The horizontal lines in the figure at 1.35 eV and 4.15 eV represent the confining barrier height of the HgS well and the QD respectively. Therefore, data indicate that whereas the unpolarized calculation predict that up to 12 electrons can be accommodated in the HgS well, the polarization effects restrict this number to 6 electrons. Similarly, the number of electrons that fit into the QD is limited to 22 in the polarized calculation while this limit considerably exceeds 25 electrons in the case of the unpolarized treatment. Concerning the
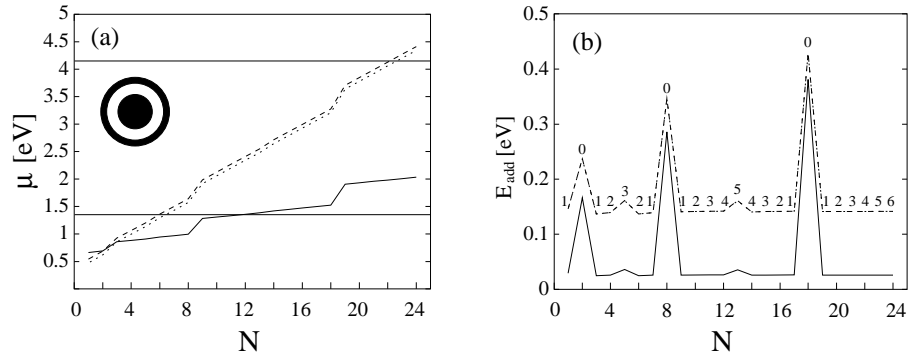
Figure 3.10: Chemical potentials (a) and electron addition energies (b) vs. the number of electrons in a QDQW. Solid lines correspond to unpolarized calculations, dotted lines to polarized calculations, and dashed lines to polarized calculations including self-energy. $2S_z$ values are indicated by numbers on the addition spectra. Inset: Schematic of the QD structure, CdS regions are represented in black and HgS regions in white.

addition energies, even though their value is noticeably destabilized by polarization effects [155], no qualitative differences can be observed between the approaches employed. The profiles obtained indicate the fulfillment of the Aufbau and Hund rules, the same spin and electronic configurations being achieved, namely, sequential filling of orbitals 1s, 1p, 1d and 1f. Therefore, only quantitative differences between approaches are obtained, originated by the extra polarization work coming from the dielectric confinement.

Two structures are now studied which present two internal quantum wells and a barrier acting core. The only difference between the structures considered is the thickness of the intermediate CdS barrier. Thus, in figure 3.11 the chemical potentials and electron addition energies are represented for the cases of a CdS/HgS/CdS/HgS/CdS system with dimensions 3/2/1/2/1 in panels (a) and (b), and 3/2/2/2/1 in panels (c) and (d). Apart from quantitative discrepancies similar to those previously analyzed, now differences between methods arise in form of reconstructions of the addition energy spectra. In the spectrum (b) one essentially observes that, unlike the unpolarized spectrum, a third maximum, corresponding to a shell closing, appears at N=10 electrons for the polarized calculation. This peak corresponds to the filling of the orbital 2s, whose stabilization is associated with a redistribution of its nodal surface in a barrier region, due to the extra interactions introduced by dielectric polarization. The extra peak shifts two positions the subsequent peak in the spectrum. In turn, the inclusion of self-energy
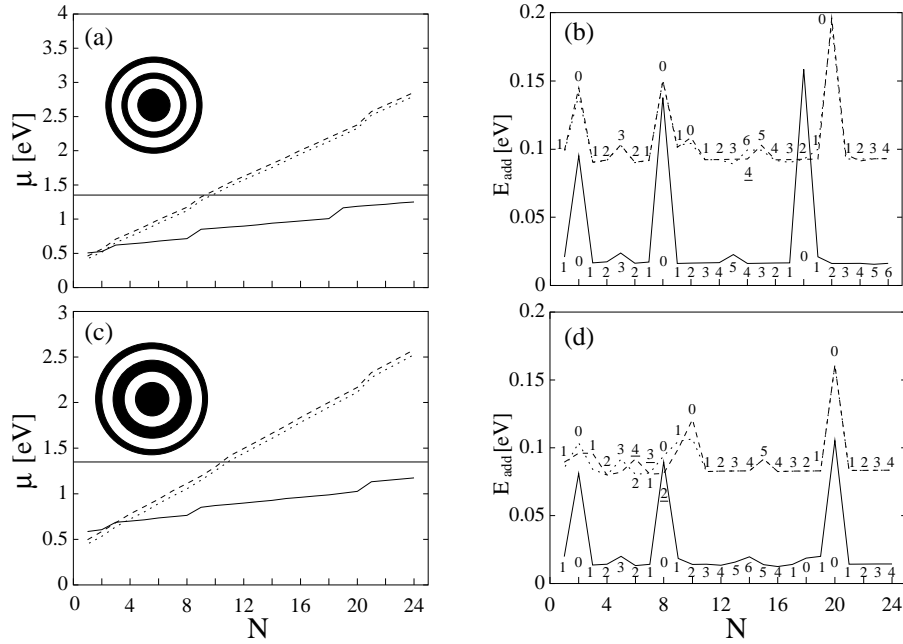
Figure 3.11: The same as figure 3.10 for the cases of the double well structures depicted in the insets and specified in the text. If the spin of polarized calculations with and without self-energy is different, underlined numbers correspond to the calculations including self-energy.

also brings about some ground state reconstructions, even leading to a spin change ($2S_z = 6$ vs. 4) at N=14.

The most relevant role of both polarization and self-energy can be seen in the case of the thicker CdS barrier. Plot 3.11(d) reveals that, in the few electron region, rather different electron addition spectra are obtained when polarization as well as self-energy are included. For instance, it can be highlighted that at N=8 electrons, the spin predicted by the unpolarized calculation is $2S_z = 0$, which turns into $2S_z = 2$ as polarization is included, and recovers a zero value as, additionally, self-energy is incorporated.

To summarize, in this section it has been shown that despite the electronic density is mainly localized in the well regions of a multishell QD, disregarding the use of position dependent material parameters in theoretical descriptions gives rise to unsatisfactory results: on the one hand, the magnitude of chemical potentials and addition energies of the systems are

underestimated, and on the other hand, the discrepancies can even include ground state configuration reconstructions, these being specially relevant as the QD complexity, i.e., the number of sells, increases.

3.2.5   Incorporation of non-parabolicity corrections

In the one-band EMA model the energy dispersion of the conduction band of a semiconductor is implicitly assumed parabolic, the curvature of the parabola being related to the electron effective mass:

$$E(k) = \frac{\hbar}{2m^*}k^2. \tag{3.19}$$

The $E - k$ relation is however parabolic only near the band edge (Γ point) of semiconductor crystals [19]. This deviation from a parabolic dispersion is more pronounced in narrow gap semiconductors due to the larger coupling between the conduction and valence bands, a fact that devalues the use of the uncoupled approach of the EMA to study this kind of semiconductors [204].

To deal with non-parabolicity, a good alternative to the computationally more demanding k·p multiband approaches is the use of an energy dependent effective mass as proposed by Kane [205]. Such technique allows one to work within the framework of the one-band model where the effective mass is self-consistently adjusted for each energy level. This latter fact entails, however, the drawback that different Hamiltonians are employed to compute the different eigenvalues, so that the associate eigenfunctions are not necessarily orthogonal. Still, the energy-dependent effective mass has been widely employed to study low dimensional systems, ranging from quantum wells (QWs) [206–210], QDs [211–214] and QRs [215, 216], as well as, artificial molecules [217, 218].

In this section the non-parabolicity corrections are incorporated into the LSDA code introduced in section 3.2.1. Then, the relevance of non-parabolicity effects on the energies and addition energy spectra of many-electron QDs is investigated. Comprising different confinement regimes, the results reveal that the interplay of both non-parabolicity and dielectric confinement may lead to changes in the electronic structure and addition energies of QDs built of narrow gap semiconductors, the effect being particularly relevant in multishell QDs.

In order to introduce the effects of a non-parabolic conduction band, a position- and energy-dependent effective mass $m_{i\sigma}^*(E, \mathbf{r})$ is employed to compute the Kohn-Sham orbitals. The energy-dependence of the effective mass is given by the Kane equation [205],

$$\frac{m_0}{m^*(E, \mathbf{r})} = 1 + \frac{2}{3}\mathcal{P}^2 \left(\frac{2}{E + E_g(\mathbf{r}) - V(\mathbf{r})} + \frac{1}{E + E_g(\mathbf{r}) - V(\mathbf{r}) + \Delta(\mathbf{r})} \right),$$
(3.20)

where m_0 is the free electron mass, $\mathcal{P}$ is the Kane parameter, and $E_g(\mathbf{r})$, $V(\mathbf{r})$, $\Delta(\mathbf{r})$ are the position-dependent band gap, confining potential and spin-orbit parameter, respectively. This formula is rewritten for practical purposes in terms of the position-dependent effective mass at the bottom of the conduction band $m^*(0, \mathbf{r})$:

$$\frac{\frac{m_0}{m^*(E, \mathbf{r})} - 1}{\frac{m_0}{m^*(0, \mathbf{r})} - 1} = \frac{(E + E_g(\mathbf{r}) - V(\mathbf{r}) + \frac{2}{3}\Delta(\mathbf{r}))(E_g(\mathbf{r}) - V(\mathbf{r}))(E_g(\mathbf{r}) - V(\mathbf{r}) + \Delta(\mathbf{r}))}{(E_g(\mathbf{r}) - V(\mathbf{r}) + \frac{2}{3}\Delta(\mathbf{r}))(E + E_g(\mathbf{r}) - V(\mathbf{r}))(E + E_g(\mathbf{r}) - V(\mathbf{r}) + \Delta(\mathbf{r}))}.$$
(3.21)

In the numerical implementation, the above position- and energy-dependent effective mass is introduced in the Kohn-Sham equations. Thereby, the problem moves from a single differential equation to a set of coupled differential equations,

$$
\begin{aligned}
\left(-\frac{\hbar^2}{2}\nabla \frac{1}{m_{1s\sigma}^*(E_{1s\sigma}, \mathbf{r})}\nabla + V_{KS,\sigma}(\rho, \zeta) \right)\varphi_{1s\sigma}(\mathbf{r}) &= E_{1s\sigma}\varphi_{1s\sigma}(\mathbf{r}) \\
\left(-\frac{\hbar^2}{2}\nabla \frac{1}{m_{1p\sigma}^*(E_{1p\sigma}, \mathbf{r})}\nabla + V_{KS,\sigma}(\rho, \zeta) \right)\varphi_{1p\sigma}(\mathbf{r}) &= E_{1p\sigma}\varphi_{1p\sigma}(\mathbf{r}) \\
&\vdots \\
\left(-\frac{\hbar^2}{2}\nabla \frac{1}{m_{i\sigma}^*(E_{i\sigma}, \mathbf{r})}\nabla + V_{KS,\sigma}(\rho, \zeta) \right)\varphi_{i\sigma}(\mathbf{r}) &= E_{i\sigma}\varphi_{i\sigma}(\mathbf{r}),
\end{aligned}
$$
(3.22)

which should be self-consistently solved. The procedure starts by solving a differential equation in which $m_{i\sigma}^*(E, \mathbf{r})$ is replaced by $m^*(0, \mathbf{r})$. Then, from the obtained Kohn-Sham orbitals the charge density ρ and spin magnetization ζ are computed and subsequently employed to construct the effective

Kohn-Sham potential $V_{KS,\sigma}(\rho, \zeta)$. In turn, the orbital energies $E_{i\sigma}$ enable to compute the effective masses $m^*_{i\sigma}(E, \mathbf{r})$ (equation 3.21) entering the kinetic energy operators. The set of coupled differential equations are then built up. In a second step, these equations are solved one by one in order to get again a set of orbitals and associate energies to build up the set of differential equations of the next iteration. This process is repeated up to simultaneous convergence of all differential equations. As stated earlier, the single-particle Kohn-Sham orbitals obtained from equations with different effective masses are not necessarily orthogonal. By this reason, to compute the total charge density a prior orthogonalization is carried out.

Next, we show the quantitative improvement introduced by the non-parabolicity corrections when dealing with narrow gap semiconductors. To this end, the experimental results obtained by Banin et al. [219] are reproduced. They performed scanning tunneling spectroscopy measurements on 2.2 nm InAs QDs ($E_g^{InAs} = 0.354$ eV) embedded in an organic solvent from which the first three electron addition energies can be obtained. Franceschetti et al. [154] theoretically reproduced these addition energies by means of atomistic pseudopotential calculations where the dielectric constant of the environment was taken as a fitting parameter. In this way, they obtained a good agreement with the experiment employing $\varepsilon_{out} = 6$. However, the LSDA results shown below have been performed with an external dielectric constant $\varepsilon_{out} = 3$, which seems more reasonable for this kind of organic solvents [220]. The summary of the obtained results is shown in table 3.2. As evident from data, non-parabolicity corrections work well improving all parabolic results, the case of $E_{add}(2)$ being specially relevant.

	Experiment	Parabolic LSDA	Non-parabolic LSDA
$E_{add}(1)$ (eV)	0.14	0.22	0.19
$E_{add}(2)$ (eV)	0.52	1.59	0.59
$E_{add}(3)$ (eV)	0.14	0.20	0.14

Table 3.2: First three electron addition energies of a 2.2 nm InAs QD obtained from scanning tunneling spectroscopy, and LSDA calculations with and without non-parabolicity corrections. The material parameters employed in the calculations are those of InAs bulk, i.e, $m^*_{QD} = 0.023$, $\varepsilon_{QD} = 12.3$, $E_g^{QD} = 0.354$ eV, $\Delta_{SO}^{QD} = 0.41$ eV, and for the environment, $m^*_{out} = 1$, $\varepsilon_{out} = 3$, $E_g^{out} = 8$ eV, $\Delta_{SO}^{out} = 0$ eV. The confining potential of carriers is set to 3.2 eV.

The non-parabolicity corrections are expected to be more important in the many-electron regime of a QD since higher energy levels come into play.
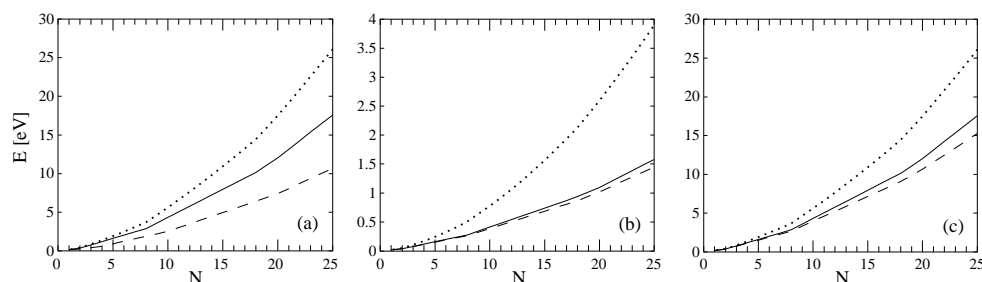
Figure 3.12: Ground state energies vs. the number of electrons of a (a) 5 nm radius HgS QD, (b) 20nm radius HgS QDs, and (c) 5 nm radius QD defined by the HgS parameters except for E_g which is set to 3 eV. Solid lines correspond to parabolic single particle (sp) calculations, dashed lines to non-parabolic sp calculations, and dotted lines to parabolic LSDA calculations.

In fact, it has been claimed that the corrections can be of the same order as many-body interactions [212, 218]. Here, such a possibility is tested for the case of a HgS QD with 5 nm and 20 nm radii in water. Given that the effective Bohr radius of HgS is $a_0^* = a_0 \varepsilon / m^* = 15$ nm, both confinement regimes are present in the rang of QD sizes studied. For the time being the dielectric confinement is neglected, i.e, the HgS dielectric constant is used for the whole system. The material parameters employed are the same as those of the previous section and are outlined in table 3.1. Figure 3.12 shows a comparison of the QD ground state energies as a function of the electronic population obtained from three different approaches: a parabolic single-particle calculation (solid lines), a single-particle calculation employing energy dependent effective mass (dashed lines), and a parabolic LSDA calculation (dotted lines). The results go along with expectations. In panel (a) one can observe how in the strong confinement regime the non-parabolicity corrections can be as large as the LSDA many-body interactions. However, in the weak confinement regime (panel (b)) the corrections are negligible. Additionally, with the aim of demonstrating to which extent the non-parabolicity depends on the material band gap, in panel (c) are depicted the corresponding results obtained for a QD described by the same parameters as the small QD except for the band gap that is set to 3 eV. The figure reveals that, despite the strong confinement regime, the role played by the non-parabolicity corrections is small, similar to the weak confinement regime case.

Having observed the large stabilization of many-electron states as a consequence of the use of an energy dependent effective mass, now attention is paid to the fairly sensitive addition energy spectrum. The case of an ho-
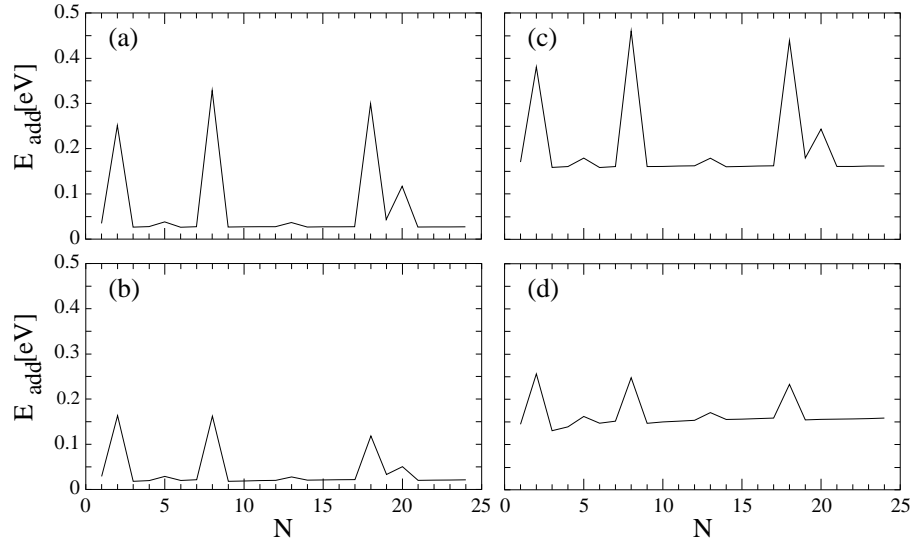
Figure 3.13: Addition energy spectra of a 5 nm radius HgS QD. (a) Parabolic and (b) non-parabolic LSDA calculations neglecting dielectric polarization, (c) and (d) are their counterparts with polarization.

mogeneous 5 nm radius HgS QD is first studied with the developed LSDA method and including dielectric polarization effects. The results are illustrated in figure 3.13, where panels on the left- and right-side correspond to unpolarized/polarized calculations, and the top/bottom row panels correspond to parabolic/non-parabolic ones. As can be observed, including non-parabolicity and dielectric polarization separately does not yield qualitative changes with respect the reference (simpler) calculation shown in panel (a). Whereas the dielectric confinement just produces the aforementioned destabilization of the addition energies [155], the main effect of non-parabolicity is the reduction of the peaks height due to a smaller interlevel spacing originating from an increase in the orbital effective masses. By contrast, when both contributions are simultaneously taken into account (figure 3.13(d)) a reconstruction is observed. The orbital filling sequence, which in the other panels is $1s^2\,1p^6\,1d^{10}\,2s^2\,1f^x$, becomes $1s^2\,1p^6\,1d^{10}\,1f^x$. This preferential filling of $1f$ orbital vs. $2s$ is produced by two facts. On the one hand, the dielectric confinement destabilizes the energy of the Kohn-Sham orbitals by increasing the role of the Coulomb interactions, thus enhancing the non-parabolicity effect. On the other hand, s-symmetry orbitals ($l=0$) have a null centrifugal term $l(l+1)/m^*r^2$ while this term is relevant for f orbitals

(l=3). Hence, the 1f orbital undergoes a larger stabilization of the centrifugal term when the non-parabolicity increases the effective mass and, as a consequence, it is filled before.
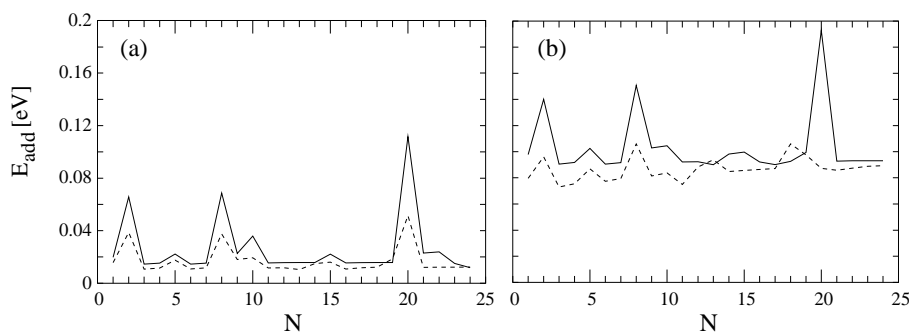
Figure 3.14: Addition energy spectra of a multishell QD (Structure details can be found in the text). (a)/(b) Shows results without/with dielectric polarization. Solid lines correspond to parabolic LSDA calculation and dashed lines to non-parabolic ones.

In the previous section, addition energy spectra of double well multishell QDs have proven to be quite sensitive to polarization effects coming from mass and dielectric mismatches. The reason relying on the extra stabilization of second shell orbitals ($2s$, $2p$,...) which, depending on the system conditions, can eventually localize their nodal surface in the barrier regions of the structure. By contrast, non-parabolicity has been observed to stabilize higher angular momentum orbitals. Therefore, the combined effect of dielectric polarization and non-parabolicity in these systems is difficult to anticipate. In figure 3.14 are represented the addition energy spectra of a multishell QD built of CdS/HgS/CdS/HgS/CdS layers with dimensions of 3/2/1/2/1 nm. Left/right panels neglect/include dielectric polarization while solid/dashed lines correspond to parabolic/non-parabolic calculations. The reference spectrum (unpolarized and parabolic, solid line of panel (a)) shows a regular sequential filling up to N=20 electrons ($1s^2$ $1p^6$ $2s^2$ $1d^{10}$). Then, a shoulder emerges at N=22 involving the $2p$ orbital. This shoulder disappears when non-parabolicity corrections are included. Again, this is due to the overstabilization of the $1f$ centrifugal term compared with that of $2p$ orbitals. Apart from this reconstruction, the main effect of the non-parabolicity is the reduction of the height peak commented above. The 2p shoulder also vanishes when polarization is taken into account in a parabolic calculation (solid line in figure 3.14(b)). Furthermore, some "noise" is ob-

served when filling the $1d$ shell. Once more, the strongest effect is observed when both contributions are simultaneously considered (dashed line in panel (b)). In such a case, the height of the half- and full-filling peaks becomes similar. What is more, the largest peak at N=20 electrons corresponding to the $1d$ shell closure drops out.

In summary, the effects of the conduction band non-parabolicity have been incorporated into the LSDA approach developed along this chapter. To this end, an energy-dependent effective mass has been introduced in the Kohn-Sham equations, which leads to a problem of a set of coupled differential equations. Using this method, the obtained results have shown that in narrow gap semiconductor QDs in strong confinement regimes the energy corrections derived from non-parabolicity can be as large as the many-body LSDA contributions. In addition, the dielectric polarization has been shown to stimulate the non-parabolicity effects, leading to the appearance of addition energy spectra reconstructions, these being mainly due to the different stabilization of the kinetic centrifugal term experienced by orbitals with different angular momentum.

3.3   Dielectrically induced surface excitonic states in spherical quantum dots

Due to the discrete energy level structure, optics of semiconductor QDs is determined by the concentration of the oscillator strength to sharp exciton transitions, which makes them attractive for linear and non-linear optical applications with tunable frequency [134, 135]. In any case, these promising optical applications are based on the formation and/or subsequent recombination of one or more electron-hole pairs when the energy of the excitation source is tuned in the system band gap. One of the classic features of QDs is the shift of the optical band gap as compared with the crystal bulk, which originates from two usually opposite contributions. On the one hand, the single-particle band gap is shifted to higher energies due to the quantum size effect on the electron and hole levels. On the other hand, the Coulomb attraction between the electron-hole pair created by photoexcitation adds a redshift correction. Both corrections are size-dependent and generally result in an overall blueshift of the optical band gap [221].

As widely commented along the present chapter, the energetic contributions arising from the dielectric constant mismatch between the semiconductor material and the environment affect the single-particle spectra as well as the Coulomb interactions. Nonetheless, in the case of an electron-hole pair, the net charge neutrality of the system yields a reduced dielectric confinement effect on the optical band gap. Indeed, the exciton peak remains almost unaltered by the dielectric constant of the environment in the ideal case of an infinitely confined exciton in a QD [138, 141]. This is not the case when the QD confining potential barriers are regarded finite [142]. In such a case, the most common situation, namely, a QD embedded in a matrix of smaller dielectric constant, leads to a blueshift of the exciton energy with respect to the case $\varepsilon_{QD} = \varepsilon_{out}$. Still, this correction of the optical gap is small compared with the quantum size effect or even with the more relevant increase of the exciton binding energy produced by the dielectric confinement.

A quite different scenario would take place in case that the system conditions are such that allow carriers to be localized in the self-polarization potential well. Such dielectrically induced surface excitons in spherical QDs were first predicted by Bányai et al. [139] under the specific conditions of strong dielectric mismatch regime, low potential height barrier and large

electron-hole effective mass ratio (m_h^*/m_e^*). The transition to surface states observed as the QD radius was reduced led to an abrupt redshift of the exciton energies even reaching negative values, i.e., lying within the forbidden band gap. In this section, the possible formation of excitonic surface states is explored in two different situations, (i) a spherical QD in air and (ii) a QD buried in a matrix with a higher dielectric constant. It is shown that transitions to surface exciton states take place in both situations. This involves an optical band gap redshift with respect to the case of no dielectric mismatch, and has strong consequences on the electron-hole overlap, and therefore, on the exciton recombination probability.

Exciton energies and wave functions are obtained by means of configuration interaction (CI) calculations. The employed basis is a set of symmetry adapted two-particle Hartree products built from the single-particle Hamiltonian eigenfunctions. The latter are obtained, both for electrons and holes within the one-band EMA [4], through numerical discretization of the Hamiltonian

$$\hat{\mathcal{H}}_i = -\frac{1}{2}\nabla[\frac{1}{m_i^*(\mathbf{r})}\nabla] + V_i(\mathbf{r}) + V_{s,i}(\mathbf{r}), \tag{3.23}$$

where $i = e, h$ is a subscript denoting electron or hole respectively, $V_i(\mathbf{r})$ is the step-like confining potential and $V_{s,i}(\mathbf{r})$ is the self-polarization potential. The spherical symmetry of the system allows to factorize the eigenstates in angular and radial parts, and find the radial solutions of Hamiltonian 3.23 $(\phi_{nlm}(\mathbf{r}_{e/h}))$ in an one-dimensional discretization grid. The 4 lowest-lying orbitals with angular momentum $l = 0, 1, 2$ and the 3 lowest-lying orbitals with $l = 3, 4, 5, 6$ have been calculated and employed in the CI calculation. Then, the interacting electron-hole Hamiltonian

$$\hat{\mathcal{H}} = \hat{\mathcal{H}}_e + \hat{\mathcal{H}}_h + \hat{\mathcal{V}}_{eh}, \tag{3.24}$$

in which the Coulomb interaction term $\hat{\mathcal{V}}_{eh}$ includes the dielectric polarization, is expanded in the CI basis set. The exciton energies and wave functions are finally computed by carrying out a diagonalization of the Hamiltonian matrix.

---

[4]This simplification on the hole description is supported by works reporting that the exciton ground state of spherical QDs, which is the only studied here, is essentially formed by a heavy-hole, the contribution of light-hole bands in this state being negligible. [146,202]

From the calculated exciton wave function $\Psi(\mathbf{r}_e, \mathbf{r}_h)$ other interesting magnitudes can be obtained, as the electron (or hole) radial density,

$$\mathcal{P}(r_e) = \int |\Psi(\mathbf{r}_e, \mathbf{r}_h)|^2 \, r_e^2 \, r_h^2 \sin\theta_e \, \sin\theta_h \, dr_h \, d\theta_e \, d\theta_h \, d\phi_e \, d\phi_h, \qquad (3.25)$$

or the electron-hole overlap,

$$\mathcal{S}_{e-h}^2 = |\int \Psi(\mathbf{r}_e = \mathbf{r}_h = \mathbf{r}) \, r^2 \sin\theta \, dr \, d\theta \, d\phi|^2 \qquad (3.26)$$

which is proportional to the exciton recombination probability.
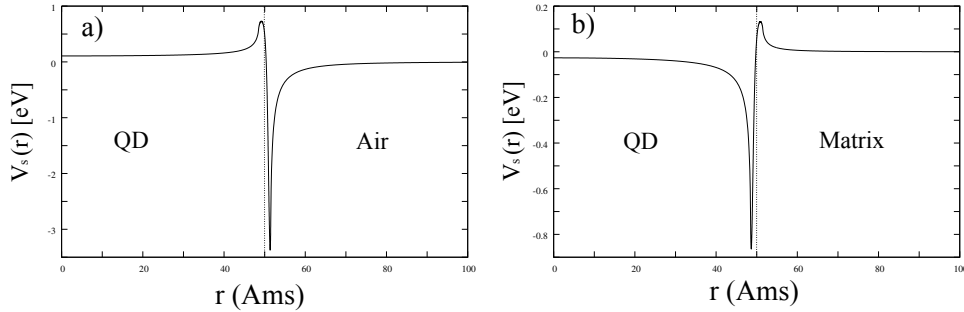
Figure 3.15: Self-polarization potential profiles for a 5 nm spherical QD of $\varepsilon_{QD} = 4$ embedded in a) air ($\varepsilon_{out} = 1$), and b) in a matrix of $\varepsilon_{out} = 15$.

The case of a 5 nm radius freestanding QD is first considered. In this system, the environment presents the smaller dielectric constant and consequently the self-polarization potential well is formed outside, by the QD border (see figure 3.15(a)). Therefore, the formation of surface states requires overcoming the QD confining barrier. This is not allowed for holes since the potential barrier height is infinite because these particles cannot be promoted to vacuum. Hence, only electrons can experience surface states. To monitor this transition three different potential barrier heights have been considered for the electron, namely, $V_e = 1$, 2, and 3 eV. It is worth noting that the aim of the present study is not to simulate a specific semiconductor material, but finding the system conditions which can lead to the appearance of surface states. The other material parameters employed in this first set of calculations are: $m_{e,QD}^* = 0.5$, $m_{h,QD}^* = 10$, $m_{e,out}^* = m_{h,out}^* = 1$ and $\varepsilon_{out} = 1$.
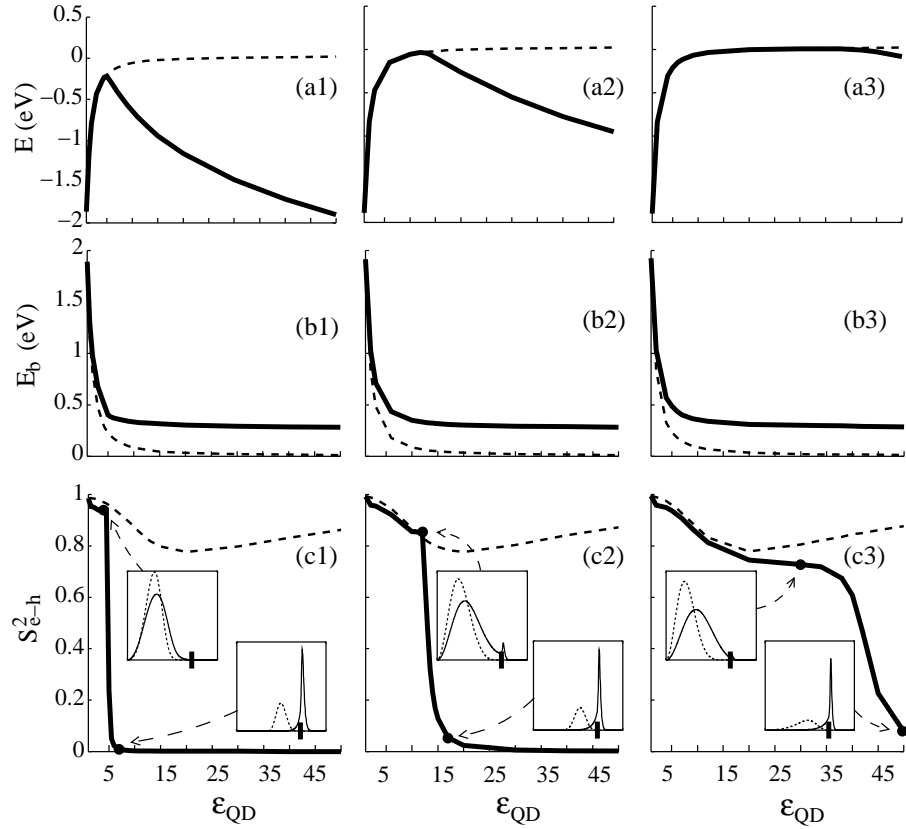
Figure 3.16: Exciton (E) and binding (E_b) energies, and electron-hole overlap (S^2_{e-h}) vs. ε_{QD}, for a 5 nm freestanding QD, with an electron confining barrier height V_e of 1 eV (left column panels), 2 eV (center column panels) and 3 eV (right column panels). Solid (dashed) lines include (exclude) dielectric polarization effects. Insets: Electron (solid lines) and hole (dotted lines) radial density distribution. The QD border is indicated by a tick in the horizontal axis.

The results are presented in figure 3.16 in form of exciton energies, binding energies and electron-hole overlap, vs. the QD dielectric constant for the three aforementioned electron potential barrier heights. As can be seen from the radial density profiles shown in the insets, the sought transition from volume to surface electron states takes place. It is also evident that the larger the confining potential height, the larger the dielectric mismatch required to confine the electron in the self-polarization potential well. The transition to surface states is paralleled by a sudden reduction of the electron-hole overlap and a change of the slope in the exciton energy vs. ε_{QD} profile. This redshift of the optical gap is consequence of the self-polarization well depth, and is

in good agreement with previous predictions [139]. By contrast, the binding energy is unaffected by the transition process and only reflects the expected reduction in module due to the screening of the bare Coulomb interaction as the dielectric constant of the dot is enhanced. Differences between polarized and unpolarized binding energies essentially show the influence of the polarization of the Coulomb interaction.

On the one hand, these results are a clear example denying the aforementioned cancellation of single- and two-body dielectric polarization contributions to the optical band gap. On the other hand, the conditions required for freestanding QDs leading to exciton surface states are rather severe, namely, quite low electron affinity χ (which determines the confining potential height in a freestanding QD) and not very light electron effective mass m_e^*. Not many semiconductors can fulfill these requirements, SiO_2 is here suggested as a potential candidate ($m_e^* = 0.5$, $\chi = 0.9$ eV, $\varepsilon = 4$ and $m_h^* = 10$, see references [222–224]). It however presents the inconvenient of having a band gap of 9 eV (insulator), so that performing optical excitations would require a really high energy excitation source.

A different scenario is the case of a QD embedded in a medium of higher dielectric constant, where the self-polarization potential well is formed in the inner side of the QD border (see, e.g., figure 3.15(b)). To model this system the same 5 nm radius QD is considered, but now defined by the following parameters: $m_e^* = 0.5$, $\varepsilon_{QD} = 4$, $V_e = 1$ eV and $V_h = 0.5$ eV. The effective masses in the outer medium are assumed to be the same as in the QD due to the lack of criterion to assign them. The key difference with respect to the previous case of a freestanding QD is that now, both the electron and the hole can be confined in the surface well, the heavier particle being more strongly attracted by this potential due to its smaller kinetic energy. To observe this influence of the effective mass, two hole effective masses are regarded now, namely, $m_{h,QD}^* = 1$ and $m_{h,QD}^* = 10$, which are slightly and much heavier than the electron effective mass, respectively.

Before analyzing the CI results of this system, it is worth noting that single-particle exploratory calculations vs. ε_{out} show a gradual localization of the carriers in the self-polarization well as ε_{out} is increased, facing three different phases: phase 1 (low ε_{out}) corresponding to volumetrically distributed electron and hole, phase 2 (intermediate ε_{out}) where the electronic density is still volumetric while the hole forms a surface state, and phase 3 (large ε_{out}) with both carriers being confined in the self-polarization well.

However, as the strong electron-hole Coulomb attraction ($\varepsilon_{QD} = 4$) is incorporated into the CI calculation, phase 2 drops out [5]. A similar transition from three-phase to two-phase processes was observed by Bányai et al. [139] when they carried Hartree-Fock and CI calculations respectively as a function of the QD radius. These findings denote the relevant role played by the electronic correlation in determining the formation of exciton surface states.
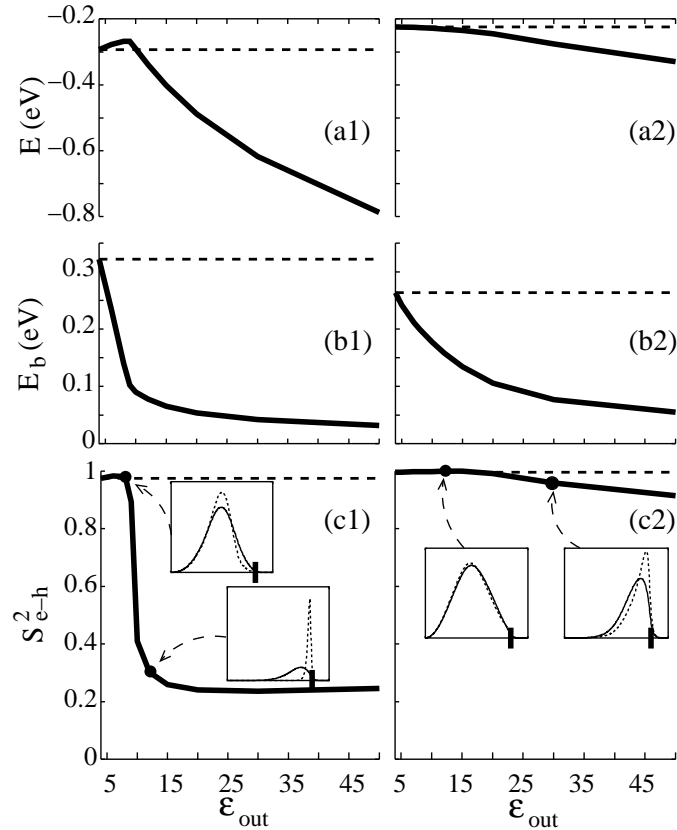
Figure 3.17: Same as figure 3.16 but for a 5 nm QD embedded in a higher dielectric constant environment. Two different hole effective masses are employed, namely, $m^*_{h,QD} = 10$ (left panels) and $m^*_{h,QD} = 1$ (right panels).

Thus, only two phases are encountered in which both particles show vol-

---

[5]In an alternative system of a QD embedded in a very high dielectric constant environment [161], this three-phase scheme is reproduced by CI results as the QD dielectric constant is increased (not shown).

umetric or surface distributions simultaneously. This is shown in figure 3.17 for a hole effective mass of $m^*_{h,QD} = 10$ in the left panels and $m^*_{h,QD} = 1$ in the right ones. The quantitative differences in excitonic and binding energies are a consequence of the different kinetic energy of the hole. Both cases show, however, similar qualitative responses to ε_{out} (increasing the energy redshift and decreasing binding energy as the dielectric mismatch is increased), as previously analyzed for a freestanding QD. A relevant difference arise in the electron-hole overlap representations. While the panel (c1) ($m^*_{h,QD} = 10$) resembles those obtained for a freestanding QD in which the transition to surface excitonic states involves a sudden drop in the electron-hole overlap, this is not the case in panel (c2) ($m^*_{h,QD} = 1$). The overlap vs. ε_{out} profile illustrated in panel (c1) is rather unexpected since in this system both particles transit from volume to surface states simultaneously. By contrast, one may expect profiles like 3.17(c2) showing an almost constant overlap vs. ε_{out}. The anomalous profile of panel (c1) is attributed to the different accommodation of particles with so different effective masses in the narrow self-polarization well (see insets in panel (c1)), yielding as a result a small overlap. However, when both carriers are spread over the QD volume they feel a weak confinement regime where effective mass differences play a minor role and show similar density distributions. It can be then concluded that in the case of a QD embedded in higher dielectric constant environments, the transition to surface states only has a relevant exciton recombination probability impact for QD materials with large m^*_h/m^*_e ratios.

In the work reviewed here [161], the effect of a shallow donor impurity located at the QD center was also considered. The main outcome of the carriers-impurity interaction is an almost total suppression of the exciton binding energy and brightness. The electron is strongly dragged by the impurity while the hole is pushed towards the QD border, favoring the formation of surface states when possible.

In conclusion, contrary to the belief that dielectric confinement has a negligible effect on the exciton properties of spherical QDs, the results exposed here reveal instances where the dielectric character of the environment can strongly influence the intensity and energy of excitonic transitions through the formation of surface states. According to the studied systems, the conditions to reach surface excitonic states in a freestanding QD are rather severe, but these seem more feasible in the case of a QD buried in higher dielectric constant matrices.

3.4   Dielectric confinement of semiconductor nano-rods

The studies of the dielectric environment effect reviewed here have been so far restricted to the case of spherical QDs. Even though the relevance of the dielectric confinement in determining energetic magnitudes has been demonstrated, the structural properties and usual sizes of these NCs hinder an observation of some other effects. The main reason for this is the strong spatial confinement regime, in which the Coulomb interactions play a minor role, being usually a first-order perturbation effect for the low-lying states [225, 226].

Colloidal and epitaxial synthesis procedures enable nowadays the fabrication of several sorts of nanostructures with shapes other than spherical, such as nanowires [227,228], nanotubes [229,230] or even nanotetrapods [231,232]. Here the attention is focused on the elongated counterparts of the spherical NCs, the so-called nanorods (NRs) [233, 234]. The left bottom panel of figure 3.1 shows a high resolution transmission image of a sample of CdSe NRs. Although they were synthesized later than spherical NCs, it was soon realized that the anisotropic shape confers the NRs a series of improved optical properties relative to spherical NCs. These range from higher photoluminescence quantum efficiency [233] and faster carrier relaxation [235] to strongly polarized emission [236]. Besides, in these elongated nanostructures the longitudinal confinement may be fairly weak, so that the dielectric polarization of the Coulomb interactions is expected to play an important role in the determination of their properties. Indeed, several studies on quasi-one-dimensional nanostructures have suggested the effects coming from the dielectric mismatch with the environment as the driving mechanism to explain some experimental findings. For instance, one can mention the large variation of the optical gap of CdSe NRs compared to the transport one [237], the effect on the excitonic energies observed in ZnS NRs [238] and type-II NRs [239], or the large magnitude of the polarization anisotropy on linear [240–242] and nonlinear [243] optical phenomena. Also, the dielectric confinement has been shown to affect electron-hole separation dynamics in type-II heterostructured NRs [244] as well as coupling between electrons and longitudinal optical phonons in CdSe NRs. [245]

NRs are the zero-dimensional version of nanowires, where variations in the dielectric constant of the embedding media have been theoretically stud-

ied and shown to produce drastic changes in the exciton binding energy and oscillator strength [150, 246, 247]. Nevertheless, the amount of theoretical works focusing on environmental effects on semiconductor NRs is rather scarce. Up to the moment of publication of the works reviewed here, just two works can be found in the literature [162, 163] and yet neglect the contributions from both the longitudinal spatial confinement and the Coulomb correlations (i.e., they treat the Coulomb interactions as first-order perturbations). Here it will be shown that these assumptions may be inappropriate when taking the dielectric effects of the environment into account.

This section performs a theoretical study of the dielectric confinement effect on interacting particles confined in semiconductor NRs. To this end, a numerical method is developed which allows to calculate the electrostatic potential in three-dimensional systems with inhomogeneous dielectric constant $\varepsilon(\mathbf{r})$ [145]. A comprehensive summary of the method is outlined in the next section. In short, it is based on the computation of the polarization charges induced at the dielectric interfaces to later calculate the electrostatic potential generated by the source charges plus these polarization charges [248, 249]. The fully three-dimensional model allows to compare the behavior of different NC shapes. Thus, several CI results are shown for two-electrons and an exciton confined in a rod and a spherical dot. Whereas the main effect of the dielectric environment observed in the dot is the well known increase of the Coulomb interactions, in the case of the elongated rod it brings the system into a regime of strong correlation. The wave functions are particularly sensitive to such correlation, which leads to qualitative changes in the electronic and optical properties of the rods. Additionally, an exhaustive study about the dielectric confinement effect on the excitonic properties of NRs is carried out. The case of recently synthesized type-II heterogeneous NRs is also studied. In these systems the asymmetric location of electron and hole charge distributions is demonstrated to magnify the dielectric confinement effect due to a reduced compensation between self-energy and Coulomb polarization terms. Finally, the NR response to longitudinal electric fields is studied. It is shown that the threshold field required to separate the electrons from holes is strongly dependent on the dielectric constant of the environment.

3.4.1 Dielectric confinement computation in axially-symmetric nanostructures

As introduced in section 3.1, the calculation of the electrostatic potential in inhomogeneous dielectric media goes through finding a solution of the Poisson equation [6]

$$\nabla \left[\varepsilon(\mathbf{r}) \nabla \Phi(\mathbf{r}) \right] = -4\pi \eta(\mathbf{r}), \tag{3.27}$$

where $\Phi(\mathbf{r})$ is the Coulomb potential generated by the charge density distribution $\eta(\mathbf{r})$, and $\varepsilon(\mathbf{r})$ is the position dependent dielectric constant. Solving this equation with appropriate boundary conditions yields a Coulomb potential which is equivalent to the one generated in a vacuum by the joint action of the source charges $\eta(\mathbf{r})$ and the charges $\tilde{h}(\mathbf{r})$ induced in the medium, i.e.,

$$\Phi(\mathbf{r}) = \Phi_s(\mathbf{r}) + \Phi_i(\mathbf{r}), \tag{3.28}$$

with $\Phi_s(\mathbf{r})$ and $\Phi_i(\mathbf{r})$ fulfilling

$$\nabla^2 \Phi_s(\mathbf{r}) = -4\pi \eta(\mathbf{r}), \tag{3.29}$$

$$\nabla^2 \Phi_i(\mathbf{r}) = -4\pi \tilde{h}(\mathbf{r}). \tag{3.30}$$

Expanding the left derivative term of equation 3.27 and introducing 3.28, 3.29 and 3.30, leads to the following expression after some algebra,

$$\varepsilon(\mathbf{r}) \tilde{h}(\mathbf{r}) = \left[1 - \varepsilon(\mathbf{r}) \right] \eta(\mathbf{r}) + \frac{1}{4\pi} \nabla \varepsilon(\mathbf{r}) \nabla \left[\Phi_s(\mathbf{r}) + \Phi_i(\mathbf{r}) \right]. \tag{3.31}$$

The method that will be here used to obtain $\tilde{h}(\mathbf{r})$ is a numerical discretization of the above equation. In the discretization process, the continuous source charge distribution $\eta(\mathbf{r})$ is defined by a distribution of point charges q_k localized at the nodes k of the discretization grid. The charge distribution can be then expressed as

$$\eta(\mathbf{r}) = \sum_k q_k \delta(\mathbf{r} - \mathbf{r}_k), \tag{3.32}$$

where $\delta(\mathbf{r} - \mathbf{r}_k)$ is the Dirac delta function centered at node k.

---

[6]Please note that this equation is the same as equation 3.8. Here, however, the explicit double dependence of the potential on the spatial coordinates, namely, $\Phi(\mathbf{r}', \mathbf{r})$, is skipped for the shake of conciseness. The Greek letter η is also used instead of ρ as the source charge density to avoid misunderstandings with the radial spatial coordinate ρ.

Apart from the polarization charges induced at the dielectric interfaces, other ones are induced by each point charge q_k. To visualize this fact, let us consider the case of a point charge q_k placed in a uniform dielectric medium with constant ε. According to the Gauss theorem, the field generated by this charge is q_k/ε, which means that an induced charge is generated around the source point charge to accomplish $q_k + q_k^i = q_k/\varepsilon$ [250]. Therefore, the induced charge around each point charge will have a density

$$q_k^i = -q_k \left(1 - \frac{1}{\varepsilon(\mathbf{r}_k)} \right) \delta(\mathbf{r} - \mathbf{r}_k), \tag{3.33}$$

and the contribution to the total density of polarization charges $\tilde{h}(\mathbf{r})$ coming from the induced charge around the source charges position is then

$$h_{SC}(\mathbf{r}) = \sum_k -q_k \left(1 - \frac{1}{\varepsilon(\mathbf{r})} \right) \delta(\mathbf{r} - \mathbf{r}_k). \tag{3.34}$$

On the other hand, a point charge in a homogeneous medium also induces the formation of image charges at infinity q_∞. The effect of these charges is perfectly negligible as is their electrostatic field: $\sim q_\infty/|r_\infty - r'|$, where the denominator (r_∞) is infinite while the numerator is finite.

Substituting $\tilde{h}(\mathbf{r}) = h(\mathbf{r}) + h_{SC}(\mathbf{r})$ in equation 3.31 and writing $\eta(\mathbf{r})$ and $h_{SC}(\mathbf{r})$ as in expressions 3.32 and 3.34 respectively, one obtains

$$\varepsilon(\mathbf{r})h(\mathbf{r}) = \frac{1}{4\pi} \nabla \varepsilon(\mathbf{r}) \nabla \left[\Phi_s(\mathbf{r}) + \Phi_i(\mathbf{r}) \right], \tag{3.35}$$

where $h(\mathbf{r})$ stands for the induced charges other than $h_{SC}(\mathbf{r})$, i.e., those induced at the dielectric interfaces.

Whenever the integration domain V includes all source and induced charges [7], $\Phi_s(\mathbf{r})$ and $\Phi_i(\mathbf{r})$ can be expressed as

$$\Phi_s(\mathbf{r}) = \int_V \frac{\eta(\mathbf{r}')}{|\mathbf{r} - \mathbf{r}'|} d\mathbf{r}', \tag{3.36}$$

$$\Phi_i(\mathbf{r}) = \int_V \frac{h(\mathbf{r}') + h_{SC}(\mathbf{r}')}{|\mathbf{r} - \mathbf{r}'|} d\mathbf{r}'. \tag{3.37}$$

Again, writing $\eta(\mathbf{r})$ and $h_{SC}(\mathbf{r})$ in the form of point charges distributions defined by 3.32 and 3.34, the next relation is obtained

---

[7]Except for charges induced at infinity.

$$\Phi_s(\mathbf{r}) + \Phi_i(\mathbf{r}) = \int_V \frac{h(\mathbf{r}')}{|\mathbf{r} - \mathbf{r}'|} d\mathbf{r}' + \int_V \frac{\eta(\mathbf{r}')}{\varepsilon(\mathbf{r}') |\mathbf{r} - \mathbf{r}'|} d\mathbf{r}', \qquad (3.38)$$

which can be introduced in equation 3.35 finally yielding

$$h(\mathbf{r})\varepsilon(\mathbf{r}) - \frac{1}{4\pi} \nabla_{\mathbf{r}} \varepsilon(\mathbf{r}) \int_V \nabla_{\mathbf{r}} \left(\frac{1}{|\mathbf{r} - \mathbf{r}'|} \right) h(\mathbf{r}') d\mathbf{r}'$$
$$= \frac{1}{4\pi} \nabla_{\mathbf{r}} \varepsilon(\mathbf{r}) \int_V \nabla_{\mathbf{r}} \left(\frac{1}{|\mathbf{r} - \mathbf{r}'|} \right) \frac{\eta(\mathbf{r}')}{\varepsilon(\mathbf{r}')} d\mathbf{r}'. \qquad (3.39)$$

Solving the above equation allows one to calculate the charge-charge interactions and the self-polarization potential of any three-dimensional system. The numerical discretization of equation 3.39 yields a linear matrix equation $\mathcal{A}h = \mathcal{B}$, where $\mathcal{B}$ depends only on the source charge and $\mathcal{A}$ on the geometry of the system. The first step in solving this matrix equation involves the LU factorization of $\mathcal{A}$. Since $\mathcal{A}$ does not depend on the source charge, the LU factorization, which as a matter of fact is the heaviest part of the calculation, needs to be performed only once, independently of the source charges evaluated. What is more, it can be seen in equation 3.39 that $h(\mathbf{r})$ is different from zero only in the regions where $\nabla\varepsilon(\mathbf{r}) \neq 0$, i.e., in the dielectric interfaces, where $\varepsilon(\mathbf{r})$ varies smoothly between the corresponding values of the adjacent materials. This reduces the dimension of the equation system considerably.

Let us now consider the case of axially-symmetric systems as those studied in next sections. To show the way of computing the many-body interactions in the corresponding inhomogeneous dielectric media, a general Coulomb matrix element is regarded, $\langle \varphi_1(\mathbf{r}_1)\varphi_2(\mathbf{r}_2)|\Phi(\mathbf{r}_1, \mathbf{r}_2)|\varphi_3(\mathbf{r}_1)\varphi_4(\mathbf{r}_2)\rangle$, where $\varphi_i(\mathbf{r}_j) = \chi_i(\rho_j, z_j)e^{\mathbf{i}m_i\phi_j}$ are the employed basis functions [8]. Particle 1 is considered as the source charge which generates the potential Ψ on particle 2. Therefore, the source charge density is written as

$$\begin{aligned} \eta(\rho, z, \phi) &= \chi_1(\rho, z)\chi_3(\rho, z)e^{\mathbf{i}(m_3 - m_1)\phi} \\ &= \eta(\rho, z)e^{\mathbf{i}(m_3 - m_1)\phi}. \end{aligned} \qquad (3.40)$$

Since η is axially-symmetric, so will h ($h(\rho, z, \phi) = h(\rho, z)e^{\mathbf{i}(m_3 - m_1)\phi}$). This allows one to compute h in a two-dimensional grid by evaluation of, e.g.,

---

[8]Usually the single-particle eigenfunctions of the system.

the plane $\phi = 0$. $h(\mathbf{r})$ is then obtained by means of numerical discretization of equation 3.39 in cylindrical coordinates [145]. Next, it is necessary to calculate the whole effective charges in vacuum, namely, $\eta(\mathbf{r}) + h_{SC}(\mathbf{r}) + h(\mathbf{r})$, producing the same effect as the source charge in the dielectric environment. Taking expressions 3.32 and 3.34 if is easy to obtain

$$\eta(\mathbf{r}) + h_{SC}(\mathbf{r}) + h(\mathbf{r}) = \sum_k \frac{q_k}{\varepsilon(\mathbf{r}_k)} \delta(\mathbf{r} - \mathbf{r}_k) + h(\mathbf{r}) = \frac{\eta(\mathbf{r})}{\varepsilon(\mathbf{r})} + h(\mathbf{r}). \quad (3.41)$$

Finally, the Coulomb matrix element can be evaluated as follows:

$$V = \int \left[\frac{\eta(\mathbf{r}_1)}{\varepsilon(\mathbf{r}_1)} + h(\mathbf{r}_1) \right] \frac{1}{|\mathbf{r}_1 - \mathbf{r}_2|} \varphi_2^*(\mathbf{r}_2) \varphi_4(\mathbf{r}_2) d\mathbf{r}_1 d\mathbf{r}_2. \quad (3.42)$$

The calculation of the self-polarization potential is a bit more involved computationally speaking. As pointed in section 3.1, this potential can be viewed as the potential felt by a unitary charge located at a given position $\mathbf{r}_0$ due to the charges that it induces in the medium, excluding those induced directly around the source charge:

$$V_s(\mathbf{r}_0) = \frac{1}{2} \int \frac{h(\mathbf{r}_0; \mathbf{r}')}{|\mathbf{r}_0 - \mathbf{r}'|} d\mathbf{r}'. \quad (3.43)$$

Given that in the calculation of the self-polarization potential the source charge is a point charge, the equation to solve becomes

$$h(\mathbf{r})\varepsilon(\mathbf{r}) - \frac{1}{4\pi} \nabla_{\mathbf{r}}\varepsilon(\mathbf{r}) \int_V \nabla_{\mathbf{r}} \left(\frac{1}{|\mathbf{r} - \mathbf{r}'|} \right) h(\mathbf{r}') d\mathbf{r}' =$$
$$\frac{1}{4\pi} \nabla_{\mathbf{r}}\varepsilon(\mathbf{r}) \nabla_{\mathbf{r}} \left(\frac{1}{|\mathbf{r} - \mathbf{r}_0|} \right) \frac{1}{\varepsilon(\mathbf{r}_0)}. \quad (3.44)$$

The self-polarization potential has the same symmetry as the system, then its calculation (equation 3.43) can be performed in the $\phi = 0$ plane only. However, the source charge is now a point charge which only preserves the axial symmetry when located at the symmetry axis (z). In any other case, the corresponding induced charge distribution does not present axial symmetry. As a consequence, the evaluation of $h(\mathbf{r})$ (equation 3.44) must be carried out in three dimensions, which multiplies by n_ϕ (n_ϕ being the number of discretization points in ϕ) the dimension of the corresponding matrix equation. The numerical calculation of the self-polarization potential is hence computationally demanding, specially if one is interested in

reproducing properly the narrow potential well generated in the smaller dielectric constant regions. Still, some strategies can be followed to reduce the computational time and storage requirements preserving a good calculation accuracy [145].

3.4.2 Nanorod vs. spherical nanocrystal: dielectric confinement effect

This section compares the effect of the dielectric polarization of the Coulomb interactions on spherical and axial symmetry zero-dimensional systems. To this end, two electrons and an exciton confined in a CdSe NC and NR are studied. The rod is composed of a cylinder of radius $R = 2$ nm and length $L = 8$ nm attached to two hemispherical caps of radius $R = 2$ nm in the extremes, giving a total length of $L_{tot} = 12$ nm (see figure 3.18). The spherical NC is chosen to have roughly the same volume, i.e., it has a radius $R = 3.15$ nm. The electron and hole single-particle states are described with EMA Hamiltonians, which in cylindrical coordinates read:

$$\hat{\mathcal{H}}_i = -\frac{1}{2}\left(\frac{1}{\rho}\frac{\partial}{\partial\rho}\left(\frac{\rho}{m^*_{\rho,i}(\rho,z)}\frac{\partial}{\partial\rho}\right) + \frac{\partial}{\partial z}\frac{1}{m^*_{z,i}(\rho,z)}\frac{\partial}{\partial z} - \frac{m_i^2}{\rho^2\,m^*_{\rho,i}(\rho,z)}\right) + V_i(\rho,z),$$

$$(3.45)$$
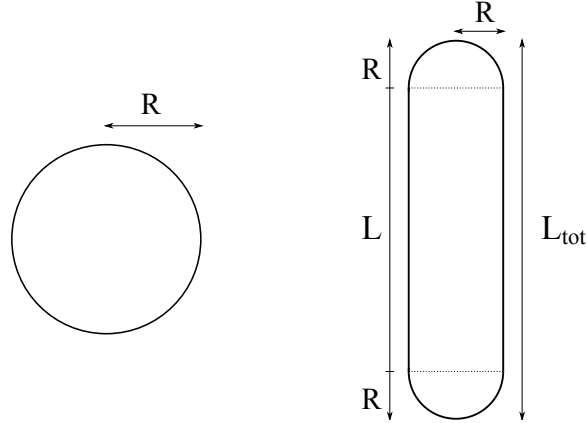
Figure 3.18: Schematics of the studied NC (left) and NR (right)

where $i = e, h$ is a subscript denoting electron or hole respectively, m_i is the azimuthal angular momentum and $V_i(\rho, z)$ is the step-like confining potential, which is zero inside the nanostructure and 4 eV outside. The electron

effective mass is taken isotropic, $m^*_{\rho,e}(\rho,z) = m^*_{z,e}(\rho,z)$. For holes, however, the mass anisotropy is important, as it is responsible for the heavy hole-to-light hole ground state transition that occurs as the aspect ratio of the nanostructure increases. [237, 251] In this regard, heavy hole masses are employed to model the ground excitonic state of the NC while light hole masses are used for the NR [252].
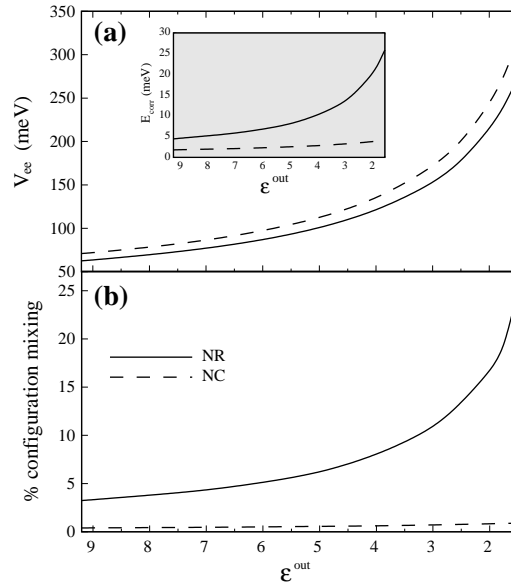
Figure 3.19: Two electron ground state properties in a NR (solid line) and a spherical NC (dashed line) of the same volume, as a function of the dielectric constant of the embedding medium.(a) Electron-electron interaction energy, (b) configuration mixing in the CI expansion. The inset represents the Correlation energy.

The dielectric contributions arising from the self-polarization potential (self-energy) are neglected in the present study because they do not influence the trends reported here. Indeed, these trends have been supported by subsequent studies in which a full treatment of the dielectric confinement is performed [145, 165]. In turn, the dielectric polarization of the Coulomb interaction has been accounted for with the methodologies outlined in the previous section. The many-body interactions are then taken into account by means of a CI procedure. The variational space for the two electrons (exciton) is built from a large number of two-body Slater determinants (Hartree products) obtained by filling in the single-particle eigenstates in all possible

ways consistent with symmetry requirements.

The case of the bielectronic system is regarded first. Figure 3.19(a) shows the electron-electron interaction energies V_{ee}, taken as the difference between the ground state energy computed by means of a CI and a single-particle calculation, for the NR and the NC as a function of the dielectric constant of the environment, the nanostructure dielectric constant being that of the CdSe bulk, $\varepsilon_{CdSe} = 9.2$. As can be seen, the repulsion energy of both systems evolves similarly, experiencing the well known enhancement of the Coulomb interactions as the dielectric mismatch is increased. To quantify the amount of V_{ee} that is not captured in perturbative treatments of the Coulomb interaction, the inset of figure 3.19 shows a sort of correlation energy defined as $E_{corr} = V_{ee} - V_{ee}^0$. [9] Here V_{ee}^0 is the expectation value of the Coulomb repulsion for the dominant configuration in the CI expansion. The plot reveals the first differences between NR and NC. In absence of dielectric mismatch the NR correlation energy is more than twice that of the NCs. This is a signature of the weak confinement regime in the longitudinal direction of the NR. Differences are however dramatic as the outer dielectric constant is reduced. Whereas the NC correlation energy remains unaltered, it experiences a strong increase for the case of the NR, reaching values six times larger than the NC correlation energy.

Electronic correlations have normally visible effects on the wave function, which is asserted in the present case. Figure 3.19(b) plots the ground state wave function configuration mixing, i.e., the weight of the CI expansion which does not come from the dominant configuration. As evidenced by the figure, the NR bielectronic wave function is severely affected by dielectric polarization. The observed enhancement in the NR configuration mixing as the dielectric mismatch is increased contrasts with the insensitivity of the NC wave function. This support the use of perturbative treatments of the Coulomb interactions in studies of spherical NCs [225, 226], but brings it into question when dealing with semiconductor NRs. Special mention deserve the study of NRs buried in insulating matrices, i.e, low dielectric constant matrices, where a full interacting and dielectric confinement treatment seems to be required to properly capture the system properties.

A consequence of the configuration mixing on the wave function is shown

---

[9] Properly speaking the correlation energy is defined as the energetic difference between the Hartree-Fock ground state and the exact many-body solution.
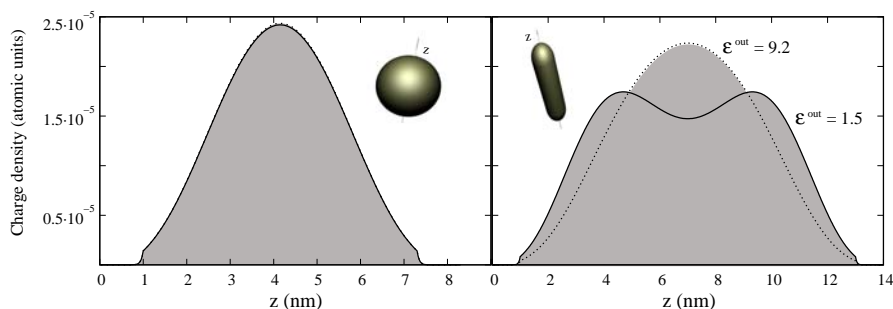
Figure 3.20: Two electron ground state charge density along the longitudinal axis of a NC (left) and a NR (right), with (solid line) and without (dotted line) dielectric mismatch. The insets are schematics of the nanostructures.

in figure 3.20. There, the charge density of one electron is plotted along the longitudinal axis after integrating the coordinates of the other electron. Two different dielectric situations are considered, one without dielectric mismatch ($\varepsilon_{out} = 9.2$), and one with a strong mismatch ($\varepsilon_{out} = 1.5$). For the case of the NC no differences are observed, in both cases the charge density is preferably located at the center of the NC where the spatial confinement is weaker. The NR charge density however suffers a relevant modification as a consequence of the dielectric confinement, it develops a valley in the center of the nanostructure. This is an indication that the dielectric polarization is inducing Wigner localization in the NR, which will have direct implications for transport processes [253] and shell-filling spectroscopy [254].

The dielectric mismatch effects on the excitonic states are addressed next. The results presented in figure 3.21 go in parallel with the bielectronic case. Thus, the electron-hole Coulomb attraction experiences for both nanostructures an increase in absolute value as the dielectric mismatch is enlarged. Again, differences arise in the correlation energy and the wave function configuration mixing. The latter advice against the use of perturbative treatments to study optical properties of semiconductor NRs. Furthermore, the high regime of wave function configuration mixing experienced by the NR in insulating environments is expected to have strong implications in the optical properties of NRs. Evidence of this has been observed in large self-assembled QDs where the electronic correlations have been shown to enhance the exciton luminescence [255]. Therefore, it is worth studying the electron-hole recombination probability in the present systems. This magnitude can be calculated from the exciton wave function by means of the
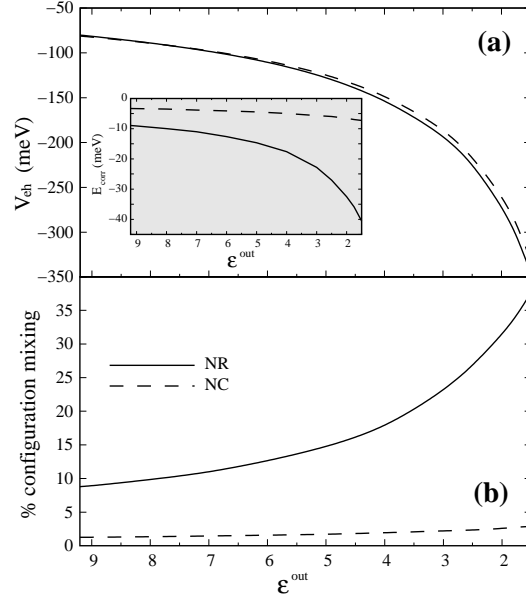
Figure 3.21: Same as figure 3.19 but for the exciton ground state

dipole approximation and Fermi golden rule [45]

$$P_{gs} \propto \left| \sum_i c_i^{gs} \langle \phi_i^e | \phi_i^h \rangle \right|^2 \mathcal{P}^2. \qquad (3.46)$$

Here c_i^{gs} is the ground state CI expansion coefficient corresponding to the Hartree product formed by the electron and hole spin-orbitals ϕ_i^e and ϕ_i^h. $\mathcal{P}$ is the Kane matrix element. A comparison of the exciton recombination probability in a NC and a NR is presented in figure 3.22 (a). The first remarkable issue is the larger NR recombination probability [162], which agrees with the improved optical properties experimentally observed with respect to their spherical counterparts [235]. Besides, the NR recombination probability shows a growing tendency as the outer dielectric constant is reduced, this being a clear signature of the strong correlations affecting the wave function.

Finally, we show how Coulomb correlated wave functions are more sensitive to external perturbations than strongly confined ones. To this end, a longitudinal electric field of 50 kV/cm is applied to the NR and the absorp-
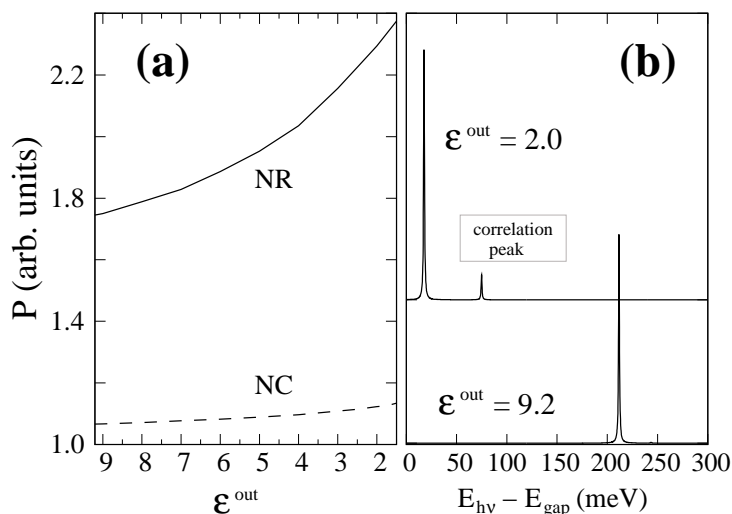
Figure 3.22: (a) Exciton recombination probability for a NR (solid line) and a NC (dashed line) vs. the dielectric constant of the embedding medium. (b) Simulated absorption spectrum for the NR under the effect of a moderate electric field in the longitudinal direction. The spectra with and without dielectric mismatch are offset for clarity.

tion spectrum is simulated. Regarding the effect of an static electric field in the theoretical simulation just entails to include the term $-e\,F\,z$ (e being the charge of the carrier, F the electric field module and z the longitudinal spatial coordinate) in the single-particle Hamiltonians (equation 3.45). The electric field breaks the parity symmetry thus enabling optical transitions from the first excited state. In turn, the absorption spectrum is obtained from $\mathcal{A}(E) = \sum_j P_j\,\delta(E - E_j)$, where E is the incident photon energy and P_j is the recombination probability of the j-th exciton state, with energy E_j. The NR spectra for two different dielectric media are represented in figure 3.22 (b). As can be seen, in the absence of dielectric mismatch only the fundamental transition takes place. However, when the dielectric confinement comes into play an additional small peak appears in the spectrum [10]. This new peak arises from recombination of the first excited state, which in absence of dielectric mismatch is still negligible as it involves the lowest single-electron orbital ($1s_e$), which is quasi-gerade, and the first excited

---

[10] The quantitative redshift experienced by the fundamental transition is modified upon inclusion of the self-polarization interactions neglected here. Actually, in the next section it will be shown that in the case $\varepsilon_{NR} > \varepsilon_{out}$ the dielectric confinement induces a blueshift of this peak.

single-hole orbital ($2s_h$), which is quasi-ungerade. The correlations induced by the dielectric mismatch are therefore behind the appearance of this peak, since they lead to strong mixing of the $1s_e\,2s_h$ and $1s_e\,1s_h$ configurations. The large overlap between the orbitals of the latter configuration yields a finite electron-hole recombination probability. A similar electric field perturbation may be generated by molecular dipoles in the vicinity of the rod, which suggests that dielectrically confined NRs are suited structures for sensing applications.

In conclusion, the results reported here provide compelling evidence that the dielectric confinement experienced by semiconductor NRs has larger consequences than in the predominantly studied case of spherical NCs. The dielectric polarization effects go beyond energetic magnitudes increasing the correlation regime and the wave function configuration mixing. This latter fact has been shown to have visible consequences on the optical and transport properties of NRs, including improved luminescence and sensitivity.

3.4.3 Dielectric environment effects on the optical properties of nanorods

The numerical results presented in the previous section have revealed that the overall NR response to the dielectric environment differs from that of spherical QDs, and hence, deserves a deep understanding of the possible consequences it can have on the optical properties of these high-performance light emitters. For this purpose, the present section carries out a wide study of the dielectric confinement of excitons in semiconductor NRs. Different NR aspect ratios are regarded, from the nearly spherical to the quasi one-dimensional limits. Furthermore, the case of heterogeneous NRs showing type-II band alignment is studied. The long-lived spatially charge-separated state developed by these systems upon excitation is shown to enable strong dielectric mismatch effects. Finally, the application of an external electric field along the NR longitudinal direction is simulated. It is shown that the response of the system to the electric field is strongly subjected to the dielectric mismatch with the environment.

The numerical methodologies employed to achieve the results presented here are essentially the same as those outlined in the previous section with two main differences. The first one is the inclusion of the self-polarization potential in the single-particle spectra description. Thereby, a full treatment of the dielectric confinement is performed. The second one is the use

of a different basis set of single-particle functions to build up the Hartree products in which the exciton Hamiltonian is expanded. The chosen basis consists in a set of floating 1s-Gaussian functions expressed as

$$g_{i,x}(\mathbf{r}) = e^{-\alpha_x(\mathbf{r}-\mathbf{R}_i)^2}. \tag{3.47}$$

The Gaussians are radially centered and equally spaced along the NR longitudinal axis, i.e., $\mathbf{R}_i = z_i \mathbf{k}$. Previously, the exponents $\alpha_x(x = e, h,$ for electron and hole) are variationally fitted in a sphere calculation where a single Gaussian function is employed. A numerical basis set formed by the single-particle Hamiltonian eigenfunctions as used in previous section would be better adapted to the spatial confinement and hence would yield lower exciton energies. However, using equidistant floating Gaussian enables a uniform saturation along the NR as well as a continuously homogeneous description of the system, from the spherical limit to the extremely elongated one. Moreover, the use of Gaussian functions allows an analytical evaluation of most of the integrals involved in the construction of the Hamiltonian matrix, which considerably reduces the computational time.

The electron-hole recombination probability is also studied here. Nonetheless, since large aspect ratio NRs are considered where the energy separation between the ground state and the low-lying excited states is just a few meV, thermal population effects are taken into account to compute the recombination probability. To this end, a Boltzmann distribution, $p_l(T) = N(g_l/g_o)e^{-\Delta E_l/kT}$, for the exciton states population is incorporated in the formula 3.46. Here, T is the temperature, g_l (g_0) is the degeneracy factor of the state l (ground state), ΔE_l the energy difference between the state l and the ground state, and k the Boltzmann constant. N is the normalization constant, which ensures that the sum of all exciton states population is equal to one.

Finally, the electric dipole moment data presented in figure 3.26 are computed as

$$\mu = \int [\rho^h - \rho^e] \, z \, dv, \tag{3.48}$$

where $\rho^{e,h}$ are the electron and hole ground state densities.

Homogeneous CdSe NRs are first considered. The rods have a constant radius of $R = 2$ nm whereas the total length is varied to simulate different

longitudinal confinements. Exciton ground state energy, binding energy, and recombination probability results are reported in figure 3.23 for media with different dielectric constant ε_{out} ($\varepsilon_{NR} = 9.2$). As can be seen in plot (a), for a given environment, the exciton energy first experiences a significant stabilization as the rod is elongated and then an asymptotic value is attained. This behavior, which has been observed in optical and transport gap measurements [237, 256], reflects the relaxation of the longitudinal spatial confinement. The asymptotic regime is usually identified with a quasi-1D system, where only radial confinement is present, and it explains the success of quasi-1D models in reproducing experimental observations [162].
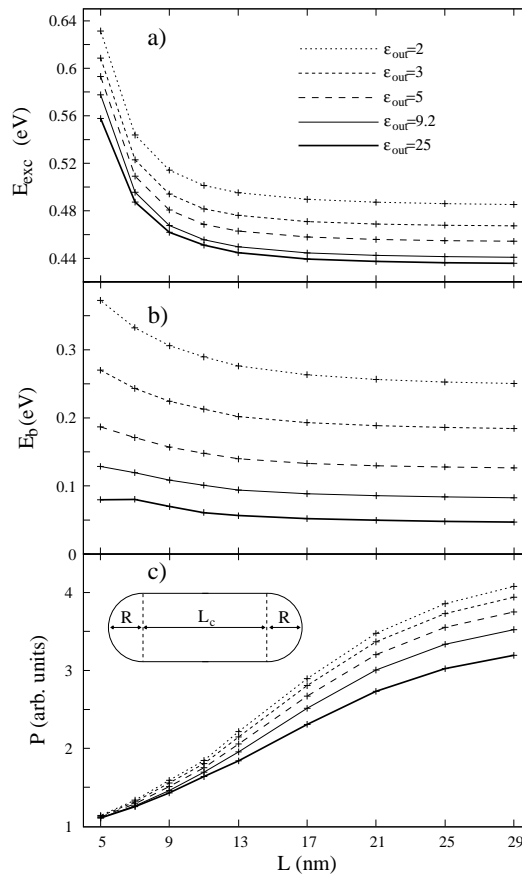
Figure 3.23: (a) Exciton ground state energy, (b) binding energy and (c) recombination probability (T=30 K) of CdSe NRs with variable length embedded in different dielectric media. Inset: schematic of the NR geometry.

A similar relaxation is observed in figure 3.23(b) for the binding energy. The plot also illustrates the dielectric enhancement of E_b mentioned on numerous occasions in this text.

Despite the observed gain in binding energy when $\varepsilon_{NR} > \varepsilon_{out}$, figure 3.23(a) reveals that insulating environments blueshift the exciton energy by up to 50 meV. This results from prevalence of the self-polarization interaction over the Coulomb polarization, being that, as introduced in section 3.1, both contributions work in opposite directions in neutral excitonic systems.

Soon after their first synthesis, a striking observation of the NRs physics was the large difference between the measured optical and the quasi-particle (or transport) gap [237]. The large stabilization of the optical gap could not be explained in terms of the bare Coulomb attraction between electron and hole, so that it was assigned to the binding energy amplification induced by the environment through dielectric polarization [162]. In this regard, it is worth noting that the dielectrically destabilized exciton observed in figure 3.23(a) does not contradict this experimental finding. The reason is that while both gaps (optical and transport) include the self-polarization effects, only the optical one experiences the stabilization caused by the Coulomb polarization.

The dielectric environment has been shown to modify the spectral position of the NR excitonic transition. Now the effects on the intensity of the associated spectral peak are investigated. With this purpose, figure 3.23(c) plots the electron-hole recombination probability computed at T=30 K. The trends observed in the figure can be essentially outlined as: (i) the recombination probability increases with the NR length, (ii) insulating environments enhance the recombination probability, and (iii) this enhancement is larger for long NRs. All these observations are originated in the high configuration mixing regime already noted in the previous section, which is favored as the longitudinal spatial confinement is weakened and the dielectric mismatch is increased. In addition, it can be seen that for long NRs the thermal population of excited states become important and the ground state recombination probability saturates towards the quantum wire limit.

Let us turn to study the case of heterogeneous NRs similar to those synthesized in references [239, 257]. The rods are composed of a central CdSe cylinder (core) of radius $R = 2$ nm and length L_c^{CdSe} attached to two external shells of CdTe. The shells in turn are formed by a hemispherical cap of

radius $R = 2$ nm and a cylinder of length L_c^{CdTe} (see figure 3.24(c) inset).
Bringing all the parts together yields two shells of length $L_s^{CdTe} = R + L_c^{CdTe}$
and a total NR length $L = 2L_s^{CdTe} + L_c^{CdSe}$. These heterostructured sys-
tems are known to display a type-II band alignment [239, 257–259], where
electrons are preferably located in CdSe regions and holes in CdTe regions.
To reproduce this situation, a band offset in the interface between both
materials has been included in the numerical calculations. For electrons a
band offset of 0.42 eV has been taken while for holes an inverse band offset
of 0.57 eV is employed [260]. Since the material parameters of CdSe and
CdTe do not offer significant differences, the CdSe effective mass and di-
electric constant have been taken for the whole NR. Thus, the system just
presents the dielectric interface between the whole NR and the environment.

The same optical magnitudes studied for homogeneous NRs are pre-
sented in figure 3.24 for the case of type-II NRs composed of a CdSe core
of length $L_c^{CdSe} = 4$ nm and CdTe shells whose length L_s^{CdTe} is increased
along the horizontal axis of the graphics. As in the case of homogeneous
NRs, for a given environment the exciton energy (panel (a)) shows an initial
stabilization and later it reaches an asymptotic value; in this case this limit
just reflects the relaxation of the longitudinal confinement felt by the holes,
though. Likewise, the response to the outer dielectric constant is qualita-
tively the same observed for CdSe NRs but now the module of the induced
shifts is twice larger, reaching values as large as 100 meV. The origin of
this larger dielectric effect on the exciton energies lies in the asymmetric
location of the electron and the hole, which leads to a less effective can-
cellation between the energetic contributions of the dielectric confinement.
Thus, whereas the Coulomb polarization is weaker than in CdSe NRs, as
reflected in the smaller binding energies illustrated in figure 3.24(b), the
self-polarization interaction has the same effect in both systems. On the
whole, this translates into enhanced dielectric mismatch effects.

At this point it is worth noting that the effect of the dielectric con-
finement predicted in figure 3.24(a) is consistent with the main trends re-
ported in reference [239], where the photoluminescence spectra of similar
CdTe/CdSe/CdTe NRs were compared for solvents with different dielec-
tric constant. A blueshift of the exciton emission energy by tens of meV
was observed under low dielectric constant environments. This confirms
the prevalence of the self-interaction potential over the polarization of the
electron-hole Coulomb interaction.
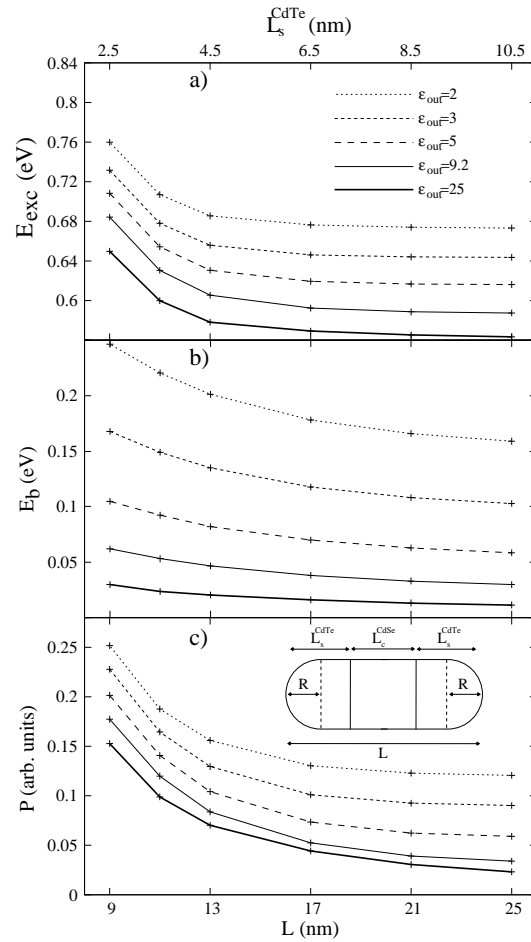
Figure 3.24: Same as figure 3.23 but for type-II NRs

The electron-hole recombination probability is illustrated in figure 3.24(c). The first difference observed with the case of homogeneous NRs is the important reduction of the recombination probability due to the smaller electron-hole overlap [257]. Also, a decreasing tendency is observed now as the rods are elongated. This is because the length increase comes from longer CdTe shells, so that the hole lies further of the electron leading to additional reduction of the electron-hole overlap. The response to the dielectric environment is also quite different from the CdSe NRs. Whilst insulating environments still enhance the recombination probability, this is a constant effect for all the NR lengths considered, unlike the homogeneous NRs case. The reason is

that in type-II NRs increasing the length of the CdTe regions do not entails an increase in the wave function configuration mixing as it just relaxes the hole spatial confinement.
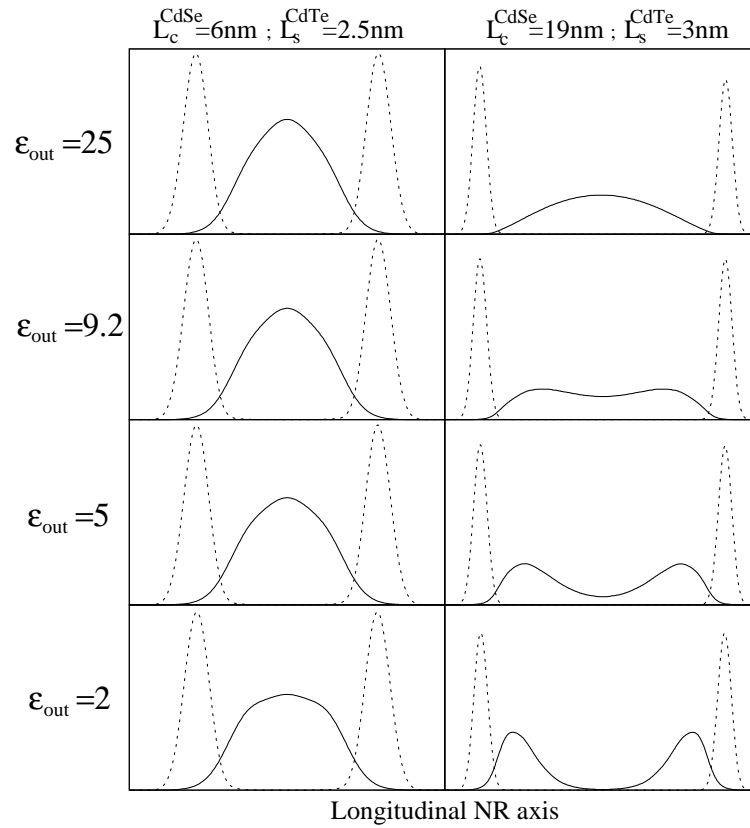
Figure 3.25: Electron (solid lines) and hole (dashed lines) charge densities along the longitudinal axis of type-II NRs.

Next it is shown how the particular linear structure of the studied type-II nanorods enables the observation of a striking effect of the dielectric confinement. It consists in the reshaping of the exciton wave function by means of changing the dielectric constant of the embedding medium. Such a process is illustrated in figure 3.25, where the electron (solid line) and hole (dashed line) density profiles along the NR longitudinal axis are plotted. Left (right) panels correspond to NRs of dimensions $L_c^{CdSe} = 6$ nm and $L_s^{CdTe} = 2.5$ nm ($L_c^{CdSe} = 19$ nm and $L_s^{CdTe} = 3$ nm). As can be observed in the left panels,

no noticeable effects arise in the case of the shorter NR. By contrast, as the longer NR is embedded in strong insulating media, the electron moves from the rod center to the CdTe shells. For a strong enough dielectric mismatch, the electron density even develops a deep valley at the center of the NR (see e.g. $\varepsilon_{out} = 2$, bottom right panel in figure 3.25). This transition of the electron density takes place as a consequence of the enhancement of the electron-hole attraction caused by the dielectric polarization of the Coulomb interaction. It does not appear in the shorter NR because the longitudinal spatial confinement avoid it, however, as the central CdSe core is elongated the longitudinal confinement felt by the electron is overtaken by the attractive Coulomb interaction and the electron is dragged by the hole towards the material interface.

The electron localization near the external shells evidences a regime where the role of the longitudinal spatial confinement is outweighed by the dielectric confinement. Moreover, important implications follow from this phenomenon, such as enhanced sensitivity of the exciton near the CdSe/CdTe interface and reduced coupling to impurities and defects in the center of the rod.

The use of an external electric field along the longitudinal direction has been pointed in the recent years as a proper way to modulate the photoluminescence emission of NRs [261–263]. On the one hand, the electric field tends to separate electrons from holes thus reducing their overlap and allowing to switch on/off the NR emission. On the other hand, the rate at which this separation appears is known to be affected by the quantum confinement, which is related to the quantum confined Stark effect. Having observed above the strong influence of the dielectric environment in NRs at zero field, here is probed how it modifies the exciton response to longitudinal electric fields.

Figure 3.26 panels show the evolution of three optical magnitudes vs. the intensity of the electric field, namely, (a) the exciton ground state energy, (b) the electron-hole recombination probability, and (c) the electric dipole moment. These excitonic magnitudes have been computed for an homogeneous CdSe NR of total length $L = 25$ nm embedded in different dielectric media. An overview of the results is enough to conclude that there exists an electric field from which the system suddenly changes its behavior. This field is identified as the field required to carry out the electron-hole separation. The consequences of the carrier separation are the redshift of the exciton
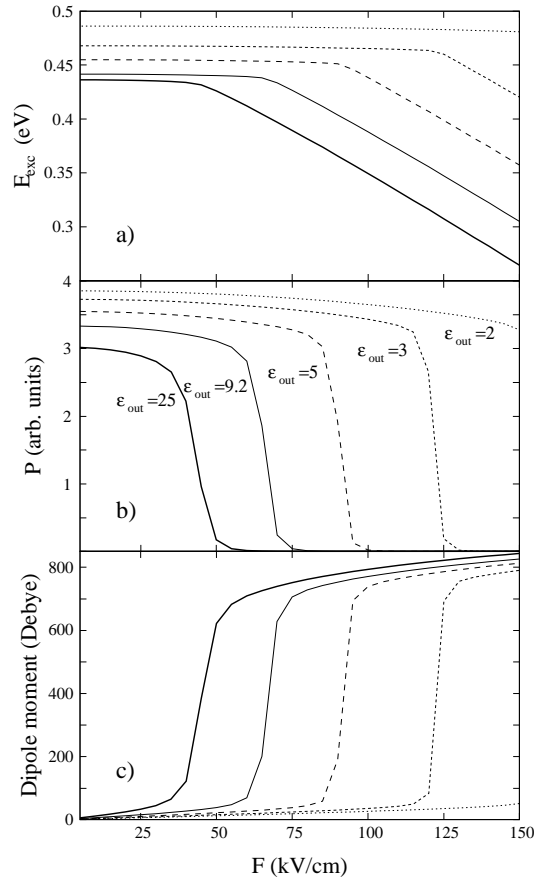
Figure 3.26: (a) Exciton ground state energy, (b) recombination probability and (c) electric dipole moment vs. the longitudinal electric field for 25 nm length CdSe NRs embedded in different dielectric media.

energy, so-called Stark shift, and a sudden reduction of the recombination probability and dipole momentum. It is worth mentioning that the abrupt response to the electric field is consistent with the rapid switches observed in optical spectroscopy experiments [263], where also a redshift of the excitonic signal is observed before it goes out.

The results presented in figure 3.26 also demonstrate the strong impact of the dielectric environment in the system response to electric fields. Thus, it can be observed that the electric field required to split the carriers out becomes larger as the outer dielectric constant is reduced. This being an-

other consequence of the increase in exciton binding energy product of the dielectric confinement.

The influence of longitudinal electric fields on excitons confined in type-II NRs was also studied obtaining the same trends as in homogeneous NRs. The only difference relied on the weaker electron-hole interaction experienced in this kind of systems, which was why smaller electric fields were required to separate the carriers and this process took place more gradually.

In conclusion, along this section evidence has been shown of the strong influence of the dielectric environment on the optical properties of semiconductor NRs. In homogeneous NRs insulating media blueshift the exciton photoluminescence peak by tens of meV, enhance electron-hole recombination rates and increase the electric field required to separate electrons from holes. In type-II NRs, the same effects hold, but now greatly enhanced due to the asymmetric charge distribution of electrons and holes, which reduces the compensation between self-interaction and electron-hole Coulomb polarization. In these systems, a strong dielectric mismatch may move the electron charge density from the center of the core towards the heterostructure interface. This result has straightforward implications in the physical response of the NRs, and it shows that the dielectric confinement can be used -in addition to spatial confinement- to manipulate the shape and size of type-II excitons.

Finally, it should be noted that the phenomena reported in the present and previous section are not exclusive of CdSe/CdTe NRs. They can be extended to rods made of different materials as long as the appropriate dielectric confinement regime is attained.

Chapter 4

Electronic structure of many-electron semiconductor nanorods

Synthesis of colloidal NRs usually starts from metallic or semiconductor precursors in form of spherical NCs. Then the anisotropic form is created by inducing preferential growth along one crystalline direction(e.g., the special c-axis in wurzite nanocrystals) [233, 234, 264]. Throughout this process the nanostructure shape experiences a transition from quasi-spherical to quasi-one-dimensional symmetry which has strong consequences on the electronic properties of the system. On the one hand, due to the change in the spatial confinement of carriers the electronic shell structure is altered. The orbitals s, p, d, ... showing atomic-like degeneracies in the precursors give way to a low-lying spectrum essentially formed by states with null angular momentum $m_l = 0$, which approach in energy as the rod is elongated and tend to form the first band of an infinite quantum wire (see, e.g., figure 4.1). On the other hand, the relaxation of the longitudinal confinement entails a transition from strong to weak confinement regime in which, as shown in previous chapter, the electronic correlations play an important role. Monitoring this change of symmetry and confinement regime in the electron addition energy spectra is the aim of this chapter.

Also, the present chapter is devoted to electron systems placed in very long quantum rods in which the electron-electron interactions dominate over the kinetic energy. In such a high correlation regime, phase transitions take place from charge-density waves (CDW) with $N/2$ peaks in the electronic

97

density distribution to spin-density waves (SDW) showing Wigner crystal-lization, i.e., N peaks in the electronic density, and broken spin-density sym-metry. Further, a fully spin polarized phase is reached at very low electronic densities.

Finally, even though most of the numerical results presented in this chap-ter have been obtained by means of DFT-LSDA calculations, a brief digres-sion about the computation problems arisen in the study of long NRs by means of diagonalization procedures is outlined at the end of the chapter. Different options are suggested to minimize this problematics through the use of basis functions from mean field calculations, as well as a variational potential-configuration interaction scheme.

4.1   Dot to wire transition in the nanorod addition energy spectrum

The electronic structure of CdSe NRs is studied here thorough a process in which a spherical NC is elongated to form a large aspect ratio NR. To this end, DFT-LSDA calculations are carried out in order to compute the addition energy spectra. The numerical approach is the same as outlined in section 2.4 at zero magnetic field and modified to account for a NR-like confining potential. As in the previous chapter, the NRs consist of a cylinder of radius $R = 2$ nm and variable length L, attached to two hemispherical caps of radius $R = 2$ nm. Now, however, discontinuities in material param-eters are disregarded. Then the CdSe parameters ($m_e^* = 0.13$, $\varepsilon = 9.2$) are employed for the whole system.

The bottom of the single-particle spectrum is shown in figure 4.1 as a function of the NR length. A preliminary analysis of this spectrum will help to achieve a subsequent understanding of the addition energies. As can be observed, the energy levels profiles go along with symmetry predictions. At $L = 0$ nm the system shows spherical degeneracies, namely, s, p and d orbitals, given that the levels with $m_l = \pm 1$ (solid lines) and $m_l = \pm 2$ (dashed lines) are doubly degenerate. As the rod is elongated one can see how a great deal of excited $m_l = 0$ states are stabilized below the $m_l = \pm 2$ and ± 1 ones, converging toward the lowest conduction band of an infinite wire. Likewise, signatures of formation of the second ($m_l = \pm 1$) and third ($m_l = \pm 2$) bands can be seen in the figure. These three bands were experi-
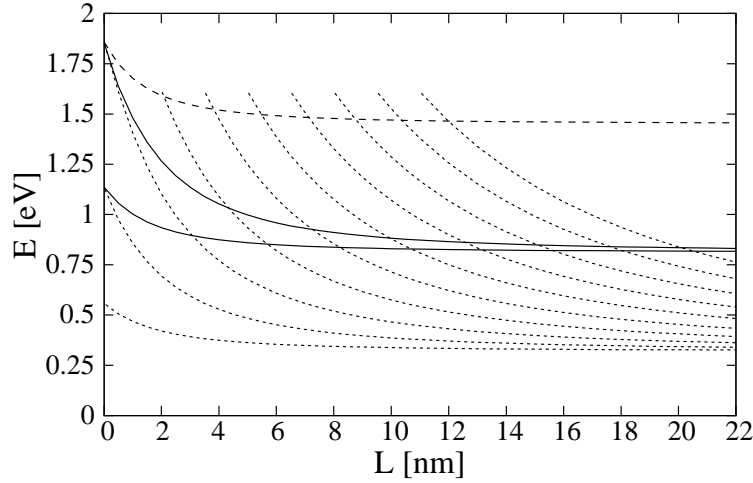
Figure 4.1: Bottom of the single-particle energy spectrum for a CdSe NR of growing length L. Dotted, solid and dashed lines correspond to states with azimuthal angular momentum $m_l = 0$, ± 1 and ± 2 respectively.

mentally identified in tunneling spectroscopy measures where, nevertheless, no traces of the longitudinal quantization were resolved [237].

The addition energies of up to 20 electrons are depicted in figure 4.2. From top to bottom the plotted lines correspond to the spectra of a NR with $L = 0$ up to $L = 22$ nm in steps of $\Delta L = 2$ nm. Also, the different spectra have been offset 400 meV in order to group all the results within a single figure. As announced, the addition energies undergo profiles closely linked to the single-particle spectra. Thus, the $L = 0$ nm profile show the typical maxima at $N = 2$, 8 and 18 electrons corresponding to the filling of the s, p and d shells. However, such a patterned profile is removed as the NR length is increased and more and more $m_l = 0$ states lie at the bottom of the energy spectrum.

Another consequence of the NR elongation is the reduction in the peaks height due to the smaller energy spacing between consecutive levels as evident from figure 4.1. Looking back at this figure, one can also observe that for long NRs the energy spacing is tiny at the bottom of the spectrum and it grows in energy as one moves toward more excited states. This fact has visible consequences in the addition spectra as the system is populated with electrons, i.e., higher energy states are occupied. Let us consider, for in-
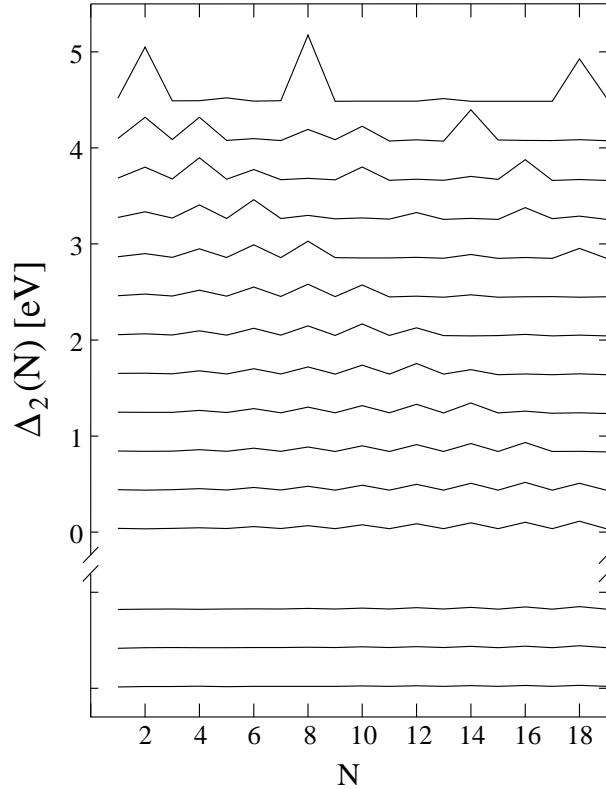
Figure 4.2: Addition energies vs. the number of electrons for NRs of growing length L. From top ($L = 0$ nm) to bottom ($L = 22$ nm) the NR length is increased in steps of $\Delta L = 2$ nm. Consecutive spectra have been offset 400 meV. The three lowest spectra correspond to NRs in the very low density regime with lengths $L = 40$, 45 and 55 nm.

stance, the line $L = 22$ nm in figure 4.2. It shows an almost flat profile at low electronic populations and wrinkles as N is increased.

The three lines represented at the bottom of figure 4.2 correspond to NRs of $L = 40$, 45, and 55 nm. In such a high aspect ratio systems quantum effects coming from the longitudinal confinement are negligible, so that the flat profile of the addition energies just reveals a constant Coulomb blockade effect more typical of metallic nanostructures [265]. Then, it is easy to deduce that tunneling spectroscopy measurements of so long NRs would lead to appearance of conductance peaks at constant shifts of the applied bias as it was observed in large Si nanowires [266].

As the main conclusion of the presented results, it can be said that for CdSe NRs with aspect ratio larger than 6 the addition spectra will become featureless, just showing a sawtooth-like profile in the many-electron regime.

4.2 Phase transitions in quasi-1D high correlation regimes

It is well known that a one-dimensional electron gas (1DEG) experiences transitions between different phases as its electronic density is reduced [267–273]. To show this process, let us consider the case of an infinite wire of variable width. As long as this width exceeds the mean inter-particle separation, the 1DEG is expected to behave as a Fermi liquid. However, it has been theoretically predicted [274], and some experimental findings can be interpreted along this line [275], that as the wire width is further reduced the electron gas becomes spin polarized. Actually, in 1D systems this transition is predicted to occur in the laboratory frame, unlike higher dimension systems [276]. Before this spin polarized state appears, an intermediate transition takes place yielding a phase that shows a periodic modulation of the spin density (spin symmetry breaking) resembling antiferromagnetic order. This phase is referred to as spin-density-wave (SDW).

In turn, since most of the experimentally realized 1D nanostructures are finite, the study of interacting electrons in quasi one-dimensional (Q1D) systems has attracted enormous theoretical interest. Such systems have been mainly modeled using 2D DFT calculations in which anisotropic potentials, both harmonic [268–271] and infinite [272], are used to simulate the spatial confinement. Apart from the spin symmetry breaking, the transition to SDW is paralleled in finite systems by a change in the number of maxima appearing in the electronic density profiles. Specifically, the system undergoes a Wigner crystallization [277, 278], in which the electrons behave like classical density charges arranged in the system to avoid each other as much as possible.

In this section, the low-density limit in which the aforementioned phase transitions are expected to happen is explored for the case of realistic structures carrying out a full 3D theoretical treatment [279]. To this end, long but finite NRs are studied within the DFT-LSDA formalisms. The results are represented in figure 4.3 in form of density profiles along the longitudinal

NR direction. There, solid lines depict the total charge density, while dashed and dotted lines correspond to spin-up and -down densities. Four NRs of lengths $L = 10$, 40, 45 and 55 nm have been considered and populated with $N = 4, 6$ and 8 electrons. At first glance, a general feature can be observed in all the charge density profiles shown in the picture, namely, the trend to accumulate charge at the NR edges. A similar behavior was already noticed in the calculation of reference [272], where infinite step-like potentials where used to confine the electrons. Conversely, the charge density profiles obtained in reference [268] show a trend to concentrate charge density at the center of the Q1D system due to the harmonic confinement used.
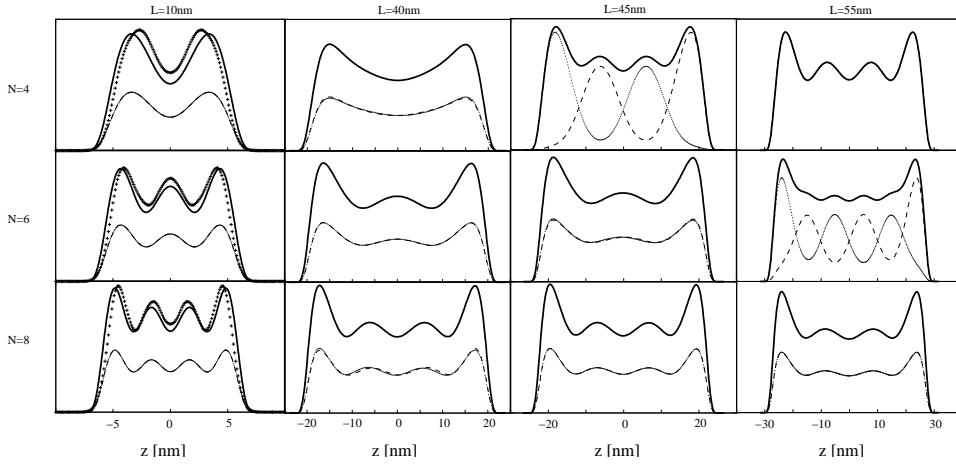
Figure 4.3: Electron density profiles along the NR longitudinal direction. Different NR lengths L and electronic population N are considered, the correspondence is pointed above and aside the panels. The total density is shown in solid lines, while the spin-up and -down densities are shown in dashed and dotted lines. CI total densities are also shown in crosses for the cases of $L = 10$ nm (left panels).

In order to check the reliability of the DFT density profiles showing charge accumulation at the NR edges, the results obtained for the shorter NR were compared with CI calculations. The obtained CI density profiles are superimposed in crosses on the left column panels of figure 4.3. It is evident from the figure that these benchmark calculations lead to the same density profiles and confirm the charge accumulation at the NR edges, which can be probably attributed to minimization of electron-electron interactions.

Figure 4.3 shows that for NRs with $L = 40$ nm and $N = 4$, 6 and 8

electrons, the charge density profiles present similar features, forming what is known as charge-density-wave (CDW). This phase is characterized by a $N/2$ number of maxima in the density profile and same spin-up and -down densities (i.e., preserved spin symmetry). When the NR is a bit longer ($L = 45$ nm), the less diluted populations, namely, $N = 6$ and 8 electrons, still show the CDW. However, the NR with $N = 4$ electrons has experienced a transition to a SDW, clearly showing N maxima in the density profile (Wigner crystallization) as well as spin densities that can be viewed as mirror images of each other. At this point, it should be noted that this spin symmetry breaking is a peculiarity of spin-dependent DFT calculations. CI calculations in such a low density regime have demonstrated that when the SDW is attained an internal-space spin order shows up [273]. Hence, the spin density breaking can be identified as a tendency of the mean field to mimic such an internal ordering.

Finally, for the longest studied NR ($L = 55$ nm), the system with $N = 8$ electrons still shows a CDW, while the $N = 6$ one has changed to a SDW with 6 relative maxima in the charge density. In turn, the most diluted system ($N = 4$) presents the abovementioned full spin polarized ground state. The existence of this phase should be tested with different methodologies. The reason is the well known trend of LSDA to overestimate exchange and correlation energies in low density regimes, thus favoring stabilization of polarized configurations [280]. Therefore, the obtained polarized phase may just be considered as a signature of attainment of the extremely diluted regime.

To summarize, a full 3D study of realistic long NRs has demonstrated that in the low density regime these systems can undergo ground state transitions between different phases previously predicted in simpler Q1D systems.

4.3 Modeling nanorods in high correlation regimes

The most accurate methodologies to account for the two-particle interactions are achieved through diagonalization of the many-body Hamiltonian in a basis set of non-interacting configurations. This is the so-called configuration interaction method (CI) which has been already mentioned and employed along this text. Disadvantages of using this approach arise from the high computational cost. Specially critical becomes the CI study of many-body systems in high correlation regimes, such as long NRs, where

the bottom of the spectrum presents a high density of states. To achieve a good description of such systems as well as a proper energy convergence, a high number of functions need to be included in the basis set, thus exponentially increasing virtual memory and computation time requirements.

The key to minimize this problematics is the optimization of the CI basis set. In this regard, a common modus operandi in studies of QD systems, where convergence problems do not usually arise, is to employ the eigenfunctions of the single-particle Hamiltonian coming in the many-body one. This approach has been followed in sections 3.3 and 3.4.2 of the present thesis to study spherical NCs and NRs with moderate aspect ratios. However, as the NRs are elongated, more and more basis functions have to be regarded to achieve the convergence criteria.

A way of reducing the number of required basis functions can be found in Quantum Chemistry. Conventionally, quantum chemical methods start from the Hartree-Fock (HF) single determinant ground state and then add correlations by means of CI or others methods [281]. Thereby, the orbitals arising from the HF calculation are employed to build up the full interacting Hamiltonian matrix. The advantage of using these orbitals is that, contrary to single-particle functions, they include in somehow the electron-electron interactions averaged in the Coulomb and exchange terms, and hence, are better adapted to the real interacting system. In the same way, employing DFT functions, i.e., Kohn-Sham orbitals, yields a further improvement of the basis set since they incorporate electronic correlations through the corresponding functional. Examples using these functions as basis set to model nanostructures can be found in the literature [71, 282, 283].
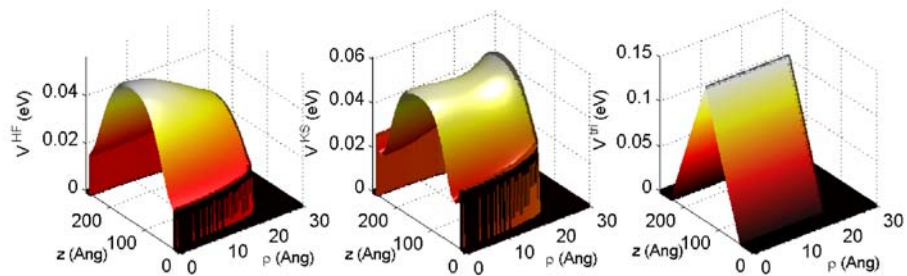
Figure 4.4: Examples of mean field potentials obtained form HF (left), DFT (center), and the variationally optimized triangular potential (right).

A simpler approach to improve the basis functions is suggested here for the case of two electrons confined in long NRs. It is based in the use of an external potential which mimics the perturbation experienced by the single-particle functions when Coulomb interactions come into play [284]. In both HF and DFT calculations, these Coulomb interactions are introduced as an external potential (mean field potential) in a single-particle Schrödinger-like equation. Examples of these mean fields are shown in figure 4.4 for the case of two electrons confined in a NR of aspect ratio 6. As can be seen, both potentials have a common feature: they destabilize the central region of the NR thereby alienating the electrons. The same effect can be produced by a simple potential with triangular form as the one presented in the right plot of figure 4.4. Unlike the HF and DFT mean fields, which are self-consistently optimized, the suggested triangular potential is optimized by variational fitting of the triangle height. This double variational scheme has been shown to outperform mean-field-CI approaches in NRs yielding robust results [284].

Chapter 5

Resum i conclusions

En aquesta tesi s'ha utilitzat l'aproximació de massa efectiva i funció envolupant per a estudiar les propietats optoelectròniques d'una ampla varietat de nanoestructures semiconductores, moltes de les quals són hui en dia assolibles en un laboratori. Dintre del formalisme de la massa efectiva la descripció d'un portador de càrrega (electró o forat) d'excés, aquell que no forma part de l'estructura interna del cristall almenys temporalment, es realitza incorporant en una constant la pertorbació electrostàtica generada pel conjunt d'àtoms i electrons que conformen el cristall. Aquesta constant és l'anomenada massa efectiva, la qual es determina empíricament a través de mesures experimentals o càlculs teòrics derivats de tractaments atomístics. Mitjançant aquesta parametrització, el model descriu el moviment d'un electró en un cristall com el d'un electró al buit on l'efecte del potencial cristal·lí es veu reflectit en una massa distinta, és a dir, en una diferent dispersió energètica front el vector d'ona. La quantització apareix llavors degut al confinament del moviment d'aquesta partícula dintre dels límits de la nanoestructura.

La senzillesa conceptual d'aquest model va acompanyada d'un tractament matemàtic que requereix un cost computacional moderat quan es compara amb altres models teòrics utilitzats en la física de semiconductors, com ara, models *tight binding* o aquells basats en l'ús de pseudopotencials. Aquest fet permet incloure factors addicionals en el modelatge dels sistemes sota estudi, com per exemple, l'efecte de camps externs o la interacció Coulòmbica entre portadors de càrrega en excés. En aquesta tesi s'ha modificat l'Hamiltonià de massa efectiva per incloure l'efecte de camps magnètics i elèctrics externs, i s'han tingut en compte els efectes de l'entorn dielèctric

sobre els estats dels portadors de càrrega. Les equacions de valors propis sorgides dels corresponents Hamiltonians han segut resoltes mitjançant mètodes d'integració numèrica en un esquema de diferencies finites. Aquesta tasca ha segut realitzada per a sistemes amb simetria esfèrica, cilíndrica i per sistemes bidimensionals en coordenades cartesianes.

La presència de més d'un portador de càrrega d'excés en un nanocristall, originada bé mitjançant excitacions òptiques o càrrega d'electrons des d'un elèctrode metàl·lic, també ha segut considerada en aquest treball. Per descriure la interacció Coulòmbica entre els portadors de càrrega s'ha fet ús de dues tècniques ben conegudes en l'àmbit de la química quàntica. Quan s'ha considerat un reduït nombre de partícules, l'Hamiltonià de massa efectiva incloent els termes d'interacció entre partícules ha segut expandit en una base de determinants d'Slater o productes de Hartree formats per funcions monoelectròniques. Posteriorment la matriu resultant ha segut diagonalitzada. Aquesta metodologia, coneguda com interacció de configuracions, resulta massa costosa computacionalment quan creix el nombre de partícules interactuants. En aquests casos s'ha fet ús de la teoria del funcional de la densitat (DFT), dins del formalisme autoconsistent introduït per Kohn i Sham, per a obtenir l'energia i la densitat de l'estat fonamental dels sistemes multipartícula.

En el primer capítol s'han investigat els efectes de camps magnètics externs sobre els estats d'electrons confinats en complexes d'anells quàntics.

- En primer lloc s'ha estudiat l'evolució de l'espectre monoelectrònic d'una molècula d'anells quàntics acoblats lateralment front a camps magnètics aplicats en les tres direccions espacials. Els resultats presentats han mostrat que al llarg d'un procés de dissociació de la molècula, la resposta del sistema a un camp magnètic perpendicular al pla molecular ve marcada per la distribució de les densitats de càrrega en absència de camp. Cosa que no ocorre quan la direcció del camp aplicat es troba en el pla molecular. Així, la forta anisotropia observada en la resposta magnètica d'aquest tipus de sistemes suggereix l'ús de mesures magnetoòptiques per a determinar l'orientació i grau d'acoblament molecular.

- En segon lloc s'ha investigat l'efecte d'un camp magnètic axial en l'espectre d'energies d'una xarxa bidimensional infinita formada per antianells quàntics. S'ha mostrat com l'espectre d'energies de la xarxa

d'antianells està format per una sèrie d'estats localitzats en els forats interiors dels anells juntament amb altres estats deslocalitzats en la matriu de la xarxa. Finalment s'ha mostrat que el camp magnètic extern és capaç d'induir transicions entre un estat fonamental localitzat i un deslocalitzat, suggerint l'ús d'aquestes xarxes bidimensionals com dispositius que controlen el transport d'electrons mitjançant camps magnètics.

- En tercer lloc, mitjançant càlculs DFT s'ha estudiat un sistema format per dos anells quàntics acoblats verticalment poblats amb un alt nombre d'electrons. L'evolució magnètica dels orbitals de Kohn-Sham i els espectres d'energies d'addició han mostrat que quan els anells es troben en règims de fort acoblament molecular el sistema es comporta bàsicament com un anell aïllat. En canvi, a mesura que la distància entre anells va creixent, un major nombre d'orbitals antienllaçants comença a estar poblat. Les conseqüències de la participació d'aquestos orbitals antisimètrics en l'estat fonamental es tradueix en l'aparició d'una sèrie d'anomalies en els espectres d'energies d'addició, l'assoliment d'un estat fonamental completament polaritzat d'espín a baixos camps magnètics i l'observació de transicions entre fases amb diferent espín i isospín a mesura que s'incrementa la intensitat del camp magnètic.

En el segon capítol de la tesi s'ha realitzat un ampli estudi dels efectes de l'entorn dielèctric sobre els estats electrònics i les propietats òptiques de nanocristalls col·loïdals. El denominat confinament dielèctric sorgeix a conseqüència del desajust de constant dielèctrica entre els promitjarmaterials semiconductors i els dissolvents on els nanocristalls són típicament dipositats, de manera que els portadors de càrrega indueixen la formació de càrregues de polarització superficials. Al llarg d'aquest capítol s'ha evidenciat que si es vol assolir una correcta descripció d'un sistema immers en un medi dielèctric, cal incloure les interaccions amb les càrregues superficials induïdes pel desajust de constant dielèctrica.

La primera part del capítol s'ha centrat en l'estudi de nanocristalls esfèrics carregats amb un alt nombre d'electrons. Per a modelar aquests sistemes s'ha desenvolupat un mètode basat en la DFT on els corresponents funcionals energètics han segut modificats per a incloure de manera apropiada paràmetres materials dependents de la posició. Posteriorment, el mètode

ha segut adaptat per tal d'incorporar les correccions de no parabolicitat de la banda de conducció, mitjançant l'ús d'una massa efectiva dependent de l'energia. Els resultats obtinguts amb el corresponent codi numèric es resumeixen a continuació:

- S'han construït diagrames de fase on les configuracions d'espín de l'estat fonamental d'un nanocristall carregat amb un moderat nombre d'electrons són representades en funció del radi dels nanocristalls i la constant dielèctrica del medi extern. Aquestes representacions mostren com per a un radi donat és possible induir transicions d'espín canviant el caràcter dielèctric del medi extern.

- S'ha evidenciat que l'ús de paràmetres materials dependents de la posició té una alta influència a l'hora de determinar potencials químics i energies d'addició de nanocristalls multicapa. Els primers són subestimats en un càlcul no polaritzat, conduint fins i tot a errors a l'hora de determinar el nombre d'electrons que caben en un nanocristall o en les capes que el formen. D'altra banda, les energies d'addició calculades amb paràmetres constants o dependents de la posició presenten diferències tant quantitatives com qualitatives, aquestes últimes esdevenen especialment rellevants a mesura que creix el nombre de capes que conformen el nanocristall.

- En nanocristalls formats per materials semiconductors de *band gap* estret i en règim de confinament fort, les correccions energètiques derivades de la no parabolicitat de la banda de conducció han resultat ser del mateix ordre que les interaccions interelectròniques. Així mateix, s'ha mostrat com l'ús d'una massa efectiva dependent de l'energia també té efectes en els espectres d'energies d'addició. D'una banda, l'altura dels pics es veu reduïda degut a l'aproximació energètica entre els nivells com a conseqüència de l'augment de la massa efectiva. D'altra banda, la no-parabolicitat pot comportar l'aparició de reconstruccions en l'espectre degut a la major estabilització del terme cinètic centrífug d'orbitals amb major moment angular. Aquests efectes es veuen amplificats pel confinament dielèctric.

Posteriorment s'han estudiat els efectes del confinament dielèctric sobre els estats excitónics de punts quàntics esfèrics. S'ha posat èmfasi en determinar les condicions que conduirien a una possible formació d'estats excitónics

superficials on l'electró i/o el forat esdevenen localitzats en el pou d'autopolarització. Aquestes condicions han resultat ser bastant severes en cas que els nanocristalls es troben a l'aire, en canvi, la formació d'estats superficials ha resultat més factible quan els nanocristalls estan immersos en una matriu amb una major constant dielèctrica. La transició d'estats volumètrics a superficials generalment s'ha vist acompanyada d'una abrupta disminució de la probabilitat de recombinació i de l'energia de l'excitó.

La part final del tercer capítol ha estat dedicada a estudiar els efectes del medi dielèctric en nanoestructures finites amb simetria axial conegudes com *nanorods* o *quantum rods* (varetes quàntiques). S'ha proposat un mètode numèric per calcular els efectes del confinament dielèctric en sistemes tridimensionals de qualsevol simetria. Aquest consisteix en el càlcul de les càrregues de polarització induïdes en la interfase dielèctrica, per a obtindre posteriorment el potencial electrostàtic generat pel conjunt dels portadors de càrrega i les càrregues de polarització. Mitjançant l'ús d'aquesta metodologia s'ha mostrat que l'entorn dielèctric afecta als portadors de càrrega confinats en *nanorods* a diferents nivells de com ho fa en el cas de punts quàntics esfèrics. A continuació s'enumeren els resultats més rellevants obtinguts en aquesta secció:

- En una comparació *nanorod* vs. nanocristall esfèric s'ha observat que mentre l'efecte més rellevant de l'entorn dielèctric en el nanocristall és l'augment d'intensitat de les interaccions Coulòmbiques, en el cas del *nanorod* el confinament dielèctric incrementa en gran mesura el paper de la correlació electrònica i fa créixer la mescla de configuracions en la funció d'ona. Com a conseqüència:

    Metodologies que incorporen les interaccions Coulòmbiques en forma de pertorbacions sobre el sistema de partícules no interactuants queden invalidades per realitzar amb elles l'estudi de les propietats electroòptiques de *nanorods* semiconductors.

    La mescla de configuracions produïda pel confinament dielèctric pot fins i tot induir la cristal·lització Wigner.

    El confinament dielèctric fa créixer la probabilitat de recombinació excitónica i la sensibilitat a pertorbacions externes dels nanorods.

- S'ha mostrat com l'entorn dielèctric pot modificar la posició energètica i intensitat de l'emissió excitónica dels *nanorods*.

- En *nanorods* tipus-II s'ha mostrat que la diferent localització de l'electró i el forat contribueix a amplificar l'efecte dielèctric en les energies excitóniques. En aquests sistemes el confinament dielèctric ha resultat inclús capaç de remodelar la forma de la funció d'ona a través de l'augment de l'atracció Coulòmbica entre electró i forat.

- Finalment s'ha evidenciat que el camp elèctric requerit per separ electró i forat del centre d'un nanorod depèn considerablement de la constant dielèctrica del medi extern.

En l'últim capítol de la tesi s'ha realitzat un estudi de l'evolució dels espectres d'energies d'addició al llarg d'un procés on un nanocristall esfèric s'ha anat allargant fins formar un sistema quasi unidimensional. Els resultats obtinguts (mitjançant càlculs DFT) han mostrat com els espectres d'energies d'addició van perdent l'estructura de capes a mesura que el sistema esdevé més anisotròpic, fins arribar a un punt on únicament s'observa una estructura tipus dents de serra. També s'ha mostrat com sota règims d'alta correlació l'estat fonamental multipartícula experimenta transicions a fases que presenten localització Wigner en la densitat electrònica amb trencament de la simetria d'espín.

Appendix A

Signatures of molecular coupling in the optical spectra of laterally coupled quantum dots

Excitons in QDs represent a particularly attractive candidate to be used as a quantum bit (*qubit*) due to their long coherence time, compared to their radiative lifetime, which enables manipulation using ultrafast laser pulses [285, 286]. However, for an isolated dot, such approaches are limited to one or two *qubit* operations [287]. More complex processes can be achieved exploiting the molecular properties of coupled QD systems [288, 289]. Thus, one of the most promising exciton-based scheme for quantum computation has been proposed in a pair of vertically stacked QDs, where the excitons form an entangled state via a molecular tunneling interaction between them [48]. Nevertheless, as usual in practical implementations of theoretical promises, several experimental drawbacks need to be overcome to set up such device. The first one comes from the implicit randomness of the QD fabrication protocols, which makes it difficult to couple two identical QDs with identical quantum levels. Consequently, it is necessary to make use of external fields to bring the levels of the individual dots into resonance. In this regard, the use of electric fields applied along the bond direction has been proved a good method to induce the molecular coupling in systems of vertically coupled QDs [290–293]. Therein, the molecular regime is identified in the exciton emission spectrum as the appearance of an anticrossing between two peaks, arising from a bright exciton with spatially direct char-

acter and a dark indirect exciton, as the electric field is tuned (see, e.g., figure A.1) [291, 294].
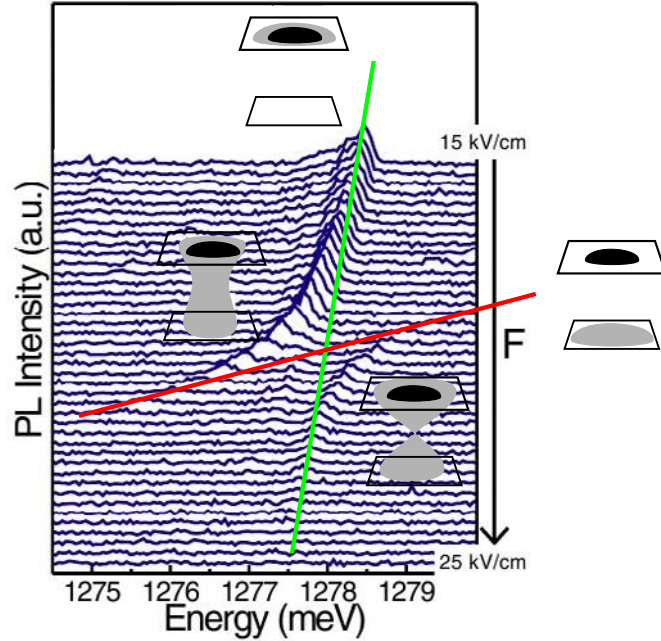
Figure A.1: Characteristic anticrossing between direct and indirect excitons in the electric field evolution of the emission spectrum of vertically coupled QDs (taken from Krenner et al., Phys. Rev. Lett. 94, 057402 (2005)). Insets: Electron (grey) and hole (black) charge distributions at different values of the electric field. At the resonance point the formation of bonding and antibonding orbitals is illustrated.

Unfortunately, the use of electric fields to model the coupling degree between the QDs has the objection of the long time required to switch this field. An alternative way to exploit molecular states that overcomes this inconvenient is based on the use of charged exciton species (trions) [100]. In such schemes, advantage is taken from the different electric field values at which the molecular regime is attained for a single particle (say the electron) and for the three-particle complex (the negative trion, X^-) [100, 293, 295]. An initial electron in one of the dots is considered as the *qubit*, and the optical excitation, which can be accomplished in a subpicosecond scale, as the mechanism to switch the resonance. Then, with the electric field tuned into one of the two resonance values (either e^- or X^-), it would be possible to switch the coupling of the dots by pulsed light via formation of a trion state.

On account of these potential applications in solid state quantum computation, the optical spectra of both neutral and charged exciton complexes in two vertically coupled QDs have been extensively studied (for an overview see reference [296], and references therein). However, for applications, one would normally prefer to couple QDs laterally. The reason is that in such systems the realization of gating between the QDs is expected to be straightforward when compared to the vertically coupled case, where gating, although feasible, is technically very demanding. Nonetheless, the preparation of laterally coupled QDs also entails experimental complications since classical growth techniques of self-assembled QDs normally generate a random spatial distribution of the dots. Therefore, to get a reliable control over the interdot distances it is necessary to employ another kind of methods [297] usually combined with lithographic techniques. On the other hand, the optical spectrum of laterally coupled QDs has been much less studied than the one of their vertical counterparts [61, 298–302], and although the signatures of molecular coupling in the electric field evolution of the exciton emission have been theoretically established [61], these have been rarely observed in experiments [298, 299]. The reason relies on the small contact surface between the constituent QDs which usually have a conical-like shape (see figure A.2).

This apendix focuses on the theoretical simulation of the photoluminescence spectra of two laterally coupled QDs modulated by an external electric field. The study is motivated by a set of micro-photoluminescence measurements carried out by experimental collaborators on samples of two InGaAs/GaAs QDs [303]. Therein, some of the gathered spectra showed an anomalous electric field evolution which can be though as an indication of molecular coupling. Supporting this suspicion by means of theoretical calculations is the main goal of this study. The project, however, was still in progress at the moment of redaction of the present thesis, so that in this section just an overview of the work carried out hitherto will be given without providing conclusive results.

Experiment

The pairs of QDs were grown by means of droplet epitaxy techniques on a GaAs matrix (see reference [297] for more detailed information). Each dot in the pair has a mean diameter of 37 ± 4 nm and, as can be seen in figure A.2, different heights with distributions centered at 5.3 ± 0.9 nm and 6.6 ± 1.6 nm. In turn, the interdot distance from peak to peak is of the same order as the diameter of one of the dots. Due to the different size of both quantum dots, an external field is used to bring the single QD levels into resonance, thus inducing the molecular coupling . With this aim, two lateral gates were deposited on top of the sample surface which allows one to apply an electric field precisely along the direction of molecular coupling.
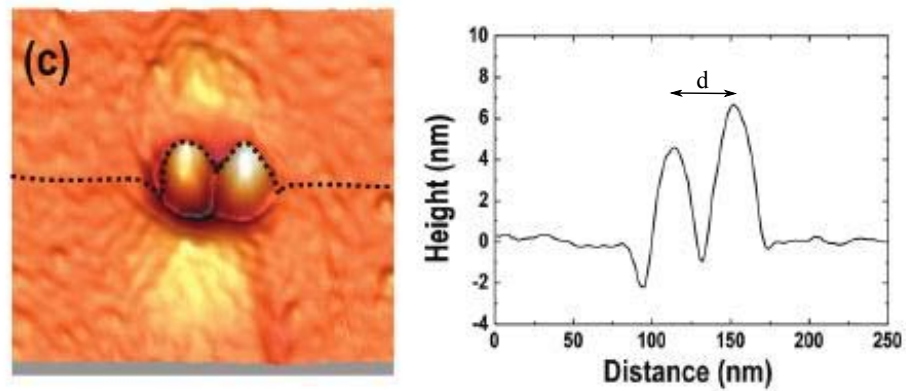
Figure A.2: Atomic force microscopy image (left) and structural profile along the molecular axis direction (right) of a pair of QDs (taken from Alonso-González et al. Cryst. Growth Des. 9, 2525 (2009)).

The emission properties of several pairs of QDs were investigated as a function of the applied electric field. In the collected spectra (a sample is shown in figure A.3), a few sets of signals can be observed which are assigned to the radiative recombination of exciton and negatively charged exciton complexes. The formation of negatively charged species at low voltages is attributed to the residual presence of electron donor impurities of As in the QDs surroundings. Furthermore, an electron migration process is observed as the voltage is tuned in both positive and negative values with the consequent disappearance of the signals coming from negatively charged complexes. As a result, the spectra shows a sort of staircase-like

evolution which has been previously observed in single-dot spectroscopy experiments [304, 305].
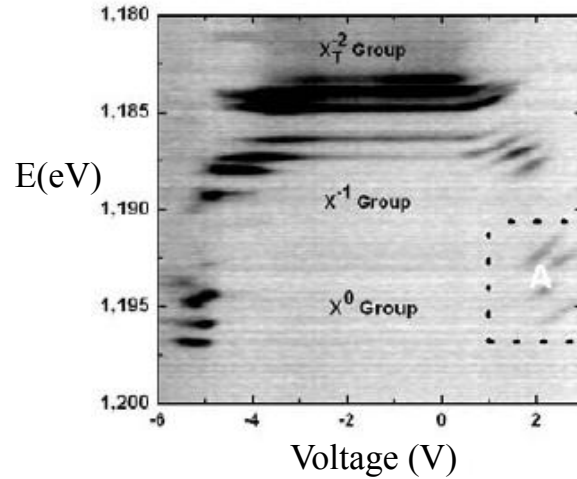
Figure A.3: Photoluminescence spectrum (the energy axis is reversed) of a pair of laterally coupled QDs as a function of the applied voltage (proportional to the electric field).

The signals appearing in figure A.3 also reveal an anomalous behavior: at positive voltages the exciton and negative trion signals develop a redshift (note that in this figure the energy axis is reversed) which does not take place at negative voltages. This asymmetric evolution can be tentatively interpreted on the basis of the formation of molecular coupling as follows. On the one hand, the origin of the redshifts at positive voltages is though to be related with anticrossings arising from molecular states formed through electron tunneling [292, 298]. On the other hand, a similar formation of molecular states at negative voltages would entail tunneling of the hole (see figure A.4). Therefore, the lack of redshifts at positive voltages can be reasoned by the large effective mass of the hole, which would greatly reduce the tunneling and hence the anticrossing.

Theoretical calculations

In order to theoretically reproduce the experimental results, the emission spectra of neutral and charged exciton complexes have been computed. The electron and hole (heavy-hole) single-particle states are calculated within a two-dimensional EMA model, whereas the many-particle interactions are computed through CI calculations. Thus, the 2D Hamiltonian for a system of N_e electrons and N_h holes can be written as,

$$
\hat{\mathcal{H}} = \sum_{i=1}^{N_e} \hat{\mathcal{H}}_e + \sum_{k=1}^{N_h} \hat{\mathcal{H}}_h + \sum_{j>i}^{N_e} \frac{1}{\varepsilon |\mathbf{r}_e(i) - \mathbf{r}_e(j)|}
$$
$$
+ \sum_{l>k}^{N_h} \frac{1}{\varepsilon |\mathbf{r}_h(k) - \mathbf{r}_h(l)|} - \sum_{i=1}^{N_e} \sum_{k=1}^{N_h} \frac{1}{\varepsilon |\mathbf{r}_e(i) - \mathbf{r}_h(k)|}. \tag{A.1}
$$

In the above equation the last three terms represent the Coulomb interactions between the carriers, while the first two correspond to the electron and hole single-particle Hamiltonians. The latter have been taken as,

$$
\hat{\mathcal{H}}_j = \frac{\hat{p}^2}{2\,m_j^*} + \frac{1}{2} m_j^* \omega_j^2 \left[min\left((x + \frac{d}{2})^2 + y^2 + \Delta, \ (x - \frac{d}{2})^2 + y^2 \right) \right] - e_j\, F_x\, x \tag{A.2}
$$

where the subindex $j = e, h$ denotes electron or hole parameters. The first term of equation A.2 is the kinetic energy operator, the second one is the spatial confining potential and the last one corresponds to an electric field applied along the molecular axis, here taken in the x direction.

To mimic the peculiar geometry of the system under study, the spatial confining potential has been modeled as two parabolas whose centers are separated in the x direction by the interdot distance d (see figure A.4 center). Thereby, the parabolic profile partly recovers the effect of the vertical confinement neglected in the 2D treatment. In addition, to simulate the different height of the individual QDs, the potential bottom of one of the dots (the left one) is offset by an amount of Δ eV. In this way, at zero field, the carriers will be preferably placed in the right dot. However, as shown in figure A.4, when the electric field is switched on, the electrons (holes) can be promoted to the left dot at positive (negative) electric field values beyond

the resonance point.
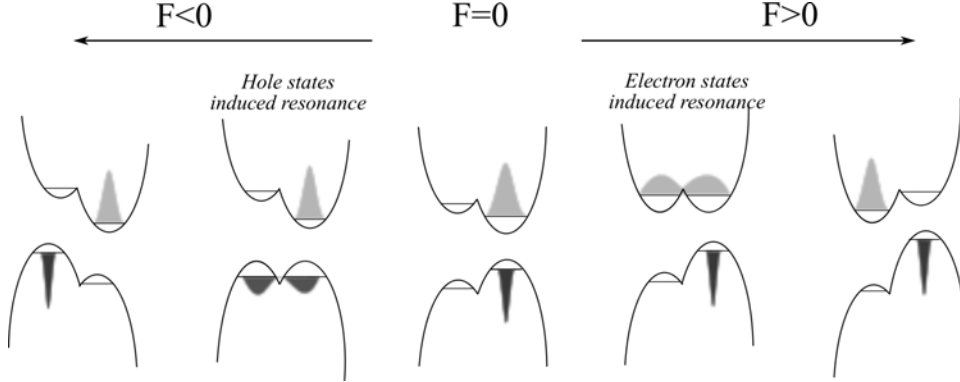
Figure A.4: Schematic representations of the electric field effect on the confining potential profiles along the x direction and the single-particle states. The most stable electron (hole) charge distributions are plotted in light (dark) gray.

In order to compute the CI energies and wave functions of the excitonic complexes, the single-particle function basis set is taken from the eigenfunctions of the electron and hole single-particle Hamiltonians (equation A.2). Then, if there is more than one electron or hole, all the possible Slater determinants are formed, including spin degrees of freedom. Next, Hartree products between the electron and hole Slater determinants (or spin-orbitals if there is only one electron or one hole) are built up. The few-body Hamiltonian (equation A.1) is then spanned on this basis and finally diagonalized.

The emission spectra are calculated from the CI energies and wave functions within the dipole approximation and Fermi's golden rule. The recombination probability from an initial state $|i\rangle$ to a final state $|f\rangle$ with one less electron-hole pair (for example, the $|i\rangle$ state of X^- and the $|f\rangle$ state of a single electron), at an energy of the emitted photon $E_{h\gamma}$, is given by

$$\mathcal{P}_{f \leftarrow i}(E_{h\gamma}) = (\langle f| \vec{\mu} |i\rangle)^2 \, \delta \left(E_i - E_f - E_{h\gamma} \right), \qquad (A.3)$$

where $\vec{\mu}$ is the transition dipole momentum and $E_{i(j)}$ is the energy of the initial (final) state. In the experiment, a non-resonant excitation is carried out, which means that if the radiative recombination rates are faster than the time required for the excitonic complexes to be relaxed at the ground state, emission from excited states can take place. Actually, this was the

case in previous experiments on vertically coupled QDs [293] and it is though
to occur in the present measurements (see figure A.3). Therefore, to the-
oretically reproduce this emission from multiple states, transitions from all
possible initial $|i\rangle$ and final $|f\rangle$ states have been estimated.

Figure A.5 shows a simulated emission spectrum for an exciton in a rang
of electric fields near the anticrossing region corresponding to an electron
tunneling process. Specifically, the spectrum corresponds to a pair of QDs
separated by an interdot distance $d = 30$ nm, where the left one has been
destabilized by $\Delta = 30$ meV. These two parameters determine to a large ex-
tent the electric field at which the anticrossing takes place. To illustrate this,
let us consider the electric field effect on the energy (the so-called Stark shift)
of the lowest electron single-particle state in both QDs. In the right one, the
Stark shift can be approximated as $E^e_{QD_r}(F_x) = E^e_0 + \frac{d}{2}e\,F_x$, with E^e_0 being
the energy at zero field. On the other hand, in the left dot one should bear
in mind that E^e_0 has been shifted by Δ, hence, $E^e_{QD_l}(F_x) = E^e_0 + \Delta - \frac{d}{2}e\,F_x$.
As illustrated in figure A.1, the anticrossing in the exciton spectrum occurs
when two states that only differ on the electron location become degener-
ate[1], this is, the electronic states in both QDs have the same energy or, in
other words, $E^e_{QD_r} = E^e_{QD_l}$. Under this condition it is easy to see that the
anticrossing will occur at a field $F_x = \frac{\Delta}{d\,e}$, apart from deviations arising from
two-body interactions.

Therefore, and given that the interdot distance d should agree with the
experimental one, the parameter Δ is modified in order to tune the electric
field value of the anticrossing. For the case studied in figure A.5, it was
intended to reproduce a possible experimental anticrossing of the exciton
signal observed at quite large electric fields (around 12 kV/cm), which is
why the QDs are so different, $\Delta = 30$ meV. As a consequence of this large
asymmetry, only signals coming from excitons hosting the hole in the bigger
dot are observed for the energy range shown in the spectrum. Apart from
the anticrossing of the exciton signal, qualitatively similar to the one previ-
ously observed in vertically coupled QDs, new features are observed in the
spectrum which can be ascribed to the lateral geometry of the system [61].
The first one is the finite Stark shift displayed by the direct exciton emis-

---

[1]Additionally, in vertically coupled QDs, molecular coupling through hole states tun-
neling has also been observed [100]. The corresponding anticrossing, however, takes place
at opposite electric field values and is less pronounced than the electronic due to the
larger hole effective mass. By this reason, this kind of molecular coupling is not expected
to occur in laterally coupled QDs where the surface contact is much smaller.
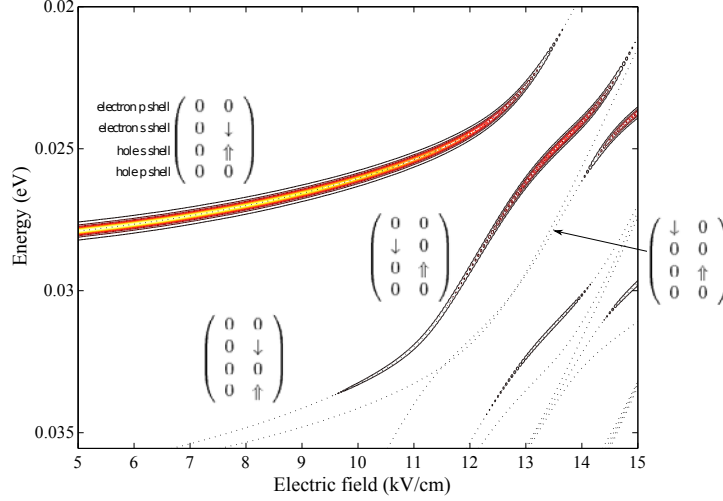
Figure A.5: Computed exciton photoluminescence spectrum for a pair of QDs as a function of the electric field. The line width is proportional to the exciton recombination probability (intensity of the emission), dotted lines correspond to dark states. The insets illustrate the predominant configurations of the CI exciton wave function.

sion, which denotes the formation of a dipole momentum inside the large QD, namely, the electron and the hole are spatially separated inside the same dot. This feature is not observed in systems of vertically coupled QDs due to the stronger confinement of such dots in the electric field direction (see, e.g., the insets of figure A.1). Secondly, the anticrossings with indirect excitons involve not only s-shell states, but also p- and d-shells, which are lowered in energy by the electric field. As a consequence, new resonances appear that can be the cause of the set of redshifted signals framed with a dotted square in figure A.5.

The negative trion photoluminescence spectrum for the same pair of QDs is illustrated in figure A.6. In great measure, the spectrum shows the same signals previously observed in experiments and calculations on vertically coupled QDs [100, 293], but again distorted by the induced dipole momentum inside the large dot. Even so, one of the main features of both positive and negative trion spectra is observed, the x-like crossing developed by the recombinations of a direct (two electrons in the same dot) and an indirect (each electron in a different dot) singlet states. Also, signatures of anticrossings with excited dark states can be observed at higher fields in the
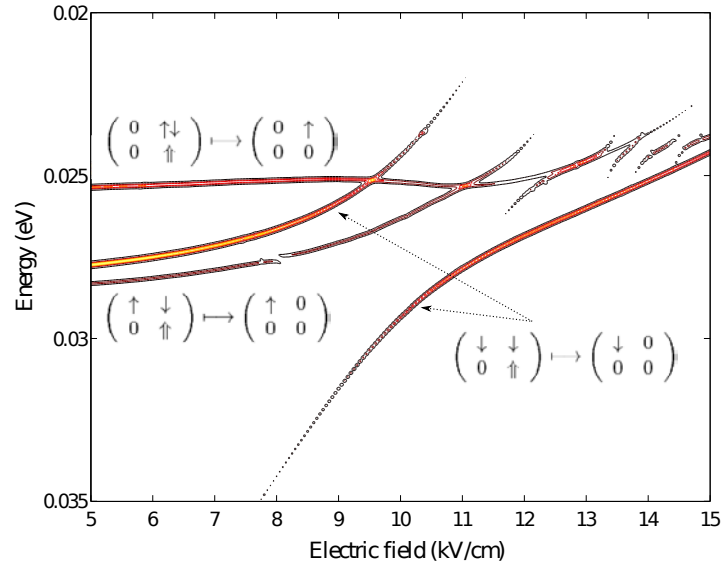
Figure A.6: Computed negative trion photoluminescence spectrum for the same pair of QDs as figure A.5. The line width is proportional to the recombination probability (intensity of the emission). The insets illustrate the predominant configurations of the initial CI trion wave function, and the final single-electron wave function involved in the transition.

spectrum. On the other hand, the remaining signal developing a large anticrossing corresponds to the recombination of an indirect spin triplet trion state. The global redshift developed by all the signals as the electric field is increased agrees with the experimental observation shown in figure A.3.

In conclusion, even though the computed spectra have some similitudes with the measured ones, the search for a conclusive confirmation of the presence of molecular coupling in the experimental samples is still underway. Work is in progress both theoretically and experimentally. For example, new optical measures have shown more possible traces of coupling in signals arising not only from the exciton and trion recombinations but also from biexcitons.

Bibliography

[1] G. E. Moore et al. *Cramming more components onto integrated circuits.* Proceed. IEEE, **86**, 82 (1998).

[2] A. P. Alivisatos. *Semiconductor clusters, nanocrystals, and quantum dots.* Science, **271**, 933 (1996).

[3] T. D. Ladd, F. Jelezko, R. Laflamme, Y. Nakamura, C. Monroe and J. L. O'Brien. *Quantum computers.* Nature, **464**, 45 (2010).

[4] M. A. Reed, R. T. Bate, K. Bradshaw, W. M. Duncan, W. R. Frensley, J. W. Lee and H. D. Shih. *Spatial quantization in GaAs–AlGaAs multiple quantum dots.* J. Vac. Sci. Technol. B, **4**, 358 (1986).

[5] Z. R. Wasilewski, S. Fafard and J. P. McCaffrey. *Size and shape engineering of vertically stacked self-assembled quantum dots.* J. Cryst. Growth, **201**, 1131 (1999).

[6] X. Z. Liao, J. Zou, X. F. Duan, D. J. H. Cockayne, R. Leon and C. Lobo. *Transmission-electron microscopy study of the shape of buried InGa As/GaAs quantum dots.* Phys. Rev. B, **58**, 4235 (1998).

[7] J. M. Garcia, G. Medeiros-Ribeiro, K. Schmidt, T. Ngo, J. L. Feng, A. Lorke, J. Kotthaus and P. M. Petroff. *Intermixing and shape changes during the formation of InAs self-assembled quantum dots.* Appl. Phys. Lett., **71**, 2014 (1997).

[8] C. N. R. Rao, A. Müller and A. Cheetham. *Nanomaterials chemistry: recent developments and new directions.* Wiley-Vch Verlagsgesellschaft Mbh (2007).

[9] D. Loss and D. P. DiVincenzo. *Quantum computation with quantum dots.* Phys. Rev. A, **57**, 120 (1998).

[10] D. Dalacu, M. E. Reimer, S. Fréderick, D. Kim, J. Lapointe, P. J. Poole, G. C. Aers, R. L. Williams, W. R. McKinnon, M. Korkusinski et al. *Directed self-assembly of single quantum dots for telecommunication wavelength optical devices.* Laser Photonics Rev., **4**, 283 (2010).

[11] P. V. Kamat. *Quantum Dot Solar Cells. Semiconductor Nanocrystals as Light Harvesters.* J. Phys. Chem. C, **112**, 18737 (2008).

[12] T. Jamieson, R. Bakhshi, D. Petrova, R. Pocock, M. Imani and A. M. Seifalian. *Biological applications of quantum dots.* Biomater., **28**, 4717 (2007).

[13] G. Bacher. *Optical spectroscopy on epitaxially grown II-VI single quantum dots. Single Quantum Dots: Fundamentals, Applications and New Concepts*, volume 90 of *Topics in Applied Physics*, 147–183 (2003).

[14] D. E. Gómez, M. Califano and P. Mulvaney. *Optical properties of single semiconductor nanocrystals.* Phys. Chem. Chem. Phys., **8**, 4989 (2006).

[15] J. P. Bird. *Electron transport in quantum dots.* kluwer Academic Publishers (2003).

[16] L. P. Kouwenhoven, A. T. Johnson, N. C. Van der Vaart, C. Harmans and C. T. Foxon. *Quantized current in a quantum-dot turnstile using oscillating tunnel barriers.* Phys. Rev. Lett., **67**, 1626 (1991).

[17] M. Field, C. G. Smith, M. Pepper, D. A. Ritchie, J. E. F. Frost, G. A. C. Jones and D. G. Hasko. *Measurements of Coulomb blockade with a noninvasive voltage probe.* Phys. Rev. Lett., **70**, 1311 (1993).

[18] F. R. Waugh, M. J. Berry, D. J. Mar, R. M. Westervelt, K. L. Campman and A. C. Gossard. *Single-electron charging in double and triple quantum dots with tunable coupling.* Phys. Rev. Lett., **75**, 705 (1995).

[19] G. Bastard. *Wave mechanics applied to semiconductor heterostructures.* John Wiley and Sons Inc., New York (1998).

[20] M. G. Burt. *Fundamentals of envelope function theory for electronic states and photonic modes in nanostructures.* J. Phys.: Condens. Matt., **11**, 53 (1999).

[21] A. Szabo and N. S. Ostlund. *Modern quantum chemistry: introduction to advanced electronic structure theory.* Dover Pubns (1996).

[22] R. G. Parr and W. Yang. *Density-Functional Theory of Atoms and Molecules.* Oxford University Press, Oxford (1989).

[23] Y. Aharonov and D. Bohm. *Significance of Electromagnetic Potentials in the Quantum Theory.* Phys. Rev., **115**, 485 (1959).

[24] J. Planelles, J. I. Climente and J. L. Movilla. *Aharonov-Bohm effect for pedestrians.* Symmetry, Spectroscopy and SCHUR, Proceedings of Prof B.G, Wybourne Commemorative Meeting, 1–8 (2006).

[25] N. Byers and C. N. Yang. *Theoretical Considerations Concerning Quantized Magnetic Flux in Superconducting Cylinders.* Phys. Rev. Lett., **7**, 46 (1961).

[26] F. Bloch. *Josephson Effect in a Superconducting Ring.* Phys. Rev. B, **2**, 109 (1970).

[27] N. A. J. M. Kleemans, I. M. A. Bominaar-Silkens, V. M. Fomin, V. N. Gladilin, D. Granados, A. G. Taboada, J. M. García, P. Offermans, U. Zeitler, P. C. M. Christianen, J. C. Maan, J. T. Devreese and P. M. Koenraad. *Oscillatory Persistent Currents in Self-Assembled Quantum Rings.* Phys. Rev. Lett., **99**, 146808 (2007).

[28] S. Olariu and I. I. Popescu. *The quantum effects of electromagnetic fluxes.* Rev. Mod. Phys., **57**, 339 (1985).

[29] V. Chandrasekhar, R. A. Webb, M. J. Brady, M. B. Ketchen, W. J. Gallagher and A. Kleinsasser. *Magnetic response of a single, isolated gold loop.* Phys. Rev. Lett., **67**, 3578 (1991).

[30] T. Chakraborty. *Quantum dots.* Elsevier Science BV, Amsterdam (1999).

[31] A. G. Aronov and Y. V. Sharvin. *Magnetic flux effects in disordered conductors.* Rev. Mod. Phys., **59**, 755 (1987).

[32] S. Viefers, P. Koskinen, P. S. Deo and M. Manninen. *Quantum rings for beginners: energy spectra and persistent currents.* Physica E, **21**, 1 (2004).

[33] N. Gisin, G. Ribordy, W. Tittel and H. Zbinden. *Quantum cryptography.* Rev. Mod. Phys., **74**, 145 (2002).

[34] E. Knill, R. Laflamme and G. J. Milburn. *A scheme for efficient quantum computation with linear optics.* Nature, **409**, 46 (2001).

[35] M. Bayer, M. Korkusinski, P. Hawrylak, T. Gutbrod, M. Michel and A. Forchel. *Optical Detection of the Aharonov-Bohm Effect on a Charged Particle in a Nanoscale Quantum Ring.* Phys. Rev. Lett., **90**, 186801 (2003).

[36] B. C. Lee, O. Voskoboynikov and C. P. Lee. *III-V Semiconductor nano-rings.* Physica E, **24**, 87 (2004).

[37] T. Mano, T. Kuroda, S. Sanguinetti, T. Ochiai, T. Tateno, J. Kim, T. Noda, M. Kawabe, K. Sakoda, G. Kido and N. Koguchi. *Self-assembly of concentric quantum double rings.* Nano Lett., **5**, 425 (2005).

[38] C. Somaschini, S. Bietti, N. Koguchi and S. Sanguinetti. *Fabrication of Multiple Concentric Nanoring Structures.* Nano Lett., **9**, 3419 (2009).

[39] A. Lorke, R. J. Luyken, A. O. Govorov, J. P. Kotthaus, J. M. Garcia and P. M. Petroff. *Spectroscopy of Nanoscopic Semiconductor Rings.* Phys. Rev. Lett., **84**, 2223 (2000).

[40] A. O. Govorov, S. E. Ulloa, K. Karrai and R. J. Warburton. *Polarized excitons in nanorings and the optical Aharonov-Bohm effect.* Phys. Rev. B, **66**, 081309 (2002).

[41] J. I. Climente, J. Planelles and W. Jaskólski. *Magneto-optical transitions in nanoscopic rings.* Phys. Rev. B, **68**, 075307 (2003).

[42] E. Ribeiro, A. O. Govorov, W. Carvalho and G. Medeiros-Ribeiro. *Aharonov-Bohm Signature for Neutral Polarized Excitons in Type-II Quantum Dot Ensembles.* Phys. Rev. Lett., **92**, 126402 (2004).

[43] I. L. Kuskovsky, W. MacDonald, A. O. Govorov, L. Mourokh, X. Wei, M. C. Tamargo, M. Tadic and F. M. Peeters. *Optical Aharonov-Bohm effect in stacked type-II quantum dots.* Phys. Rev. B, **76**, 035342 (2007).

[44] R. Rosas, R. Riera and J. L. Marín. *Electron states in a magnetic quantum ring.* J. Phys.: Condens. Matter, **12**, 6851 (2000).

[45] L. Jacak, P. Hawrylak and A. Wójs. *Quantum dots.* Springer, Berlin (1998).

[46] L. Kowenhoven. *Coupled quantum dots as artificial molecules.* Science, **268**, 1440 (1995).

[47] A. P. Alivisatos, K. P. Johnsson, X. G. Peng, T. E. Wilson, C. J. Loweth, M. P. Bruchez and P. G. Schultz. *Organization of 'nanocrystal molecules' using DNA.* Nature, **382**, 609 (1996).

[48] M. Bayer, P. Hawrylak, K. Hinzer, S. Fafard, M. Korkusinski, Z. R. Wasilewski, O. Stern and A. Forchel. *Coupling and entangling of quantum states in quantum dot molecules.* Science, **291**, 451 (2001).

[49] R. H. Blick, D. Pfannkuche, R. J. Haug, K. v. Klitzing and K. Eberl. *Formation of a Coherent Mode in a Double Quantum Dot.* Phys. Rev. Lett., **80**, 4032 (1998).

[50] A. W. Holleitner, R. H. Blick, A. K. Huttel, K. Eberl and J. P. Kotthaus. *Probing and controlling the bonds of an artificial molecule.* Science, **297**, 70 (2002).

[51] M. Pi, A. Emperador, M. Barranco, F. Garcias, K. Muraki, S. Tarucha and D. G. Austing. *Dissociation of Vertical Semiconductor Diatomic Artificial Molecules.* Phys. Rev. Lett., **87**, 066801 (2001).

[52] M. F. Doty, J. I. Climente, M. Korkusinski, M. Scheibner, A. S. Bracker, P. Hawrylak and D. Gammon. *Antibonding Ground States in InAs Quantum-Dot Molecules.* Phys. Rev. Lett., **102**, 047401 (2009).

[53] W. Dybalski and P. Hawrylak. *Two electrons in a strongly coupled double quantum dot: From an artificial helium atom to a hydrogen molecule.* Phys. Rev. B, **72**, 205432 (2005).

[54] F. Suárez, D. Granados, M. L. Dotor and J. M. García. *Laser devices with stacked layers of InGaAs/GaAs quantum rings.* Nanotech., **15**, S126 (2004).

[55] D. Granados, J. M. García, T. Ben and S. I. Molina. *Vertical order in stacked layers of self-assembled In(Ga)As quantum rings on GaAs (001).* Appl. Phys. Lett., **86**, 071918 (2005).

[56] J. I. Climente and J. Planelles. *Far-infrared absorption of vertically coupled self-assembled quantum rings.* Phys. Rev. B, **72**, 155322 (2005).

[57] Y. Li and H.-M. Lu. *Electron Transition Energy for Vertically Coupled InAs/GaAs Semiconductor Quantum Dots and Rings.* Japan. J. Appl. Phys., **43**, 2104 (2004).

[58] F. Malet, M. Barranco, E. Lipparini, R. Mayol, M. Pi, J. I. Climente and J. Planelles. *Vertically coupled double quantum rings at zero magnetic field.* Phys. Rev. B, **73**, 245324 (2006).

[59] M. Royo, F. Malet, M. Barranco, M. Pi and J. Planelles. *Isospin phases of vertically coupled double quantum rings under the influence of perpendicular magnetic fields.* Phys. Rev. B, **78**, 165308 (2008).

[60] L. K. Castelano, G. Q. Hai, B. Partoens and F. M. Peeters. *Artificial molecular quantum rings: Spin density functional theory calculations.* Phys. Rev. B, **74**, 045313 (2006).

[61] B. Szafran, S. Bednarek and M. Dudziak. *Electron correlations in charge coupled vertically stacked quantum rings.* Phys. Rev. B, **75**, 235323 (2007).

[62] L. K. Castelano, G.-Q. Hai, B. Partoens and F. M. Peeters. *Control of the persistent currents in two interacting quantum rings through the Coulomb interaction and interring tunneling.* Phys. Rev. B, **78**, 195315 (2008).

[63] L. K. Castelano, G. Q. Hai, B. Partoens and F. M. Peeters. *Artificial molecular quantum rings under magnetic field influence.* J. Appl. Phys., **106**, 073702 (2009).

[64] G. Piacente and G. Q. Hai. *Electron-acoustic-phonon scattering and electron relaxation in two-coupled quantum rings.* J. Appl. Phys., **101**, 124308 (2007).

[65] L. G. G. V. Dias da Silva, J. M. Villas-Bôas and S. E. Ulloa. *Tunneling and optical control in quantum ring molecules.* Phys. Rev. B, **76**, 155306 (2007).

[66] G. Fuster, M. Pacheco and Z. Barticevic. *Electronic properties of coupled quantum rings in the presence of a magnetic field.* Braz. J. Appl. Phys., **34**, 666 (2004).

[67] J. Planelles and J. I. Climente. *Semiconductor concentric double rings in a magnetic field.* Eur. Phys. J. B, **48**, 65 (2005).

[68] B. Szafran and F. M. Peeters. *Few-electron eigenstates of concentric double quantum rings.* Phys. Rev. B, **72**, 155316 (2005).

[69] J. I. Climente, J. Planelles, M. Barranco, F. Malet and M. Pi. *Electronic structure of few-electron concentric double quantum rings.* Phys. Rev. B, **73**, 235327 (2006).

[70] F. Malet, M. Pi, M. Barranco, E. Lipparini and L. Serra. *Optical response of two-dimensional few-electron concentric double quantum rings: A local-spin-density-functional theory study.* Phys. Rev. B, **74**, 193309 (2006).

[71] J. M. Escartín, F. Malet, A. Emperador and M. Pi. *Isomeric electronic states in concentric quantum rings.* Phys. Rev. B, **79**, 245317 (2009).

[72] A. Mühle, W. Wegscheider and R. J. Haug. *Coupling in concentric double quantum rings.* Appl. Phys. Lett., **91**, 133116 (2007).

[73] B. C. Lee and C. P. Lee. *Formation of semiconductor quantum rings using GaAs/AlAs partially capped layers.* Nanotech., **15**, 848 (2004).

[74] A. Schramm, T. Kipp, F. Wilde, J. Schaefer, C. Heyn and W. Hansen. *Shape transformation of self-assembled InAs quantum dots during overgrowth with AlAs.* J. Cryst. Growth, **289**, 81 (2006).

[75] J. Planelles, F. Rajadell, J. I. Climente, M. Royo and J. L. Movilla. *Electronic states of laterally coupled quantum rings.* J. Phys. Conf. Ser., **61**, 936 (2007).

[76] H. Hu, J. L. Zhu and J. J. Xiong. *Energy levels and far-infrared spectroscopy for two electrons in a nanoscopic semiconductor ring.* Phys. Rev. B, **62**, 16777 (2000).

[77] J. Planelles, J. I. Climente and F. Rajadell. *Quantum rings in tilted magnetic fields.* Phyica. E, **33**, 370 (2006).

[78] M. Yamagiwa, N. Sumita, F. Minami and N. Koguchi. *Confined electronic structure in GaAs quantum dots.* J. of Lumin., **108**, 379 (2004).

[79] H. Silberbauer. *Magnetic minibands in lateral semiconductor superlattices.* J. Phys.: Condens. Matter, **4**, 7355 (1992).

[80] O. Kühn, V. Fessatidis, H. L. Cui, P. E. Selbmann and N. J. M. Horing. *Energy spectrum for two-dimensional periodic potentials in a magnetic field.* Phys. Rev. B, **47**, 13019 (1993).

[81] S. Uryu and T. Ando. *Electronic states in antidot lattices: Scattering-matrix formalism.* Phys. Rev. B, **53**, 13613 (1996).

[82] O. Steffens, T. Schlösser, P. Rotter, K. Ensslin, M. Suhrke, J. P. Kotthaus, U. R.össler and M. Holland. *From the two-dimensional electron gas to antidot superlattices: magnetoresistance effects in the transition regime.* J. Phys.: Condens. Matter, **10**, 3859 (1998).

[83] E. Anisimovas and P. Johansson. *Butterfly-like spectra and collective modes of antidot superlattices in magnetic fields.* Phys. Rev. B, **60**, 7744 (1999).

[84] P. H. Rivera, M. A. Andrade Neto, P. A. Schulz and N. Studart. *Tamm-like states in finite antidot lattices.* Phys. Rev. B, **64**, 035313 (2001).

[85] J. G. Analytis, S. J. Blundell and A. Ardavan. *Magnetic oscillations, disorder and the Hofstadter butterfly in finite systems.* Synth. Met., **154**, 265 (2005).

[86] E. Muñoz, Z. Barticevic and M. Pacheco. *Electronic spectrum of a two-dimensional quantum dot array in the presence of electric and magnetic fields in the Hall configuration.* Phys. Rev. B, **71**, 165301 (2005).

[87] F. Claro and Z. Barticevic. *Two-dimensional crystalline electrons in the Hall configuration.* Phys. Rev. B, **38**, 361 (1988).

[88] L. D. Landau and E. M. Lifshitz. *Quantum Mechanics: Nonrelativistic Theory.* Pergamon Press (1977).

[89] D. R. Hofstadter. *Energy levels and wave functions of Bloch electrons in rational and irrational magnetic fields.* Phys. Rev. B, **14**, 2239 (1976).

[90] D. Weiss, M. L. Roukes, A. Menschig, P. Grambow, K. von Klitzing and G. Weimann. *Electron pinball and commensurate orbits in a periodic array of scatterers.* Phys. Rev. Lett., **66**, 2790 (1991).

[91] D. Weiss, K. Richter, A. Menschig, R. Bergmann, H. Schweizer, K. von Klitzing and G. Weimann. *Quantized periodic orbits in large antidot arrays.* Phys. Rev. Lett., **70**, 4118 (1993).

[92] R. Schuster, K. Ensslin, J. P. Kotthaus, G. Böhm and W. Klein. *Classical and quantum transport in rectangular antidot superlattices.* Phys. Rev. B, **55**, 2237 (1997).

[93] J. Planelles and M. Royo. *Magnetic-field control of ground-state transition from delocalized-to-localized electronic density in antiring superlattices.* Phys. Rev. B, **73**, 113306 (2006).

[94] E. Brown. *Bloch Electrons in a Uniform Magnetic Field.* Phys. Rev., **133**, A1038 (1964).

[95] Y. W. Cao and U. Banin. *Growth and properties of semiconductor core/shell nanocrystals with InAs cores.* J. Am. Chem. Soc, **122**, 9692 (2000).

[96] A. Stroppa and M. Peressi. *Composition and strain dependence of band offsets at metamorphic $In_xGa_{1-x}As/In_yAl_{1-y}As$ heterostructures.* Phys. Rev. B, **71**, 205303 (2005).

[97] I. Vurgaftman, J. R. Meyer and L. R. Ram-Mohan. *Band parameters for III–V compound semiconductors and their alloys.* J. Appl. Phys., **89**, 5815 (2001).

[98] M. Tadić, F. M. Peeters, K. L. Janssens, M. Korkusiński and P. Hawrylak. *Strain and band edges in single and coupled cylindrical InAs/GaAs and InP/InGaP self-assembled quantum dots.* J. Appl. Phys., **92**, 5819 (2002).

[99] J. R. Petta, A. C. Johnson, J. M. Taylor, E. A. Laird, A. Yacoby, M. D. Lukin, C. M. Marcus, M. P. Hanson and A. C. Gossard. *Coherent manipulation of coupled electron spins in semiconductor quantum dots.* Science, **309**, 2180 (2005).

[100] E. A. Stinaff, M. Scheibner, A. S. Bracker, I. V. Ponomarev, V. L. Korenev, M. E. Ware, M. F. Doty, T. L. Reinecke and D. Gammon. *Optical signatures of coupled quantum dots.* Science, **311**, 636 (2006).

[101] R. . Blick, R. J. Haug, J. Weis, D. Pfannkuche, K.v. Klitzing and K. Eberl. *Single-electron tunneling through a double quantum dot: The artificial molecule.* Phys. Rev. B, **53**, 7899 (1996).

[102] F. Ancilotto, D. G. Austing, M. Barranco, R. Mayol, K. Muraki, M. Pi, S. Sasaki and S. Tarucha. *Vertical diatomic artificial molecule in the intermediate-coupling regime in a parallel and perpendicular magnetic field.* Phys. Rev. B, **67**, 205311 (2003).

[103] D. G. Austing, S. Tarucha, H. Tamura, K. Muraki, F. Ancilotto, M. Barranco, A. Emperador, R. Mayol and M. Pi. *Integer filling factor phases and isospin in vertical diatomic artificial molecules*. Phys. Rev. B, **70**, 045324 (2004).

[104] M. Pi, A. Emperador, M. Barranco and F. Garcias. *Vertically coupled quantum dots in the local spin-density functional theory*. Phys. Rev. B, **63**, 115316 (2001).

[105] B. Partoens and F. M. Peeters. *Molecule-Type Phases and Hund's Rule in Vertically Coupled Quantum Dots*. Phys. Rev. Lett., **84**, 4433 (2000).

[106] M. Rontani, F. Troiani, U. Hohenester and E. Molinari. *Quantum phases in artificial molecules*. Solid State Commun., **119**, 309 (2001).

[107] B. Partoens and F. M. Peeters. *Magnetic-field-induced spin and isospin blockade in two vertically coupled quantum dots*. Europhys. Lett., **56**, 86 (2001).

[108] D. Bellucci, M. Rontani, G. Goldoni and E. Molinari. *Quantum phases of correlated electrons in artificial molecules under magnetic fields*. Phys. Rev. B, **74**, 035331 (2006).

[109] J. J. Palacios and P. Hawrylak. *Correlated few-electron states in vertical double-quantum-dot systems*. Phys. Rev. B, **51**, 1769 (1995).

[110] K. H. Ahn and P. Fulde. *Parity effects in stacked nanoscopic quantum rings*. Phys. Rev. B, **62**, R4813 (2000).

[111] B. Szafran. *Correlated persistent currents in a stack of semiconductor quantum rings*. Phys. Rev. B, **77**, 235314 (2008).

[112] A. Fuhrer, T. Ihn, K. Ensslin, W. Wegscheider and M. Bichler. *Singlet-triplet transition tuned by asymmetric gate voltages in a quantum ring*. Phys. Rev. Lett., **91**, 206802 (2003).

[113] E. Lipparini. *Modern Many-Particle Physics*. World Scientific, Singapore (2008).

[114] M. Ferconi and G. Vignale. *Current-density-functional theory of quantum dots in a magnetic field*. Phys. Rev. B, **50**, 14722 (1994).

[115] W. Kohn and L. J. Sham. *Self-Consistent Equations Including Exchange and Correlation Effects*. Phys. Rev., **140**, A1133 (1965).

[116] A. Puente and L. Serra. *Ground state and far-infrared absorption of two-electron rings in a magnetic field.* Phys. Rev. B, **63**, 125334 (2001).

[117] J. I. Climente, J. Planelles and F. Rajadell. *Energy structure and fat-infrared spectroscopy of two electrons in a self-assembled quantum ring.* J. Phys.: Condens. Matter., **17**, 1573 (2005).

[118] S. Lundqvist. *Theory of the Inhomogeneous Electron Gas.* Plenum, New York (1983).

[119] J. P. Perdew and A. Zunger. *Self-interaction correction to density-functional approximations for many-electron systems.* Phys. Rev. B, **23**, 5048 (1981).

[120] T. H. Oosterkamp, J. W. Janssen, L. P. Kouwenhoven, D. G. Austing, T. Honda and S. Tarucha. *Maximum-Density Droplet and Charge Redistributions in Quantum Dots at High Magnetic Fields.* Phys. Rev. Lett., **82**, 2931 (1999).

[121] B. L. Cushing, V. L. Kolesnichenko and C. J. O'Connor. *Recent advances in the liquid-phase syntheses of inorganic nanoparticles.* Chem. Rev, **104**, 3893 (2004).

[122] C. Burda, X. Chen, R. Narayanan, M. A. El-Sayed et al. *Chemistry and properties of nanocrystals of different shapes.* Chem. Rev, **105**, 1025 (2005).

[123] Y. Jun, J. Choi and J. Cheon. *Shape control of semiconductor and metal oxide nanocrystals through nonhydrolytic colloidal routes.* Angew. Chem. Int. Ed., **45**, 3414 (2006).

[124] J. Li and L. W. Wang. *Shape effects on electronic states of nanocrystals.* Nano lett., **3**, 1357 (2003).

[125] V. I. Klimov, A. A. Mikhailovsky, S. Xu, A. Malko, J. A. Hollingsworth, C. A. Leatherdale, H. J. Eisler and M. G. Bawendi. *Optical gain and stimulated emission in nanocrystal quantum dots.* Science, **290**, 314 (2000).

[126] V. L. Colvin, M. C. Schlamp and A. P. Alivisatos. *Light-emitting diodes made from cadmium selenide nanocrystals and a semiconducting polymer.* Nature, **370**, 354 (1994).

[127] V. I. Klimov, S. A. Ivanov, J. Nanda, M. Achermann, I. Bezel, J. A. McGuire and A. Piryatinski. *Single-exciton optical gain in semiconductor nanocrystals.* Nature, **447**, 441 (2007).

[128] W. C. W. Chan and S. Nie. *Quantum dot bioconjugates for ultrasensitive nonisotopic detection.* Science, **281**, 2016 (1998).

[129] M. Bruchez Jr, M. Moronne, P. Gin, S. Weiss and A. P. Alivisatos. *Semiconductor nanoparticles as fluorescent biological labels.* Science, **281**, 2013 (1998).

[130] M. Nirmal, B. O. Dabbousi, M. G. Bawendi, J. J. Macklin, J. K. Trautman, T. D. Harris and L. E. Brus. *Fluorescence intermittency in single cadmium selenide nanocrystals.* Nature, **383**, 802 (1996).

[131] X. Wang, X. Ren, K. Kahen, M. A. Hahn, M. Rajeswaran, S. Maccagnano-Zacher, J. Silcox, G. E. Cragg, A. Efros and T. Krauss. *Non-blinking semiconductor nanocrystals.* Nature, **459**, 686 (2009).

[132] G. E. Cragg and A. L. Efros. *Suppression of Auger Processes in Confined Structures.* Nano Lett., 141101 (2010).

[133] K. Sanderson. *Quantum dots go large.* Nature, **459**, 760 (2009).

[134] U. Woggon. *Optical properties of semiconductor quantum dots.* Springer, Berlin (1996).

[135] S. V. Gaponenko. *Optical properties of semiconductor nanocrystals.* Cambridge University Press, Cambridge (1998).

[136] U. Banin and O. Millo. *Tunneling and optical spectroscopy of semiconductor nanocrystals.* Ann. Rev. Phys. Chem., **54**, 465 (2003).

[137] L. E. Brus. *A simple model for the ionization potential, electron affinity, and aqueous redox potentials of small semiconductor crystallites.* J. Chem. Phys., **79**, 5566 (1983).

[138] L. E. Brus. *Electron–electron and electron-hole interactions in small semiconductor crystallites: The size dependence of the lowest excited electronic state.* J. Chem. Phys., **80**, 4403 (1984).

[139] L. Banyai, P. Gilliot, Y. Z. Hu and S. W. Koch. *Surface-polarization instabilities of electron-hole pairs in semiconductor quantum dots.* Phys. Rev. B, **45**, 14136 (1992).

[140] V. M. Fomin, V. N. Gladilin, J. T. Devreese, E. P. Pokatilov, S. N. Balaban and S. N. Klimin. *Photoluminescence of spherical quantum dots.* Phys. Rev. B, **57**, 2415 (1998).

[141] P. G. Bolcatto and C. R. Proetto. *Shape and dielectric mismatch effects in semiconductor quantum dots.* Phys. Rev. B, **59**, 12487 (1999).

[142] P. G. Bolcatto and C. R. Proetto. *Partially confined excitons in semiconductor nanocrystals.* J. Phys. Condens. Matt., **13**, 319 (2001).

[143] J. L. Movilla and J. Planelles. *Image charges in spherical quantum dots with an off-centered impurity: algorithm and numerical results.* Comp. Phys. Commun., **170**, 144 (2005).

[144] S. Deng. *A robust numerical method for self-polarization energy of spherical quantum dots with finite confinement barriers.* Comp. Phys. Commun., **181**, 787 (2010).

[145] J. L. Movilla, J. I. Climente and J. Planelles. *Dielectric polarization in axially-symmetric nanostructures: A computational approach.* Comp. Phys. Commun., **181**, 92 (2010).

[146] V. A. Fonoberov, E. P. Pokatilov and A. A. Balandin. *Exciton states and optical transitions in colloidal CdS quantum dots: Shape and dielectric mismatch effects.* Phys. Rev. B, **66**, 85310 (2002).

[147] G. Goldoni, F. Rossi and E. Molinari. *Strong Exciton Binding in Quantum Structures through Remote Dielectric Confinement.* Phys. Rev. Lett., **80**, 4995 (1998).

[148] L. V. Keldysh. *Coulomb interaction in thin semiconductor and semimetal films.* JETP Lett.(USSR), **29**, 658 (1979).

[149] V. S. Dneprovskii, E. A. Zhukov, E. A. Muljarov and S. G. Tikhodeev. *Linear and nonlinear excitonic absorption in semiconducting quantum wires crystallized in a dielectric matrix.* J. Exp. Theor. Phys., **87**, 382 (1998).

[150] E. A. Muljarov, E. A. Zhukov, V. S. Dneprovskii and Y. Masumoto. *Dielectrically enhanced excitons in semiconductor-insulator quantum wires: Theory and experiment.* Phys. Rev. B, **62**, 7420 (2000).

[151] N. V. Bondar and M. S. Brodyn. *Evolution of excitonic states in two-phase systems with quantum dots of II-VI semiconductors near the percolation threshold.* Physica E, **42**, 1549 (2010).

[152] N. V. Bondar and M. S. Brodyn. *Quantum and surface states of charge carriers in the optical spectra of nanoclusters in a low-permittivity matrix.* Low Temp. Phys., **34**, 55 (2008).

[153] N. V. Bondar. *Emission and energy relaxation of excitons in quantum dots with disordered interfaces grown in a low-permittivity matrix.* Opts. Spectros., **108**, 728 (2010).

[154] A. Franceschetti, A. Williamson and A. Zunger. *Addition spectra of quantum dots: the role of dielectric mismatch.* J. Phys. Chem. B, **104**, 3398 (2000).

[155] A. Orlandi, M. Rontani, G. Goldoni, F. Manghi and E. Molinari. *Single-electron charging in quantum dots with large dielectric mismatch.* Phys. Rev. B, **63**, 045310 (2001).

[156] A. Orlandi, G. Goldoni, F. Manghi and E. Molinari. *The effect of dielectric polarization-induced surface states on many-body configurations in a quantum dot.* Semicond. Sci. Technol., **17**, 1302 (2002).

[157] M. Royo, J. Planelles and M. Pi. *Effective mass and dielectric constant mismatch effects in spherical multishell quantum dots.* Phys. Rev. B, **75**, 033302 (2007).

[158] D. Jena and A. Konar. *Enhancement of Carrier Mobility in Semiconductor Nanostructures by Dielectric Engineering.* Phys. Rev. Lett., **98**, 136805 (2007).

[159] M. Pi, M. Royo and J. Planelles. *A consistent extension of the local spin density approximation to account for quantum dot mass and dielectric mismatches.* J. Appl. Phys., **100**, 073712 (2006).

[160] J. Planelles, M. Royo and M. Pi. *Nonparabolicity and dielectric effects on addition energy spectra of spherical nanocrystals.* J. Appl. Phys., **102**, 094304 (2007).

[161] F. Rajadell, J. L. Movilla, M. Royo and J. Planelles. *Theory of dielectrically induced surface excitonic states in spherical quantum dots.* Phys. Rev. B, **76**, 115312 (2007).

[162] A. Shabaev and A. Efros. *1D exciton spectroscopy of semiconductor nanorods.* Nano Lett., **4**, 1821 (2004).

[163] W. Xiong and S. S. Li. *Electronic structure and exciton states in the freestanding ZnO nanorods.* J. Appl. Phys., **105**, 094327 (2009).

[164] J. I. Climente, M. Royo, J. L. Movilla and J. Planelles. *Strong configuration mixing due to dielectric confinement in semiconductor nanorods.* Phys. Rev. B, **79**, 161301 (2009).

[165] M. Royo, J. I. Climente, J. L. Movilla and J. Planelles. *Dielectric confinement of excitons in type-I and type-II semiconductor nanorods.* Submitted (2010).

[166] O. Millo, D. Katz, Y. Cao and U. Banin. *Scanning tunneling spectroscopy of InAs nanocrystal quantum dots.* Phys. Rev. B, **61**, 16773 (2000).

[167] O. Millo, D. Katz, Y. Cao and U. Banin. *Imaging and Spectroscopy of Artificial-Atom States in Core/Shell Nanocrystal Quantum Dots.* Phys. Rev. Lett., **86**, 5751 (2001).

[168] E. Bakkers, Z. Hens, A. Zunger, A. Franceschetti, L. P. Kouwenhoven, L. Gurevich and D. Vanmaekelbergh. *Shell-tunneling spectroscopy of the single-particle energy levels of insulating quantum dots.* Nano Lett., **1**, 551 (2001).

[169] P. Liljeroth, L. Jdira, K. Overgaag, B. Grandidier, S. Speller and D. Vanmaekelbergh. *Can scanning tunnelling spectroscopy measure the density of states of semiconductor quantum dots?* Phys. Chem. Chem. Phys., **8**, 3845 (2006).

[170] R. C. Ashoori. *Electrons in artificial atoms.* Nature, **379**, 413 (1996).

[171] M. Jung, T. Machida, K. Hirakawa, S. Komiyama, T. Nakaoka, S. Ishida and Y. Arakawa. *Shell structures in self-assembled InAs quantum dots probed by lateral electron tunneling structures.* Appl. Phys. Lett., **87**, 203109 (2005).

[172] M. Zdrojek, M. J. Esplandiu, A. Barreiro and A. Bachtold. *Electron counting cpectroscopy of CdSe quantum dots.* Phys. Rev. Lett., **102**, 226804 (2009).

[173] D. J. BenDaniel and C. B. Duke. *Space-Charge Effects on Electron Tunneling.* Phys. Rev., **152**, 683 (1966).

[174] D. M. Ceperley and B. J. Alder. *Ground State of the Electron Gas by a Stochastic Method.* Phys. Rev. Lett., **45**, 566 (1980).

[175] I. Zutic, J. Fabian and S. Das Sarma. *Spintronics: Fundamentals and applications.* Rev. Mod. Phys., **76**, 323 (2004).

[176] A. Imamog¯lu, D. D. Awschalom, G. Burkard, D. P. DiVincenzo, D. Loss, M. Sherwin and A. Small. *Quantum Information Processing Using Quantum Dot Spins and Cavity QED.* Phys. Rev. Lett., **83**, 4204 (1999).

[177] K. Hirose and N. S. Wingreen. *Spin-density-functional theory of circular and elliptical quantum dots.* Physical Review B, **59**, 4604 (1999).

[178] A. Franceschetti and A. Zunger. *Hund's rule, spin blockade, and the Aufbau principle in strongly confined semiconductor quantum dots.* Europhys. Lett., **50**, 243 (2000).

[179] M. Ediger, G. Bester, A. Badolato, P. M. Petroff, K. Karrai, A. Zunger and R. J. Warburton. *Peculiar many-body effects revealed in the spectroscopy of highly charged quantum dots.* Nature Phys., **3**, 774 (2007).

[180] S. Tarucha, D. G. Austing, Y. Tokura, W. G. van der Wiel and L. P. Kouwenhoven. *Direct Coulomb and Exchange Interaction in Artificial Atoms.* Phys. Rev. Lett., **84**, 2485 (2000).

[181] D. Weinmann, W. Häusler, W. Pfaff, B. Kramer and U. Weiss. *Spin Blockade in Non-linear Transport through Quantum Dots.* Europhys. Lett., **26**, 467 (1994).

[182] D. Weinmann, W. Häusler and B. Kramer. *Spin Blockades in Linear and Nonlinear Transport through Quantum Dots.* Phys. Rev. Lett., **74**, 984 (1995).

[183] M. Ciorga, M. Pioro-Ladriere, P. Zawadzki, P. Hawrylak and A. S. Sachrajda. *Tunable negative differential resistance controlled by spin blockade in single-electron transistors.* Appl. Phys. Lett., **80**, 2177 (2002).

[184] M. Pioro-Ladriere, M. Ciorga, J. Lapointe, P. Zawadzki, M. Korkusiński, P. Hawrylak and A. Sachrajda. *Spin-blockade spectroscopy of a two-level artificial molecule.* Phys. Rev. Lett., **91**, 26803 (2003).

[185] A. Pfund, I. Shorubalko, R. Leturcq and K. Ensslin. *Pauli spin-blockade in an InAs nanowire double quantum dot.* Physica E, **40**, 1279 (2008).

[186] P. Hohenberg and W. Kohn. *Inhomogeneous Electron Gas.* Phys. Rev., **136**, B864 (1964).

[187] O. Gunnarsson and B. I. Lundqvist. *Exchange and correlation in atoms, molecules, and solids by the spin-density-functional formalism.* Phys. Rev. B, **13**, 4274 (1976).

[188] A. Eychmüller, A. Mews and H. Weller. *A quantum dot quantum well: CdS/HgS/CdS.* Chem. Phys. Lett., **208**, 59 (1993).

[189] A. Mews, A. Eychmüller, M. Giersig, D. Schooss and H. Weller. *Preparation, characterization, and photophysics of the quantum dot quantum well system cadmium sulfide/mercury sulfide/cadmium sulfide.* J. Phys. Chem., **98**, 934 (1994).

[190] M. Braun, C. Burda and M. El-Sayed. *Variation of the Thickness and Number of Wells in the CdS/HgS/CdS Quantum Dot Quantum Well System†.* J. Phys. Chem. A, **105**, 5548 (2001).

[191] R. Xie, U. Kolb, J. Li, T. Basche and A. Mews. *Synthesis and Characterization of Highly Luminescent CdSe- Core $CdS/Zn_{0.5}Cd_{0.5}S/ZnS$ Multishell Nanocrystals.* J. Am. Chem. Soc, **127**, 7480 (2005).

[192] D. Dorfs and A. Eychmüller. *A series of double well semiconductor quantum dots.* Nano Lett., **1**, 663 (2001).

[193] B. O. Dabbousi, J. Rodriguez-Viejo, F. V. Mikulec, J. R. Heine, H. Mattoussi, R. Ober, K. F. Jensen and M. G. Bawendi. *(CdSe) ZnS Core- Shell Quantum Dots: Synthesis and Characterization of a Size Series of Highly Luminescent Nanocrystallites.* J. Phys. Chem. B, **101**, 9463 (1997).

[194] M. Danek, K. F. Jensen, C. B. Murray and M. G. Bawendi. *Synthesis of luminescent thin-film CdSe/ZnSe quantum dot composites using CdSe quantum dots passivated with an overlayer of ZnSe.* Chem. Mater, **8**, 173 (1996).

[195] M. Braun, S. Link, C. Burda and M. El-Sayed. *Determination of the localization times of electrons and holes in the HgS well in a*

CdS/HgS/CdS quantum dot–quantum well nanoparticle. Phys. Rev. B, **66**, 205312 (2002).

[196] H. Borchert, D. Dorfs, C. McGinley, S. Adam, T. Moller, H. Weller and A. Eychmuller. *Photoemission Study of Onion Like Quantum Dot Quantum Well and Double Quantum Well Nanocrystals of CdS and HgS.* J. Phys. Chem. B, **107**, 7486 (2003).

[197] A. Mews, A. V. Kadavanich, U. Banin and A. P. Alivisatos. *Structural and spectroscopic investigations of CdS/HgS/CdS quantum-dot quantum wells.* Phys. Rev. B, **53**, R13242 (1996).

[198] G. W. Bryant and W. Jaskólski. *Designing Nanocrystal Nanosystems: Quantum-Dot Quantum-Wells to Quantum-Dot Solids.* Phys. Stat. Sol. B, **24**, 751 (2001).

[199] J. Planelles, J. Climente, J. G. Díaz and W. Jaskólski. *Hole energy structure of multishell nanocrystals in a magnetic field.* J. Phys.: Condens. Matt., **14**, 12537 (2002).

[200] J. Climente, J. Planelles, W. Jaskólski and J. I. Aliaga. *Magneto-optical transitions in multilayer semiconductor nanocrystals.* J. Phys.: Condens. Matt., **15**, 3593 (2003).

[201] K. Chang and J.-B. Xia. *Spatially separated excitons in quantum-dot quantum well structures.* Phys. Rev. B, **57**, 9780 (1998).

[202] A. D. Yoffe. *Semiconductor quantum dots and related systems: electronic, optical, luminescence and related properties of low dimensional systems.* Adv. Phys., **50**, 1 (2001).

[203] W. Jaskólski and G. W. Bryant. *Multiband theory of quantum-dot quantum wells: Dim excitons, bright excitons, and charge separation in heteronanostructures.* Phys. Rev. B, **57**, R4237 (1998).

[204] A. L. Efros and M. Rosen. *Quantum size level structure of narrow-gap semiconductor nanocrystals: Effect of band coupling.* Physical Review B, **58**, 7120 (1998).

[205] E. O. Kane. *Band structure of indium antimonide.* J. Phys. Chem. Sol., **1**, 249 (1957).

[206] W. Chen and T. G. Andersson. *Effect of the nonparabolic mass on the electron confinement in arbitrarily shaped quantum wells.* Phys. Rev. B, **44**, 9068 (1991).

[207] D. Huang. *Formula for Coulomb effect on the nonlinear optical responses in quantum wells.* Phys. Rev. B, **53**, 13645 (1996).

[208] X. Chen. *Influences of conduction band non-parabolicity on intersubband absorption and photon drag in a single quantum well.* Physica B, **270**, 88 (1999).

[209] C. A. Ullrich and M. E. Flatté. *Intersubband spin-density excitations in quantum wells with Rashba spin splitting.* Phys. Rev. B, **66**, 205305 (2002).

[210] N. Kotera and K. Tanaka. *Determination of electron effective mass from optical transition energy in InGaAs/InAlAs quantum wells.* Physica E, **32**, 199 (2006).

[211] Y. Li, O. Voskoboynikov, C. P. Lee and S. M. Sze. *Energy and coordinate dependent effective mass and confined electron states in quantum dots.* Solid State Commun., **120**, 79 (2001).

[212] Y. Li, J.-L. Liu, O. Voskoboynikov, C. P. Lee and S. M. Sze. *Electron energy level calculations for cylindrical narrow gap semiconductor quantum dot.* Comput. Phys. Commun., **140**, 399 (2001).

[213] Y. Li, O. Voskoboynikov, C. P. Lee and S. M. Sze. *Computer simulation of electron energy levels for different shape InAs/GaAs semiconductor quantum dots.* Comput. Phys. Commun.s, **141**, 66 (2001).

[214] I. Filikhin, E. Deyneka and B. Vlahovic. *Single-electron levels of InAs/GaAs quantum dot: Comparison with capacitance spectroscopy.* Physica E, **31**, 99 (2006).

[215] O. Voskoboynikov, Y. Li, H.-M. Lu, C.-F. Shih and C. P. Lee. *Energy states and magnetization in nanoscale quantum rings.* Phys. Rev. B, **66**, 155306 (2002).

[216] I. Filikhin, V. M. Suslov and B. Vlahovic. *Modeling of InAs/GaAs quantum ring capacitance spectroscopy in the nonparabolic approximation.* Phys. Rev. B, **73**, 205332 (2006).

[217] Y. Li, O. Voskoboynikov, C. P. Lee and S. M. Sze. *Calculation of induced electron states in three-dimensional semiconductor artificial molecules.* Comput. Phys. Commun., **147**, 209 (2002).

[218] J.-L. Liu, J.-H. Chen and O. Voskoboynikov. *A model for semiconductor quantum dot molecule based on the current spin density functional theory.* Comput. Phys. Commun., **175**, 575 (2006).

[219] U. Banin, Y. Cao, D. Katz and O. Millo. *Identification of atomic-like electronic states in indium arsenide nanocrystal quantum dots.* Nature, **400**, 542 (1999).

[220] M. Drndić, M. V. Jarosz, N. Y. Morgan, M. A. Kastner and M. G. Bawendi. *Transport properties of annealed CdSe colloidal nanocrystal solids.* J. Appl. Phys., **92**, 7498 (2002).

[221] M. A. El-Sayed. *Small is different: shape-, size-, and composition-dependent properties of some colloidal semiconductor nanocrystals.* Acc. Chem. Res, **37**, 326 (2004).

[222] Z. A. Weinberg. *On tunneling in metal-oxide-silicon structures.* J. Appl. Phys., **53**, 5052 (1982).

[223] F. Giustino, P. Umari and A. Pasquarello. *Dielectric effect of a thin SiO2 interlayer at the interface between silicon and high-k oxides.* Microelectron. Eng., **72**, 299 (2004).

[224] J. M. Ferreyra and C. R. Proetto. *Strong-confinement approach for impurities in quantum dots.* Phys. Rev. B, **52**, 2309 (1995).

[225] N. A. Hill and K. B. W. *Size Dependence of Excitons in Silicon Nanocrystals.* Phys. Rev. Lett., **75**, 1130 (1995).

[226] A. Franceschetti and A. Zunger. *Direct Pseudopotential Calculation of Exciton Coulomb and Exchange Energies in Semiconductor Quantum Dots.* Phys. Rev. Lett., **78**, 915 (1997).

[227] M. Law, J. Goldberger and P. D. Yang. *Semiconductor nanowires and nanotubes.* Ann. Rev. Mat. Res., **34**, 83 (2004).

[228] Y. N. Xia, P. D. Yang, Y. G. Sun, Y. Y. Wu, B. Mayers, B. Gates, Y. D. Yin, F. Kim and Y. Q. Yan. *One-dimensional nanostructures: Synthesis, characterization, and applications.* Adv. Mat., **15**, 353 (2003).

[229] L. J. Lauhon, M. S. Gudiksen, C. L. Wang and C. M. Lieber. *Epitaxial core-shell and core-multishell nanowire heterostructures.* Nature, **420**, 57 (2002).

[230] P. Mohan, J. Motohisa and T. Fukui. *Fabrication of InP/InAs/InP core-multishell heterostructure nanowires by selective area metalorganic vapor phase epitaxy.* Appl. Phys. Lett., **88**, 133105 (2006).

[231] L. Manna, E. C. Scher and A. P. Alivisatos. *Synthesis of soluble and processable rod-, arrow-, teardrop-, and tetrapod-shaped CdSe nanocrystals.* J. Am. Chem Soc., **122**, 12700 (2000).

[232] L. Manna, D. J. Milliron, A. Meisel, E. C. Scher and A. P. Alivisatos. *Controlled growth of tetrapod-branched inorganic nanocrystals.* Nature Mat., **2**, 382 (2003).

[233] X. Peng, L. Manna, W. Yang, J. Wickham, E. Scher, A. Kadavanich and A. P. Alivisatos. *Shape control of CdSe nanocrystals.* Nature, **404**, 59 (2000).

[234] S. Kan, T. Mokari, E. Rothenberg and U. Banin. *Synthesis and size-dependent properties of zinc-blende semiconductor quantum rods.* Nature Mat., **2**, 155 (2003).

[235] M. B. Mohamed, C. Burda and M. A. El-Sayed. *Shape dependent ultrafast relaxation dynamics of CdSe nanocrystals: Nanorods vs nanodots.* Nano Lett., **1**, 589 (2001).

[236] J. Hu, L. Li, W. Yang, L. Manna, L. Wang and A. P. Alivisatos. *Linearly polarized emission from colloidal semiconductor quantum rods.* Science, **292**, 2060 (2001).

[237] D. Katz, T. Wizansky, O. Millo, E. Rothenberg, T. Mokari and U. Banin. *Size-Dependent Tunneling and Optical Spectroscopy of CdSe Quantum Rods.* Phys. Rev. Lett., **89**, 086801 (2002).

[238] S. K. Mandal, A. R. Mandal, S. Das and B. Bhattacharjee. *Strong excitonic confinement effect in ZnS and ZnS:Mn nanorods embedded in polycarbonate membrane pores.* J. Appl. Phys., **101**, 114315 (2007).

[239] S. S. Lo, Y. Khan, M. Jones and G. D. Scholes. *Temperature and solvent dependence of CdSe/CdTe heterostructure nanorod spectra.* J. Chem. Phys., **131**, 084714 (2009).

[240] J. Wang, M. S. Gudiksen, X. Duan, Y. Cui and C. M. Lieber. *Highly polarized photoluminescence and photodetection from single indium phosphide nanowires.* Science, **293**, 1455 (2001).

[241] A. Lan, J. Giblin, V. Protasenko and M. Kuno. *Excitation and photoluminescence polarization anisotropy of single CdSe nanowires.* Appl. Phys. Lett., **92**, 183110 (2008).

[242] K. J. Wu, K. C. Chu, C. Y. Chao, Y. F. Chen, C. W. Lai, C. C. Kang, C. Y. Chen and P. T. Chou. *CdS nanorods imbedded in liquid crystal cells for smart optoelectronic devices.* Nano Lett., **7**, 1908 (2007).

[243] V. Barzda, R. Cisek, T. L. Spencer, U. Philipose, H. E. Ruda and A. Shik. *Giant anisotropy of second harmonic generation for a single ZnSe nanowire.* Appl. Phys. Lett., **92**, 113111 (2008).

[244] N. N. Hewa-Kasakarage, P. Z. El-Khoury, N. Schmall, M. Kirsanova, A. Nemchinov, A. N. Tarnovsky, A. Bezryadin and M. Zamkov. *The effect of dielectric friction on the rate of charge separation in type II ZnSe/CdS semiconductor nanorods.* Appl. Phys. Lett., **94**, 133113 (2009).

[245] Z. Sun, I. Swart, C. Delerue, D. Vanmaekelbergh and P. Liljeroth. *Orbital and Charge-Resolved Polaron States in CdSe Dots and Rods Probed by Scanning Tunneling Spectroscopy.* Phys. Rev. Lett., **102**, 196401 (2009).

[246] L. V. Keldysh. *Excitons in Semiconductor-Dielectric Nanostructures.* Phys. Stat. Sol. A, **164**, 3 (1997).

[247] A. F. Slachmuylders, B. Partoens, W. Magnus and F. M. Peeters. *Dielectric mismatch effect on the exciton states in cylindrical nanowires.* Phys. Rev. B, **74**, 235321 (2006).

[248] D. Boda, D. Gillespie, W. Nonner, D. Henderson and B. Eisenberg. *Computing induced charges in inhomogeneous dielectric media: Application in a Monte Carlo simulation of complex ionic systems.* Phys. Rev. E, **69**, 046702 (2004).

[249] H. Hoshi, M. Sakurai, Y. Inoue and R. Chûjô. *Medium effects on the molecular electronic structure. I. The formulation of a theory for the estimation of a molecular electronic structure surrounded by an anisotropic medium.* J. Chem. Phys., **87**, 1107 (1987).

[250] J. D. Jackson. *Classical Electrodynamics.* Wiley, New York (1999).

[251] P. C. Sercel and K. J. Vahala. *Polarization dependence of optical absorption and emission in quantum wires.* Phys. Rev. B, **44**, 5681 (1991).

[252] J. Planelles, F. Rajadell and J. I. Climente. *Hole Band Mixing in CdS and CdSe Quantum Dots and Quantum Rods.* J. Phys. Chem. C, **114**, 8337 (2010).

[253] J. S. Meyer and K. A. Matveev. *Wigner crystal physics in quantum wires.* J. Phys. Condens. Matt., **21**, 023203 (2009).

[254] L. Jdira, P. Liljeroth, E. Stoffels, D. Vanmaekelbergh and S. Speller. *Size-dependent single-particle energy levels and interparticle Coulomb interactions in CdSe quantum dots measured by scanning tunneling spectroscopy.* Phys. Rev. B, **73**, 115305 (2006).

[255] S. Corni, M. Braskén, M. Lindberg, J. Olsen and D. Sundholm. *Size dependence of the electron-hole recombination rates in semiconductor quantum dots.* Phys. Rev. B, **67**, 045313 (2003).

[256] D. Steiner, D. Katz, O. Millo, A. Aharoni, S. H. Kan, T. Mokari and U. Banin. *Zero-dimensional and quasi one-dimensional effects in semiconductor nanorods.* Nano Lett., **4**, 1073 (2004).

[257] F. Shieh, A. E. Saunders and B. A. Korgel. *General shape control of colloidal CdS, CdSe, CdTe quantum rods and quantum rod heterostructures.* J. Phys. Chem. B, **109**, 8538 (2005).

[258] S. Kumar, M. Jones, S. S. Lo and G. D. Scholes. *Nanorod heterostructures showing photoinduced charge separation.* Small, **3**, 1633 (2007).

[259] A. E. Saunders, B. Koo, X. Wang, C. K. Shih and B. A. Korgel. *Structural characterization and temperature-dependent photoluminescence of linear CdTe/CdSe/CdTe heterostructure nanorods.* ChemPhysChem, **9**, 1158 (2008).

[260] H. Lee, S. W. Yoon, J. P. Ahn, Y. D. Suh, J. S. Lee, H. Lim and D. Kim. *Synthesis of type II CdTe/CdSe heterostructure tetrapod nanocrystals for PV applications.* Sol. Energy Mater. Sol. Cells, **93**, 779 (2009).

[261] X.-Z. Li and J.-B. Xia. *Effects of electric field on the electronic structure and optical properties of quantum rods with wurtzite structure.* Phys. Rev. B, **68**, 165316 (2003).

[262] J. Muller, J. M. Lupton, P. G. Lagoudakis, F. Schindler, R. Koeppe, A. L. Rogach, J. Feldmann, D. V. Talapin and H. Weller. *Wave function engineering in elongated semiconductor nanocrystals with heterogeneous carrier confinement.* Nano Lett., **5**, 2044 (2005).

[263] E. Rothenberg, M. Kazes, E. Shaviv and U. Banin. *Electric field induced switching of the fluorescence of single semiconductor quantum rods.* Nano lett., **5**, 1581 (2005).

[264] S. H. Kan, A. Aharoni, T. Mokari and U. Banin. *Shape control of III–V semiconductor nanocrystals: Synthesis and properties of InAs quantum rods.* Faraday discuss., **125**, 23 (2004).

[265] L. J. Geerligs, V. F. Anderegg, J. Romijn and J. E. Mooij. *Single Cooper-pair tunneling in small-capacitance junctions.* Phys. Rev. Lett., **65**, 377 (1990).

[266] S. Huang, N. Fukata, M. Shimizu, T. Yamaguchi, T. Sekiguchi and K. Ishibashi. *Classical Coulomb blockade of a silicon nanowire dot.* Appl. Phys. Lett., **92**, 213110 (2008).

[267] E. B. Kolomeisky and J. P. Straley. *Phase diagram and correlation exponents for interacting fermions in one dimension.* Rev. Mod. Phys., **68**, 175 (1996).

[268] S. M. Reimann, M. Koskinen and M. Manninen. *End states due to a spin-Peierls transition in quantum wires.* Phys. Rev. B, **59**, 1613 (1999).

[269] E. J. Mueller. *Wigner crystallization in inhomogeneous one-dimensional wires.* Phys. Rev. B, **72**, 75322 (2005).

[270] S. M. Reimann, M. Koskinen, P. E. Lindelof and M. Manninen. *Spin-density waves in superdeformed quantum dots.* Physica E, **2**, 648 (1998).

[271] S. H. Abedinpour, M. Polini, G. Xianlong and M. P. Tosi. *Emergence of Wigner molecules in one-dimensional systems of repulsive fermions under harmonic confinement.* Phys. Rev. A, **75**, 15602 (2007).

[272] E. Räsänen, H. Saarikoski, V. N. Stavrou, A. Harju, M. J. Puska and R. M. Nieminen. *Electronic structure of rectangular quantum dots.* Phys. Rev. B, **67**, 235307 (2003).

[273] B. Szafran, F. M. Peeters, S. Bednarek, T. Chwiej and J. Adamowski. *Spatial ordering of charge and spin in quasi-one-dimensional Wigner molecules.* Phys. Rev. B, **70**, 035401 (2004).

[274] A. Heyman, I. I. Yakimenko and K. F. Berggren. *Band structure and spin polarization for a one-dimensional array of quantum point contacts.* Nanotech., **15**, 143 (2004).

[275] R. M. Potok, J. A. Folk, C. M. Marcus and V. Umansky. *Detecting Spin-Polarized Currents in Ballistic Nanostructures.* Phys. Rev. Lett., **89**, 266602 (2002).

[276] J. Fransson, I. Sandalov and O. Eriksson. *A perfect spin-filter quantum dot system.* J. Phys.: Condens. Matt., **16**, L249 (2004).

[277] E. Wigner. *On the Interaction of Electrons in Metals.* Phys. Rev., **46**, 1002 (1934).

[278] E. Wigner. *Effects of the electron interaction on the energy levels of electrons in metals.* Trans. Far. Soc., **34**, 0678 (1938).

[279] J. Planelles, M. Royo, A. Ballester and M. Pi. *From quantum dots to quantum wires: Electronic structure of semiconductor nanorods.* Phys. Rev. B, **80**, 45324 (2009).

[280] F. Pederiva, A. Emperador and E. Lipparini. *Electron localization in low-density quantum rings.* Phys. Rev. B, **66**, 165314 (2002).

[281] A. Szabo and N. S. Ostlund. *Modern quantum chemistry: introduction to advanced electronic structure theory.* Dover Pubns (1996).

[282] R. M. Abolfath and P. Hawrylak. *Real space Hartree-Fock configuration interaction method for complex lateral quantum dot molecules.* J. Chem. Phys., **125**, 034707 (2006).

[283] A. Emperador, E. Lipparini and F. Pederiva. *Many-electron quantum dots in the fractional quantum Hall regime.* Phys. Rev. B, **72**, 033306 (2005).

[284] J. Planelles, J. I. Climente, M. Royo and J. L. Movilla. *Correlation in narrow nanorods: a variational potential–configuration interaction scheme.* J. Phys.: Condens. Matt., **21**, 215801 (2009).

[285] E. Biolatti, R. C. Iotti, P. Zanardi and F. Rossi. *Quantum Information Processing with Semiconductor Macroatoms.* Phys. Rev. Lett., **85**, 5647 (2000).

[286] A. Zrenner, E. Beham, S. Stufler, F. Findeis, M. Bichler and G. Abstreiter. *Coherent properties of a two-level system based on a quantum-dot photodiode.* Nature, **418**, 612 (2002).

[287] X. Li, Y. Wu, D. Steel, D. Gammon, T. H. Stievater, D. S. Katzer, D. Park, C. Piermarocchi and L. J. Sham. *An all-optical quantum gate in a semiconductor quantum dot.* Science, **301**, 809 (2003).

[288] G. Schedelbeck, W. Wegscheider, M. Bichler and G. Abstreiter. *Coupled quantum dots fabricated by cleaved edge overgrowth: From artificial atoms to molecules.* Science, **278**, 1792 (1997).

[289] J. M. Villas-Bôas, A. O. Govorov and S. E. Ulloa. *Coherent control of tunneling in a quantum dot molecule.* Phys. Rev. B, **69**, 125342 (2004).

[290] W. Sheng and J.-P. Leburton. *Anomalous Quantum-Confined Stark Effects in Stacked InAs/GaAs Self-Assembled Quantum Dots.* Phys. Rev. Lett., **88**, 167401 (2002).

[291] H. J. Krenner, M. Sabathil, E. C. Clark, A. Kress, D. Schuh, M. Bichler, G. Abstreiter and J. J. Finley. *Direct Observation of Controlled Coupling in an Individual Quantum Dot Molecule.* Phys. Rev. Lett., **94**, 057402 (2005).

[292] R. Oulton, A. I. Tartakovskii, A. Ebbens, J. J. Finley, D. J. Mowbray, M. S. Skolnick and M. Hopkinson. *Anomalous Stark shifts in single vertically coupled pairs of InGaAs quantum dots.* Physica E, **26**, 302 (2005).

[293] H. J. Krenner, E. C. Clark, T. Nakaoka, M. Bichler, C. Scheurer, G. Abstreiter and J. J. Finley. *Optically Probing Spin and Charge Interactions in a Tunable Artificial Molecule.* Phys. Rev. Lett., **97**, 076403 (2006).

[294] B. Szafran, T. Chwiej, F. M. Peeters, S. Bednarek, J. Adamowski and B. Partoens. *Exciton and negative trion dissociation by an external electric field in vertically coupled quantum dots.* Phys. Rev. B, **71**, 205316 (2005).

[295] M. H. Degani and M. Z. Maialle. *Resonances of trion states in quantum dot molecules tuned by an electric field.* Phys. Rev. B, **75**, 115322 (2007).

[296] L. Wang, A. Rastelli, S. Kiravittaya, M. Benyoucef and O. G. Schmidt. *Self-Assembled Quantum Dot Molecules.* Adv. Mater., **21**, 2601 (2009).

[297] P. Alonso-González, J. Martín-Sánchez, Y. González, B. Alén, D. Fuster and L. González. *Formation of Lateral Low Density In(Ga)As Quantum Dot Pairs in GaAs Nanoholes.* Cryst. Growth Des., **9**, 2525 (2009).

[298] G. J. Beirne, C. Hermannstädter, L. Wang, A. Rastelli, O. G. Schmidt and P. Michler. *Quantum Light Emission of Two Lateral Tunnel-Coupled $(In, Ga)As/GaAs$ Quantum Dots Controlled by a Tunable Static Electric Field.* Phys. Rev. Lett., **96**, 137401 (2006).

[299] M. Baira, L. Sfaxi, L. Bouzaiene, H. Maaref, N. Chauvin and C. Bru-Chevallier. *Broken symmetry in laterally coupled InAs/GaAs quantum dots molecule.* J. Appl. Phys., **104**, 064314 (2008).

[300] C. Hermannstädter, M. Witzany, G. J. Beirne, W. M. Schulz, M. Eichfelder, R. Rossbach, M. Jetter, P. Michler, L. Wang, A. Rastelli and O. G. Schmidt. *Polarization fine structure and enhanced single-photon emission of self-assembled lateral InGaAs quantum dot molecules embedded in a planar microcavity.* J. Appl. Phys., **105**, 122408 (2009).

[301] J. Peng, C. Hermannstädter, M. Witzany, M. Heldmaier, L. Wang, S. Kiravittaya, A. Rastelli, O. G. Schmidt, P. Michler and G. Bester. *Heterogeneous confinement in laterally coupled InGaAs/GaAs quantum dot molecules under lateral electric fields.* Phys. Rev. B, **81**, 205315 (2010).

[302] C. Hermannstädter, G. J. Beirne, M. Witzany, M. Heldmaier, J. Peng, G. Bester, L. Wang, A. Rastelli, O. G. Schmidt and P. Michler. *Influence of the charge carrier tunneling processes on the recombination dynamics in single lateral quantum dot molecules.* Phys. Rev. B, **82**, 085309 (2010).

[303] G. Muñoz-Matutano, J. Canet-Ferrer, P. Alonso-González, B. Alén, I. Fernández-Martínez, J. Martín-Sánchez, D. Fuster, J. Martínez-Pastor, Y. González, F. Briones and L. González. *Emission properties*

of single InAs/GaAs quantum dot pairs and molecules grown in GaAs nanoholes. J. Phys.: Conf. Ser., **210**, 012028 (2010).

[304] M. Baier, F. Findeis, A. Zrenner, M. Bichler and G. Abstreiter. *Optical spectroscopy of charged excitons in single quantum dot photodiodes.* Phys. Rev. B, **64**, 195326 (2001).

[305] J. J. Finley, P. W. Fry, A. D. Ashmore, A. Lemaître, A. I. Tartakovskii, R. Oulton, D. J. Mowbray, M. S. Skolnick, M. Hopkinson, P. D. Buckle and P. A. Maksym. *Observation of multicharged excitons and biexcitons in a single InGaAs quantum dot.* Phys. Rev. B, **63**, 161305 (2001).

Publications

Magnetic-field control of ground-state transition from delocalized-to-localized electronic density in antiring superlattices

J. Planelles* and M. Royo

Departament de Ciències Experimentals, Universitat Jaume I, Box 224, E-12080 Castelló, Spain

(Received 23 December 2005; published 9 March 2006)

The electronic properties of strongly modulated antiring superlattices pierced by a uniform axial magnetic field are studied theoretically. The one-band effective-mass Hamiltonian in the envelope function approximation, with appropriate boundary conditions, is integrated numerically. We show that the low-lying electronic states of the antiring superlattice can be viewed as a superposition of localized states trapped in the antiring core and states that are delocalized in the surrounding matrix, which do not penetrate into the antiring region. We demonstrate that by choosing the antiring geometry and spacing properly, a transition from delocalized to localized ground state can be controlled by a magnetic field applied externally.

In the last two decades, advances in nanofabrication and crystal growth techniques have inspired a considerable amount of both theoretical and experimental work aimed at furthering our understanding of the physics governing the behavior of two-dimensional electron systems modulated by a periodic repulsive/attractive potential [antidot (AD)/quantum dot (QD) superlattice] subject to a perpendicular magnetic field.[1] The modulation of the potential leads to a mixing of Landau bands which split up into subbands,[2] the spatial dispersion of these magnetic minibands being related to observed maxima of magnetoresistence.[3] Various interesting phenomena have been observed in AD lattices pierced by a uniform perpendicular magnetic field, including the quenching of the Hall effect,[4] periodic oscillations versus magnetic field B (Aharonov-Bohm type) and versus $1/B$ (Shubnikov–de Haas type).[5]

On the other hand, tailoring sizes, shapes, and compositions of the building block nanocrystals is a fundamental issue, as these parameters control the electronic and physical properties of the sample. This fact has induced an intensive research so that QDs with geometries including pyramids, truncated pyramids and lens can be obtained using a self-assembly growth technique.[6] More recently ring-shaped QDs, often referred to as quantum rings (QR) have also been synthesized[7] and even concentric double rings[8] and QD embedded in QR[9] have been obtained.

The spatial confinement of a nanocrystal comes from the band-offset at the nanocrystal-surrounding matrix heterojunction, which produces a steplike potential influencing the dynamics of carriers (electrons and holes). We talk of a quantum dot (QD) or an antidot (AD) depending on the sign of the band-offset. Thus, if the surrounding matrix material acts as a barrier, the carrier can be spatially confined within the well-acting nanocrystal, and we refer to this nanocrystal as a QD. In contrast, if the nanocrystal acts as a quantum bump for the carriers, i.e., a finite barrier region surrounded by connected well regions, we refer to it as an AD. In a similar way, we can define quantum rings (QR) and antirings (AR).

In the present paper we study the electronic properties of AR superlattices pierced by a uniform axial magnetic field. QD and AD superlattices are also calculated for the sake of

comparison. We consider strongly modulated superlattices, as most synthesized artificial crystals are of this type, and we focus our study on the very bottom of the energy spectrum, namely the quantum limit. We will show that the low-lying electronic states of the AR superlattice can be viewed as a superposition of localized states trapped within the AR core (which acts as a QD) and delocalized states which do not penetrate into the AR region (the ARs acting as ADs for these states). Two domains will be clearly observed in the energy versus magnetic field plot, where either the spatial periodic potential or the magnetic field potential terms become dominant (weak and high magnetic regime). In particular we will show that by properly choosing the geometry, a ground state transition between localized/delocalized electronic density can be controlled by an externally applied magnetic field, this fact suggesting the possibility of employing self-assembled arrays of ARs as the building blocks of magnetic field-controlled transport nanodevices.

The Hamiltonian for an electron in the two-dimensional (x,y) plane, in the presence of a magnetic field, reads (in a.u.),

$$\mathcal{H} = \frac{1}{2m^*}(\mathbf{p} + \mathbf{A})^2 + V(x,y), \qquad (1)$$

where m^* stands for the effective mass, $\mathbf{A}$ is the vector potential and $V(x,y)$ represents periodic potential of the lattice, which is steplike: It has a constant value V_0 in the AR and it is zero both in the AR-core and outside the AR, the AR being located at the center of the unit cell.[10]

The eigenvalue equation of the above-mentioned Hamiltonian has been solved numerically using the finite-difference method on the two-dimensional grid (x,y). This discretization yields an eigenvalue problem of a huge asymmetric sparse matrix that has been solved in turn by employing the iterative Arnoldi factorization.[11]

Concerning boundary conditions, it should be pointed out that despite $V(x,y)$ being periodic, translations in the (x,y) plane do not commute with the Hamiltonian as they do not commute with the kinetic energy operator. This mathematical property, which can be easily checked, reveals the fact that if
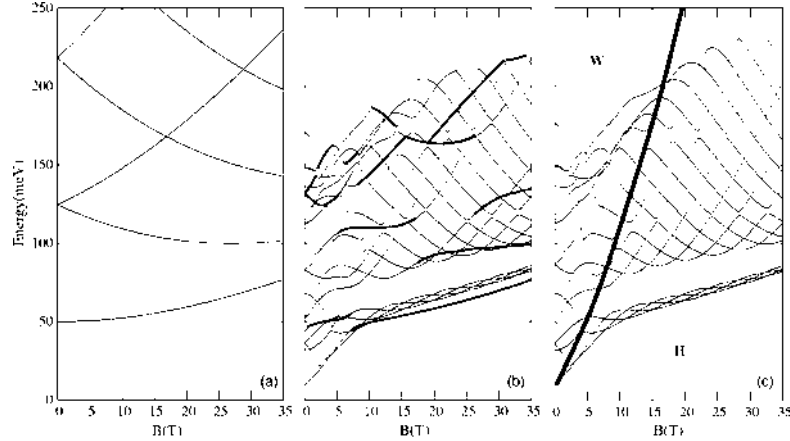
FIG. 1. Energy spectra of nanocrystal superlattices (d=45 nm) for three different potential profiles as a function of the magnetic field (a) QD, (b) AR, and (c) AD. Solid lines in (b) correspond to states localized within the AR core. The thick solid line in (c) is the border between the weak field (W) and the high field (H) regimes.

one were to transport an electron from one point of a periodic lattice pierced by an axial magnetic field to an equivalent one, it would be necessary to exert a Lorentz force along the way (in order to cancel out the effect of the magnetic field, so that the electron is in an equivalent state of motion at the new site). But if the field is homogeneous, the physical system is mapped back onto itself. In order to obtain an operator representing that symmetry and, therefore, commuting with the Hamiltonian operator, one has to compose the translation with the inverse of the associated gauge transformation, which is classically related to the shift in kinetic momentum that must be provided, in addition to the shift in position, in order to leave the electron in an invariant condition. This symmetry is referred to as magnetotranslation:[12]

$$\hat{T}(\mathbf{R}) = e^{-i\mathbf{R}\cdot(\mathbf{p}-\mathbf{A})}. \tag{2}$$

We have that $\hat{T}(\mathbf{R})f(\mathbf{r})$ should yield $f(\mathbf{r})$ up to a phase factor $e^{i\phi}$. Therefore,

$$\hat{T}(\mathbf{R})f(\mathbf{r}) = e^{i\mathbf{R}\cdot\mathbf{A}}f(\mathbf{r}-\mathbf{R}) = e^{i\phi}f(\mathbf{r}), \tag{3}$$

i.e.,

$$f(\mathbf{r}) = e^{-i\phi}e^{i\mathbf{R}\cdot\mathbf{A}}f(\mathbf{r}-\mathbf{R}) \tag{4}$$

is the practical boundary conditions we should impose on the eigenfunctions.

Concerning the vector potential $\mathbf{A}$ employed to describe the uniform axial magnetic field $\mathbf{B}=(0,0,B)$, we assume the Coulomb condition $\nabla\mathbf{A}=0$. The remaining freedom still present allows us to implement two different gauges: The symmetric gauge $\mathbf{A}=B/2(-y,x,0)$, and the Landau gauge $\mathbf{A}=B(0,x,0)$. The latter preserves the translational symmetry of the periodic potential along the vector $\mathbf{R}=(d,0,0)$ (with d

being the lattice constant) so that x-magnetotranslations are just translations [i.e., $\mathbf{R}\cdot\mathbf{A}=0$ in Eq. (4)]. As the physics must be gauge-independent the twofold implementation helps to check the codes that are employed.

The resulting computational scheme is very convenient and general as it can be employed in the high, intermediate, and weak magnetic regime (i.e., from $l \ll d$ up to $l \gg d$, with l representing the Landau radius and d the lattice constant).

In a first set of calculations we consider small GaAs ARs of radii r_i=10 nm and r_e=13 nm, embedded in an InAs matrix and forming a square superlattice of constant d=45 nm, the AR being located at the center of the unit cell. The GaAs material acts as a barrier for the electrons in the InAs matrix. Due to the diffusion of material we actually assume that the ARs embedded in the InAs are made of InGaAs instead of pure GaAs. Thus, a conduction-band offset reduced to 0.3 eV (from the value of 0.9 eV for InAs/GaAs interfaces[13]) and an effective mass m^*=0.03, corresponding to the InAs,[14] are employed.[15] For the sake of comparison, a superlattice of r=10 nm InAs QD embedded in InGaAs and a superlattice of r=13 nm InGaAs AD embedded in InAs with the same lattice constant d=45 nm have been calculated for different values of the externally applied magnetic field. The results corresponding to the low-lying states at the Γ point of the reciprocal lattice are shown in Fig. 1. The simplest set of results corresponds to the QD lattice [Fig. 1(a)]. A few well-separated levels appeared in the range of energies that was studied. The field dependence of these energy levels is almost exclusively linear. This behavior stems from the confinement of the electronic density in the small well-acting QD. It is the ratio between the radius of the maximum charge density in the lowest Landau level and the radius of the maximum of the radial charge density in a given quantum dot state that decides whether only the linear Zeeman term or
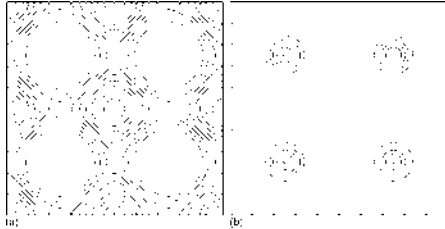
FIG. 2. Electronic densities of the ground state at (a) $B=0$ T and (b) $B=15$ T corresponding to the smaller unit cell ($d=45$ nm) AR superlattice. Four neighbor unit cells are represented.

FIG. 3. Energy spectrum of the wide unit cell AR superlattice ($d=145$ nm). Inset: Close-up view of the marked region.

also the quadratic term of the magnetic field are significant.[16] In this case only the linear term is significant. The symmetry of the lattice is C_{4v} at $B=0$ being reduced to C_4 in the presence of a magnetic field. However, the electronic density of the calculated states reveals axial symmetry with a value of nearly zero at the unit cell border. In other words, the studied system does not feel the lattice point and translational symmetries and behaves as a set of isolated circular QDs.[17]

The situation is the opposite in the AD energy spectrum [Fig. 1(c)]. In this case, the electronic density of the calculated states does not penetrate into the AD region; instead it is spread over the unit cell, outside the AD region, with finite values at the cell border, thus revealing the symmetry of the lattice. At first glance, the spectrum resembles that of an isolated QR with typical Aharonov-Bohm crossings stemming from the nonsimply connected nature of the electron domain. However, important differences should be stressed. On the one hand, we can observe two regions, the high and weak field regimes (regions labeled W and H in Fig. 1(c), above and below the solid thick line). In the W region the lattice potential dominates and the energy spectrum does not show regularities. In the H region a high degree of regularity is observed in the energy spectrum. Crossings similar to those occurring in QR, but also anticrossings coming from the lattice symmetry, split the low-lying part of the spectrum into noncrossing sets of four states. Within each set, the states repeatedly cross one another as B increases. Every set contains one instance of each of four C_4 symmetries, namely, A, B, E_+, and E_-.[18]

Figure 1(b) shows the AR spectrum. It can be viewed as a superposition of the QD and AD spectra. The solid lines represent states completely localized within the AR core while the thin lines correspond to delocalized states (the electronic density of which does not penetrate into the AR core). Note that at low magnetic field values, the ground state, which belongs to the totally symmetric irreducible representation A of C_4, is a delocalized state. It becomes strongly destabilized by increasing the magnetic field. The second A-symmetry state is completely localized within the AR core [lowest solid line in Fig. 1(b)] and it is almost unaffected by the magnetic field (it behaves like the $M=0$ state of a QD). As a consequence, an anticrossing between these two A states occurs and leads the ground state to become localized for magnetic fields higher than $B=9$ T. In
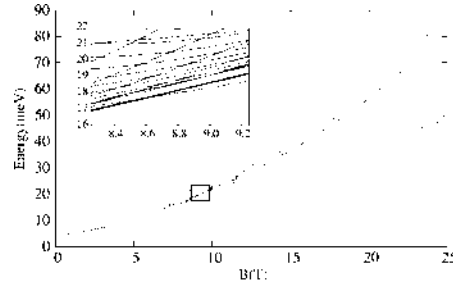
order to show the electronic density ground state transition from delocalized to localized, the electronic density of the ground state at $B=0$ and $B=15$ T is represented in Fig. 2.

Coming back to Fig. 1(b) we can see, at higher energies, several solid lines corresponding to localized states. The figure shows several anticrossings they undergo. As a consequence, the high field regime AR energy spectrum does not look as regular as the AD one [Fig. 1(c)].

Finally, we calculate a larger superlattice of unit cell edge $d=145$ nm. At its center we locate the InGaAs AR of radii $r_i=25$ nm and $r_e=35$ nm. The AR is also embedded in an InAs matrix. Therefore, here we use the same effective mass and band-offset parameters as before. The results are summarized in Fig. 3. The inset represents a close-up view of the selected area. As the unit cell of this new lattice is wider than the one studied previously, the magnetic flux piercing it is larger and so the oscillation frequency increases strongly. Nevertheless, the basic picture described in Fig. 1(b) is present here too. The energy spectrum looks like a superposition of those of AD and QD. The AD-like states are strongly destabilized by the magnetic field and show a parabolic collective destabilization profile. On the other hand, the QD-like states are much less influenced by the field. Therefore, as the magnetic field increases, the initially more excited low-lying localized QD-like states anticross the delocalized AD-like states, come into the bottom of the energy spectrum and converge towards the low Landau levels.

In summary, in the present paper we study the electronic properties of strongly modulated AR superlattices pierced by a uniform axial magnetic field. We focus our study on the quantum limit and show that the low-lying electronic states can be viewed as a superposition of localized states trapped within the AR core and delocalized states, which do not penetrate into the AR region. We have demonstrated that by choosing the AR geometry and spacing properly, a transition from a delocalized to a localized ground state can be controlled by the externally applied magnetic field. This suggests the possibility of employing self-assembled arrays of ARs as the building blocks of magnetic field-controlled transport nanodevices.

*Electronic address: josep.planelles@exp.uji.es

[1] H. Silberbauer, J. Phys.: Condens. Matter **4**, 7355 (1992); O. Kühn, V. Fessatidis, H. L. Cui, P. E. Selbmann, and N. J. M. Horing, Phys. Rev. B **47**, 13019 (1993); S. Uryu and T. Ando, *ibid.* **53**, 13613 (1996); O. Steffens, T. Schlösser, P. Rotter, K. Ensslin, M. Suhrke, J. P. Kotthaus, U. Rössler, and M. Holland, J. Phys.: Condens. Matter **10**, 3859 (1998); E. Anisimovas and P. Johansson, Phys. Rev. B **60**, 7744 (1999); P. H. Rivera, M. A. AndradeNeto, P. A. Schulz, and N. Studart, *ibid.* **64**, 035313 (2001); J. G. Analytis, S. J. Blundell, and A. Ardavan, Synth. Met. **154**, 265 (2005); E. Muñoz, Z. Barticevic, and M. Pacheco, Phys. Rev. B **71**, 165301 (2005).

[2] F. Claro and Z. Barticevic, Phys. Rev. B **38**, 361 (1988); A. Kunold and M. Torres, *ibid.* **61**, 9879 (2000).

[3] H. Silberbauer and U. Rössler, Phys. Rev. B **50**, 11911 (1994); R. Neudert, P. Rotter, U. Rössler, and M. Suhrke, *ibid.* **55**, 2242 (1997).

[4] D. Weiss, M. L. Roukes, A. Menschig, P. Grambow, K. von Klitzing, and G. Weimann, Phys. Rev. Lett. **66**, 2790 (1991).

[5] D. Weiss, K. Richter, A. Menschig, R. Bergmann, H. Schweizer, K. von Klitzing, and G. Weimann, Phys. Rev. Lett. **70**, 4118 (1993); R. Schuster, K. Ensslin, J. P. Kotthaus, G. Böhm, and W. Klein, Phys. Rev. B **55**, 2237 (1997).

[6] D. Bimberg, M. Grundmann, and N. N. Ledentsov, *Quantum Dot Heterostructures* (Wiley, Chichester, 2001).

[7] B. C. Lee, O. Voskoboynikov, and C. P. Lee, Physica E (Amsterdam) **24**, 87 (2004), and references therein; T. Mano and N. Koguchi, J. Cryst. Growth **278**, 108 (2005).

[8] T. Mano, T. Kuroda, S. Sanguinetti, T. Ochiai, T. Tateno, J. Kim, T. Noda, M. Kawabe, K. Sakoda, G. Kido, and N. Koguchi, Nano Lett. **5**, 425 (2005).

[9] M. Sigrist, A. Fuhrer, T. Ihn, K. Ensslin, W. Wegscheider, and M. Bichler, Physica E (Amsterdam) **21**, 708 (2004).

[10] It is worthwhile to note that when the effective-mass approach (EMA) and the envelope function approximation are used, the confining potential has well defined steplike character at interfaces separating two different media: The rectangular steps are determined by the corresponding band offsets.

[11] W. E. Arnoldi, Q. Appl. Math. **9**, 17 (1951); Y. Saad, *Numerical Methods for Large Scale Eigenvalue Problems* (Halsted Press, New York, 1992); R. B. Morgan, Math. Comput. **65**, 1213 (1996).

[12] E. Brown, Phys. Rev. **133**, A1038 (1964).

[13] Y. W. Cao and U. Banin, J. Am. Chem. Soc. **122**, 9692 (2000); A. Stroppa and M. Peressi, Phys. Rev. B **71**, 205303 (2005).

[14] I. Vurgaftman, J. R. Meyer, and L. R. Ram-Mohan, J. Appl. Phys. **89**, 5815 (2001); M. Tadić, F. M. Peeters, K. L. Janssen, M. Korkusiński, and P. Hawrylak, *ibid.* **92**, 5819 (2002); J. I. Climente, J. Planelles, and F. Rajadell, J. Phys.: Condens. Matter **17**, 1573 (2005).

[15] The main conclusions of the present calculation are completely unaffected by increasing the heterojuction band-offset.

[16] If we inject the vector potential **A** in terms of the magnetic field in Eq. (1), a linear and a quadratic term on B arise, regardless of the employed gauge.

[17] A stronger coupling between the individual QDs would enhance the sensitivity of the spectrum to the lattice symmetry.

[18] The main difference between the AD lattice spectrum and that of a QR comes from symmetry. While the symmetry group of the AD lattice is C_4 with four irreducible representations which determine the number of states (four) in a set, the QR symmetry group is C_∞ (often referred to as SO_2) with an infinite number of irreducible representations labeled by the magnetic quantum number $M = 0 \pm 1 \pm 2 \ldots$, so that no splitting can be seen in the low-lying energy spectrum.

A consistent extension of the local spin density approximation to account for quantum dot mass and dielectric mismatches

M. Pi
Departament ECM, Facultat de Física and IN² UB, Universitat de Barcelona, E-08028 Barcelona, Spain

M. Royo and J. Planelles[a)]
Departament de Ciències Experimentals, Universitat Jaume I, Box 224, E-12080 Castelló, Spain

A consistent extension of local spin density approximation (LSDA) to account for mass and dielectric mismatches in nanocrystals is presented. The extension accounting for variable effective mass is exact. Illustrative comparisons with available configuration interaction calculations show that the approach is also very reliable when it comes to account for dielectric mismatches. The modified LSDA is as fast and computationally low demanding as LSDA. Therefore, it is a tool suitable to study large particle systems in inhomogeneous media without much effort. © *2006 American Institute of Physics*. [DOI: 10.1063/1.2356791]

I. INTRODUCTION

Quantum dot (QD) devices where the Coulomb interaction is exploited to control charge injection at the single-electron level have been achieved in recent years.[1,2] This has a huge technological interest. For example, the operation of QD memory devices basically consists of storing (programming), holding (retention), and removing (erase) charges in the QD by means of the device gate voltage.[3] The importance of the single-electron transistors relies on the extremely low power required for their operation (of the order of nanowatts). A key quantity that characterizes transport into a QD is the addition energy, i.e., the energy $E_{add}(N)$ required in order to place an extra electron into a dot that is initially occupied by $N-1$ particles. Such quantity, analogous to electron affinity in atomic physics, can be measured experimentally as a function of N. Thus, when the conductance is measured as a function of an applied gate voltage V_g, a series of conductance peaks appears. Each peak corresponds to an additional electron in the dot, and the spacings between the conductance peaks ΔV_g are proportional to the change in the chemical potential of the dot as an additional electron enters. This conductance peak spacing is mainly determined by the charging energy and it is known as Coulomb blockade.[4] The possibility to measure addition spectra of quantum dots by single-electron capacitance[5] or transport spectroscopy[6] stimulated many ground-state calculations. The most rigorous, and computationally very demanding, exact diagonalization can only be applied to few-electron systems. Larger systems require less-demanding methods, such as the density functional theory (DFT). The practical limitations of this method comes from the not exactly known exchange-correlation potential, but general experience is that DFT results are quite reliable[7] and they have contributed substantially to an understanding of quantum dot addition spectra.[8,9]

As pointed out above, single-electron transistors require extremely low power for their operation. This opens the way to their possible integration in bioenvironments. The integration in these environments is generally incompatible with the large power dissipation of current microelectronic transistors, which are orders of magnitude larger. Colloidal chemistry techniques allow QDs to be synthesized in the form of semiconductor spherical nanocrystals, with very low defect densities and size dispersion. These QDs can also be fabricated as multishell structures,[10] i.e., built of concentric layers (shells) of different semiconductors with the shell thickness down to a single monolayer. The size of the nanocrystals and the composition of layers can be easily manipulated in the process of fabrication, which makes it possible to tailor to a large extent their discrete energy spectra.[11] These QDs can be embedded in various kinds of matrices, such as glasses[12] or organic and biological materials[13] being very promising for applications, in particular, for the integration of nanoelectronic devices in biological environments.[14] It has been also shown that these QDs embedded in low-dielectric-constant matrices can be built into single-electron transistors[1,14] and that capacitance or tunneling spectroscopies can be used to obtain their addition spectra.[15–17] A specific characteristic of organic environments is their huge dielectric mismatch with typical inorganic semiconductor QD structures. When QDs are embedded in such materials, the formation of polarization charges at the interface may strongly influence confinement and charging energies and modify the distribution of charge carriers inside the QD. Therefore, the effects of the large mass and dielectric mismatches cannot be overlooked in the interpretation of single-electron charging phenomena in these dots. These effects have been incorporated for spherical few-electron QDs by employing diagonalization procedures within a Hubbard-like approximation, whereby only the semidiagonal elements of the Hamiltonian matrix are retained.[18,19] Some attempts to incorporate these effects in the local density approximation (LDA), which allows to deal with large systems, have also been reported.[20,21] In the present paper we extend, in a consistent way, the successful local spin density approximation (LSDA) to account for quantum dot mass and dielectric mismatches. The paper is

---
[a)]Electronic mail: josep.planelles@exp.uji.es

organized as follows: the next section presents the formulation of the method. Next, illustrative comparisons with more sophisticated calculations available are carried out, and some concluding remarks end the paper.

II. THEORY

A. Outline of density functional theory

Density functional theory[22,23] (DFT) in the self-consistent formulation of Kohn and Sham[24] has proven to be a particularly powerful tool to study large electron systems in the presence of correlation. According to Hohenberg and Kohn[25] and its generalization by Levy,[26] the exact ground-state energy of a many-body system is a unique functional of the electron density $n(\mathbf{r})$. Although DFT was initially developed in a spin-independent formalism, effects of spin polarization were later incorporated in the so-called spin density functional theory (SDFT).[27] In this approach the total energy is a functional of the spin-up and spin-down densities $n_\sigma(\mathbf{r})$, where $\sigma=(+,-)$ labels the spin. Equivalently, the energy is a functional of the total density $n(\mathbf{r})=n_+(\mathbf{r})+n_-(\mathbf{r})$ and spin polarization $\zeta(\mathbf{r})=[n_+(\mathbf{r})-n_-(\mathbf{r})]/n(\mathbf{r})$. The ground state is found by minimizing the energy functional, leading to the well known Kohn-Sham equations,

$$\left[-\frac{\hbar^2}{2m}\nabla^2 + V_{\mathrm{KS},\sigma}(n,\zeta)\right]\Phi_{i\sigma}(\mathbf{r}) = E_{i\sigma}\Phi_{i\sigma}(\mathbf{r}), \qquad (1)$$

with

$$V_{\mathrm{KS},\sigma}(n,\zeta) = V_{\mathrm{conf}}(\mathbf{r}) + \int d\mathbf{r}' \frac{n(\mathbf{r}')}{|\mathbf{r}-\mathbf{r}'|} + \frac{\delta E_{\mathrm{xc}}(n,\zeta)}{\delta n_\sigma(\mathbf{r})}, \qquad (2)$$

the last term being the exchange-correlation contribution.[28]

For a finite system with nonuniform density $n(\mathbf{r})$, the assumption that, locally, the exchange-correlation energy can be obtained by applying uniform-electron-gas results $e_{\mathrm{xc}}[n(\mathbf{r}),\zeta(\mathbf{r})]$ to infinitesimal portions of the nonuniform electron distribution is commonly made:

$$E_{\mathrm{xc}}(n,\zeta) = \int d\mathbf{r} n(\mathbf{r}) e_{\mathrm{xc}}[n(\mathbf{r}),\zeta(\mathbf{r})]. \qquad (3)$$

The functional $E_{\mathrm{xc}}(n,\zeta)$ can in turn be divided into exchange and correlation contributions,

$$E_{\mathrm{xc}}(n,\zeta) = E_x(n,\zeta) + E_c(n,\zeta). \qquad (4)$$

In the local approximation, the exchange part is given by the Dirac exchange energy functional, corresponding to a homogeneous electron gas,

$$E_x(n,\zeta) = \frac{C_x}{2}\int d\mathbf{r} n(\mathbf{r})^{4/3}\{[1+\zeta(\mathbf{r})]^{4/3} + [1-\zeta(\mathbf{r})]^{4/3}\}, \qquad (5)$$

where $C_x = \frac{3}{4}(3/\pi)^{1/3}$. It can be rewritten as

$$E_x(n,\zeta) = \int d\mathbf{r} n(\mathbf{r})\epsilon_x(n,\zeta). \qquad (6)$$

All approximations introduced so far should be compensated by a proper selection of the correlation term $E_c(n,\zeta)$. In the local approximation,

$$E_c(n,\zeta) = \int d\mathbf{r} n(\mathbf{r})\epsilon_c(n,\zeta). \qquad (7)$$

There are different parametrizations for this term. In our calculations we have selected the commonly employed Perdew and Zunger functional,[29] which is expressed in terms of the (adimensional) spin polarization ζ and the Wigner-Seitz parameter r_s, r_s being the radius of an effective sphere including a single electron, $1/n = 4\pi r_s^3/3$.

B. Variable mass

In multishell QDs and also in homogeneous QDs embedded in a weak confining medium (allowing the electronic density to penetrate in the surroundings), the electron experiences different masses in different materials. We may say, alternatively, that the effective electron mass $m^*(\mathbf{r})$ has a multisteplike profile.

For a position-dependent mass, the appropriate Hermitian kinetic energy operator is given by[30]

$$\hat{T} = -\frac{\hbar^2}{2}\nabla\left[\frac{1}{m(\mathbf{r})}\nabla\right]. \qquad (8)$$

The corresponding functional in the Kohn-Sham formulation should then be

$$\hat{T}_s[n] = \sum_i^{\mathrm{occ}} \int d\mathbf{r}\psi_i(\mathbf{r})^*\nabla\left[-\frac{\hbar^2}{2m(\mathbf{r})}\nabla\psi_i(\mathbf{r})\right]. \qquad (9)$$

For bounded systems, i.e., for systems with zero electronic density at the boundaries, it may be rewritten as

$$\hat{T}_s[n] = \sum_i^{\mathrm{occ}} \int d\mathbf{r}\frac{\hbar^2}{2m(\mathbf{r})}|\nabla\psi_i(\mathbf{r})|^2. \qquad (10)$$

It is worth remembering that the effective mass model, used to describe the electronic structure of QDs, integrates the microscopic details of the QD building block material lattice. Therefore, one cannot go into details of this unit cell with the model. This means, in particular, that the abrupt change of mass occurring when going from the QD to the surrounding matrix, or from shell to shell in a multishell QD, should be understood in a *weak* sense (an abrupt mismatch at the mathematical surface separating two materials may be a too severe imposition). Indeed, it is known that a dielectric mismatch so severe leads to a divergence in the single-particle self-polarization potential. This divergence produces a pathology in the Schrödinger equation not allowing it to be integrable.[31] In order to bypass this drawback, the abrupt mismatch is replaced by a continuous variation of the dielectric constant within a thin layer at the interface with a thickness down to a lattice constant.[31–33] In this paper we assume this kind of smooth mismatch for all physical variables involved, namely, effective mass, dielectric constant, and confining potential (this last given by the band offset of the adjacent materials).

As the effective mass does not come into Coulomb and exchange functionals, we do not consider these functionals for now. However, the correlation functional depends on the (dimensional) Wigner-Seitz radius r_s and some scalings should be introduced, as we show next.

Correlation is an analytical functional $\epsilon_c(r_s, \zeta)$ written in atomic units, i.e., ϵ_c (hartree) and $r_s(\mathbf{r})$ (Bohr radius a_0), ζ being adimensional. A free mass m_0 is implicit for electrons. We may use, though, this very same functional for electrons with masses other than m_0 if we employ effective atomic units throughout. In such a case, the functional, as it is, will yield correlation energy in effective hartree if we inject r_s in effective Bohr radii. In order to get back true atomic units, we should multiply ϵ_c by m^*/ε^2, where $m^* = m/m_0$ is the effective mass of the electron and ε is the dielectric constant.[34]

This simple reasoning gives us the key to deal with variable mass systems: we should use true atomic units throughout, just making sure, at each $\mathbf{r}$, that both ϵ_c and its argument r_s are properly scaled by $m^*(\mathbf{r})/\varepsilon(\mathbf{r})^2$ and $m^*(\mathbf{r})/\varepsilon(\mathbf{r})$, respectively.

C. Variable dielectric constant

Dielectric constant comes into Coulomb, exchange, and correlation functionals. The classical Coulomb term in vacuum,

$$\Phi(\mathbf{r}) = \int d\mathbf{r}' \frac{n(\mathbf{r}')}{|\mathbf{r} - \mathbf{r}'|}, \tag{11}$$

should be replaced by the one coming from the integrations of the Poisson equation,

$$\nabla[\varepsilon(\mathbf{r}) \nabla \Phi(\mathbf{r})] = -4\pi n(\mathbf{r}). \tag{12}$$

More involved is the exchange, as it is nonclassical. It can be obtained, in a homogeneous medium, in terms of the spin density matrices $n_\sigma(\mathbf{r}_1, \mathbf{r}_2)$ as[22]

$$E_x(n_+, n_-) = \frac{1}{2} \int \int d\mathbf{r}_1 d\mathbf{r}_2 \frac{1}{r_{12}} [|n_+(\mathbf{r}_1, \mathbf{r}_2)|^2 + |n_-(\mathbf{r}_1, \mathbf{r}_2)|^2]. \tag{13}$$

If the dielectric constant of the homogeneous medium ε is not unity as in a vacuum, we should replace r_{12} with εr_{12} in the above equation. Next, by assuming homogeneous electron gas, which allows us to write the density matrix in terms of plane waves, we may end up with Eq. (5) (it should be divided by ε if this constant is not unity).

The question arises in case ε changes from a point to another. In a first attempt one may just replace $\epsilon_x(n, \zeta)$ with $\epsilon_x(n, \zeta)/\varepsilon(\mathbf{r})$ in Eq. (6). However, it is not consistent with the Coulomb functional, since Eq. (12) is not equivalent to $\varepsilon(\mathbf{r})\nabla^2\Phi(\mathbf{r}) = -4\pi n(\mathbf{r})$. However, we may define the scaling parameter

$$\kappa = \frac{\int d\mathbf{r}[n(\mathbf{r})/\varepsilon(\mathbf{r})] \int d\mathbf{r}'[n(\mathbf{r}')/|\mathbf{r} - \mathbf{r}'|]}{\int d\mathbf{r}\Phi(\mathbf{r})n(\mathbf{r})} \tag{14}$$

and an effective local dielectric constant $\bar{\varepsilon}(\mathbf{r}) = \kappa \varepsilon(\mathbf{r})$ that allows to write the next identity,

$$\int d\mathbf{r}\Phi(\mathbf{r})n(\mathbf{r}) = \int \int d\mathbf{r}d\mathbf{r}' \frac{n(\mathbf{r})n(\mathbf{r}')}{\bar{\varepsilon}(\mathbf{r})|\mathbf{r} - \mathbf{r}'|}. \tag{15}$$

Therefore, scaling $\epsilon_x(n, \zeta)$ by $[\kappa \varepsilon(\mathbf{r})]^{-1}$ is globally consistent with the employed Coulomb functional. For the same reasons, we will replace $\varepsilon(\mathbf{r})$ by $[\kappa \varepsilon(\mathbf{r})]$ in the scaling factors coming into the correlation functional ϵ_c.

The present extension of LSDA is, on one hand, local in the sense that the electronic density feels locally the physical properties of the medium, but, on the other hand, it is consistent with a rigorous calculation of Coulomb energy in an inhomogeneous medium.

III. ILLUSTRATIVE CALCULATIONS

As discussed in the previous section, if the permittivity is a constant, we may account for variable mass without introducing any approximation on top of LSDA (as far as the system is bounded, which will always be the case). Therefore, we devote this section to check the robustness of the proposed approach dealing with a variable permittivity. To this end, we have written a code for spherical quantum dots and calculated the very sensitive addition energies of electrons and holes in InAs and CdSe nanocrystals embedded in media with different dielectric constants. Our benchmark to compare with is a set of full configuration interaction (FCI) calculations carried out by Orlandi *et al.*[18] The calculations employ an orbital basis set including 1s, 1p, 1d, and 2s orbitals[35] and are exact up to seven particles. Larger QD populations up to 20 particles are calculated within a Hubbard-like approximation, i.e., only semidiagonal elements of the Hamiltonian are retained.

The present implementation of our approach for spherical multishell QDs uses a multistep function for the dielectric constant, for the confining potential, and for the effective mass, where, as discussed above, the abrupt mismatches are replaced by continuous variations within an extremely thin layer at the interface with a thickness down to a lattice constant. Mathematically, we do it by adding a set of Fermi functions as follows:

$$X(r) = \sum_{l=1}^{n \text{ shell}} X(l)\left(1 - \frac{1}{1 + \exp\{[r - R_i(l)]/a\}}\right) \times \left(\frac{1}{1 + \exp\{[r - R_f(l)]/a\}}\right), \tag{16}$$

where $X(r)$ is either the multistep dielectric constant $\varepsilon(r)$, the confining potential $V_{\text{conf}}(r)$, or the effective mass $m^*(r)$, R_i and R_f are the initial and final shell radii, and a the corresponding interface thickness.
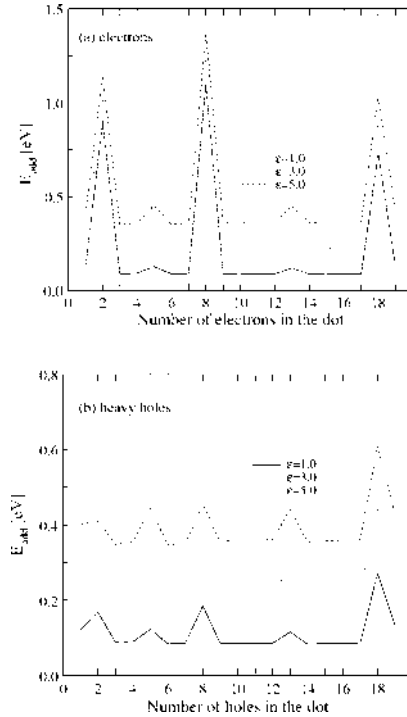
FIG. 1. Calculated addition energies (a) for electrons and (b) for heavy holes as a function of the number N of particles in the dot (addition spectrum). Results are shown for a CdSe QD. Each curve corresponds to a different value of $\varepsilon = \varepsilon_{QD}/\varepsilon_{ex}$.

FIG. 2. Calculated addition energies (a) for electrons and (b) for heavy holes as a function of the number N of particles in the dot (addition spectrum). Results are shown for an InAs QD. Each curve corresponds to a different value of $\varepsilon = \varepsilon_{QD}/\varepsilon_{ex}$.

Kohn-Sham [Eq. (1)] and Poisson [Eq. (12)] equations have been solved numerically using the finite-difference method on the one-dimensional grid in spherical coordinates. The discretization scheme on a grid, extended far beyond the QD radius, yields either eigenvalue problems (Kohn-Sham) or linear systems of equations (Poisson) of asymmetric huge and sparse matrices that have been solved by standard matrix methods. The scaling parameter κ is self-consistently calculated. The iterative process ends when complete self-consistency is achieved.

The geometries and parameters employed in our calculations are those of Ref. 18, namely, a 2 nm radius CdSe QD ($m_e^* = 0.11$ for electrons, $m_h^* = 1$ for holes, and $\varepsilon_{QD} = 10$) and a 3.2 nm InAs QD ($m_e^* = 0.023$ for electrons, $m_h^* = 0.41$ for holes, and $\varepsilon_{QD} = 10.9$); both QDs are subjected to an infinite confinement and embedded in three different dielectric media defined by $\varepsilon = \varepsilon_{QD}/\varepsilon_{ex} = 1, 3, 5$.

The results for addition energies of electrons in CdSe/InAs QDs are represented in Figs. 1(a) and 2(a) and should be compared with Figs. 1(a) and 2(a) of Ref. 18. As we can see, both qualitative and quantitative agreements are extremely good. The same agreement is achieved for addi-

tion energies of holes in InAs QD, Fig. 2(b), which should be compared with its partner in Ref. 18. Finally, addition energies of holes in CdSe QD are represented in Fig. 1(b) (to be compared with its partner in Ref. 18). The agreement is perfect if we allow the configurations that can be inferred from Ref. 18 [see Fig. 1(b)] to converge. However, a full research of the absolute energy minimum leads us to find out, just in this case of holes in CdSe, a few reconstructions. All of them

TABLE I. Disagreements between CI and LSDA: Holes in CdSe QD. The dominant CI configuration, the most stable LSDA configuration, and the relative energy spacing between these two configurations at LSDA level are shown.

CI configuration	LSDA configuration	ΔE	(%)
$\varepsilon = 3$			
$1s^2 1p^2$	$1s 1p^3$	1.0	
$\varepsilon = 5$			
$1s^2 1p^2$	$1s 1p^3$	1.7	
$1s^2 1p^6 1d$	$1s 1p^3 1d^5$	0.2	
$1s^2 1p^6 1d^2$	$1s 1p^3 1d^5$	0.1	
$1s^2 1p^6 1d^3$	$1s 1p^4 1d^5$	0.01	
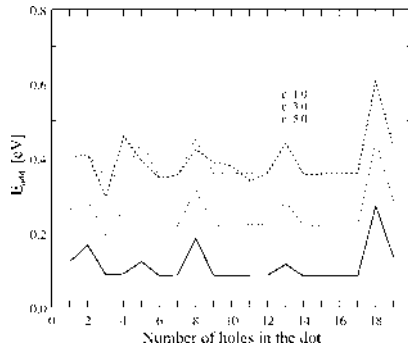
FIG. 3. Comparison of addition spectra for heavy holes in CdSe QD as a function of the number N of particles in the dot, computed using LSDA absolute energy minimum configurations (thick lines) and dominant CI configurations (thin lines). Each curve corresponds to a different value of ε $=\varepsilon_{QD}/\varepsilon_{ex}$. For $\varepsilon=1$ both configurations come to be identical.

are summarized in Table I, and the comparison of addition energies corresponding to both hole sequential fillings can be seen in Fig. 3. As we can see, the agreement with Ref. 18 is absolute also for holes in CdSe and $\varepsilon=1$. For $\varepsilon=3$ we find out a single reconstruction, the fourth hole comes into a $1s1p^3$ configuration instead of a $1s^21p^2$. Our calculations show that the $1s1p^3$ configuration is (just) 20 meV more stable than $1s^21p^2$ (less than 1% of the total energy). It is worth stressing that holes in CdSe have an effective mass $m_h^*=1$. Therefore, the kinetic energy is small and the orbital levels turn out to be quite close, so that correlation plays a crucial role. On the other hand it is known that in high correlation regime LSDA shows a tendency to stabilize high spin. Then, it is difficult to assign this small disagreement with exact FCI results either to the own LSDA or to the scaling approximation employed. Finally, for $\varepsilon=5$ we find four reconstructions. Again, as can be seen in Table I the energetic differences between configurations are small.

In summary, a consistent extension of LSDA to account for mass and dielectric mismatches is presented in this paper. We prove that the extension to account for variable effective mass is exact. Some illustrative comparisons with more sophisticated CI calculations available show that our approach is also very reliable accounting for dielectric mismatches. Finally, it is worth stressing that the proposed extension of LSDA is extremely fast and computationally very low demanding (just as much as LSDA) in comparison with sophisticated CI calculations, so that one may deal with large many-particle system in inhomogeneous media without much effort.

ACKNOWLEDGMENTS

[1]R. C. Ashoori, Nature (London) **379**, 413 (1996).

[2]L. Jacak, P. Hawrylak, and A. Wójs, *Quantum Dots* (Springer, Berlin, 1998).

[3]B. De Salvo, G. Ghibaudo, G. Pananakakis, P. Masson, T. Baron, N. Buffet, A. Fernandes, and B. Guillaumot, IEEE Trans. Electron Devices **48**, 1789 (2001).

[4]D. V. Averin and K. K. Likhraev, in *Mesoscopic Phenomena in Solids*, edited by B. L. Altshuler, P. A. Lee, and R. A. Webb (North-Holland, Amsterdam, 1991).

[5]R. C. Ashoori, H. L. Störmer, J. S. Weiner, L. N. Pfeiffer, S. J. Pearton, K. W. Baldwin, and K. W. West, Phys. Rev. Lett. **68**, 3088 (1992); R. C. Ashoori, H. L. Störmer, J. S. Weiner, L. N. Pfeiffer, K. W. Baldwin, and K. W. West, *ibid.* **71**, 613 (1993).

[6]S. Tarucha, D. G. Austing, T. Honda, R. J. van der Hage, and L. P. Kouwenhoven, Phys. Rev. Lett. **77**, 3613 (1996).

[7]J. Kainz, S. A. Mikhailov, A. Wensauer, and U. Rössler, Phys. Rev. B **65**, 115305 (2002).

[8]S. M. Reimann and M. Manninen, Rev. Mod. Phys. **74**, 1283 (2002).

[9]M. Pi, D. G. Austing, R. Mayol, K. Muraki, S. Sasaki, H. Tamura, and S. Tarucha, in *Trends in Quantum Dots Research*, edited by P. A. Ling (Nova Science, New York, 2005); D. G. Austing *et al.*, in *Nano-Physics and Bio-Electronics: A New Odyssey*, edited by T. Chakraborty, F. Peeters, and U. Sivan (Elsevier, New York, 2002).

[10]H. Ow, D. R. Larson, M. Srivastava, B. A. Baird, W. W. Webb, and U. Wiesner, Nano Lett. **5**, 113 (2005); M. Darbandi, R. Thomann, and T. Nann, Chem. Mater. **17**, 5720 (2005); A. Mews, A. V. Kadavanich, U. Banin, and A. P. Alivisatos, Phys. Rev. B **53**, R13242 (1996); D. Schooss, A. Mews, A. Eychmüller, and H. Weller, *ibid.* **49**, 17072 (1994); A. Mews, A. Eychmüller, M. Giersig, D. Schooss, and H. Weller, J. Phys. Chem. **98**, 934 (1994).

[11]G. W. Bryant and W. Jaskólski, Phys. Status Solidi B **224**, 751 (2001); J. Planelles, J. G. Díaz, and J. Climente, Phys. Rev. B **65**, 245302 (2002); J. Planelles, J. Climente, J. Díaz, and W. Jaskólski, J. Phys.: Condens. Matter **14**, 12537 (2002); J. Climente, J. Planelles, J. Díaz, W. Jaskólski, and I. Aliaga, *ibid.* **15**, 3593 (2003).

[12]U. Woggon, *Optical Properties of Semiconductor Quantum Dots* (Springer, Berlin, 1996).

[13]See, e.g., M. Bruchez Jr., M. Moronne, P. Gin, S. Weiss, and A. P. Alivisatos, Science **281**, 2013 (1998); W. C. W. Chan and S. Nie, *ibid.* **281**, 2016 (1998).

[14]A. P. Alivisatos, Science **271**, 933 (1996); MRS Bull. **23**, 18 (1998).

[15]U. Banin, Y. W. Cao, D. Katz, and O. Millo, Nature (London) **400**, 542 (1999).

[16]B. Alperson, I. Rubinstein, and G. Hodes, Appl. Phys. Lett. **75**, 1751 (1999).

[17]D. L. Klein, R. Roth, A. K. L. Lim, A. P. Alivisatos, and P. L. Mceuen, Nature (London) **389**, 699 (1997).

[18]A. Orlandi, M. Rontani, G. Goldoni, F. Manghi, and E. Molinari, Phys. Rev. B **63**, 045310 (2001).

[19]A. Orlandi, G. Goldoni, F. Manghi, and E. Molinari, Semicond. Sci. Technol. **17**, 1302 (2002).

[20]J. Sée, P. Dollfus, and S. Galdin, J. Appl. Phys. **92**, 3141 (2002).

[21]M. Şahin and M. Tomak, Phys. Rev. B **72**, 125323 (2005); Physica E (Amsterdam) **28**, 247 (2005).

[22]R. G. Parr and W. Yang, *Density-Functional Theory of Atoms and Molecules* (Oxford University Press, Oxford, 1989).

[23]E. Lipparini, *Modern Many-Particle Physics* (World Scientific, Hackensack, NJ, 2003).

[24]W. Hohenberg and L. J. Sham, Phys. Rev. **140**, A1133 (1965).

[25]P. Hohenberg and W. Khon, Phys. Rev. **136**, B864 (1964).

[26]M. Levy, Proc. Natl. Acad. Sci. U.S.A. **76**, 6062 (1979).

[27]U. von Barth and L. Hedin, J. Phys. C **5**, 1629 (1972).

[28]It should be emphasized that the Kohn-Sham equation [Eq. (1)] should be solved in a geometrically unrestricted scheme, i. e., the symmetry of the solution should not be constrained by the symmetry of the confinement. In such a case, symmetry broken ground states may be found for large values of the Wigner-Seitz parameter r_s (strong correlation regime). However, in general, a symmetry restricted DFT scheme gives reliable approximations to the exact ground-state energies and densities.

[29]J. P. Perdew and A. Zunger, Phys. Rev. B **23**, 5048 (1981).

[30]D. BenDaniel and C. B. Duke, Phys. Rev. **152**, 683 (1966).

[31]L. Bányai and S. W. Koch, *Semiconductor Quantum Dots* (Word Scientific, Singapore, 1993).

[32]F. Stern, Phys. Rev. B **17**, 5009 (1978).
[33]P. G. Bolcatto and C. R. Proetto, J. Phys.: Condens. Matter **13**, 319 (2001).
[34]Actually, one does not inject r_s into ϵ_c, but $n(\mathbf{r})$. In such a case, we should inject it in effective units, i.e., by scaling $n(\mathbf{r})$ (a.u.) by a factor $(\varepsilon/m^*)^3$.

[35]Using our approach we have seen that this basis set is appropriate for electrons in the two QDs studied. In the case of holes this basis set is large enough up to 18 holes. The 19th and 20th holes come then to fill $1f$ instead of $2s$. However, in order to carry out proper comparison, we have used the same basis set as in Ref. 18.

Effective mass and dielectric constant mismatch effects in spherical multishell quantum dots

M. Royo and J. Planelles
Departament de Ciències Experimentals, Universitat Jaume I, Box 224, E-12080 Castelló, Spain

M. Pi
Departament ECM, Facultat de Física and IN^2 UB, Universitat de Barcelona, E-08028 Barcelona, Spain
(Received 21 September 2006; published 9 January 2007)

The role of effective mass and dielectric mismatches on chemical potentials and addition energies of many-electron multishell quantum dots (QDs) is explored within the framework of a recent extension of the spin density functional theory. It is shown that although the gross electronic density is located in the wells of these multishell QDs, taking position-dependent effective mass and dielectric constant into account can lead to the appearance of relevant differences in chemical potential and addition energies as compared to standard calculations in which the effective mass and the dielectric constant of the well is assumed for the whole multishell structure.

PACS number(s): 73.21.La, 71.15.Mb

Over a decade ago, Eychmüller and coworkers[1,2] opened the door to the nano-heterostructures called quantum dot quantum wells (QDQW). These primal spherical multishell nanostructures were composed of a CdS central core surrounded by an HgS shell, a little thicker than a monolayer, capped with additional CdS. The synthesis route was based on the chemical control of the composition of the shells as the structure was grown layer by layer, so that the thickness of the core, well, and clad can be varied during the course of the synthesis. The basic physics of QDQWs derives from the band gap differences between neighboring materials leading to a radial confinement profile for carriers both in the conduction and in valence bands. Thus, in a CdS QD with an HgS quantum well inside, the electronic density, coming from either optical excitations or electronic levels charging, is localized in the HgS well.[3] The relatively easy control of the size and composition of these structures and, therefore, the possibility of modifying the charge density localization, grants a high degree of flexibility for tailoring the discrete energy spectra of these systems.[4] More recently, Al-Sayed and coworkers,[5] by means of alternative precipitation of HgS and CdS on a CdS central core, successfully obtained spherical nanoparticles containing two HgS quantum wells separated by a double CdS barrier. This work, together with other multishell synthesis reported in recent years,[6,7] prompt multishell nanostructures as firm candidates to become versatile components of electronic devices.

Theoretical studies on spherical multishell systems at the monoelectronic or excitonic level employing atomistic tight-binding models[8] or macroscopic-like methods, such as the one-band effective mass approach[9,10] and the more accurate multiband approaches,[11] have been reported. The influence of a magnetic field on the electron and hole energy spectra of multishell QDs has also been been reported.[12] Nevertheless, not many works on charging electrons in spherical multishell quantum dots have been carried out. We mention the work by Banin *et al.*,[13,14] who studied an electronically charged core/shell InAs/ZnSe spherical nanocrystal spectroscopically. Some of the features observed in this heterostructure were theoretically reproduced by Dai *et al.*[15] using unrestricted Hartree-Fock-Roothaan calculations, including up to nine electrons.

In a recent paper,[16] we developed a method, within the framework of the spin density functional theory (SDFT), capable of studying many-electron spherical QDs including effective mass and dielectric mismatches. In a multishell QD, an electron feels different effective masses and dielectric constants in the different layers. In systems composed of CdS and HgS, the electronic density is mainly concentrated in the HgS wells. This fact might lead one to think that it is safe to employ the effective mass and dielectric constant of the HgS for the whole multishell QD. In the present work we will show that a correct description of such systems requires consideration of a proper variable, i.e. position-dependent, effective mass, and dielectric constant. SDFT results, which employ the effective mass and dielectric constant of the well for the whole QD (hereafter referred to as *unpolarized* calculation) and those with position-dependent parameters (*polarized* calculation), show differences in chemical potential. This leads to differences in the number of electrons coming into the HgS well and also differences in addition energies, in some cases reflecting distinct ground state electronic configurations in either the polarized or the unpolarized case. Differences increase with the number of layers of the multishell QD.

A fully detailed description of the method employed can be found in Ref. 16. In short, it is an extension of the SDFT,[18] which includes (i) position-dependent effective mass by replacing the standard kinetic energy operator $-\frac{\hbar^2}{2m^*}\nabla^2$ by $-\frac{\hbar^2}{2}\nabla\left(\frac{1}{m^*}\nabla\right)$, corresponding to the case of variable effective mass, (ii) polarization of the Coulomb interaction arising from the dielectric mismatch, by numerically integrating the Poisson equation $\nabla[\varepsilon(r)\nabla\Psi(r)]=-4\pi n(r)$; (iii) Self-energy, also coming from the dielectric mismatch, by incorporating the mono-electronic self-polarization potential according to the equations reported in Ref. 19. This dielectric confinement and the spatial confinement potentials are the genuine single-particle components of the Konh-Sham potential; (iv) the effect of dielectric mismatch on exchange by means an appropriate scaling of the exchange functional, which is consistent with the Coulomb functional employed; and finally, (v) the correlation functional is also modified to incorporate the position-dependent parameters properly by

means of a consistent scaling of the Perdew-Zunger analytical functional employed.[20]

The material parameters employed in our calculations, namely electron effective masses m^*_{HgS}=0.04, m^*_{CdS}=0.15, $m^*_{H_2O}$=1, dielectric constants ε_{HgS}=11.4, ε_{CdS}=5.5, ε_{H_2O}=1.78, and band offsets $V_{HgS/CdS}$=1.35 eV, V_{HgS/H_2O}=4.15 eV, and V_{CdS/H_2O}=2.8 eV are taken from Refs. 10 and 17. The bottom of the HgS conduction band is assumed to be the origin of energies. We have carried out calculations from one up to 25 electrons, the orbital basis set employed including orbitals $1s$, $1p$, $1d$, $1f$, $2s$, and $2p$.

Figure 1(a) shows the calculated chemical potential[21] vs the number of electrons of one of the multishell QDs synthesized by Al-Sayed *et al.*[5] The heterostructure is represented in the inset. It is built of an internal CdS core of radius 3.2 nm, a middle well-acting HgS shell with a thickness of 0.8 nm and an external 0.4 nm thick CdS clad. The QD is surrounded by water.

Chemical potentials obtained from the polarized calculations, either including self-energy or not, indicate that up to two electrons can come into the HgS well, while unpolarized calculations already yield a chemical potential for the single-electron QD exceeding the HgS/CdS confining potential. The two horizontal lines in Fig. 1 at 1.35 and 4.15 eV represent the confining barrier height of the HgS well and the QD, respectively. Therefore, Fig 1(a) indicates that while the polarized calculations predict that the QD can accept up to a maximum of 16 electrons, the limit of electrons that can come into the QD yielded by the unpolarized calculations exceeds 25. Concerning addition energies [see Fig. 1(f)], no qualitative differences can be seen between the two approaches employed. The profiles obtained indicate the fulfillment of the Afbau and Hund rules, the same spin and electronic configurations being achieved by all approaches. As a consequence, no appreciable quantitative differences are found when the single-particle self-energy is included, as it almost cancels completely out. Only quantitative differences between polarized and unpolarized calculations can be seen that reveal the extra polarization work.

Since, as pointed out above, it is relatively easy to control the layer thickness in a multishell QD experimentally, we then calculate several multishell structures, including one or more HgS wells separated by CdS barriers of different widths in order to illustrate the relevance of including position-dependent effective mass and dielectric constant in the calculation of chemical potentials and additions energies. The notation $A/B/A/\ldots$ $x/y/z/\ldots$ that will be employed hereafter means a QD built of an x nm radius internal core of material A covered by successive $y,z,\ldots$ nm thickness shells of materials $B/A/\ldots$. In all cases the medium surrounding the QD is water.

Figure 1(b) and 1(g) correspond to CdS/HgS/CdS 3/2/1 multishell QD. The same general trends as in the previous case are found here. Namely, the same spin and electronic configuration are achieved by all approaches, all of them yielding qualitatively similar addition energies, these revealing the fulfillment of the Afbau and Hund rules, but quantitative differences related to the polarization work. Finally, relevant differences in chemical potentials between the po-

larized and unpolarized approach are found, the self-energy playing a minor role.

We deal next with double quantum wells. We first consider HgS/CdS/HgS/CdS 3.5/3/2/1 QD, whose well-acting core is separated from the second well by a barrier, the last shell also being barrier-acting [see Figs. 1(c) and 1(h)]. As above, the main differences between polarized and unpolarized approaches can be found when calculating chemical potentials. Thus, while the unpolarized calculation predicts that all 25 electrons come into the HgS wells, the polarized calculation already does not allow the 11th electron to come into the wells, as the chemical potential of this QD populated with 11 electrons exceeds the well-confining potential height. The addition energy profile reveals a peculiar change of maxima positions with respect to the other QDs that have been studied. This is the outcome of a different orbital sequential filling $1s, 2s, 1p, 1d\ldots$ (instead of $1s, 1p, 1d\ldots$) which has its origins in a relative stabilization of the $2s$ orbital that locates its radial node in the barrier region. Regarding differences between polarized and unpolarized calculations, a first qualitative difference between them appears at $E_{add}(2)$, which is not a maximum if polarization is included, this fact being related to the extra stability of the $2s$ orbital originated by polarization.

The last two structures we consider are QDs with double quantum wells having a barrier-acting core (CdS/HgS/CdS/HgS/CdS), the only difference between them being the thickness of the intermediate CdS barrier. Figure 1(d) and 1(i) show the result for $3/2/1/2/1$ while Fig. 1(e) and 1(j) correspond to $3/2/2/2/1$. Besides the discrepancies in chemical potential between polarized and unpolarized calculations, qualitatively similar to the previously outline for the other QDs studied, now differences arise in the addition energy plot. In the case of the thinner CdS barrier, Fig. 1(i), the third big maximum appears at a different number of electrons N in the unpolarized and polarized case, which is the result of a different sequential filling, $1s^2, 1p^6, 1d^{10}, 1f^6$, vs $1s^2, 1p^6, 2s^2, 1d^{10}, 1f^4$, originated by an extra stabilization of the $2s$ orbital coming from polarization. It should also be mentioned that self-energy gives rise to a few ground-state reconstructions that are reflected in small changes in the addition energy profile, even leading to a spin change ($2S_z$=6 vs 4) at N=14.

The most relevant role of both polarization and self-energy can be seen in the case of the thicker CdS barrier. Thus, Fig. 1(j) reveals that, in the region of few electrons, a quite different E_{add} vs N profile results when polarization is included, this profile undergoing a further relevant change as the self-energy is accounted for. We can mention, for example, that at N=8 electrons, the spin predicted by the unpolarized calculation is $2S_z$=0, which turns into $2S_z$=2 as polarization is included, and recovers a zero value as, additionally, self-energy is incorporated.

In short, we have shown that despite the fact that the electron density may be mainly concentrated in the wells of a multishell QD, position-dependent effective mass and dielectric constant should be employed for a proper calculation of chemical potentials and addition energies, this being specially relevant as the QD complexity, i.e. the number of shells, increases.
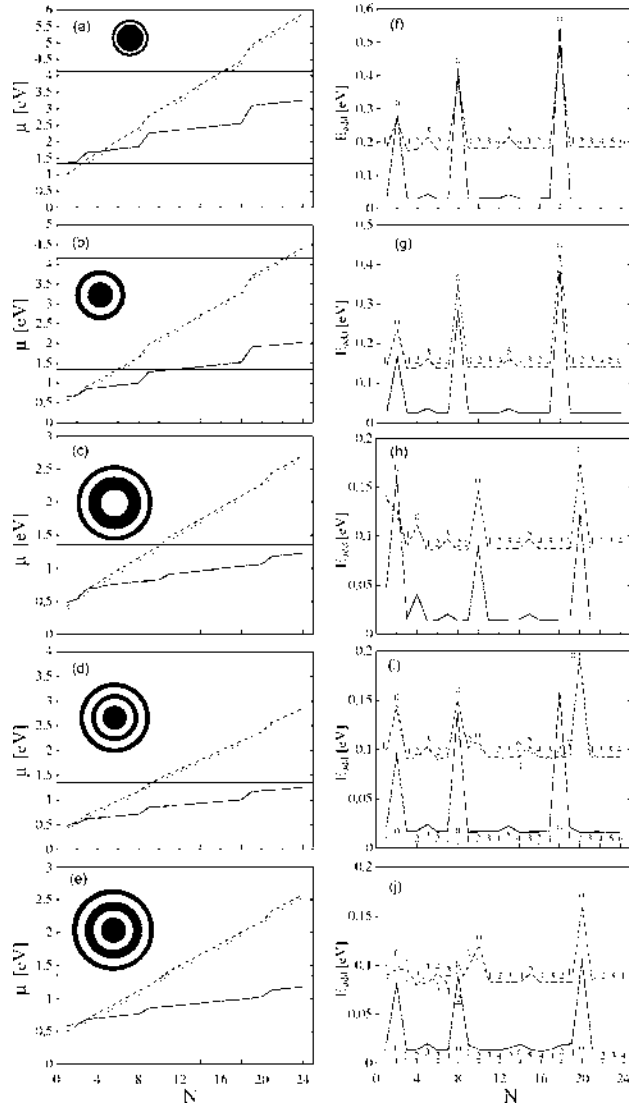
FIG. 1. Chemical potentials (left) and addition energies (right) vs the number N of electrons, corresponding to the QDs outlined in the insets (black for CdS and white for HgS). Solid line: unpolarized calculation. Dotted line: polarized calculation. Dashed line: polarized calculation including self-energy. The horizontal solid lines at 1.35 and 4.15 eV illustrate the confining barrier height for the HgS well and the QD, respectively. $2S_z$ values are indicated by numbers on the addition spectra. If the spins of the polarized calculation with and without self-energy are different, underlined numbers correspond to the calculation including self-energy.

[1] A. Eychmüller, A. Mews, and H. Weller, Chem. Phys. Lett. **208**, 59 (1993).

[2] A. Mews, A. Eychmüller, M. Giersig, D. Schooss, and H. Weller, J. Phys. Chem. **98**, 934 (1994).

[3] M. Braun, S. Link, C. Burda, and M. El-Sayed, Phys. Rev. B **66**, 205312 (2002); H. Borchet, D. Dorfs, C. Mc Gingle, S. Adam, T. Möller, H. Weller, and A. Eychmüller, J. Phys. Chem. B **107**, 7486 (2003); D. Dorfs, H. Henschel, J. Kolny, and A. Eychmüller, *ibid.* **108**, 1578 (2004); A. Mews, A. V. Kadavanich, U. Banin, and A. P. Alivisatos, Phys. Rev. B **53**(20), R13242 (1996).

[4] G. W. Bryant and W. Jaskólski, Phys. Status Solidi B **224**, 751 (2001); J. Planelles, J. Climente, J. G. Díaz, and W. Jaskólski, J. Phys.: Condens. Matter **14**, 12537 (2002); J. Climente, J. Planelles, J. G. Díaz, and I. Aliaga, *ibid.* **15**, 3539 (2003).

[5] M. Braun, C. Burda, and M. El-Sayed, J. Phys. Chem. A **105**, 5548 (2001).

[6] D. Dorfs and A. Eychmüller, Nano Lett. **1**(11), 663 (2001); R. Xie, U. Kolb, T. Basché, and A. Mews, J. Am. Chem. Soc. **127**, 7480 (2005).

[7] A. Aharoni, T. Mohari, I. Popov, and U. Banin, J. Am. Chem. Soc. **66**, 205312 (2006).

[8] J. Pérez Conde and A. K. Bhattacharjee, Phys. Status Solidi B **229**, 485 (2002); R. H. Xie, G. W. Bryant, S. Lee, and W. Jaskólski, Phys. Rev. B **65**, 235306 (2002); G. W. Bryant and W. Jaskólski, *ibid.* **67**, 205320 (2003).

[9] D. Schooss, A. Mews, A. Eychmüller, and H. Weller, Phys. Rev. B **49**, 17072 (1994); Garnett W. Bryant, *ibid.* **52**, R16997 (1995).

[10] K. Chang and J. B. Xia, Phys. Rev. B **57**, 9780 (1998).

[11] W. Jaskólski and Garnett W. Bryant, Phys. Rev. B **57**, R4237 (1998).

[12] J. Planelles, J. Díaz, J. Climente, and W. Jaskólski Phys. Rev. B **65**, 245302 (2002); J. Planelles, J. Climente, J. Díaz, and W. Jaskólski, J. Phys.: Condens. Matter **14**, 12537 (2002); J. Climente, J. Planelles, W. Jaskólski, and J. I. Aliaga, *ibid.* **15**, 3593 (2003).

[13] Y. W. Cao and U. Banin, Angew. Chem., Int. Ed. **38**, 3692 (1999).

[14] O. Millo, D. Katz, Y. W. Cao, and U. Banin, Phys. Rev. Lett. **86**, 5751 (2001).

[15] Z. Dai, J. Sun, L. Zhang, S. Huang, and J. Zhang, Physica B **324**, 373 (2002).

[16] M. Pi, M. Royo, and J. Planelles, J. Appl. Phys. **100**, 073712 (2006).

[17] A. D. Yoffe, Adv. Phys. **50**, 1 (2001).

[18] U. Von Barth and L. Hedin, J. Phys. C **5**, 1629 (1972).

[19] J. L. Movilla and J. Planelles, Comput. Phys. Commun. **170**, 144 (2005).

[20] J. P. Perdew and A. Zunger, Phys. Rev. B **23**, 5048 (1981).

[21] Chemical potentials and addition energies are calculated as the first and second energy differences, $\mu(i) = E(i+1) - E(i)$, and $E_{add}(i) = E(i+1) + E(i-1) - 2E(i)$, respectively.

Theory of dielectrically induced surface excitonic states in spherical quantum dots

F. Rajadell, J. L. Movilla, M. Royo, and J. Planelles*

Departament de Química Física i Analítica, UJI, Box 224, E-12080 Castelló, Spain

The formation of quantum dot (QD) excitonic surface states induced by dielectric mismatch is theoretically explored in spherical nanocrystals embedded in very high and in very low permittivity media. It is found that the transition from volume to surface exciton states ($V \rightarrow S$) always parallels a sudden drop of exciton brightness if the QD is embedded in low dielectric constant media. This is not the case of a QD buried in high permittivity media. In this case, the $V \rightarrow S$ transition is monitored by a reduction in exciton brightness or not depending on the m_h^*/m_e^* ratio between the effective masses of electron and hole. The presence of a hydrogenic donor impurity at the QD center can drastically reduce the electron-hole density overlap and thus the excitonic binding energy and the drop of brightness that parallels the formation of surface states.

PACS number(s): 71.35.Cc, 73.21.La, 73.22.−f, 73.20.At

I. INTRODUCTION

Most of the active key components of modern information technologies rely on semiconductor devices with electronic or optoelectronic functions. It is believed that quantum bits, which are generic quantum mechanical two-level systems, will become the basic building blocks of this technology in the next future. One possible realization of these two-level systems is an exciton ground state in a quantum dot (QD).[1] The formation of QD excitons or electron-hole *e-h* pairs and *e-h* recombination leading to photoluminescence has received a great deal of attention in the literature.[2] A very interesting feature of semiconductor QDs spectra is the shift of excitonic peaks as compared to bulk values. This originates from two usually opposite contributions. On the one hand, the single-particle band gap is shifted to higher energies due to the quantum size effect. On the other hand, the Coulomb attraction between the *e-h* pair created by photoexcitation adds a redshift correction. Both corrections are size dependent and generally result in an overall blueshift of the optical band gap as compared to the bulk.[3] Since the pioneering work by Brus,[4,5] the influence of QD surface dielectric polarization on energy and density distribution of carriers has been taken into account for a proper comparison between theory and experiments. This surface polarization is especially strong for QDs in a glass matrix, liquid solution, air, or a vacuum, where the background dielectric constant of the QD and the surrounding medium are substantially different. Two contributions to the energy originate from the dielectric mismatch, namely, single-particle contributions coming from the interaction of carriers with their own induced charges (self-polarization energy) and two-particle contributions coming from the interaction of a carrier with the charge induced by the other one (polarization of the Coulomb interaction). By assuming infinitely (or very) high confinement barriers and steplike dielectric functions, the dielectric mismatch corrections on excitonic energies in spherical QDs almost totally cancel each other out.[4,6–9] However, dielectric mismatch corrections on excitonic energies no longer cancel out if finite confining barrier heights are considered.[10] Under specific conditions, the attractive self-polarization potential well originated from the dielectric mismatch is even able to confine carriers in surface states.[11–15] Dielectrically induced exciton surface states in semiconductor QDs were predicted for the first time by Bányai *et al.*[11,17] using a model where electron and hole are confined in a QD by a common low potential height barrier and have a large effective *e-h* mass ratio $m_h^*/m_e^* = 10$, the QD being subject to a strong dielectric mismatch $\varepsilon_{QD}/\varepsilon_{out} = 10$.

In this Brief Report, we explore the possible formation of excitonic surface states in two different situations, (i) a spherical QD in air, where the hole confining barrier height is much higher than the electron one, and (ii) a QD buried in a matrix with a higher dielectric constant (in this case, as is usual, we will assume that the confinement barrier height for holes is about 1/2 that corresponding to electrons). We will show that in both cases, a dielectric mismatch-induced transition from a volume to a surface state involving an optical band gap redshift (with respect to the case of no dielectric mismatch) can be reached under specific conditions. Relevant differences between the two cases are found. Thus, in case (i), only the electron can be confined in the self-polarization potential well, beyond the QD border. However, the hole, despite its heavier mass, as it is subject to a higher confining barrier, cannot overcome the spatial confinement and remains within the QD but close to the border due to the *e-h* attraction. The transition from volume to surface states can be monitored in this case by a sudden change in the overlap between electron and hole wave functions, i.e., by a decrease in the exciton brightness. A quite different situation holds in case (ii) because the self-polarization potential well is now located on the inner side of the QD border so that no spatial confining barrier prevents localization of particles in it. In this case, we find that the transition from volume to surface states can be monitored by a reduction in the excitonic brightness or not, depending on the m_h^*/m_e^* ratio. In addition, the influence of an on-center shallow donor impurity on the binding energy and oscillator strength of the fundamental exciton is also addressed. It results in an almost total suppression of binding and brightness.

II. THEORY AND COMPUTATIONAL DETAILS

We deal with the fundamental exciton of spherical QDs. It has been reported[2,16] that this exciton basically involves the

fundamental $1S_e$ electron and $1S_{3/2}$ hole states. Then, the hole in the fundamental exciton has a strong heavy-hole character, being well described by the one-band model. The missing small contribution of the light holes in the exciton configuration interaction (CI) expansion is expected to be negligible. This simplification on the hole description leads to a computational workable approach. Also, the electron-hole spin-exchange interaction that splits the optically active exciton ground state into a few states,[2,18,19] the lowest of which is optically passive, has been neglected in the present study. Then, to account for excitonic states, we first solve the one-particle effective-mass Schrödinger equation,

$$H = -\frac{1}{2}\nabla\left[\frac{1}{m^*(\mathbf{r})}\nabla\right] + V(\mathbf{r}) + V_s(\mathbf{r}), \quad (1)$$

where the first term is the generalized kinetic energy operator, $V(\mathbf{r})$ represents the spatial confining potential, and $V_s(\mathbf{r})$ stands for the self-polarization potential. The calculation of this potential is carried out by employing a dielectric function profile that changes smoothly within a thin interface (of the order of a lattice constant) between the semiconductor QD and its surroundings.[10,20] This approach bypasses the (unphysical) self-polarization potential divergences that arise at the interface when a steplike dielectric profile is employed[17,21] and avoids the lack of size scaling of the nondivergent regularization method.[11,17]

The radial parts of the exact single-particle eigenfunctions $\phi_{n\ell m}(\mathbf{r}_{e/h})$ are determined numerically on the grid extending far beyond the dot radius R. Hartree products of the basis functions $\phi_{n\ell m}(\mathbf{r}_e)\cdot\phi_{n'\ell'm'}(\mathbf{r}_h)$ are then used to construct CI expansions $\Psi_{LM}=\Sigma_j\Phi_j$ of the symmetry-adapted *e-h* configurations, where L and M are the total and *z*-component angular quantum numbers, respectively. The *e-h* Hamiltonian containing Coulomb interaction and polarization terms[10] is then diagonalized in the CI basis set. As a result, we get two-particle wave functions $\Psi_{LM}(\mathbf{r}_e,\mathbf{r}_h)$ and energies $E(L)$. We carry out full CI employing a very large orbital basis set $\phi_{n\ell m}$ including the $n=4$ lowest-lying orbitals with $\ell=0,1,2$ and the $n=3$ lowest-lying orbitals with $\ell=3,4,5,6$. The same basis set is employed for electron and holes, this basis set being by far larger than that required to achieve the accuracy shown in the figures.

From the wave function, we can define the electron *radial density* $P(r_e)$,

$$P(r_e) = \int |\Psi(\mathbf{r}_e,\mathbf{r}_h)|^2 r_e^2 r_h^2 \sin\theta_e \sin\theta_h dr_h d\theta_e d\theta_h d\phi_e d\phi_h,$$

$$(2)$$

the hole *radial density* $P(r_h)$ in a similar way, and the *e-h* overlap $S_{e\text{-}h}^2$,

$$S_{e\text{-}h}^2 = \left|\int \Psi(\mathbf{r}_e=\mathbf{r}_h=\mathbf{r})r^2 \sin\theta dr d\theta d\phi\right|^2, \quad (3)$$

which is proportional to the oscillator strength of the electron-hole state.[16,22–24]
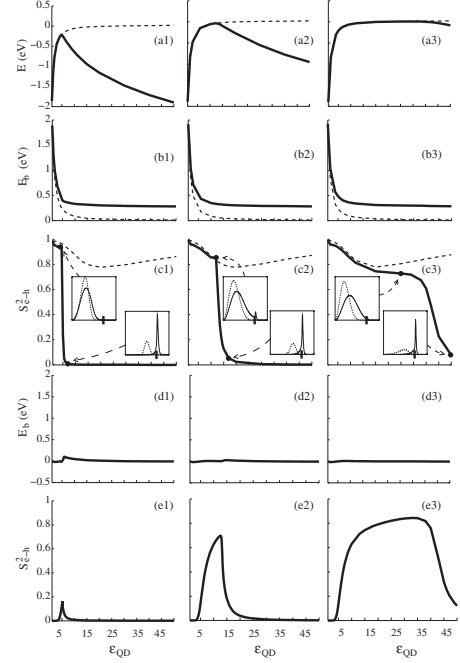
FIG. 1. Excitonic E and binding E_b energies and *e-h* overlap $S_{e\text{-}h}^2$ of a $R=5$ nm, $m_{e,QD}^*=0.5$, $m_{h,QD}^*=10$ freestanding QD with a confining barrier height V_e of 1 eV [(a1), (b1), and (c1)], 2 eV [(a2), (b2), (c2)], and 3 eV [(c1), (c2), (c3)], as a function of the QD dielectric constant ε_{QD}. Solid (dashed) lines include (exclude) dielectric polarization effects. Insets: electron (solid line) and hole (dotted line) radial density distributions [Eq. (2)] (the QD border is indicated by a tick in the horizontal axis). Panels (d1)–(d3) and (e1)–(e3) correspond to (b1)–(b3) and (c1)–(c3) when a hydrogenic donor impurity is located at the QD center.

III. RESULTS AND DISCUSSION

Case (i): QD in air or a vacuum. We first investigate the role of image charges on the excitonic properties of a freestanding QD. Our model consists of a spherical $R=5$ nm radius nanocrystal. We employ the following parameters:[25] $m_{e,QD}^*=0.5$, $m_{e,out}^*=m_{h,out}^*=1$, $m_{h,QD}^*=10$, and $\varepsilon_{out}=1$. Since we cannot promote holes into a vacuum, we will assume an infinite height for the spatial confining barrier of a hole when a QD is in air or a vacuum. As for electrons, we consider the QD electroaffinity as the barrier height V_e.

We have carried out three series of calculations of the overlap $S_{e\text{-}h}^2$ and excitonic E and binding E_b energies[26] vs ε_{QD} ranging from 1 up to 50, corresponding to $V_e=1$, 2, and 3 eV. The results are summarized in Fig. 1, together with partner calculations with $\varepsilon_{out}=\varepsilon_{QD}$, i.e., in the absence of

dielectric mismatch effects, that will help to analyze the obtained results.

Figures 1(c1)–1(c3) show sudden changes of *e-h* overlap S^2_{e-h} that parallel the transition from volume to surface exciton states, as can be seen in the corresponding insets. This transition is also reflected as a change of sign of the slope in the excitonic energy vs ε_{QD} profile [Figs. 1(a1)–1(a3)], while it is not reflected in the binding energy plots [Figs. 1(b1)–1(b3)], whose profile vs ε_{QD} is very smooth. Differences between polarized and unpolarized excitonic energies [see Figs. 1(a1)–1(a3)] basically reflect self-polarization effects, while differences between polarized and unpolarized binding energies [see Figs. 1(b1)–1(b3)] essentially show the influence of the polarization of the Coulomb interaction, as we have verified in a series of calculations (not shown). Our results are an extreme example denying the cancellation of single- and two-particle polarization contributions to the excitonic energy. Also, they lead to the conclusion that the main effect of single-particle self-polarization is the production of a redshift in the optical band gap, while the polarization of the Coulomb interaction basically enhances the exciton binding energy. Figure 1 additionally reveals that the conditions for the QD materials to yield exciton surface states when the QD is in air or a vacuum are rather severe, namely, quite low electroaffinity χ and not very light electron effective mass m^*_e. Not many semiconductors can fulfill this requirement. We may mention SiO_2 as a possible candidate (m^*_e=0.5, χ=0.9 eV, ε=4, and m^*_h=10, see Refs. 27–30).

Next, we study the same QD doped with a hydrogenic donor impurity at its center. This impurity exerts the most relevant influence for low values of the dielectric constant by binding the electron while repelling the hole, thus leading to a drop in excitonic binding energy[31] and brightness [see panels (d1)–(d3) and (e1)–(e3) in Fig. 1]. Our calculations also reveal that the heavier the electron effective mass is, the closer its density distribution bound to the impurity site is. Accordingly, an acceptor impurity attracts the heavier hole very close to the QD center and creates an effective neutral entity that leads the electron to behave as an almost independent particle in the QD.

Case (ii): QD embedded in a medium with a larger dielectric constant. We consider, as above, a spherical 5 nm radius QD defined by the following parameters: $m^*_{e,QD}$=0.5, ε_{QD}=4, V_e=1 eV, and V_h=0.5 eV, the ratio V_e/V_h simulating typical alignments of different materials. Two different effective masses for holes have been considered, namely, $m^*_{h,QD}$=1 and 10, slightly and much heavier than $m^*_{e,QD}$, respectively. This QD is embedded in a fictitious medium with a dielectric constant ranging from $\varepsilon_{out}=\varepsilon_{QD}$ up to ε_{out}=50. The effective masses in this medium are assumed to be the same as in the QD since we have no criterion to assign them.

The key difference with respect to the previous case (i) of a QD in air is that now, the self-polarization potential has the attractive well located on the inner side of the QD border. Then, both particles can be confined in it, the heavier particle being more strongly attracted by this well due to its smaller kinetic energy. This is in contrast with the above case (i) where the hole (the heavier particle) was unable to overcome its large confining potential barrier, while the electron (the
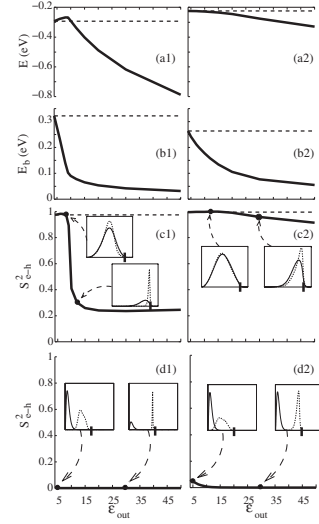
FIG. 2. Same as Fig. 1 but for a R=5 nm, ε_{QD}=4 QD with V_e=1 eV, V_h=0.5 eV, and $m^*_{e,QD}$=0.5, and two different hole effective masses, namely, $m^*_{h,QD}$=10 [(a1), (b1), and (c1)] and $m^*_{h,QD}$=1 [(a2), (b2), and (c2)], as a function of the dielectric constant of the environment ε_{out}. Panels (d1) and (d2) correspond to (c1) and (c2) when a hydrogenic donor impurity is located at the QD center.

lighter particle), confined by a shorter wall, could jump to the self-polarization potential well. Indeed, in case (ii), our exploratory single-particle calculations vs ε_{out} showed a gradual localization of the carriers in the self-polarization well, facing three different phases: namely, phase 1 (low ε_{out}) corresponding to volumetrically distributed electron and hole, phase 2 (intermediate ε_{out}) where the electronic density distribution is still volumetric while the hole forms a surface state, and phase 3 (large ε_{out}) in which both electron and hole are located in the surface well. However, as the strong *e-h* attraction (ε_{QD}=4) is incorporated into the CI calculation, phase 2 drops out.[32] Thus, only two phases are encountered, in which both particles show volumetric or facial distributions simultaneously. This is shown in Fig. 2, which shows the overlap S^2_{e-h}, excitonic E, and binding E_b energies of the considered QD with $m^*_{h,QD}$=1 and 10 vs ε_{out} ranging from $\varepsilon_{out}=\varepsilon_{QD}$ up to ε_{out}=50. The quantitative differences in excitonic and binding energies in either case are a direct consequence of the quite different kinetic energy of the hole. Both cases show, however, similar qualitative trends (increasing band gap redshift and decreasing E_b vs an increasing dielectric mismatch), which is in turn similar to the behavior already shown for a QD in air (see Fig. 1). A relevant difference arises in the overlap vs ε_{out} profile. While Fig. 2(c1) ($m^*_{h,QD}$=10) resembles Figs. 1(c1)–1(c3), in which the transition from volume to surface excitonic states involves a sudden S^2_{e-h} drop and therefore a sudden reduction in the

exciton brightness, this is not the case in Fig. 2(c2) ($m_{h,QD}^*$ =1). Since in the present case (ii) the transition from volume to surface state holds simultaneously for electron and hole, one may expect profiles like Fig. 2(c2), revealing an almost constant overlap vs ε_{out}. Then, the plot in Fig. 2(c1) looks like an anomaly that deserves an explanation. Indeed, the parameters m_e^*=0.5, m_h^*=10, R=5 nm, and ε_{QD}=4 yield quite a small effective Bohr radius, thus revealing that both electron and hole are in the weak confinement regime, the (volumetric) electron and hole density distributions being similar [see insets in Fig. 2(c1)]. However, once the trapping of particles in the narrow, deep self-polarization potential well occurs, both particles feel different spatial confinement. The heavier particle becomes strongly localized in the well, whereas the lighter one has a relevant leaking outside it [see insets in Fig. 2(c1)], yielding as a result a smaller overlap. In other words, in contrast to case (i) where the transition from volume to surface states always parallels a sudden decrease in brightness, in case (ii), this transition only has relevant brightness impact for QD materials with large m_h^*/m_e^* ratios.

Also, the influence of a hydrogenic donor impurity is addressed. As above, it attracts the electron toward the QD center and repels the hole [see Figs. 2(d1) and 2(d2)], resulting in a negligible binding energy and a strong reduction in oscillator strength.

In a last series of calculations, we explore the possibility of surface exciton formation in QDs built of higher dielectric constant materials. Now we set, as above, R=5 nm, m_e^* =0.5, m_h^*=1 and 10, V_e=1 eV, and V_h=0.5 eV. The permittivity of the external medium is set very high, ε_{out}=100, and we calculate the *e-h* overlap S_{e-h}^2 and binding energy E_b vs ε_{QD}. The results are shown in Fig. 3. As previously discussed, sudden changes in overlap reflecting transition from volume to surface exciton states only occur for large m_h^*/m_e^* ratios. As can be seen in Fig. 3(b1) (corresponding to a large m_h^*/m_e^* ratio), small (large) ε_{QD} values yield surface (volume) excitonic states with small (large) overlaps, in agreement with previous reasoning. However, intermediate ε_{QD} values are characterized by extremely small overlaps that parallel an anomalous minimum in the binding energy [Fig. 3(a1)]. This behavior occurs because, in this range of QD dielectric constants, the electron and hole single-particle densities are distributed as in the above mentioned phase 2, but now the *e-h* Coulomb attraction is not strong enough to drop phase 2 out, so we get a "broken" exciton in which the hole is localized in the self-polarization potential well, whereas the electron spreads over the whole QD volume [see insets in Fig. 3(b1)]. The small overlap and the decrease in the exciton binding energy are a direct consequence of the *e-h* spatial separation in this phase, which does not exist [see Figs. 3(a2) and 3(b2)] unless the effective masses of electron and hole are very dissimilar. Finally, Figs. 3(c1) and 3(c2) show the influence of a hydrogenic donor impurity located at the QD center. We see that the (D^+,X) exciton can approximately be described as D^0+h, i.e., a neutral electron-impurity pair and an almost
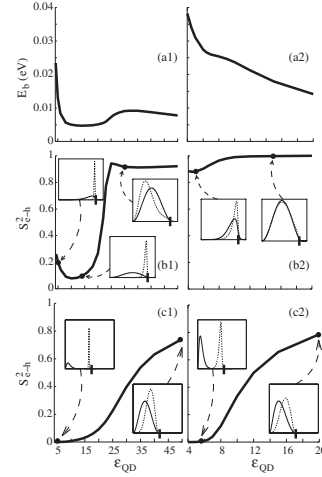
FIG. 3. Binding energy E_b and *e-h* overlap S_{e-h}^2 of a R=5 nm QD with V_e=1 eV, V_h=0.5 eV, and $m_{e,QD}^*$=0.5, and two different hole effective masses, namely, $m_{h,QD}^*$=10 [(a1) and (b1)] and $m_{h,QD}^*$=1 [(a2) and (b2)], as a function of ε_{QD} for a fixed ε_{out} =100. Insets: same criterion as in Fig. 1. Panels (c1) and (c2) correspond to (b1) and (b2) when a hydrogenic donor impurity is located at the QD center.

independent hole, as it is revealed by the negligible binding energy calculated.

IV. CONCLUDING REMARKS

We have shown that the dielectric properties of the QD environment can strongly influence the brightness of confined excitons, as well as excitonic and binding energies, due to the formation of surface states. While a sudden decrease in exciton brightness parallels the formation of surface excitons in the case of a QD in air or a vacuum, only QD materials with a large m_h^*/m_e^* ratio present a considerable reduction in exciton brightness when the QD is buried in a large dielectric constant medium. Our calculations also reveal[33] that the conditions to reach surface exciton states in this last case are less severe than if the QD is surrounded by air or a vacuum. A shallow donor impurity located at the QD center leads to an almost total suppression of exciton binding and brightness.

*josep.planelles@qfa.uji.es

[1] A. Zrenner, S. Stufler, P. Ester, S. Michaelis de Vasconcellos, M. Hübner, and M. Bichler, Phys. Status Solidi B **243**, 3696 (2006).

[2] A. D. Yoffe, *Advances in Physics* (Taylor & Francis, London, 2001), Vol. 50.

[3] J. M. Ferreyra and C. R. Proetto, Phys. Rev. B **60**, 10672 (1999).

[4] L. E. Brus, J. Chem. Phys. **80**, 4403 (1984).

[5] L. E. Brus, J. Chem. Phys. **79**, 5566 (1983).

[6] M. Lannoo, C. Delerue, and G. Allan, Phys. Rev. Lett. **74**, 3415 (1995).

[7] P. G. Bolcatto and C. R. Proetto, Phys. Rev. B **59**, 12487 (1999).

[8] A. Bagga, P. K. Chattopadhyay, and S. Ghosh, Phys. Rev. B **71**, 115327 (2005).

[9] A. Franceschetti, A. Williamson, and A. Zunger, J. Phys. Chem. B **104**, 3398 (2000).

[10] P. G. Bolcatto and C. R. Proetto, J. Phys.: Condens. Matter **13**, 319 (2001).

[11] L. Bányai, P. Gilliot, Y. Z. Hu, and S. W. Koch, Phys. Rev. B **45**, 14136 (1992).

[12] A. Orlandi *et al.*, Semicond. Sci. Technol. **17**, 1302 (2002).

[13] J. L. Movilla, J. Planelles, and W. Jaskólski, Phys. Rev. B **73**, 035305 (2006).

[14] J. Planelles and J. L. Movilla, Phys. Rev. B **73**, 235350 (2006).

[15] J. L. Movilla and J. Planelles, Phys. Rev. B **74**, 125322 (2006).

[16] V. A. Fonoberov, E. P. Pokatilov, and A. A. Balandin, Phys. Rev. B **66**, 085310 (2002).

[17] L. Bányai and S. W. Koch, *Semiconductor Quantum Dots* (Word Scientific, Singapore, 1993).

[18] F. A. Reboredo and A. Zunger, Phys. Rev. B **63**, 235314 (2001); A. Franceschetti, L. W. Wang, H. Fu, and A. Zunger, *ibid.* **58**, R13367 (1998).

[19] K. Leung and K. B. Whaley, Phys. Rev. B **56**, 7455 (1997).

[20] J. L. Movilla and J. Planelles, Comput. Phys. Commun. **170**, 144 (2005).

[21] F. Stern, Phys. Rev. B **17**, 5009 (1978).

[22] J. Climente, J. Planelles, W. Jaskólski, and J. I. Aliaga, J. Phys.: Condens. Matter **15**, 3593 (2003).

[23] G. Bastard, *Wave Mechanics Applied to Semiconductor Heterostructures* (Les Éditions de Physique, Les Ulis, 1988).

[24] J. P. Loehr, *Physics of Strained Quantum Well Lasers* (Kluwer Academic, Boston, 1998).

[25] We do not consider any particular QD material, although these parameters are close to those of SiO_2.

[26] The excitonic energy gives us the shift of the optical band gap. The binding energy is calculated by subtracting the excitonic energy to the ground single-particle electron and hole energies.

[27] Z. A. Weinberg, J. Appl. Phys. **53**, 5052 (1982).

[28] F. Gustini, P. Umari, and P. Pasquarello, Microelectron. Eng. **72**, 299 (2004).

[29] J. M. Ferreyra and C. R. Proetto, Phys. Rev. B **52**, R2309 (1995).

[30] E. F. da Silva, Jr., E. A. de Vasconcelos, B. D. Stošić, J. S. de Sousa, G. A. Farias, and V. N. Freire, Mater. Sci. Eng., B **74**, 188 (2000).

[31] We define binding energy in the presence of a hydrogenic impurity $E_b(D^+, X)$ as in W. Xie, Phys. Lett. A **270**, 343 (2000), i.e., $E_b(D^+, X) = E(D^0) + E_h - E(D^+, X)$, where $E(D^+, X)$ is the energy of the exciton in the doped QD, E_h the lowest level of a hole in the QD without impurity, and $E(D^0)$ is the ground state of an electron in the doped QD.

[32] For QD dielectric constants of the order of $\varepsilon_{QD} = 4$, we can only get a phase 2 or "broken" exciton if the electron is in an extremely strong confinement regime (that we may get using a very light effective mass) while the regime of confinement for the hole is weak. In such a case, the CI calculations reveal only two phases in which the electron is always volumetric and the hole is either volumetric or facial, depending on ε_{out}.

[33] A 5 nm radius QD embedded in an $\varepsilon_{out} = 100$ medium presents a superficial excitonic ground state if $\varepsilon_{QD} < 20$ ($m_e^* = 0.5$, $m_h^* = 10$), $\varepsilon_{QD} < 7$ ($m_e^* = 0.5$, $m_h^* = 1$), and $\varepsilon_{QD} < 11$ ($m_e^* = 0.2$, $m_h^* = 2$).

Nonparabolicity and dielectric effects on addition energy spectra of spherical nanocrystals

J. Planelles[a)] and M. Royo
Departament de Química Física i Analítica, UJI, Box 224, E-12080 Castelló, Spain

M. Pi
Departament ECM, Facultat de Física and IN^2 UB, Universitat de Barcelona, E-08028 Barcelona, Spain

An extension of the spin density functional theory simultaneously accounting for dielectric mismatch between neighboring materials and nonparabolicity corrections originating from interactions between conduction and valence bands is presented. This method is employed to calculate ground state and addition energy spectra of homogeneous and multishell spherical quantum dots. Our calculations reveal that corrections become especially relevant when they come into play simultaneously in strong regimes of spatial confinement. © *2007 American Institute of Physics*. [DOI: 10.1063/1.2803722]

I. INTRODUCTION

The conduction band of semiconductors shows a nearly parabolic dispersion at the surroundings of the Γ point and is commonly described by the one-band model, the interactions with the remaining bands being included in the electron effective mass. This is a sensible approach for wide-gap semiconductors. However, the small gap between the conduction and valence bands in narrow gap semiconductors has important nonparabolicity effects on the conduction band dispersion that warrant an improvement of the model. The use of an energy-dependent effective mass, as proposed by Kane,[1,2] allows us to study narrow gap semiconductors still within the framework of the one-band model. Nevertheless, as the effective mass is self-consistently adjusted for each energy level, different kinetic energy, and therefore Hamiltonian operators, are employed to compute the different eigenvalues, so that the associate eigenfunctions are not necessarily orthogonal. In order to deal with orthogonal eigenfunctions, the electron effective mass is kept constant and a power series expanded dispersion relation is incorporated into the kinetic energy term of the Hamiltonian yielding a fourth (or higher) order differential Schrödinger-like equation.[3] Although this approach has been successfully employed to study donor states in spherical quantum dots (QDs),[4] it will be accurate only to the extent that the truncated power series succeed in describing the dispersion relation.

The energy-dependent effective mass, leading to nonorthogonal eigenfunctions, has been employed to study the electronic structure[5] and optical excitations[6,7] of quantum wells (QWs). Intersubband spin-density excitations in QWs have been addressed using the Kohn–Sham equations with energy-dependent effective mass.[8] Extensive single particle studies of different shaped QDs,[9–11] quantum rings,[12] and artificial molecules[13] have also been carried out. Recently, the energy-dependent effective mass approach has reproduced experimental effective masses obtained from optical

transition energies in QWs[14] and provided quantitative interpretations of capacitance voltage spectroscopy experiments.[15]

Nonparabolicity has larger effects in the strong confinement regime and for excited states, where the energetic correction can even exceed the electron-electron interaction.[9] A recent spin density functional theory[16] (SDFT) study of a QD molecule with six electrons[17] shows that the energy-dependent effective mass correction is comparable to the exchange energy that is obtained. Since the energy-dependent effective mass corrects the kinetic contribution to the total energy, minor effects coming from nonparabolicity could be expected in the weak confinement regime. In the present paper we incorporate nonparabolicity corrections into our SDFT code,[18–20] which also accounts for polarization and self-polarization coming from dielectric mismatch between neighboring materials. We then explore the relevance of nonparabolicity corrections on the addition energies of homogeneous and multishell QDs subjected to different confinement regimes. We will show that the interplay of both dielectric mismatch and nonparabolicity effects may lead to relevant changes in the electronic structure and addition energies of QDs, the effect being particularly relevant in multishell QDs.

II. THEORY AND COMPUTATIONAL DETAILS

The formulation of the extension of the SDFT which accounts for position-dependent effective mass, polarization of the Coulomb interaction, and self-polarization coming from the dielectric mismatch between the QD and its surrounding medium (and also between neighboring materials in the case of multishell QDs) can be found in Ref. 18 and will not be outlined here for the sake of conciseness. For the present study we also implemented energy-dependent effective masses in a similar way to that reported in Ref. 17. It is worth pointing out that the use of orbital energy-depending masses is just an effective way of incorporating the perturbation produced by the valence bands on the conduction electron levels (the scheme we proposed here can be viewed

a)Electronic mail: josep.planelles@qfa.uji.es

as an approximation to the multiband calculation). Therefore, it is equivalent to leaving the kinetic energy operator as it is and introducing the appropriate perturbation external potential. As a consequence, same exchange-correlation functional should be employed in parabolic and nonparabolic calculations. In our implementation we basically include $m^*_{i\sigma}(E_{i\sigma}, \mathbf{r})$ instead of $m^*(\mathbf{r})$ in the Kohn–Sham (KS) equation, i.e., a single differential equation is replaced by a set of coupled differential equations

$$\left[-\frac{\hbar^2}{2}\nabla \frac{1}{m^*_{i\sigma}(E_{i\sigma}, \mathbf{r})}\nabla + V_{KS,\sigma}(n,\zeta) \right]\Phi_{i\sigma}(\mathbf{r}) = E_{i\sigma}\Phi_{i\sigma}(\mathbf{r}) \tag{1}$$

that are solved up to simultaneous convergence. In the earlier equation n is the total density and ζ represents the spin polarization. In terms of the spin-up and spin-down densities $n_\sigma(\mathbf{r})$ [where $\sigma = (+,-)$ labels the spin] they can be written as

$n(\mathbf{r}) = n_+(\mathbf{r}) + n_-(\mathbf{r})$ and $\zeta(\mathbf{r}) = [n_+(\mathbf{r}) - n_-(\mathbf{r})]/n(\mathbf{r})$, respectively.

The energy-dependent effective mass in Eq. (1) is given by the Kane formula[1,2]

$$\frac{m_0}{m^*(E,\mathbf{r})} = 1 + \frac{2}{3}\mathcal{P}^2\left[\frac{2}{E + E_g(\mathbf{r}) - V(\mathbf{r})} + \frac{1}{E + E_g(\mathbf{r}) - V(\mathbf{r}) + \Delta(\mathbf{r})} \right], \tag{2}$$

where $m^*(E,\mathbf{r})$ is the energy- and position-dependent effective mass, m_0 is the free electron mass, $\mathcal{P}$ is the Kane parameter, and $E_g(\mathbf{r})$, $V(\mathbf{r})$, $\Delta(\mathbf{r})$ are the position-dependent band gap, confining potential, and spin-orbit parameter, respectively. For a practical implementation, we employ the relationship between the position- and energy-dependent effective mass $m^*(E,\mathbf{r})$ and the position-dependent effective mass at the bottom of the conduction band $m^*(0,\mathbf{r})$,

$$\frac{\dfrac{m_0}{m^*(E,\mathbf{r})} - 1}{\dfrac{m_0}{m^*(0,\mathbf{r})} - 1} = \frac{\left[E + E_g(\mathbf{r}) - V(\mathbf{r}) + \dfrac{2}{3}\Delta(\mathbf{r}) \right][E_g(\mathbf{r}) - V(\mathbf{r})][E_g(\mathbf{r}) - V(\mathbf{r}) + \Delta(\mathbf{r})]}{\left[E_g(\mathbf{r}) - V(\mathbf{r}) + \dfrac{2}{3}\Delta(\mathbf{r}) \right][E + E_g(\mathbf{r}) - V(\mathbf{r})][E + E_g(\mathbf{r}) - V(\mathbf{r}) + \Delta(\mathbf{r})]}. \tag{3}$$

Many implementations[2,9–13,17] approximate the left-hand side of Eq. (3) by $m^*(0.\mathbf{r})/m^*(E.\mathbf{r})$. Here we use Eq. (3) as it is.

In order to achieve a solution to the set of differential Eq. (1) we start by solving a single differential equation where $m^*_{i\sigma}(E_{i\sigma}, \mathbf{r})$ is replaced by $m^*(0,\mathbf{r})$. From the $\Phi_{i\sigma}(\mathbf{r})$ orbitals and $E_{i\sigma}$ energies thus obtained we compute the total density n, spin polarization ζ, and effective masses $m^*_{i\sigma}(E_{i\sigma}, \mathbf{r})$ and build up the set of differential Eq. (1). In a second step, we solve these differential equations one by one to get the couple orbital and associate energy $[\Phi_{i\sigma}(\mathbf{r}), E_{i\sigma}]$ from the $i\sigma$th differential equation. Then, from the new set of energies we get the next energy- and position-dependent effective masses $m^*_{i\sigma}(E_{i\sigma}, \mathbf{r})$ and from the new orbitals the next total density n and spin polarization ζ are obtained. The process is repeated up to simultaneous convergence of all differential equations. We can build the first order density matrix from a set of nonorthogonal orbitals or equivalently, we may first orthogonalize them and then construct the density matrix. We follow the second procedure in our code.

The good performance of our method computing addition energies of QDs with nearly parabolic conduction band has already been tested.[18] Additionally, the use of energy-dependent effective masses has widely recognized as an appropriate effective way of incorporating the perturbation produced by the valence bands on the conduction energy levels (see the earlier section). Nevertheless, it is worth testing these approaches working together on a narrow-gap semiconductor QD. Certainly, the amount of experimental data on addition energies of spherical narrow-gap QDs in the presence of relevant dielectric mismatch with the environment is rather scarce. We employ here experimental results by Banin *et al.*[21] on a 2.2 nm radius InAs QD embedded in an organic environment which first three experimental addition energies have already been very well reproduced by means of heavy atomistic pseudopotential calculations.[22] In these calculations the dielectric constant of the organic environment was taken as a fitting parameter, yielding a value $\varepsilon_{out} = 6$. In our test we have assumed, though, a value $\varepsilon_{out} = 3$, which seems more reasonable for this kind of environment.[23] The remaining parameters employed are those of bulk InAs, namely $m^*_{QD} = 0.023$, $\varepsilon_{QD} = 12.3$, $E_g^{QD} = 0.354$ eV, $\Delta_{SO}^{QD} = 0.41$ eV, and for the external medium $m^*_{out} = 1$, $\varepsilon_{out} = 3$, $E_g^{out} = 8$ eV, $\Delta_{SO}^{out} = 0$ eV. Finally, the confining potential is assumed to be $V = 3.2$ eV, the same as in Ref. 22. Parabolic/no-parabolic calculations predict (experimental data in parentheses) $\Delta_{1,2} = 0.22/0.19(0.14)$ eV, $\Delta_{2,3} = 1.59/0.59(0.52)$ eV, and $\Delta_{3,4} = 0.20/0.14(0.14)$ eV. We see in this example that nonparabolic corrections work well improving all parabolic results, the improvement of $\Delta_{2,3}$ being especially relevant. The obtained results also show that our nonparabolic approach supplied with bulk parameters compares well with reported experimental data by Banin *et al.*[21] Further improvement may be reached by fitting.

III. RESULTS AND DISCUSSION

We study the ground state and addition energies of spherical QDs built of narrow gap semiconductors versus the number N of electrons. Spherical nanocrystals are commonly

TABLE I. Parameters employed in this paper (taken from Ref. 25). Namely, effective mass (m_0^*), dielectric constant (ε), band gap (Eg), split of (Δ), and spatial confining potential barrier (V).

Material	m_0^*	ε	Eg (eV)	Δ (eV)
HgS	0.04	11.4	0.5	0.08
CdS	0.15	5.5	2.5	0.08
H_2O	1	1.78	8.	0.08
		HgS/H_2O	CdS/H_2O	HgS/Cds
V (eV)		4.15	2.8	1.35

synthesized in colloidal solutions. This technique allows the smallest QDs with sizes of very few nanometers to be produced. The QDs can be either homogeneous or onionlike, i.e., built up of concentric layers (shells) of different semiconductors with controllable shell thicknesses down to a single monolayer. In the present paper, we consider both homogeneous HgS nanocrystals and multishell double quantum well CdS/HgS/CdS/HgS/CdS, similar to those experimentally synthesized in Ref. 24. Then, in all cases the surrounding medium of the QD is considered to be water. The parameters employed in our calculations for the different materials, namely effective masses, dielectric constants, band gaps, split-off parameters, and spatial confining potentials are the same as those employed in Ref. 25 and are shown in Table I. The bottom of the HgS conduction band is assumed to be the origin of energies in all cases. We have carried out calculations from 1 up to 25 electrons, using an orbital basis $1s$, $1p$, $1d$, $1f$, $2s$, and $2p$.

A. Homogeneous nanocrystal

In this section we consider HgS QDs with 5 and 20 nm radii in water. From the HgS effective Bohr radius, a_0^* $= a_0 \varepsilon / m^* = 15$ nm, we see that the confinement regime of the small/large QD is strong/weak. For the time being the polarization coming from the dielectric mismatch is disregarded in our calculations, i.e., we use the dielectric constant of the QD for the whole system. We carry out three series of calculations versus the number N of electrons in the QD ranging from 1 up to 25. These are (i) independent particle (IP) calculations employing a parabolic effective mass; (ii) IP calculations with energy-dependent masses; and (iii) interacting electrons at the SDFT level with a parabolic effective mass (excluding dielectric mismatch effects). The results for the small and large QD, as representative of strong/weak confinement regime, are summarized in Figs. 1(a) and 1(b). Solid lines represent IP with parabolic mass, dashed lines correspond to IP including nonparabolicity corrections, and dotted lines refer to interacting particles with parabolic effective mass. The obtained results go along with expectations, i.e., nonparabolicity corrections increase with the number of electrons in the QD; in the strong confinement regime these corrections can be as large as the corrections originating from the electron-electron interaction [Fig. 1(a)] while in the weak confinement regime they are negligibly small [Fig. 1(b)]. The inset in Fig. 1(b) shows the evolution of the
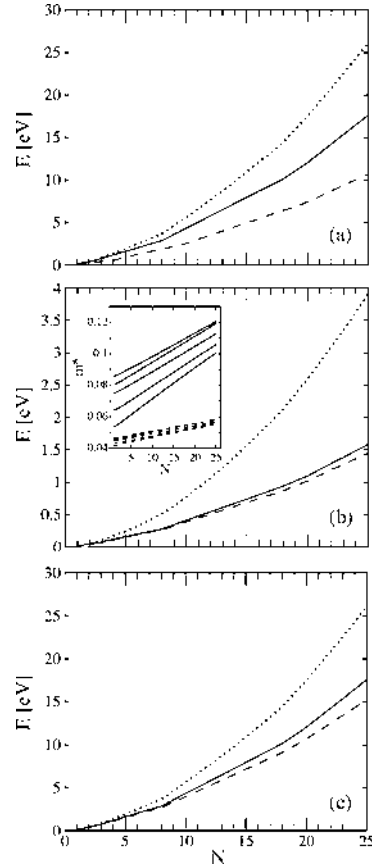
FIG. 1. Ground state energy vs number N of electrons of a (a) 5 nm radius HgS QD, (b) 20 nm radius HgS QD, and (c) 5 nm radius QD defined by the HgS material parameters except for Eg that is set to 3 eV. Solid lines correspond to the parabolic IP calculations, dashed lines to IP including nonnonparabolicity corrections, and dotted lines to parabolic SDFT. The inset encloses the energy-dependent effective masses of the 5 nm radius HgS QD (solid lines) and 20 nm radius HgS QD (dotted lines) corresponding to the low-lying KS orbitals.

energy-dependent effective masses in the low-lying $1s$, $1p$, $1d$, $1f$, and $2s$ states versus the number N of electrons in the QD. Solid/dashed lines correspond to strong/weak confinement regimes. The results reveal that higher energy states have larger effective masses and that the electron effective mass increases almost linearly with N (within the range studied here), these changes in effective masses being relevant only in the strong confinement regime. Interestingly, corrections coming from nonparabolicity and from electron-electron interactions are of opposite signs. In the strong confinement regime where nonparabolicity corrections are relevant [Fig. 1(a)], these corrections partially cancel out
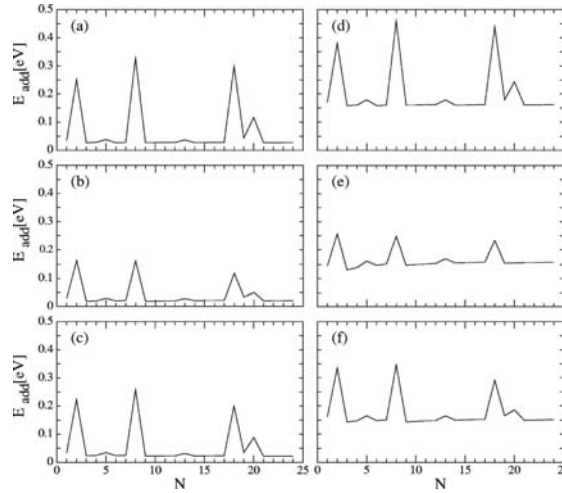
FIG. 2. Calculated addition energy spectra of a 5 nm radius HgS QD. (a) With a parabolic mass. (b) Including nonparabolicity corrections. (c) Same as (a) except that the QD material Eg is set to 3 eV. (d), (e), and (f) Same as (a), (b), and (c) but also including polarization coming from the dielectric mismatch between neighboring materials.

with the electron-electron interaction corrections, so that calculations including both corrections yield energies close to those of the simple IP parabolic approach. In other words, it appears that simple parabolic IP calculations yield a reasonable, at least qualitative, description of the QD electronic structure in the strong confinement regime. In the weak confinement regime, where Coulomb interactions cannot be excluded for a reasonable description of the QD electronic structure, nonparabolicity corrections are negligibly small [see Fig. 1(b)], and it seems they can safely be ignored, at least for a qualitative description.

In order to show the extent to which these corrections can influence the electronic structure of QDs built of wide-gap semiconductor materials, we carried out a third series of calculations for a QD described by the same parameters as the small HgS nanocrystal except for the band gap that was set to 3 eV. Then, this QD is in the (same) strong confinement regime where nonparabolicity corrections become large. However, the results obtained reveal, as expected, that despite the strong confinement regime, nonparabolicity corrections are much smaller than those coming from Coulomb interactions [see Fig. 1(c)]. The behavior observed is therefore similar to narrow gap semiconductor QDs in the weak confinement regime [Fig. 1(b)].

So far we have excluded polarization coming from the dielectric mismatch and focused on total energies, the calculations revealing that nonparabolicity corrections are not small in the strong confinement regime, although no particular situations have been found in which these corrections play a fundamental role. Next, we consider a QD in the strong confinement regime, carry out calculations of the quite sensitive addition energy,[26] and allow polarization effects to come into play. To this end, we study the small 5 nm radius HgS QD in water again and estimate addition energies including and excluding polarization effects coming from the dielectric mismatch between the QD and its surrounding me-

dium (hereafter we will refer to these calculations as polarized and unpolarized) and with/without nonparabolicity corrections. The calculations are summarized in Fig. 2. Panels on the left- and right-hand side show unpolarized/polarized calculations. Top row panels correspond to parabolic effective mass while those in the middle row include corrections from nonparabolicity. As earlier, for the sake of comparison, we enclose a series of calculations on a wide-gap semiconductor QD (panels at the bottom of Fig. 2). Thus, the calculations shown in the panels in the middle and bottom rows correspond to QDs defined with the same parameters and geometry except for the band gap (set to 0.5 and 3.0 eV, respectively). The unpolarized calculations with parabolic effective mass, assumed to be the reference, are shown in Fig. 2(a). We see that polarization and nonparabolicity corrections in isolation do not yield qualitative changes in the addition energy profile [Figs. 2(b) and 2(d), respectively]. In all three panels (a), (b), and (d), one can neatly recognize that the shell filling is done according to the Afbau and Hund rules. Large peaks reveal complete shell filling, small peaks show half filling. Then, the observed filling sequence is $1s^21p^61d^{10}2s^21f^x$. Only when both corrections are simultaneously included, can a reconstruction be observed. The orbital $2s$ is not filled before $1f$ [see Fig. 2(e)]. The reconstruction disappears if the QD is built of a wide-band semiconductor material [Figs. 2(c) and 2(f)]. The earlier mentioned reconstruction originates from the following facts. On the one hand, polarization corrections increase the orbital energies, thus enhancing the nonparabolicity corrections. On the other hand, s-symmetry orbitals ($l=0$) have a null centrifugal term $l(l+1)/m^*r^2$ while this term is relevant for f orbitals ($l=3$). When nonparabolicity corrections come into play and increase the effective masses, $1f$ undergoes a larger stabilization than $2s$, and it is filled first. This is not the case for the wide-gap semiconductor QD because it has small
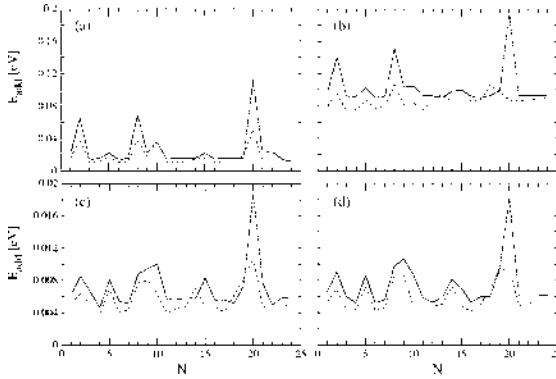
FIG. 3. Calculated SFDT addition energy spectra of a multishell CdS/HgS/CdS/HgS/CdS spherical QD double QW with core radius and shells of (a) 3/2/1/2/1 nm, (b) same as (a) but also including polarization coming from the dielectric mismatch, (c) core radius and shells of 10/5/2/5/1 nm, and (d) Same as (c) but also including polarization. Solid lines represent calculations with parabolic effective mass. Dashed lines indicate that nonparabolicity corrections are included.

nonparabolicity corrections, that never allow $1f$ to reach an energy lower than that of $2s$. Then $2s$ is again filled first [see Fig. 2(f)].

In summary, in addition to exceptional situations where the interplay of nonparabolicity and polarization corrections may yield reconstructions and thus changes in the addition energy profile, the main effect that nonparabolicity corrections produce on the addition energy spectrum is a reduction in the height of the peaks [see e.g., Fig. 2(b) versus Fig. 2(a)] as the result of a higher degree of closeness of the orbital energies originating from an increase in the effective mass.

B. Multishell quantum dots

In the previous section we found a reconstruction in the addition energy spectrum originating from the relative closeness of orbital energies and the differential nonparabolicity effects on energy levels with distinct angular momentum quantum number l. Double quantum wells are good candidates for a nonregular energy spectrum. Thus, in this section we consider a multishell CdS/HgS/CdS/HgS/CdS spherical QD double QW like those synthesized in Ref. 24. The parameters employed in our calculations can be found in Table I. It is no straightforward task to unambiguously define the confinement regime of these heterogeneous systems in which the electronic density is mainly concentrated in the wells, but it seems reasonable to assume that the volume of the wells will basically determine it.

We consider two systems with different confinement strengths defined by the following core radius and shell thickness, $3/2/1/2/1$ and $10/5/2/5/1$ nm, respectively, and carry out polarized/unpolarized calculations with/ without the inclusion of nonparabolicity corrections. The results can be seen in Fig. 3. Panels (a) and (b) in Fig. 3 correspond to the stronger spatial confinement while panels (c) and (d) correspond to the weaker confinement. Solid/ dashed lines refer to parabolic/nonparabolic effective masses.

First we analyze the smaller (strong confined) system. The reference addition energy spectrum [unpolarized and parabolic, solid line in Fig. 3(a)] shows a regular sequential

filling up to 20 electrons ($1s^2 1p^6 2s^2 1d^{10}$). Then, a shoulder emerges at $N=22$ involving the $2p$ orbital. This shoulder disappears when nonparabolicity corrections are included (dashed line in the same panel), which reveals a regular filling of the $1f$ orbital, due to the fact that $1f(l=3)$ undergoes a larger energy stabilization coming from nonparabolicity corrections than $2p(l=1)$, this fact being mainly related to the centrifugal term. Except for this reconstruction, unpolarized calculations with and without nonparabolicity corrections yield similar addition spectra. The main difference is a reduction in the height of the peaks when corrections are taken into account. This reduction comes from a higher degree of closeness of the orbital energies as the effective masses increase, due to nonparabolicity effects.

When polarization is taken into account in the parabolic mass calculation [solid line in Fig. 3(b)] no relevant changes in the addition energy spectrum can be seen. We may mention the disappearance of the shoulder at $N=22$ and some "noise" when filling orbital $1d$. However, when both polarization and nonparabolicity corrections are simultaneously taken into account [dashed line in Fig. 3(b)] severe changes in the addition energy spectrum occur. On the one hand, full- and half-filling peaks become similar in height. On the other hand, the largest peak at $N=20$ corresponding to the full filling of orbital $1d$ drops out.

The shell structure of the larger multishell QD is not neatly apparent in the addition spectrum. However, the reference unpolarized and parabolic addition energy spectrum [solid line in Fig. 3(c)] still shows peaks at $N=2(1s^2)$, $N=5(1s^2 1p^3)$, $N=8(1s^2 1p^6)$, $N=10(1s^2 1p^6 2s^2)$, $N=15(1s^2 1p^6 2s^2 1d^5)$, and $N=20(1s^2 1p^6 2s^2 1d^{10})$, although the profile is far from being as regular as the one for the smaller multishell QD [solid line in Fig. 3(a)]. When nonparabolicity corrections are taken into account [dashed line in Fig. 3(c)] the most significant change observed is a peak flip from $N=15$ (corresponding to the filling $1s^2 1p^6 2s^2 1d^5$) up to $N=14$ (when corrections are included and that corresponds to $1s^2 1p^6 2s^2 1d^5$). Additionally, as in all previously studied examples, the height of the peaks are reduced due to a higher

degree of closeness of orbital energies coming from an increase in effective mass induced by nonparabolicity.

Accounting for polarization while employing a parabolic mass does not introduce qualitative changes in the addition energy spectrum [solid line in Fig. 3(d)] except, as earlier, for the shift from $N=15$ to $N=14$ of the half filling of $1d$. Finally, in contrast with the results corresponding to the smaller (more strongly confined) multishell QD, by including both polarization and nonparabolicity corrections, no severe changes occur in the spectrum [dashed line in Fig. 3(d)]. This is related to the fact that both corrections are smaller in larger systems.

IV. CONCLUSIONS

In this paper we have studied the relevance of corrections coming from nonparabolicity on the ground state and addition energies of homogeneous and multishell spherical QDs and their interplay with effects coming from the presence of dielectric mismatch. To this end we employ a SDFT approach modified to include polarization coming from the dielectric mismatch between neighboring materials and nonparabolicity originating from the interaction between conduction and valence bands. This approach basically translates into a set of coupled differential equations that are solved up to simultaneous convergence.

Our calculations show that homogeneous QDs built of narrow gap semiconductor materials show large nonparabolicity energy corrections if the QD regime of spatial confinement is strong. In such a case, these corrections are of the same order and opposite sign as corrections coming from electron-electron interaction and partially cancel each other out, so that the simple parabolic IP approach yields reasonable, at least qualitative, results. A similar conclusion applies to the addition energy spectra. Since most of the spherical QDs are chemically synthesized in colloidal solutions, in our calculations we have incorporated the polarization originated by the dielectric mismatch between the QD and its surroundings that we consider to be water (and also between different materials in the case of multishell QDs). Our results reveal that the interplay of polarization and nonparabolicity corrections may yield reconstructions in the addition energy spectrum. Our analysis points out two reasons for this. On the one hand, polarization increases orbital energies thus enhancing nonparabolicity corrections. On the other hand, the different centrifugal terms felt by orbitals with different angular momentum quantum number l include the effective mass in the denominator. As a result, nonparabolicity corrections may even flip the orbital energy and the filling sequence of orbital with different l. As a major conclusion we can say that the calculations on addition energy spectra of multishell

QDs is the scenario where corrections play a prominent role. The most significant changes arise in the stronger spatial confinement when the dielectric mismatch effects are also relevant and come into play together with nonparabolicity corrections.

[1]E. O. Kane, J. Phys. Chem. Solids **1**, 249 (1957).
[2]G. Bastard, *Wave Mechanics Applied to Semiconductor Heterostructures* (Les Editions de Physique, Les Ulis Cedex, 1988).
[3]A. Persson and R. M. Cohen, Phys. Rev. B **38**, 5568 (1988).
[4]C. Bose, K. Midya, and M. K. Bose, Physica E (Amsterdam) **33**, 116 (2006).
[5]W. Chen and T. G. Andersson, Phys. Rev. B **44**, 9068 (1991).
[6]D. Huang, Phys. Rev. B **53**, 13645 (1996).
[7]X. Chen, Physica B (Amsterdam) **270**, 88 (1999).
[8]C. A. Ullrich and M. E. Flatté, Phys. Rev. B **66**, 205305 (2002).
[9]Y. Li, O. Voskoboynikov, C. P. Lee, and S. M. Sze, Solid State Commun. **120**, 79 (2001).
[10]Y. Li, J. L. Liu, O. Voskoboynikov, C. P. Lee, and S. M. Sze, Comput. Phys. Commun. **140**, 399 (2001).
[11]Y. Li, O. Voskoboynikov, C. P. Lee, and S. M. Sze, Comput. Phys. Commun. **141**, 66 (2001).
[12]O. Voskoboynikov, Y. Li, H. M. Lu, C. F. Shih, and C. P. Lee, Phys. Rev. B **66**, 155306 (2002).
[13]Y. Li, O. Voskoboynikov, C. P. Lee, and S. M. Sze, Comput. Phys. Commun. **147**, 209 (2002).
[14]N. Kotera and K. Tanaka, Physica E (Amsterdam) **32**, 199 (2006).
[15]I. Filikhin, E. Deyneka, and B. Vlahovic, Physica E (Amsterdam) **31**, 99 (2006); I. Filikhin, V. M. Suslov, and B. Vlahovic, Phys. Rev. B **73**, 205332 (2006).
[16]U. von Barth and L. Hedin, J. Phys. C **5**, 1629 (1972).
[17]J. L. Liu, J. H. Chen, and O. Voskoboynikov, Comput. Phys. Commun. **175**, 575 (2006).
[18]M. Pi, M. Royo, and J. Planelles, J. Appl. Phys. **100**, 073712 (2006).
[19]M. Royo, J. Planelles, and M. Pi, Phys. Rev. B **75**, 033302 (2007).
[20]W. Kohn and L. J. Sham, Phys. Rev. **140**, A1133 (1965).
[21]U. Banin, Y. Cao, D. Katx, and D. Millo, Nature (London) **400**, 542 (1999).
[22]A. Franceschetti, A. Williamson, and A. Zunger, J. Phys. Chem. B **104**, 3398 (2000).
[23]See, e.g., M. Drndić, M. V. Jarosz, N. Y. Morgan, M. A. Kastner, and M. G. Bawendi, J. Appl. Phys. **92**, 7498 (2002).
[24]M. Braun, C. Burda, and M. A. El-Sayed, J. Phys. Chem. A **105**, 5548 (2001).
[25]K. Chang and J. B. Xia, Phys. Rev. B **57**, 9780 (1998); W. Jaskólski and G. W. Bryant, *ibid.* **57**, R4237 (1998); A. D. Yoffe, Adv. Phys. **50**, 1 (2001).
[26]Addition energies are defined as $E_{add}(N)=E(N+1)+E(N-1)-2E(N)$, where $E(N)$ is the total energy of the QD populated with N electrons. Experimentally, the shell structure of QDs is often inferred from their addition spectrum that can be obtained from, e.g., capacitance voltage spectroscopy experiments.

179

Electronic states of laterally coupled quantum rings

J. Planelles[1], F. Rajadell[1], J.I. Climente[2,1], M. Royo[1] and J.L. Movilla[1]

[1]Departament de Ciències Experimentals, UJI, Box 224, E-12080 Castelló, Spain
[2]CNR-INFM S3, Via Campi 213/A, 41100 Modena, Italy

E-mail: `josep.planelles@exp.uji.es`

Abstract.

The conduction band electron states of laterally-coupled semiconductor quantum rings are studied within the frame of the effective mass envelope function theory. We consider the effect of axial and in-plane magnetic fields for several inter-ring distances, and find strong changes in the energy spectrum depending on the coupling regime. Our results indicate that the magnetic response accurately monitors the quantum ring molecule dissociation process. Moreover, the anisotropic response of the electron states to in-plane magnetic fields provides information on the orientation of the quantum ring molecule.

1. Introduction

Quantum rings (QRs) stand as an alternative to quantum dots (QDs) as zero-dimensional structures for eventual use in nanotechnology devices. The main differences between the physics of QRs and that of QDs follow from the doubly-connected geometry of the rings, which provides them with a characteristic electronic shell structure, magnetic field response and transport properties.[1, 2, 3] While much attention has been devoted in the last years to the study of 'artificial molecules' made of coupled QDs (see e.g. Refs.[4, 5, 6] and references therein), only recently their QR counterparts have started being addressed. A number of experimental and theoretical works have studied vertically-coupled[7, 8, 9], and concentrically-coupled[10, 11, 12, 13] QRs. Conversely, to our knowledge, laterally-coupled quantum rings (LCQRs) have not been investigated yet. This is nonetheless an interesting problem: on the one hand, LCQRs constitute 'artificial molecules' with unique topology (two LCQRs may be triply-connected), what should be reflected in unique energy structures; on the other hand, the formation of pairs of LCQRs in the synthesis of self-assembled QRs is apparent.[14] Therefore, one could investigate LCQRs experimentally by probing spectroscopically the reponse of selected individual entities from a macroscopic sample of self-assembled QRs, as done e.g. in Ref.[15] for single QRs.

In this work we study the conduction band single-electron energy levels and wave functions of a pair of nanoscopic LCQRs, as a function of the distance between the two constituent QRs. Particular emphasis is placed on the effect of external magnetic fields, applied along the axial and two transversal in-plane directions, which lead to characteristic magnetic responses depending on the strength of the inter-ring coupling regime.

2. Theoretical considerations

Since usual QRs have much stronger vertical than lateral confinement,[2] we calculate the low-lying states of LCQRs using a two-dimensional effective mass-envelope function approximation Hamiltonian which describes the in-plane $(x - y)$ motion of the electron in the ring. In atomic units, the Hamiltonian may be written as:

$$H = \frac{1}{2m^*}(\mathbf{p} + \mathbf{A})^2 + V(x,y) \tag{1}$$

where m^* stands for the electron effective mass and $V(x,y)$ represents a finite scalar potential which confines the electron within the lateral limits of the double ring heterostructure. Here we define x as the direction of dissociation of the LCQRs. $\mathbf{A}$ is the vector potential, whose value depends on the orientation of the magnetic field B. Actually, the choice of $\mathbf{A}$ is limited by the requirement that it should make it possible to separate $(x - y)$ coordinates from z in the Hamiltonian.[16] Within the Coulomb gauge, for a field applied along z (axial magnetic field), this is fulfilled e.g. by $\mathbf{A_{B_z}} = (-y, x, 0)\frac{1}{2}B$. For an in-plane magnetic field applied along x (y), this is fulfilled e.g. by $\mathbf{A_{B_x}} = (0, 0, y)B$ $(\mathbf{A_{B_y}} = (0, 0, -x)B)$. Replacing these values of the vector potential in Hamiltonian (1) we obtain:

$$H(B_z) = \frac{\hat{p}_\parallel^2}{2m^*} + \frac{B_z^2}{8\,m^*}(x^2 + y^2) - i\frac{B_z}{2\,m^*}\left(x\frac{\partial}{\partial y} - y\frac{\partial}{\partial x}\right) + V(x,y), \tag{2}$$

$$H(B_x) = \frac{\hat{p}_\parallel^2}{2m^*} + \frac{B_x^2}{2\,m^*}y^2 + V(x,y), \tag{3}$$

$$H(B_y) = \frac{\hat{p}_\parallel^2}{2m^*} + \frac{B_y^2}{2\,m^*}x^2 + V(x,y). \tag{4}$$

The eigenvalue equations of Hamiltonians (2-4) are solved numerically using a finite-difference method on a two-dimensional grid (x, y) extended far beyond the LCQR limits. This discretization yields an eigenvalue problem of a huge asymmetric complex sparse matrix that is solved in turn by employing the iterative Arnoldi factorization.[17]

In this work we investigate nanoscopic laterally-coupled GaAs QRs embedded in an $Al_{0.3}Ga_{0.7}As$ matrix. We then use an effective mass m^*=0.067 and a band-offset of 0.262 eV.[18] The pair of rings which constitute the artificial molecule have inner radius $r_{in} = 12$ nm and outer radius $r_{out} = 16$ nm, and the separation between their centers is given by the variable d.

3. Results and discussion

3.1. Zero magnetic field

We start by studying the electron wave function localization in LCQRs for increasing inter-ring distances, from the strongly coupled to the weakly coupled regime (a process we shall hereafter refer to as *dissociation of the quantum ring molecule*), in the absence of external fields. Figure 1 illustrates the wave functions of the three lowest-lying electron states for several values of d. The corresponding profiles of the confining potential barrier are also represented using dotted lines. When the QRs are strongly coupled ($d = 12$ nm), one clearly identifies a s-like ground state and two p-like excited states. The states localize along the arms of the LCQRs, as if in a single elliptical QR, with some excess charge deposited in the region where the two QRs overlap. As the inter-ring distance increases, the available space in the overlapping regions first increases. This tends to localize the ground and first excited states in such regions ($d = 18$ nm) until they eventually become the even and odd solutions of a double quantum well ($d \sim 26$ nm). For further increased inter-ring distance, an inner arm of the LCQRs is formed. As a result, the ground state tends to localize along it ($d = 28$ nm), thus benefiting from a reduced centrifugal energy.

Meanwhile, the first excited state, which is not so prone to minimize centrifugal forces due to its p-like symmetry, prefers to spread along the external arms of the rings. Finally, for longer inter-ring distances, the QRs start detaching. When the rings are close to each other, tunneling between the two structures is significant and the ground state remains localized mostly in the middle of the LCQRs ($d = 36$ nm), but it soon evolves into the ground state of single QRs, with a tunneling acting as a small perturbation ($d = 38$ nm). All along the dissociation process, the second and higher excited states remain relatively insensitive to changes in d due to their larger kinetic energy.
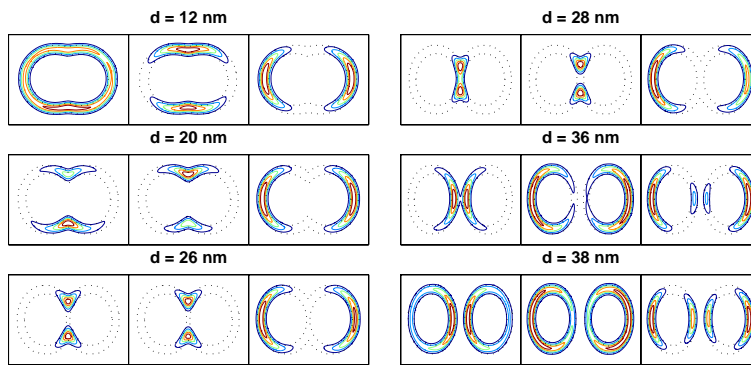
Figure 1. (Color online). Contours of the wave functions corresponding to the three lowest-lying electron states (from left to right) of LCQRs with different inter-ring distance d at $B = 0$. Dotted lines denote the confinement potential profile.

3.2. Effect of external magnetic fields

We next study the response of the electron energy levels to external magnetic fields. In general, the magnetic response can be understood from the $B = 0$ charge distribution described in the previous section. This is particularly clear in the case of an axial magnetic field, where the field barely squeezes the wave functions shown in Fig.1. To illustrate this, let us analyze Figure 2, which depicts the low-lying energy levels against B_z for several inter-ring distances. For $d = 12$ nm, the picture resembles the usual Aharonov-Bohm spectrum of single QRs,[1, 16] save for the anticrossings appearing between sets of two consecutive energy levels. These are due to the fact that the electron states no longer have circular (C_∞) symmetry as in single QRs, but rather elliptical (C_2) one. Therefore, the pairs of eigenvalues which cross one another correspond to the two irreducible representations of the C_2 symmetry group. As d increases and the confining potential elongates, the anticrossing gaps become larger. Moreover, as the two lowest-lying states tend to become the even and odd solutions of a double quantum well, they become nearly degenerate and, being less efficient to trap magnetic flux, the amplitude of their energy oscillations is reduced (see panel corresponding to $d = 20$ nm in Fig. 2). In the next stage, around $d = 28$ nm, the ground state localizes to a large extent along the middle arm of the LCQRs and it takes essentially a singly-connected shape, thus preserving a QD-like magnetic response. On the other side, the first excited state tends to retrieve the p-like symmetry. Therefore, its energy and magnetic behavior become similar to that of the second QD excited state. In the last stage, when the QRs are already detached and the ground state wave function starts delocalizing among the two structures ($d = 36 - 38$ nm), the magnetic response

is essentially that of a single QR with a perturbation arising from the tunneling between the rings, which rapidly diminishes with d. Notice that in this weak-coupling limit, the period of the Aharonov-Bohm oscillations is larger than in the strongly coupled limit. This is due to the smaller area of the inner holes of the individual rings as compared to that of the strongly coupled structure.
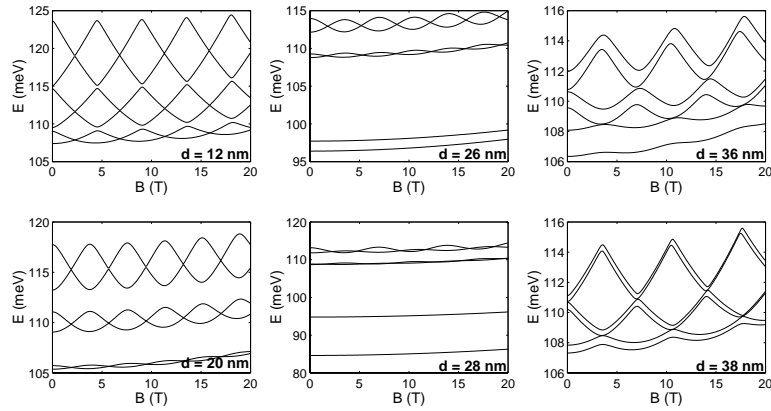
Figure 2. Low-lying electron energy levels vs axial magnetic field in LCQRs with different inter-ring distance.
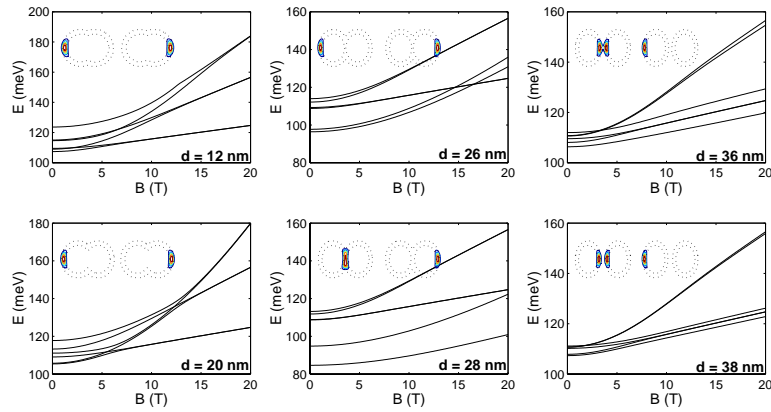
Figure 3. (Color online). Low-lying electron energy levels vs in-plane magnetic field in LCQRs with different inter-ring distance. The field is applied parallel to the dissociation axis. The insets show the wave functions of the two lowest-lying electron states (from left to right) at $B = 20$ T.

Figures 3 and 4 show the energy levels against in-plane magnetic fields directed along the x and y directions, respectively. B_x is applied along the dissociation axis and it tends to squeeze the electron wave function in the y direction. The opposite holds for B_y. In both cases, when the

940

QRs are strongly coupled ($d = 12 - 20$ nm) the effect of the field is to form pairs of degenerate energy levels. These are the even and odd solutions of double quantum wells building up in the longitudinal (B_x) or transversal (B_y) edges of the ring structure, as illustrated in the insets of the figures for the lowest-lying states. The formation of double well solutions at moderate values of in-plane magnetic fields has been also reported for nanoscopic single QRs.[16] An additional feature is however present in LCQRs, because the asymmetric confinement in the x and y directions leads to anisotropic magnetic response. As a result, for instance, one observes that the values of the field at which the double quantum well solutions are obtained are much smaller for B_y than for B_x. Thus, the two lowest-lying states at $d = 12$ nm become degenerate at $B \sim 5$ T for B_y, while they do so at $B \sim 8$ T for B_x. Another difference in the spectrum is the presence of crossings between given energy levels for B_x (e.g. between the first and second excited states), which are missing for B_y. This is because the two p-like states of the strongly coupled QRs are non-degenerate at zero magnetic field, due to the eccentricity of the LCQR system, and the applied field may reverse their energy order depending on the direction. When the coupling between the LCQRs is intermediate ($d \sim 26$ nm), the states which at $B = 0$ have singly-connected wave functions behave as in QD, i.e. they depend weakly on the external field. On the contrary, the doubly-connected states keep on behaving as in a QR, i.e. they tend to form double quantum well solutions. Finally, for weakly coupled QRs ($d \sim 38$ nm), different limits are reached depending on the in-plane magnetic field direction. B_y strongly enhances tunneling between the two QRs, so that the lowest-lying states are double well solutions mostly localized in the vicinity of the tunneling region (see insets in Fig. 4). Conversely, for B_x double well solutions localized either in the inner or in the outer edges of the QRs alternate (see insets in Fig. 3).
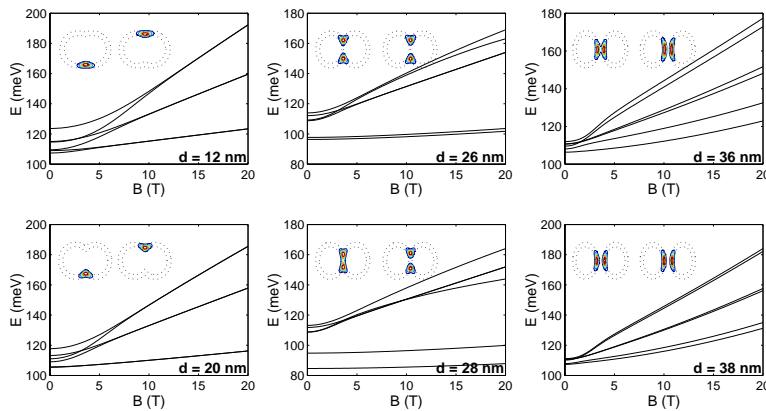
Figure 4. (Color online). Low-lying electron energy levels vs in-plane magnetic field in LCQRs with different inter-ring distance. The field is applied perpendicular to the dissociation axis. The insets show the wave functions of the two lowest-lying electron states (from left to right) at $B = 20$ T.

4. Conclusions

We have studied the electron states of nanoscopic LCQRs as a function of the inter-ring distance and external magnetic fields. The wave function localization at $B = 0$ changes dramatically

depending on the inter-ring distance, and this gives rise to characteristic magnetic responses for strong, intermediate and weak coupling regimes. Moreover, a clearly anisotropic response is found for in-plane fields applied parallel or perpendicular to the LCQRs dissociation direction. These results suggest that probing spectroscopically the magnetic response of electrons in LCQRs may provide valuable information on the strength of coupling and the orientation of the QR molecule.

[1] Viefers S, Koskinen P, Deo PS, and Manninen M, *Physica* E **21**, 1 (2004), and references therein.
[2] Lee BC, Voskoboynikov OP, and Lee CP, *Physica* E **24**, 87 (2004), and references therein.
[3] Neder I, Heiblum M, Levinson Y, Mahalu D, and Umansky V, *Phys. Rev. Lett.* **96**, 016804 (2006).
[4] Austing DG, Sasaki S, Muraki K, Tokura Y, Ono K, Tarucha S, Barranco M, Emperador A, Pi M, and Garcias F, Chapter 2 in *Nano-Physics & Bio-Electronics: A New Odyssey*, Elsevier (2002).
[5] DiVicenzo DP, *Science* **309**, 2173 (2005).
[6] Jaskolski W, Bryant GW, Planelles J, and Zielinski M, *Int. J. Quantum Chem.* **90**, 1075 (2002).
[7] Granados D, Garcia JM, Ben T, and Molina SI, *Appl. Phys. Lett.* **86**, 071918 (2005); Suarez F, Granados D, Dotor ML, and Garcia JM, *Nanotechnology* **15**, S126 (2004).
[8] Climente JI, and Planelles J, *Phys. Rev.* B **72**, 155322 (2005).
[9] Malet F, Barranco M, Lipparini E, Mayol R, Pi M, Climente JI, and Planelles J, to be published in *Phys. Rev.* B (2006).
[10] Mano T, Kuroda T, Sanguinetti S, Ochiai T, Tateno T, Kim J, Noda T, Kawabe M, Sakoda K, Kido G, and Koguchi N, *Nanoletters* **5**, 425 (2005); Kuroda T, Mano T, Ochiai T, Sanguinetti S, Sakoda K, Kido G, and Koguchi N, *Phys. Rev.* B **72**, 205301 (2005).
[11] Szafran B, and Peeters FM, *Phys. Rev.* B **72** 155316 (2005).
[12] Planelles J, and Climente JI, *Eur. Phys. J.* B **48**, 65 (2005).
[13] Climente JI, Planelles J, Barranco M, Malet F, Pi M, to be published in *Phys. Rev.* B (2006).
[14] Lee BC, and Lee CP, Nanotechnology **15**, 848 (2004); Schramm A, Kipp T, Wilde F, Schaefer J, Hyen Ch, and Hansen W, *J. Cryst. Growth* **289**, 81 (2006).
[15] Warburton RJ, Schaflein C, Haft D, Bickel F, Lorke A, Karrai K, Garcia JM, Schoenfeld W, and Petroff PM, *Nature* **405**, 926 (2000).
[16] Planelles J, Climente JI, and Rajadell F, to be published in *Physica* E (2006).
[17] Arnoldi WE, Quart. J. Applied Mathematics **9**, 17 (1951); Saad Y, *Numerical Methods for large Scale Eigenvalue Problems* (Halsted Press, New York, 1992); Morgan RB, Math. Comp. **65**, 213 (1996).
[18] Yamagiwa M, Sumita N, Minami F, and Koguchi N, *J. Lumin.* **108**, 379 (2004).

Dielectric control of spin in semiconductor spherical quantum dots

J. Planelles,[a)] F. Rajadell, and M. Royo
Departament de Química Física i Analítica, UJI, Box 224, E-12080 Castelló, Spain

The ground state electronic configuration of semiconductor spherical quantum dots populated with different numbers of excess electrons, for different radii and dielectric constants of the embedding medium is calculated and the corresponding phase diagram drawn. To this end, an extension of the spin density functional theory to study systems with variable effective mass and dielectric constant is employed. Our results show that high/low spin configurations can be switched by appropriate changes in the quantum dot embedding environment and suggest the use of the quantum dot spin as a sensor of the dielectric response of media. © *2008 American Institute of Physics*.
[DOI: 10.1063/1.2952070]

I. INTRODUCTION

Control over single, localized spins has long been recognized as a relevant issue in fabricated nanostructures and devices.[1] The new building blocks for such devices are quantum dots (QDs), i.e., semiconductor nanostructures that confine carriers in all three spatial dimensions. A very precise fabrication process allows the strength of the QD confinement to be tailored while a gate voltage can tune its countable number of electrons.[2] The great flexibility in designing QDs with precise properties has attracted a large amount of research both in science and technology in the last decade,[3] leading QDs to be employed in many technological applications such as optical switches,[4] light-emitting diodes,[5] photovoltaic cells,[6] etc. Recently, colloidal spherical quantum dots have also proven to offer high performance in biological and medical applications.[7] A specific characteristic of biological and, in general, organic environments is their huge dielectric mismatch with typical inorganic semiconductor QD structures. When QDs are embedded in such environments, the formation of polarization charges at the interface may strongly influence confinement and modify the distribution of charge carriers inside the QD. The effects of dielectric mismatches therefore cannot be overlooked in the theoretical description.[8] Thus, enhancement of the electron-electron Coulomb interaction, which arises from polarization effects, is found to induce reconstructions of the electronic configurations as the dot is filled with carriers.[9–12]

There are various parameters that influence the electronic configuration in semiconductor quantum dots, such as the number of electrons, the shape and strength of the confining potential and external fields. The key ingredient for manipulating the way of spin filling is the tuning of orbital degeneracies. One can have, for example, a triplet state with two parallel spin electrons in two different but nearly degenerate orbitals. The excited state is then a spin singlet having the same orbital configuration but with antiparallel spins.

Manipulation of orbital degeneracies in quantum dots is usually carried out by magnetic fields in the relatively low range of magnetic field strengths. Among others, we may mention studies on triplet-singlet transitions induced by a magnetic field.[13] In the high magnetic field range the interaction effect becomes more important than the effect of quantum mechanical confinement because all the electrons are confined to the lowest Landau level. This gives rise to a fully spin-polarized state.

A remarkable many-particle phenomenon observed in a quantum dot, when tuning ground-state degeneracy between triplet- and singlet-spin states, is the so-called integer Kondo effect.[14] This effect is also predicted as coming from degeneracy tuned by disorder[15] and can occur for impurities and quantum dots that have a spin of 1, or higher.[16]

We focus our attention on the role of dielectric mismatch in QD spin transitions. We draw the ground state spin phase diagram of a semiconductor spherical quantum dot populated with different numbers of electrons versus the dielectric response of the embedding media. To this end, we work within the spin density functional theory (SDFT) framework. Particularly, we use a method we recently developed[11] and tested[11,12] that is capable of studying many-electron spherical QDs including effective mass and dielectric mismatches between the QD and the surrounding medium. Our results evidence the possibility of switching between high/low spin configurations by changing the QD embedding environment, and suggest the use of QD spin as a sensor of the dielectric response of a given medium.

II. THEORY AND COMPUTATIONAL DETAILS

Calculations are carried out within the framework of the density functional theory (DFT) in the self-consistent formulation of Kohn and Sham.[17] This theory has proven to be particularly powerful for studying large electron systems in the presence of correlation.[18,19] According to Hohenberg and Kohn[20] and its generalization by Levy,[21] the exact ground-state energy of a many-body system is a unique functional of the electron density $n(\mathbf{r})$. DFT was initially developed in a spin-independent formalism. Later, effects of spin polarization were incorporated into the so-called SDFT.[22] In this approach the total energy is a functional of the spin-up and spin-down densities $n_\sigma(\mathbf{r})$, where $\sigma=(+,-)$ labels the spin. Equivalently, the energy is a functional of the total density

a)Electronic mail: josep.planelles@qfa.uji.es.

$n(\mathbf{r})=n_+(\mathbf{r})+n_-(\mathbf{r})$ and spin-polarization $\zeta(\mathbf{r})=[n_+(\mathbf{r})-n_-(\mathbf{r})]/n(\mathbf{r})$. The ground state is found by minimizing the energy functional, leading to the well-known Kohn–Sham equations. Although the original proof of Hohenberg and Kohn[20] applies only to the ground state, it can be generalized to a large class of excited states, namely the energetically lowest state of each symmetry.[23] For example, it can be applied to the lowest state of a spherical QD with specific quantum numbers L, S, M, and M_S of the total orbital and spin angular momenta. This allows us, in particular, to study several low-lying electronic configurations with different M_S and to draw the spin phase diagram of the ground state of a semiconductor spherical quantum dot populated with different numbers of electrons versus a given control parameter.[24]

Since the calculations in this paper concern spherical QDs embedded in media with different dielectric constants and, additionally, carriers have different effective masses in the QD and the surrounding environment, we have to extend the SDFT to include variable effective mass and dielectric constants. We have recently carried out this extension and built the corresponding code. A fully detailed description of it can be found in Ref. 11. In short, it is an extension of the SDFT,[22] which includes (1) position-dependent effective mass by replacing the standard kinetic energy operator $-(\hbar^2/2m^*)\nabla^2$ by $-(\hbar^2/2)\nabla[(1/m^*)\nabla]$, corresponding to the case of variable effective mass. (2) Polarization of the Coulomb interaction arising from the dielectric mismatch, by numerically integrating the Poisson equation $\nabla[\varepsilon(r)\nabla\Psi(r)]=-4\pi n(r)$. (3) Self-energy, also coming from the dielectric mismatch, by incorporating the monoelectronic self-polarization potential according to the equations reported in Ref. 25. This dielectric confinement and the spatial confinement potentials are the genuine single-particle components of the Kohn–Sham potential. (4) The effect of dielectric mismatch on exchange by means of an appropriate scaling of the exchange functional, which is consistent with the Coulomb functional employed. And finally, (5) the correlation functional is also modified to incorporate the position-dependent parameters properly by means of a consistent scaling of Perdew–Zunger analytical functional that was employed.[26]

By using this code, we have thus drawn the ground state spin phase diagrams versus the QD radius R and the dielectric constant ε_{ext} of the surrounding medium. We have performed the calculations in the case of ZnS QD populated with $N=3$, 4, and 9 electrons, although, as discussed later, the qualitative trends obtained can be generalized to other materials and different numbers of electrons. The material parameters employed in our calculations, namely the electron effective mass $m^*_{ZnS}=0.34$ and dielectric constant $\varepsilon_{ZnS}=5.7$, are taken from Ref. 27. Spherical QDs are often prepared in water solutions ($\varepsilon_{H_2O}=1.78$) and polymeric media (dielectric constants ranging from $\varepsilon=2$ up to $\varepsilon=25$ have been reported for these media[28,29]). Thus, in our calculations, the external dielectric constant ε_{ext} of the surrounding medium ranges from $\varepsilon_{ext}=1$, corresponding to air or a vacuum, up to $\varepsilon_{ext}=50$. We assume an external effective mass $m^*_{ext}=1$ and a 4 eV confining potential barrier height.[30]
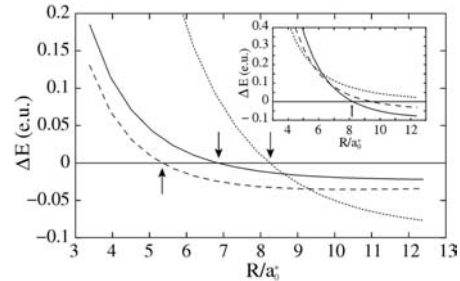
FIG. 1. Energy difference ΔE (e.u.) between spin polarized minus spin least-polarized electronic configurations vs QD radius R (e.u.) corresponding to a QD populated with three (full line), four (dashed line), and nine (dotted line) excess electrons. Arrows indicate the transition phase. Inset: Energy difference ΔE (e.u.) between the electronic configuration $1s1p^31d^5$ (full line), $1s^21p^31d^4$ (dashed line), and $1s1p^61d^2$ (dotted line) minus $1s^21p^61d$ vs QD radius R (e.u.). The arrow indicates the transition phase.

III. RESULTS AND DISCUSSION

The electronic configuration of an atom or a QD is determined by the balance of two factors, namely, the energy difference between consecutive orbitals and the pairing energy. In general, the Aufbau principle of sequential filling and the Hund rule of largest spin multiplicity in a shell are followed. However, as pointed out earlier, QDs can be tailored with precise properties, such as their radius. This fact allows the spin filling to be manipulated by tuning the energy gap between consecutive orbital levels.

We therefore start our study by exploring the critical radius leading to a change in the electronic configuration. In a first set of calculations we consider the same effective mass and dielectric constant for the QD and the surrounding medium. This allows us to work in effective atomic units and thus yield universal results. The only parameter included in these calculations is the height of the confining barrier, which is fixed to a value as large as 14 e.u. (effective Hartree). 14 e.u. corresponds to 4 eV for ZnS. We carry out calculations for a range of radii from 3 up to 12 effective Bohr radius a^*_0 and a number of electrons $N=3$, 4, and 9. The results thus obtained are summarized in Fig. 1, where the energy difference ΔE (e.u.) between fully spin-polarized minus least spin-polarized configurations is plotted versus the QD radius R/a^*_0.

In all the cases that were studied, only two configurations, namely least-polarized and fully polarized, become the ground state. Thus, for $N=3$ the configuration $1s^21p$ is the lowest lying for $R<7a^*_0$ and $1s1p^2$ otherwise. For $N=4$ it is $1s^21p^2$ up to $R\sim5.5a^*_0$ and then $1s1p^3$. Finally, when $N=9$, $1s^21p^61d$ is the ground state if $R<8.3a^*_0$ and $1s1p^31d^5$ if R is larger.

One may wonder whether configurations others than least-polarized and fully polarized can lie the lowest. However, this does not hold for the cases that were studied. In order to show this in the most challenging case of $N=9$ electrons, in the inset in Fig. 1 we plot the difference ΔE between the energy of configurations $1s1p^31d^5$, $1s^21p^31d^4$, and

187

014313-3   Planelles, Rajadell, and Royo   J. Appl. Phys. **104**, 014313 (2008)

$1s1p^6 1d^2$, on the one hand, and $1s^2 1p^6 1d$, on the other, versus the QD radius. It can be seen that, for short effective radii, the larger the polarization is, the greater the resulting energy will be, while the opposite holds for large radii. There is, however, a central region where the energy ordering of configurations is neither one nor the other. Nevertheless, it can also be seen that only the spin least-polarized $1s^2 1p^6 1d$ and the fully spin-polarized $1s1p^3 1d^5$ configurations become the ground state.

Finally, since Fig. 1 is drawn in effective units, it is straightforward to conclude that QDs built of materials with small Bohr radii are the best candidates to be used for dielectric control of spin because the transition between configurations occurs at shorter radii and the energetic change resulting from QD manipulation is larger. In order to show the dielectric control of spin we chose QDs built of ZnS. It is a wide-gap semiconductor material, so that the conduction-valence coupling is negligible, i.e., nonparabolicity corrections can be safely neglected. This material has an effective Bohr radius of $a_0^* \sim 17a_0$ and an effective energy (1 e.u.) of $\sim 10^{-2}$ a.u. We then consider, first, the case of $N=3$ excess electrons and proceed as follows. From Fig. 1 we can see that the transition between configurations occurs at about $7a_0^*$, i.e., ~ 6 nm for ZnS. Thus, working within the range of radii between 4 and 8 nm, we calculate the energy of the relevant configurations of $N=3$ excess electrons ZnS QD embedded in media with a dielectric constant ranging from 1 up to 50. From these calculations we determine the ground state configuration for each pair (R, ε_{ext}). From this phase diagram shown in Fig. 2(a) can be drawn. The line in this figure corresponds to the phase transition. Above the line the spin-polarized $1s1p^2$ configuration is the lowest lying, i.e., the ground state, while below it the ground state corresponds to the least-polarized $1s^2 1p$ configuration.

The physical source of dielectric control is polarization coming from the dielectric mismatch between the QD and the surroundings. In order to show this, we select the critical QD radius corresponding to the degeneracy of the two configurations when the QD is buried in a medium without dielectric mismatch ($\varepsilon_{ext} = \varepsilon_{QD}$). We then replace the external medium by another with a lower dielectric constant ($\varepsilon_{ext} < \varepsilon_{QD}$). The resulting dielectric mismatch leads each electron in the QD to induce a negative polarized charge at the QD border, thus enhancing the Coulomb interaction between carriers. This means that pairing energy is also enhanced and therefore the polarized configuration is preferred. In a similar way, the situation $\varepsilon_{ext} > \varepsilon_{QD}$ leads to a decrease in the Coulomb interaction and consequently to a decrease in the pairing energy so that a transition toward least-polarized configurations now occurs. This can be shown in Fig. 2(a) by choosing any point on the transition line and then moving left (toward smaller dielectric constants). By so doing we find the fully spin-polarized configuration. Nevertheless, moving right, and thus increasing ε_{ext}, we find the other least-polarized configuration.

The inset in Fig. 2(a) corresponds to a 5.5 nm radius ZnS QD. In this inset we have drawn the energy difference (meV) between the spin least- and fully polarized configuration versus ε_{ext}. This plot allows us to see, for example, that a "dry"

FIG. 2. Ground state phase diagram of a ZnS QD populated with three (a), four (b), and nine (c) excess electrons. Schematic diagrams for electronic configurations label the regions of existence (below/above the transition line) in the QD radius R (nm) vs the external dielectric constant ε_{ext} phase diagram. Insets: Energy difference ΔE (meV) of the spin least-polarized minus spin full polarized configuration vs the external dielectric constant ε_{ext} for a fixed value of the QD radius R (indicated at the top right of the inset). The arrow indicates the transition phase.

5.5 nm radius ZnS QD, i.e., this QD in air ($\varepsilon_{ext} = 1$), has a fully polarized ground state configuration ($S = 3/2$). However, if this QD is embedded in a polymeric solution of dielectric response, for example, $\varepsilon_{ext} = 4$, a transition toward the least-polarized ($S = 1/2$) configuration occurs. A solution with a dielectric constant of about 2.8 is able to tune degeneracy between both lowest-lying electronic configurations.

Figures 2(b) and 2(c) display the phase diagrams corresponding to $N=4$ and $N=9$ excess electrons. The results and diagrams obtained are qualitatively the same as in the case of $N=3$ electrons, but the changes in spin and/or energy are

larger. In the case $N=4$, the configurations involved have spins $S=1$ and $S=2$, while for $N=9$ a change in the dielectric environment can yield a transition between $S=1/2$ and $S=9/2$.

IV. CONCLUDING REMARKS

This paper is devoted to studying the role of dielectric mismatch in QD spin transitions. To this end, spin phase diagrams of QDs populated with different numbers of electrons versus the dielectric constant of the QD surroundings have been calculated. Our results show that it is possible to switch between high/low spin configurations by means of an appropriate QD environment and suggest the use of QD spin as a sensor of the dielectric response of a given medium.

[1]G. A. Prinz, Science **282**, 1660 (1998).
[2]S. Tarucha, D. G. Austing, T. Honda, R. J. van der Hage, and L. P. Kouwenhoven, Phys. Rev. Lett. **77**, 3613 (1996).
[3]*Semiconductor Spintronics and Quantum Computation*, edited by D. D. Awschalom, D. Loss, and N. Samarth (Springer, Berlin, 2002); Y. Masumoto and T. Takagahara, *Semiconductor Quantum Dots* (Springer, Berlin, 2002); A. D. Yoffe, Adv. Phys. **50**, 1 (2001); L. Jacak, P. Hawrylak, and A. Wójs, *Quantum Dots* (Springer, Berlin, 1998); T. Chakraborty, *Quantum Dots* (Elsevier, Amsterdam, 1999).
[4]C. Wang, M. Shim, and P. Guyot-Sionnest, Science **291**, 2390 (2001).
[5]S. Coe, W.-K. Woo, M. Bawendi, and V. Bulović, Nature (London) **420**, 800 (2002).
[6]W. U. Huynh, J. J. Dittmer, and A. P. Alivisatos, Science **295**, 2425 (2002).
[7]J. M. Klostranec and W. C. W. Chan, Adv. Mater. **18**, 1953 (2006).
[8]J. L. Movilla and J. Planelles, Phys. Rev. B **71**, 075319 (2005); J. L. Movilla, J. Planelles, and W. Jaskólski, *ibid.* **73**, 035305 (2006); J.

Planelles and J. L. Movilla, *ibid.* **73**, 235350 (2006); J. L. Movilla and J. Planelles, *ibid.* **74**, 125322 (2006); F. Rajadell, J. L. Movilla, M. Royo, and J. Planelles, *ibid.* **76**, 115312 (2007).
[9]A. Orlandi, M. Rontani, G. Goldoni, F. Manghi, and E. Molinari, Phys. Rev. B **63**, 045310 (2001); A. Orlandi, G. Goldoni, F. Manghi, and E. Molinari, Semicond. Sci. Technol. **17**, 1302 (2002).
[10]A. Franceschetti and A. Zunger, Phys. Rev. B **62**, 2614 (2000).
[11]M. Pi, M. Royo, and J. Planelles, J. Appl. Phys. **100**, 073712 (2006).
[12]M. Royo, J. Planelles, and M. Pi, Phys. Rev. B **75**, 033302 (2007); J. Appl. Phys. **102**, 094304 (2007).
[13]S. Tarucha, D. G. Austing, Y. Tokura, W. G. van der Wiel, and L. P. Kouwenhoven, Phys. Rev. Lett. **84**, 2485 (2000).
[14]S. Sasaki, S. De Franceschi, J. M. Elzerman, W. G. van der Wiel, M. Eto, S. Tarucha, and L. P. Kouwenhoven, Nature (London) **405**, 764 (2000).
[15]M.-H. Chung, Phys. Rev. B **70**, 113302 (2004).
[16]L. Kouwenhoven and L. Glazman, Phys. World **14**, 33 (2001).
[17]W. Kohn and L. J. Sham, Phys. Rev. **140**, A1133 (1965).
[18]R. G. Parr and W. Yang, *Density-Functional Theory of Atoms and Molecules* (Oxford University Press, Oxford, 1989).
[19]E. Lipparini, *Modern Many-Particle Physics* (World Scientific, Singapore, 2003).
[20]P. Hohenberg and W. Kohn, Phys. Rev. **136**, B864 (1964).
[21]M. Levy, Proc. Natl. Acad. Sci. U.S.A. **76**, 6062 (1979).
[22]U. von Barth and L. Hedin, J. Phys. C **5**, 1629 (1972).
[23]O. Gunnarsson and B. I. Lundqvist, Phys. Rev. B **13**, 4274 (1976).
[24]Please note that, as in the case of unrestricted Hartree–Fock, SDFT wave functions are M_S but not S adapted.
[25]J. L. Movilla and J. Planelles, Comput. Phys. Commun. **170**, 144 (2005).
[26]J. P. Perdew and A. Zunger, Phys. Rev. B **23**, 5048 (1981).
[27]D. Dorfs, H. Henschel, J. Kolny, and A. Eychmüller, J. Phys. Chem. B **108**, 1578 (2004).
[28]A. Issac, Ch. von Borczyskowski, and F. Cichos, Phys. Rev. B **71**, 161302(R) (2005).
[29]J. Lee, B. Yang, R. Li, T. A. P. Seery, and F. Papadimitrakopoulos, J. Phys. Chem. B **111**, 81 (2007).
[30]The height for the spatial confining barrier of a QD in a vacuum should be set to the QD electroaffinity and, for a QD embedded in a given medium, to the corresponding band offset. In our calculation this height is always very large, and we deal with the ground state. Then, as the numerical results are insensitive to relatively small changes in the height of this very high spatial confining barrier, we have always assumed the same 4 eV height.

189

Isospin phases of vertically coupled double quantum rings under the influence of perpendicular magnetic fields

M. Royo,[1] F. Malet,[2,*] M. Barranco,[2] M. Pi,[2] and J. Planelles[1,†]

[1]*Departament de Química Física i Analítica, Universitat Jaume I, Box 224, E-12080 Castelló, Spain*
[2]*Departament ECM and IN2UB, Facultat de Física, Universitat de Barcelona, Diagonal 647, 08028 Barcelona, Spain*
(Received 30 July 2008; published 7 October 2008)

Vertically coupled double quantum rings submitted to a perpendicular magnetic field B are addressed within the local spin-density-functional theory. We describe the structure of quantum ring molecules containing up to 40 electrons considering different inter-ring distances and intensities of the applied magnetic field. When the rings are quantum mechanically strongly coupled, only bonding states are occupied and the addition spectrum of the artificial molecules resembles that of a single-quantum ring, with some small differences appearing as an effect of the magnetic field. Despite the latter's tendency to flatten the spectra, in the strong-coupling limit, some clear peaks are still found even when $B \neq 0$ that can be interpreted from the single-particle energy levels similarly as in the zero magnetic field case, namely, in terms of closed-shell and Hund's-rule configurations. By increasing the inter-ring distance, the occupation of the first antibonding orbitals washes out such structures and the addition spectra become flatter and irregular. In the weak-coupling regime, numerous isospin oscillations are found as functions of B.

PACS number(s): 73.21.−b, 85.35.Be, 71.15.Mb, 75.75.+a

I. INTRODUCTION

Systems made of correlated electrons confined in semiconductor nanoscopic dot and ring structures, the so-called quantum dots (QDs) and rings (QRs), respectively, have been the subject of intense theoretical and experimental researches (see, e.g., Refs. 1 and 2 and references therein). From the latter point of view, for quantum dots, it has been proved[3] the possibility to tune over a wide range the number of electrons contained in the system, as well as to control both the size and the shape of the dots by means of external gate voltages—a goal that has not been achieved yet for ring geometries due to the higher complexity of their fabrication process,[4–6] which involves several experimental techniques such as atomic force microscopy,[7] strain-induced self-organization,[4] and droplet molecular-beam epitaxy.[8]

The interest of QRs arises from their peculiar behavior in the presence of a perpendicularly applied magnetic field (B), which is very distinct from that observed in QDs and shows up as an oscillatory behavior of their energy levels as a function of B. This property, together with the fact that in narrow enough QRs the electrons experiment a nearly one-dimensional Coulomb repulsion, leads to the integer and fractional Aharonov-Bohm effects usually associated with the appearance of the so-called persistent currents in the ring.[9] These quantum-interference phenomena have been experimentally reported[10] and have motivated a series of theoretical works whose number is steadily increasing (see, e.g., Refs. 11–16 and references therein).

One of the most appealing possibilities offered by electron systems confined in semiconductor heterostructures is their ability to form coupled entities, usually referred to as "artificial molecules," in which the role of the constituent "atoms" is played by single-quantum dots or rings and that have analogies with natural molecules such as the hybridization of the electronic states forming moleculelike orbitals. In addition, these artificially coupled systems present important

advantages such as a tunable "interatomic" coupling by means of, e.g., the modification of the relative position/size of the constituents. This fact has, besides its intrinsic interest, potential relevance to quantum information processing schemes since basic quantum gate operations require controllable coupling between qubits. In this sense, artificial molecules based on two coupled QDs called quantum dot molecules (QDMs) have been proposed as scalable implementations for quantum computation purposes and have received great attention from the scientific community in the last years (see, e.g., Refs. 17–26 and references therein).

Also, molecular-beam epitaxy techniques have recently allowed the synthesis of *quantum ring molecules* (QRMs) in the form of concentric double QRs (Refs. 27 and 28) and vertically stacked layers of self-assembled QRs.[29,30] The optical and structural properties of the latter have also been characterized by photoluminescence spectroscopy and by atomic force microscopy, respectively. This has sparked theoretical studies on the structure and optical response of both vertically and concentrically coupled QRs of different complexity and scope, revealing properties different from those of their dot counterparts due to the nonsimply connected ring topology. For instance, studies on the single-electron spectrum of vertical QRMs (Refs. 31 and 32) have shown that the electronic structure of these systems is more sensitive to the inter-ring distance than that of coupled QDs. As a consequence, in ring molecules, quantum tunneling effects are enhanced since less tunneling energy is required to enter the moleculelike phase. Also, the consideration of "heteronuclear" artificial molecules constituted by slightly different QRs offers the interesting possibility to control the effective coupling of direct-indirect excitons[33] by means of the application of a magnetic field and taking advantage of the fact that charge tunneling between states with distinct angular momentum is strongly suppressed by orbital selection rules. To this end, some authors have considered the case of QRMs

165308-1

made of strictly one-dimensional zero-thickness QRs and have used diagonalization techniques to address the few-electron problem.[31,33–35] The simultaneous effect of both electric and magnetic fields applied to a single-electron QRM has also been studied[36] (see also Ref. 31), and the optical response of QRMs where the thickness of the constituent QRs is taken into account has been obtained.[37] In addition, the spatial correlation between electron pairs in vertically stacked QRs has been shown to undergo oscillations as functions of the magnetic flux, with strongly correlated situations between ground states (gs's) with odd angular momentum turning out to occur even at large inter-ring distances.[34] More recently, the structure of a QRM made of two vertically stacked quantum rings has been addressed at zero magnetic field for a few tens of electrons within the local spin-density-functional theory (LSDFT) neglecting[38] and incorporating[39] the vertical thickness of the constituent QRs.

In this work we address the gs of two thick vertically coupled identical quantum rings forming "homonuclear" QRMs populated with up to 40 electrons and pierced by a perpendicularly applied magnetic field. We extend in this way our previous study,[39] addressing the appearance and physical interplay between the spin and isospin[23] degrees of freedom as functions of the variation in both the intensity of the magnetic field and the inter-ring separation. Modeling systems charged with such large number of electrons requires the employment of methodologies that minimizes the computational cost. Here we have made use of the LSDFT,[13,15] whose accuracy for the considered values of the magnetic field has been assessed[24] by comparing the obtained results for a single QD with those given by the current-spin-density-functional theory,[40] which is in principle better suited for high magnetic fields and also with exact results for artificial molecules.[41]

This paper is organized as follows. In Sec. II we briefly introduce the LSDFT and the model used to represent the vertical QRMs. In Sec. III we discuss the obtained results for some selected configurations and a summary is given in Sec. IV.

II. DENSITY-FUNCTIONAL CALCULATION FOR MANY-ELECTRON VERTICAL QUANTUM RING HOMONUCLEAR MOLECULES

The axial symmetry of the system allows one to work in cylindrical coordinates. The confining potential $V_{cf}(r,z)$ has been taken parabolic in the xy plane with a repulsive core around the origin, plus a symmetric double quantum well in the z direction, each one with width w, depth V_0, and separated by a distance d. To improve on the convergence of the calculations, the double-well profile has been slightly rounded off as illustrated in Fig. 2 of Ref. 24. The potential thus reads $V_{cf}(r,z)=V_r(r)+V_z(z)$, where

$$V_r(r) = V_0\Theta(R_0 - r) + \frac{1}{2}m\omega_0^2(r - R_0)^2\Theta(r - R_0),$$

$$V_z(z) = V_0 \begin{cases} \dfrac{1}{1 + e^{(z+d/2+w)/\sigma}} - \dfrac{1}{1 + e^{(z+d/2)/\sigma}} & \text{if } z \leq 0 \\[3mm] \dfrac{1}{1 + e^{(z-d/2)/\sigma}} - \dfrac{1}{1 + e^{(z-d/2-w)/\sigma}} & \text{if } z > 0, \end{cases}$$

$$(1)$$

with $\sigma=2\times10^{-3}$ nm and $\Theta(x)=1$ if $x>0$ and zero otherwise. The convenience of using a hard-wall confining potential to describe the effect of the inner core in QRs is endorsed by several works in the literature.[42] We have taken $R_0=10$ nm, $V_0=350$ meV, $\hbar\omega_0=6$ meV, and $w=5$ nm. These parameters determine the confinement for the electrons together with the distance between the constituent quantum wells that is varied to study QRMs in different inter-ring coupling regimes.

For small electron numbers (N), it is justified to take ω_0 to be N independent. However, in a more realistic scheme its value should be tuned according to the number of electrons contained in the system, relaxing the confinement as the latter is increased. In the case of quantum dots it has often been used a $N^{-1/4}$ dependence that arises from the r expansion near the origin of the Coulomb potential created by a two-dimensional uniform positive charge distribution (jellium model) and that it is generalized to the case of quantum dot molecules as $\omega_0=\kappa N_B^{-1/4}$ with N_B being the number of electrons filling bonding (B) orbitals (see below). The rationale for this generalization is given in Ref. 25. It is clear that the mentioned N dependence would be harder to justify for QRs, and in fact no alternative law is known for a single QR that could be generalized to the case of QRMs. For this reason, in this work, we have taken ω_0 to be N independent, which is to some extent less realistic for the largest values of N we have considered.

Considering the N-electron system placed in a magnetic field parallel to the z axis, within LSDFT in the effective mass, dielectric constant approximation, the Kohn-Sham equations[24,43] in cylindrical coordinates read

$$\left[-\frac{1}{2}\left(\frac{\partial^2}{\partial r^2} + \frac{1}{r}\frac{\partial}{\partial r} - \frac{l^2}{r^2} + \frac{\partial^2}{\partial z^2} \right) - \frac{\omega_c}{2}l + \frac{1}{8}\omega_c^2 r^2 + V_{cf}(r,z) + V_H \right.$$
$$\left. + V_{xc} + \left(W_{xc} + \frac{1}{2}g^*\mu_B B \right)\eta_\sigma \right] u_{nl\sigma}(r,z) = \varepsilon_{nl\sigma} u_{nl\sigma}(r,z),$$

$$(2)$$

where the single-particle (sp) wave functions have been taken to be of the form $\phi_{nl\sigma}(r,z,\theta,\sigma)=u_{nl\sigma}(r,z)e^{-il\theta}\chi_\sigma$, where $n=0,1,2,\ldots$, $l=0,\pm1,\pm2,\ldots$ with $-l$ being the projection of the single-particle orbital angular momentum on the symmetry axis, and $\sigma=\uparrow$ ($\downarrow$) representing spin-up (-down) states. The vector potential has been chosen in the symmetric gauge, namely, $\mathbf{A}=B(-y,x,0)/2$; $\mu_B=\hbar e/(2m_ec)$ and $\omega_c=eB/c$ are, respectively, the Bohr magneton and the cyclotron frequency and $\eta_\sigma=+1$ (−1) for $\sigma=\uparrow$ ($\downarrow$); $V_H(r,z)$ is the direct Coulomb potential and $V_{xc}=\partial\mathcal{E}_{xc}(n,m)/\partial n|_{gs}$ and $W_{xc}=\partial\mathcal{E}_{xc}(n,m)/\partial m|_{gs}$ are the variations in the exchange-correlation energy density $\mathcal{E}_{xc}(n,m)$ in terms of the electron density $n(r,z)$ and of the local spin magnetization $m(r,z)$
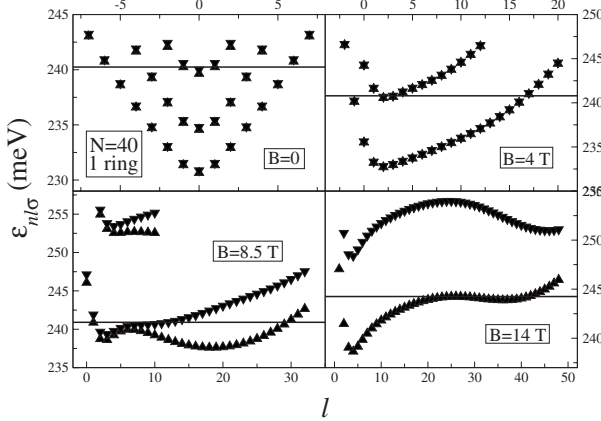
FIG. 1. Single-electron energies (meV) as functions of l for a $N=40$ single ring. Upward (downward) triangles denote ↑ (↓) spin states. The horizontal lines represent the Fermi levels. The value of B(T) is indicated in each panel.

$\equiv n^{\uparrow}(r,z)-n^{\downarrow}(r,z)$ taken at the gs. $\mathcal{E}_{xc}(n,m) \equiv \mathcal{E}_{x}(n,m) + \mathcal{E}_{c}(n,m)$ has been built from three-dimensional homogeneous electron gas calculations; this yields a well-known[44] simple analytical expression for the exchange contribution $\mathcal{E}_{x}(n,m)$. For the correlation term $\mathcal{E}_{c}(n,m)$ we have used the parametrization proposed by Perdew and Zunger.[45] Details about how the Kohn-Sham and the Poisson equations have been solved can be found in Ref. 43. Notice the use of effective atomic units $\hbar=e^{2}/\epsilon=m=1$ in Eq. (2), where ϵ is the dielectric constant and m is the electron effective mass. In units of the bare electron mass m_{e} one has $m=m^{*}m_{e}$ with the length unit being the effective Bohr radius $a_{0}^{*}=a_{0}\epsilon/m^{*}$ and the energy unit the effective Hartree $H^{*}=Hm^{*}/\epsilon^{2}$. In the numerical applications we have considered GaAs quantum rings, for which we have taken $\epsilon=12.4$ and $m^{*}=0.067$; this yields $a_{0}^{*}\sim 97.9$ Å and $H^{*}\sim 11.9$ meV with the effective gyromagnetic constant $g^{*}=-0.44$.

To label the gs configurations ("phases") we use an adapted version of the ordinary spectroscopy notation,[41] namely, $^{2S+1}L_{g,u}^{\pm}$, where S and L are the total $|S_{z}|$ and $|L_{z}|$, respectively. The superscript $+$ $(-)$ corresponds to symmetric (antisymmetric) states under reflection with respect to the $z=0$ plane bisecting the QRMs and the subscript $g(u)$ refers to positive (negative) parity states. All of these are good quantum numbers even in the presence of an axial magnetic field. By analogy with natural molecules, symmetric and antisymmetric states are referred to as B and antibonding (AB) orbitals, respectively. We have defined the "isospin" quantum number I_{z} (bond order in Molecular Physics) as[22,24,41] $I_{z}=(N_{B}-N_{AB})/2$ with $N_{B(AB)}$ being the number of occupied bonding (antibonding) sp states.

III. RESULTS

Due to the large number of variables needed to characterize a given QRM configuration (electron number, magnetic field, and inter-ring distance), we limit ourselves to present results in a limited range of values for such variables, aiming

at discussing calculations that might illustrate the appearance of some properties of the systems under study. For the sake of comparison, we have also addressed one single QR symmetrically located with respect to the $z=0$ plane with the same thickness (5 nm) and radial confinement as the coupled rings.

Figure 1 shows the Kohn-Sham sp levels for one single ring hosting $N=40$ electrons as a function of l for different values of the applied magnetic field. As it is well known, these levels are $\pm l$ degenerate at $B=0$. In this particular case, the gs has $S_{z}=1$, and it is made up of symmetric (with respect to $z=0$) sp states with up to $n=3$. In the noninteracting single-electron model, in which the Coulomb energy is not considered and consequently the sp wave functions factorize into a r-dependent and a z-dependent part with associated quantum numbers n_{r} and n_{z}, i.e., $u_{nl}(r,z)\rightarrow \mathcal{U}_{n_{r}}(r)\mathcal{Z}_{n_{z}}(z)$, one would say that the gs is made up of sp states with $n_{z}=0$ and radial quantum numbers up to $n_{r}=3$.

When $B\neq 0$, the $\pm l$ degeneracy is lifted and, on the other hand, the $l<0$ sp levels become progressively depopulated in favor of those with $l>0$ as the magnetic field increases until eventually (at about ~ 4 T) only $l>0$ orbitals are filled. At this point, only a few states with $n=2$ are occupied and the ring has $S_{z}=0$. From this value of B, the simultaneous filling of increasingly higher-l states and those close to $l=0$ gives rise to configurations containing only states with $n=1$ and with large values of the total spin (e.g., $S_{z}=9$ for $B=8$ T). Eventually, the system becomes fully spin polarized at $B\sim 13.5$ T. It is worth noticing the conspicuous bending of the "Landau bands" (sets of bonding or antibonding states characterized by the same n and spin and different value of l) instead of displaying a fairly flat region, as it happens when the in-plane confinement is produced by a jelliumlike potential[13] but not with our present choice of a N-independent parabola. It is also worth to stress that, due to the much stronger confinement in the vertical direction as compared to that in the radial one, only symmetric states are occupied.
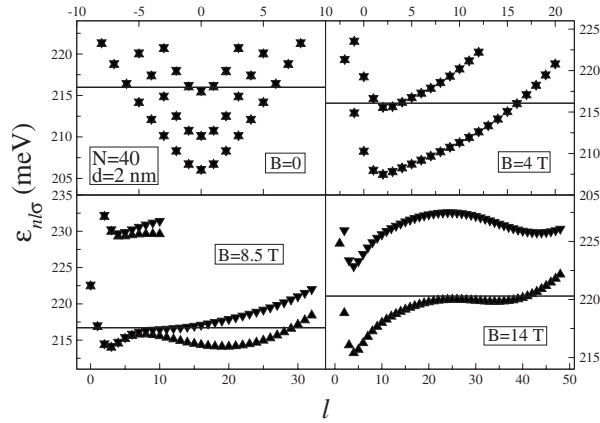
FIG. 2. Same as Fig. 1 for a QRM with $N=40$ electrons and $d=2$ nm. Notice that due to the small separation between the rings only bonding states are occupied. The antibonding ones are lying at much higher energies.

Analogously, the energy levels corresponding to QRMs with $N=40$ and inter-ring distances $d=2$, 4, and 6 nm are shown in Figs. 2–4. One can see the gradual evolution of the system as d increases; indeed, at $d=2$ nm the spectrum is very similar to that of the single ring with only bonding sp states being occupied. As d increases, a few antibonding orbitals become populated at small B's, as one can see from the top panels of Fig. 3, corresponding to $d=4$ nm; but eventually, for increasing values of B, the QRMs have again ground states where only bonding states are populated as can be seen from the bottom panels of the same figure. For this inter-ring distance, the fully spin-polarized state is reached at $B \sim 13.75$ T. Finally, for the largest ring separation considered, namely, $d=6$ nm, a large amount of antibonding orbitals becomes occupied giving rise to small I_z's instead of the fairly large isospin values found for similar configurations at smaller distances (compare the bottom panels in Fig. 4 with

those in Figs. 2 and 3). In particular, the fully spin-polarized gs is found at about $B \sim 7$ T with $I_z=2$, whereas for $d=2$ and 4 nm it appears near $B=14$ T and has the maximum possible isospin value, namely, $I_z=20$. At $d=6$ nm, the maximum-spin state naturally consists of two distinct bands: one made up of bonding and another of antibonding states. These configurations are the QRM analogs of the maximum density droplet (MDD) configurations found for QDMs at similar inter-dot distances called, respectively, MDD$_B$ and MDD$_{AB}$ in Ref. 25. Increasing further the magnetic field causes the progressive occupation of higher-l orbitals, which provokes the depopulation of the antibonding band and the consequent increase in I_z. For the highest considered magnetic field ($B \sim 14$ T), some antibonding orbitals are still occupied yielding $I_z=17$.

These results are a consequence of the evolution with d of the energy difference between bonding and antibonding
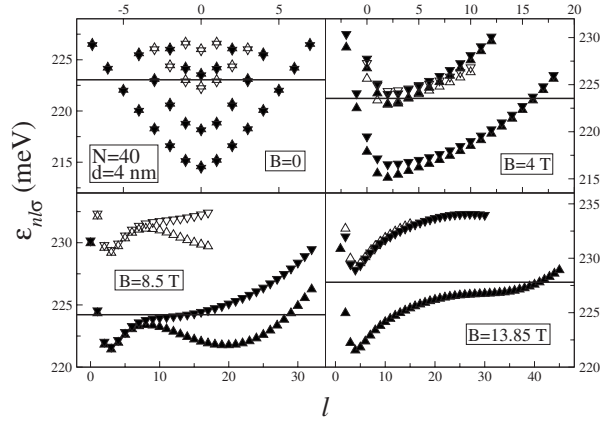
FIG. 3. Same as Fig. 2 for $d=4$ nm. The increase in the inter-ring separation allows for the occupation of both bonding and antibonding states indicated by solid and open triangles, respectively.
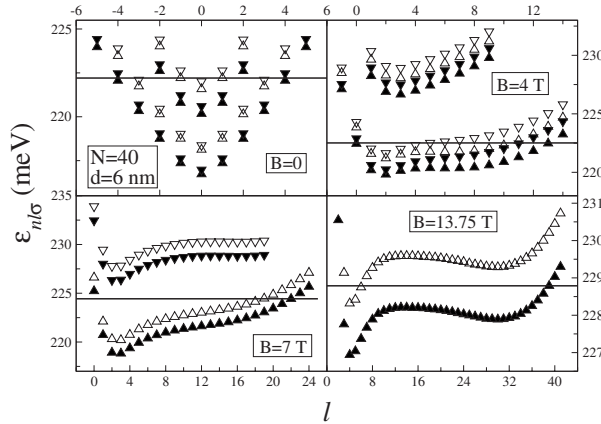
FIG. 4. Same as Fig. 3 for *d* =6 nm.

states Δ_{SAS}, which accurately varies as a function of the inter-ring distance according to the law $\Delta_{SAS}=\Delta_0 e^{-d/d_0}$ already found for QDMs.[22] In our case, from the difference in energy of single-electron (bonding and antibonding) QRMs we have obtained $\Delta_0=82$ meV and $d_0=1.68$ nm,[39] values which have turned out to be unaffected by the applied magnetic field. Clearly, the value of $\hbar\omega_0$ as compared to Δ_{SAS}, which allows discerning between the strong ($\hbar\omega_0 \lesssim \Delta_{SAS}$) and the weak ($\hbar\omega_0 \gtrsim \Delta_{SAS}$) quantum-mechanical coupling regimes, has a crucial influence on the actual filling of bonding and antibonding sp states at a given inter-ring distance. Indeed, increasing ω_0 while keeping the double-well structure constant may favor the population of antibonding orbitals for large enough values of *N*.[24] This can be understood from the noninteracting electron model, in which the single-electron energies are the sum of two independent terms: one arising from the *z* localization and characterized by the quantum number n_z and another, which increases as ω_0 does, arising from the *r* localization and depending on *l* and the radial quantum number n_r. If *N* is large enough, the QRMs can minimize their energy by populating antibonding states with low values of n_r and *l* instead of going on populating bonding states with higher quantum numbers. This explains why some antibonding states were filled even for $d=2$ nm at $B=0$ and $N=40$ for the QRMs of Ref. 39, where ω_0 was taken to be 15 meV, a value almost three times larger than the one considered in the present work.[24]

This particular structure of the bonding and antibonding bands at high magnetic fields may have some observable effects on the far-infrared response of QRMs. Indeed, since the dipole operator cannot connect bonding with antibonding sp states, for QRMs in the weak-coupling limit, one would expect the dipole spectrum to display additional fragmentation in the characteristic edge modes of the ring geometry[13] due to the contribution of the antibonding electron-hole pairs (see, e.g., the bottom panels of Fig. 4).

Figure 5 shows the evolution with *d* of the gs energy and the molecular phase of QRMs made up of $N=8$ electrons and

submitted to magnetic fields of different intensities. Notice that even moderate values of *B* give rise to ground states with large total angular momentum, which increases as the magnetic field does. For this reason, we have denoted it by its actual value instead of employing the usual notation with upper Greek letters except for the cases with $L_z=0$. Similar conclusions can be drawn for all the values of the magnetic field we have considered; on the one hand, for the studied inter-ring distances, the energy of the molecular phases increases with *d* due to the enhancement of the energy of the bonding states,[43] which dominates over the decrease in the Coulomb energy—for larger distances the constituent QRs
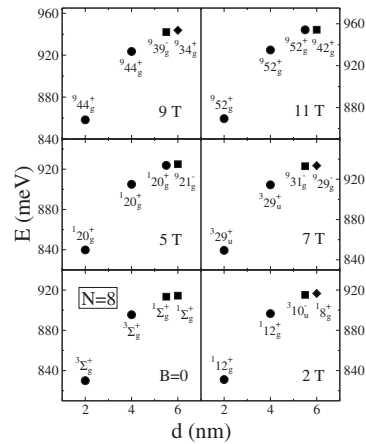
FIG. 5. Energy (meV) and gs molecular phases of the QRM with $N=8$ electrons as functions of the inter-ring distance for different values of *B*. For a given *B* value, different phases are represented by different symbols.
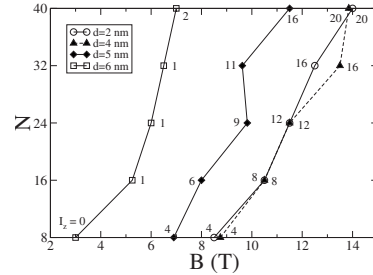
FIG. 6. *B* values at which the selected QRMs become fully spin polarized for the inter-ring distances *d*=2, 4, and 6 nm. The isospin of each configuration is also indicated. The lines have been drawn to guide the eyes.

are so apart that eventually this decrease dominates and the tendency is reversed. On the other hand, one can see that the first phase transitions are always found at the largest inter-ring distances since, as happens for QDMs in the few-electron limit, they are due to the replacement of an occupied bonding sp state with an empty antibonding one. This also explains why in most of the cases, and especially for the highest magnetic fields, the total angular momentum of the QRMs in the weakest coupling regime is reduced. The filled antibonding orbitals have lower *l*'s than the replaced bonding states.

We have determined the magnetic field that gives rise to ring molecules with fully spin-polarized gs and show it in Fig. 6 as a function of *N* for different inter-ring distances going from the strong to the weak quantum-mechanical coupling regimes. The isospin value of each configuration is also indicated. The number of electrons, $N=8\times M$ with *M* =1–5, was chosen with the aim of producing closed-shell structures at *B*=0 in the weak-coupling limit. One can see that the results for *d*=2 and 4 nm are very close with only noticeable differences for *N*=32. This can be understood from the bottom panels of Figs. 2 and 3, which show that for rather large magnetic fields only bonding orbitals are occupied for both ring separations. Contrarily, from Fig. 4 one can see that in weaker coupling regimes the filling of anti-bonding states favors the fully spin-polarization of the QRMs at low *B* intensities as compared to those needed when the rings are closer to each other, which explains the differentiated results corresponding to *d*=5 and 6 nm in Fig. 6.

When antibonding orbitals are populated, the variation in the magnetic field yields numerous transitions between different molecular phases with different isospin that are more complex than these observed in vertically coupled QDs. This particular behavior is mainly due to the periodic destabilization suffered by the lowest-*l* occupied orbitals induced by the magnetic field, which is a direct consequence of the Aharonov-Bohm effect, and makes it rather difficult to find a pattern among the observed evolutions for the different electronic populations. The spin and isospin phases as functions of the magnetic field are shown in Fig. 7 for *d*=6 nm cor-
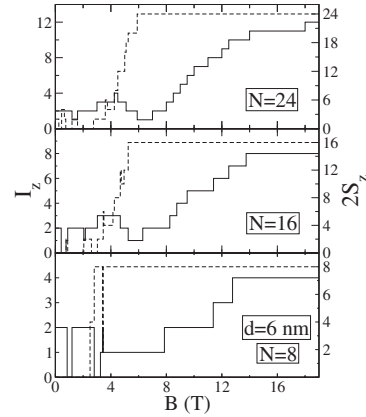
FIG. 7. Isospin (solid line, left scale) and spin (dotted line, right scale) values as functions of *B* for the QRMs with *d*=6 nm and *N*=8,16, and 24.

responding to *N*=8, 16, and 24. It can be seen that in all cases at *B*=0 the QRMs have $I_z=2$ and $S_z=1$; when *B* is increased, nonmonotonic spin and isospin oscillations with $\Delta I_z=\pm 1$ and $\Delta S_z=\pm 1$ and 2 appear, respectively. Two facts, also present in QDMs,[24,25] are worth to be stressed: on one hand, molecular phase changes from − (+) to + (−) ground states (recall that, as explained in Sec. II, this sign is related to the symmetry of the molecular configuration) involve $\Delta I_z=+1$ (−1) flips; on the other hand, quite often the transitions in both magnitudes take place simultaneously except obviously when the QRMs reach the full spin-polarization point, from which on the isospin increases in one-unit jumps until the system is made up of only bonding states.

The comparison of the isospin phases for QRMs with *d* =4 and 6 nm is presented in Fig. 8 for *N*=32 and 40. Clearly, the highest values of I_z appear for the smallest inter-ring distances, as expected from the single-particle levels shown
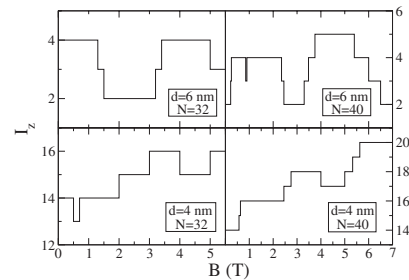
FIG. 8. Isospin values as functions of *B* for the QRMs with *d* =4 and 6 nm, and *N*=32 and 40.
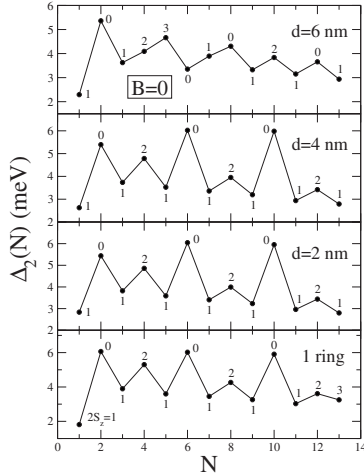
FIG. 9. Addition energies for QRMs at $B=0$ and inter-ring distances $d=2$, 4, and 6 nm and for a single QR (bottom panel). The value of $2S_z$ corresponding to each N is also indicated.

FIG. 10. Same as Fig. 9 for $B=3$ T.

in Fig. 3, corresponding to $d=4$ nm and $N=40$, in which only a few antibonding orbitals are occupied for low values of B. Indeed, one can see from the bottom panels of Fig. 8 that, for this inter-ring distance, magnetic fields of about 5 T are enough to yield configurations with the maximum isospin value $N/2$, whereas for the QRMs with $d=6$ nm such values of B still correspond to small I_z's due to the large amount of filled antibonding states.

We have also calculated the addition energies defined by

$$\Delta_2(N) = E(N+1) - 2E(N) + E(N-1), \qquad (3)$$

with $E(N)$ being the total energy of the N-electron system for QRMs made up of up to 14 electrons at different inter-ring distances submitted to several magnetic fields as functions of N. For the sake of comparison, we have also calculated $\Delta_2(N)$ for the corresponding single rings. The results for $B=0$, 3, and 6 T are shown in Figs. 9–11, respectively, in which the bottom panels correspond to the single ring.

From Fig. 9 one can see that at zero magnetic field the single-QR addition spectrum presents the usual intense peaks at $N=2$, 6, and 10 with zero total spin and those at $N=4$ and 8 with $S_z=1$ satisfying the Hund's rule. Similar results are found for the QRMs with $d=2$ and 4 nm, indicating that such systems behave as a single ring owing to the strong quantum-mechanical coupling corresponding to these inter-ring distances (notice that, except for $N=13$, the spin values coincide for all the configurations). This fact contrasts with the results found for the vertical ring molecules of Ref. 39, where at $d=4$ nm the spectrum clearly reflected an intermediate coupling situation due to the filling of the first antibonding orbitals. As commented before, for the systems studied in the present paper such states are only occupied for

larger inter-ring separations (or N's of the order of 30).

The spectrum corresponding to $d=6$ nm is shown in the top panel of the same figure. One can see that, although some of the marked peaks are preserved, in particular those at $N=2$ and 8, the ones at $N=4$ and 6 no longer exist. Notice that for 6 electrons the spectrum presents now a minimum and also a new peak is found at $N=5$. This intricate structure can be understood from the corresponding single-particle energy levels. Indeed, it appears that the QRMs with $N \leq 4$ are made up of only bonding states with the first antibonding state being filled when $N=5$. From $N \geq 7$, the QRMs have always occupied both B and AB orbitals but, however, the intermediate six-electron configuration has again only symmetric states. This alternate behavior evidences that 6 nm is not a separation large enough for the QRMs to be in the weak-coupling limit but rather corresponds to an intermediate regime. Notice also that, from the results of Ref. 39, in the weak-coupling limit one would expect to find clearly marked peaks at the same N values as for the single ring multiplied by 2, i.e., at $N=4$, 12, and 20, indicating that the rings are so apart that they behave as isolated entities. We have checked that, for our QRMs to present such spectrum, we should consider inter-ring distances of about 10 nm. The different spin values for $d=6$ nm as compared to those in the strong-coupling regime can also be explained from the sp levels. For example, the $2S_z=3$ assignation of the QRM with $N=5$ is due to the above-mentioned filling of an antibonding (spin up with $l=0$) orbital replacing the spin-down $|l|=1$ state occupied for $d=2$ and 4 nm. Analogously, the configuration with $S_z=1$ (instead of $S_z=0$) for $N=10$ can also be explained from the sp levels. In the strong-coupling limit, the QRM is formed by the spin-degenerated sp levels with $l=0$, $|1|$, and $|2|$, but this closed-shell configuration is prevented by the filling of the antisymmetric orbitals at $d=6$ nm. Finally, the reverse situation occurs at $N=8$, where the closing of the

antibonding $l=0$ and $|1|$ shells contrasts with the Hund's-rule configurations found for the strongly coupled molecules.

Figure 10 shows the addition energies corresponding to the situation in which a magnetic field of 3 T is applied to the rings. Like what is found at $B=0$, the spectrum of the single system and of the molecules with $d=2$ and 4 nm are rather similar. Notice the different energy scales with the most remarkable difference being the salient minimum that appears for the single QR at $N=5$. For the above-mentioned inter-ring distances, peaks with $S_z=0$ are found at $N=2, 4, 8, 10$, and 12, as well as a peak at $N=6$ with $S_z=2$, although they are not as clearly marked as at $B=0$. It turns out that, even in the presence of a magnetic field, when the single-particle energy levels no longer display the $\pm l$ degeneration, the QRMs can adopt configurations that are somehow analog to these characteristics of the situation at $B=0$, namely, the closed-shell ones and those fulfilling the Hund's rule. Indeed, for, e.g., $d=4$ nm and $N=10$, the ring molecule is made up of the spin-degenerate bonding states with $l=0-4$ (instead of those with $|l|=0-2$ of the $B=0$ case). Similarly, at $N=6$ the occupied orbitals are the spin-up and -down ones with $l=1$ and 2, and the spin-up ones with $l=0$ and 3 (instead of the spin-degenerate states with $|l|=0$ and 1 filled at zero magnetic field). For larger inter-ring separations, the occupancy of the first antibonding orbitals washes out these structures and the addition spectrum becomes flatter and irregular. One can notice also the different spin assignations between the single and the coupled systems especially for the lowest-populated configurations. In particular, the single QRs with $N \leq 5$ turn out to be fully spin polarized, which can be attributed to the combined effect of the magnetic field and a relatively strong exchange-correlation interaction characteristic of few-electron single-quantum rings. The relatively higher spin values at $d=6$ nm for $N \geq 7$ are due to the filling of the antibonding states.

Finally, the addition energies for $B=6$ T are shown in Fig. 11. It can be seen that in all cases the only clearly marked peak is the one at $N=2$, with the rest of the spectra being rather flat, following the trend observed at $B=3$ T. Nevertheless, some weak peaks are still found and can be interpreted as in the previous cases, e.g., the one at $N=8$ for $d=4$ nm with $2S_z=2$. The system fills the spin-up and -down states with $l=2-4$ and the spin-up ones with $l=1$ and 5. One can also notice that the faint peak of the four-electron configurations of both the single ring and the QRM with $d=2$ nm becomes a minimum at larger inter-ring distances. Concerning the spin, the single QRs and the QRMs with $d=2$ and 4 nm turn out to be fully polarized for $N \leq 7, 5$, and 3, respectively, whereas the filling of the antibonding states favors the fully spin polarization of molecules with the largest ring separation for all the considered electron numbers.

IV. SUMMARY

Within the local spin-density-functional theory, we have addressed the ground state of quantum ring molecules containing up to 40 electrons, with different inter-ring distances, submitted to perpendicular magnetic fields. In the strong-coupling regime the energy levels and the addition energies
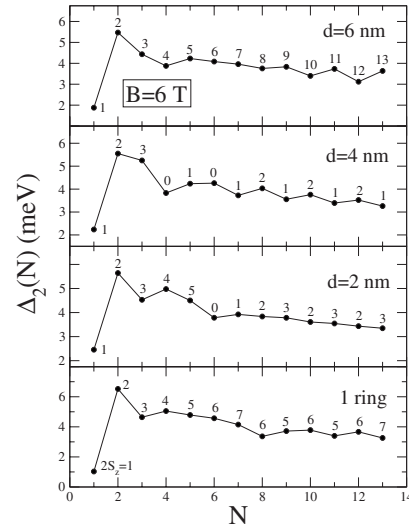
FIG. 11. Same as Fig. 9 for $B=6$ T.

of the QRMs are similar to those of a single QR, although some differences are found due to the effect of the magnetic field, which has a tendency to wash out the clearly marked peaks characteristic of the $B=0$ case as well as to yield flatter addition spectra. However, even at $B \neq 0$, some peaks are still present and they can be interpreted as in the zero magnetic field case.

When the ring separation is increased until the first antibonding orbitals are occupied, the addition spectra become irregular and the ring molecules are fully spin polarized at relatively low magnetic fields. The filling of such states yields isospin oscillations as functions of B increasing in one-unit jumps once the corresponding molecular configurations reach the maximum spin value.

Despite the lack of experimental results to compare ours with, we believe that the ones herewith presented may be helpful in the analysis of future experiments on vertically coupled QRs concerning, e.g., the realization of single-electron transistor measurements, where the evolution of the chemical potential $\mu(N)$ with the magnetic field can be experimentally identified as the variation in the position of the current peaks as a function of the applied field, showing irregularities arising from phase transitions.

ACKNOWLEDGMENTS

*fmalet@ecm.ub.es

†planelle@exp.uji.es

[1] L. Jacak, P. Hawrylak, and A. Wjs, *Quantum Dots* (Springer, Berlin, 1998); T. Chakraborty, *Quantum Dots* (Elsevier, Amsterdam, 1999); D. Bimberg, M. Grundmann, and N. N. Ledentsov, *Quantum Dot Heterostructures* (Wiley, London, 2001).

[2] E. Lipparini, *Modern Many-Particle Physics* (World Scientific, Singapore, 2008).

[3] S. Tarucha, D. G. Austing, T. Honda, R. J. van der Hage, and L. P. Kouwenhoven, Phys. Rev. Lett. **77**, 3613 (1996).

[4] J. M. García, G. Medeiros-Ribeiro, K. Schmidt, T. Ngo, J. L. Feng, A. Lorke, J. Kotthaus, and P. M. Petroff, Appl. Phys. Lett. **71**, 2014 (1997).

[5] A. Lorke, R. J. Luyken, A. O. Govorov, J. P. Kotthaus, J. M. Garcia, and P. M. Petroff, Phys. Rev. Lett. **84**, 2223 (2000).

[6] A. Fuhrer, S. Lüscher, T. Ihn, T. Heinzel, K. Ensslin, W. Wegscheider, and M. Bichler, Nature (London) **413**, 822 (2001); T. Ihn, A. Fuhrer, T. Heinzel, K. Ensslin, W. Wegscheider, and M. Bichler, Physica E (Amsterdam) **16**, 83 (2003).

[7] R. Held, S. Lüscher, T. Heinzel, K. Ensslin, and W. Wegscheider, Appl. Phys. Lett. **75**, 1134 (1999).

[8] Z. Gong, Z. C. Niu, S. S. Huang, Z. D. Fang, B. Q. Sun, and J. B. Xia, Appl. Phys. Lett. **87**, 093116 (2005).

[9] N. A. J. M. Kleemans, I. M. A. Bominaar-Silkens, V. M. Fomin, V. N. Gladilin, D. Granados, A. G. Taboada, J. M. García, P. Offermans, U. Zeitler, P. C. M. Christianen, J. C. Maan, J. T. Devreese, and P. M. Koenraad, Phys. Rev. Lett. **99**, 146808 (2007).

[10] T. Ihn, A. Fuhrer, K. Ensslin, W. Wegscheider, and M. Bichler, Physica E (Amsterdam) **26**, 225 (2005).

[11] T. Chakraborty and P. Pietiläinen, Phys. Rev. B **50**, 8460 (1994).

[12] I. V. Krive, R. I. Shekhter, S. M. Girvin, and M. Jonson, Phys. Scr., T **t54**, 123 (1994).

[13] A. Emperador, M. Barranco, E. Lipparini, M. Pi, and Ll. Serra, Phys. Rev. B **59**, 15301 (1999).

[14] J. C. Lin and G. Y. Guo, Phys. Rev. B **65**, 035304 (2001).

[15] M. Aichinger, S. A. Chin, E. Krotscheck, and E. Räsänen, Phys. Rev. B **73**, 195310 (2006).

[16] Y. M. Liu, G. M. Huang, and T. Y. Shi, Phys. Rev. B **77**, 115311 (2008).

[17] R. H. Blick, R. J. Haug, J. Weis, D. Pfannkuche, K. v. Klitzing, and K. Eberl, Phys. Rev. B **53**, 7899 (1996).

[18] G. Schedelbeck, W. Wegscheider, M. Bichler, and G. Abstreiter, Science **278**, 1792 (1997).

[19] M. Rontani, F. Troiani, U. Hohenester, and E. Molinari, Solid State Commun. **119**, 309 (2001).

[20] A. W. Holleitner, R. H. Blick, A. K. Hüttel, K. Eberl, and J. P. Kotthaus, Science **297**, 70 (2002).

[21] T. Ota, M. Rontani, S. Tarucha, Y. Nakata, H. Z. Song, T. Miyazawa, T. Usuki, M. Takatsu, and N. Yokoyama, Phys. Rev. Lett. **95**, 236801 (2005).

[22] B. Partoens and F. M. Peeters, Phys. Rev. Lett. **84**, 4433 (2000); Europhys. Lett. **56**, 86 (2001).

[23] J. J. Palacios and P. Hawrylak, Phys. Rev. B **51**, 1769 (1995).

[24] F. Ancilotto, D. G. Austing, M. Barranco, R. Mayol, K. Muraki, M. Pi, S. Sasaki, and S. Tarucha, Phys. Rev. B **67**, 205311 (2003).

[25] D. G. Austing, S. Tarucha, H. Tamura, K. Muraki, F. Ancilotto, M. Barranco, A. Emperador, R. Mayol, and M. Pi, Phys. Rev. B **70**, 045324 (2004).

[26] D. Bellucci, M. Rontani, G. Goldoni, and E. Molinari, Phys. Rev. B **74**, 035331 (2006).

[27] T. Mano, T. Kuroda, S. Sanguinetti, T. Ochiai, T. Tateno, J. Kim, T. Noda, M. Kawabe, K. Sakoda, G. Kido, and N. Koguchi, Nano Lett. **5**, 425 (2005).

[28] T. Kuroda, T. Mano, T. Ochiai, S. Sanguinetti, K. Sakoda, G. Kido, and N. Koguchi, Phys. Rev. B **72**, 205301 (2005).

[29] F. Suárez, D. Granados, M. L. Dotor, and J. M. García, Nanotechnology **15**, S126 (2004).

[30] D. Granados, J. M. García, T. Ben, and S. I. Molina, Appl. Phys. Lett. **86**, 071918 (2005).

[31] K.-H. Ahn and P. Fulde, Phys. Rev. B **62**, R4813 (2000).

[32] Y. Li and H. M. Lu, Jpn. J. Appl. Phys., Part 1 **43**, 2104 (2004).

[33] L. G. G. V. Dias da Silva, J. M. Villas-Bôas, and S. E. Ulloa, Phys. Rev. B **76**, 155306 (2007).

[34] B. Szafran, S. Bednarek, and M. Dudziak, Phys. Rev. B **75**, 235323 (2007).

[35] B. Szafran, Phys. Rev. B **77**, 235314 (2008).

[36] G. Piacente and G.-Q. Hai, J. Appl. Phys. **101**, 124308 (2007).

[37] J. I. Climente and J. Planelles, Phys. Rev. B **72**, 155322 (2005).

[38] L. K. Castelano, G.-Q. Hai, B. Partoens, and F. M. Peeters, Phys. Rev. B **74**, 045313 (2006).

[39] F. Malet, M. Barranco, E. Lipparini, R. Mayol, M. Pi, J. I. Climente, and J. Planelles, Phys. Rev. B **73**, 245324 (2006).

[40] M. Ferconi and G. Vignale, Phys. Rev. B **50**, 14722 (1994).

[41] M. Rontani, F. Rossi, F. Manghi, and E. Molinari, Solid State Commun. **112**, 151 (1999); M. Rontani, S. Amaha, K. Muraki, F. Manghi, E. Molinari, S. Tarucha, and D. G. Austing, Phys. Rev. B **69**, 085327 (2004).

[42] S. S. Li and J. B. Xia, J. Appl. Phys. **89**, 3434 (2001); A. Puente, and Ll. Serra, Phys. Rev. B **63**, 125334 (2001); J. I. Climente, J. Planelles, and F. Rajadell, J. Phys.: Condens. Matter **17**, 1573 (2005).

[43] M. Pi, A. Emperador, M. Barranco, and F. Garcias, Phys. Rev. B **63**, 115316 (2001).

[44] S. Lundqvist, in *Theory of the Inhomogenous Electron Gas*, edited by S. Lundqvist and N. H. March (Plenum, New York, 1983), p. 149.

[45] J. P. Perdew and A. Zunger, Phys. Rev. B **23**, 5048 (1981).

Strong configuration mixing due to dielectric confinement in semiconductor nanorods

J. I. Climente, M. Royo, J. L. Movilla, and J. Planelles[*]

Departament de Química Física i Analítica, Universitat Jaume I, Box 224, E-12080, Castelló, Spain

(Received 30 December 2008; published 1 April 2009)

The interaction between electron-electron and electron-hole pairs in semiconductor nanorods embedded in dielectric media is investigated using a configuration-interaction method. Contrary to spherical quantum dots of similar volume, the dielectric confinement is shown to bring nanorods into a regime of strong configuration mixing. The wave functions are particularly sensitive to such mixing, which leads to qualitative changes in the electronic and optical properties of the rods.

Semiconductor quantum rods or nanorods (NRs) are colloidal quantum dots with strong radial confinement and variable length.[1,2] Even though NRs were first synthesized long after spherical nanocrystals (NCs), it was soon realized that their anisotropic shape posed many benefits for optical and transport applications.[3] This prompted a large number of studies, often revealing characteristic physical phenomena which stem from the weak longitudinal confinement, for NRs bridge the gap between zero-dimensional and one-dimensional quantum-confined systems.[4–10]

Similar to NCs, NRs are usually embedded in insulating media, whose dielectric constant is much lower than that of the semiconductor structure. This dielectric mismatch gives rise to a so-called dielectric confinement, which greatly enhances the Coulomb interactions inside the semiconductor.[11,12] In spherical NCs, however, owing to the strong quantum confinement, Coulomb interactions are usually a first-order perturbation effect for the low-lying states.[13] Furthermore, a strong spatial confinement leads to compensations between electron and hole charge distributions,[14,15] so that the optical properties are barely affected by the dielectric environment.

None of these restrictions apply to NRs, where the longitudinal confinement may be fairly weak. Indeed, the dielectric confinement has been held responsible for the large variation in the optical gap of CdSe NRs as compared to the transport one.[7,16] What is more, NRs are the zero-dimensional counterpart of quantum wires, where variations in the dielectric confinement have been shown to induce drastic changes in the binding energy and oscillator strength of excitons,[17–19] thus enabling Coulomb interaction engineering. One may then wonder to which extent the single-particle and perturbational treatments of Coulomb interactions that dominate the literature of NRs (Refs. 6–10) provide a valid description of the optoelectronic properties.

In this work, we perform a theoretical study of the effect of the dielectric confinement on interacting particles (two electrons or one electron and one hole) confined in a semiconductor NR. A numerical procedure is used which allows us to estimate the effect of the dielectric environment for arbitrary three-dimensional potentials, thus addressing realistic geometries. Electron correlations are then accounted for exactly using an effective mass-configuration-interaction (CI) scheme. We go beyond energetic effects and illustrate the influence of the dielectric confinement on the wave function, as well as on derived properties such as the electron-hole recombination probability.

The fully three-dimensional model allows us to compare the behavior of rods with that of spherical dots. In the absence of dielectric mismatch, both systems may be well described by a perturbational model of the Coulomb interaction. However, with increasing mismatch, electronic correlations in the rod can reach very high values. This is made possible by the rod shape. The small radius makes the charge confined inside very sensitive to the external dielectric medium, while the weak longitudinal confinement renders the system prone to configuration mixing. It then follows that the physics of NRs in dielectric surroundings is far from the strong confinement picture. Signatures of the severe configuration mixing, such as enhanced exciton emission, the appearance of new optical modes, or Wigner localization of few-electron states, are predicted.

The electron and hole single-particle states are described with effective-mass Hamiltonians which, in cylindrical coordinates and atomic units, read as[20]

$$\mathcal{H}_i = -\frac{1}{2}\left[\frac{1}{\rho}\frac{\partial}{\partial\rho}\left(\frac{\rho}{m^*_{\rho,i}(\rho,z)}\frac{\partial}{\partial\rho}\right) + \frac{\partial}{\partial z}\frac{1}{m^*_{z,i}(\rho,z)}\frac{\partial}{\partial z} - \frac{m_i^2}{\rho^2 m^*_{\rho,i}(\rho,z)}\right] + \hat{V}_i(\rho,z),$$

where $i=e,h$ is a subscript denoting electron or hole, respectively. m_i is the azimuthal angular momentum and $\hat{V}_i(\rho,z)$ is the spatial confinement potential, which is zero inside the nanostructure and V_i^{out} outside. $m^*_{\rho,i}(\rho,z)$ and $m^*_{z,i}(\rho,z)$ are the position-dependent effective masses in the plane and along the vertical direction. For electrons we use isotropic masses $m^*_{\rho,e}(\rho,z)=m^*_{z,e}(\rho,z)$. For holes, however, the mass anisotropy is important, as it is responsible for the heavy-hole to light-hole ground-state transition that occurs as the aspect ratio of the nanostructure increases.[7,21] Thus, for heavy holes we use $m^*_{\rho,h}=1/(\gamma_1+\gamma_2)$ and $m^*_{z,h}=1/(\gamma_1-2\gamma_2)$, while for light holes we use $m^*_{\rho,h}=1/(\gamma_1-\gamma_2)$ and $m^*_{z,h}=1/(\gamma_1+2\gamma_2)$. Here γ_1 and γ_2 are the Luttinger parameters.[21] Hamiltonian (1) is integrated numerically using a finite differences scheme.

In order to determine the electrostatic potential $V_{\text{Coulomb}}(\mathbf{r})$, in a medium with spatially inhomogeneous dielectric constant $\varepsilon(\mathbf{r})$, we rewrite the Poisson equation in terms of volumetric source charges plus induced polarization charges,
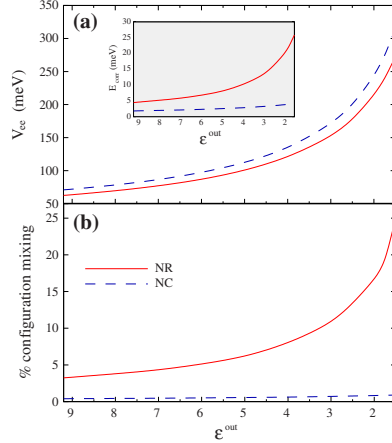
FIG. 1. (Color online) Two-electron ground-state properties in a NR (solid line) and a spherical NC (dashed line) of the same volume, as a function of the dielectric constant of the surrounding medium. (a) Electron-electron repulsion energy. (b) Weight of configuration mixing in the CI expansion. The inset represents the energy coming from Coulomb correlation (see text).

$$\nabla^2 V_{\text{Coulomb}}(\mathbf{r}) = -4\pi[\eta(\mathbf{r}) + \eta_p(\mathbf{r})]. \qquad (2)$$

Here $\eta(\mathbf{r})$ is the source charge density, which is obtained from the electron eigenstates of Eq. (1), and $\eta_p(\mathbf{r})$ is the polarization charge density, which we calculate with a method equivalent to the *induced charge computation* one proposed by Boda *et al.*[22] The Coulomb interaction is then taken into account by means of a CI procedure. The two-electron (exciton) states are built as a linear combination of a large number of Slater determinants (Hartree products) obtained by filling in the single-particle eigenstates in all possible ways consistent with symmetry requirements, granting energy convergence within 0.1 meV.[23] The fully interacting

Hamiltonian is diagonalized, exploiting orbital and spin symmetries.[24]

In our calculations, we study a typical CdSe NR. The rod is composed by a cylinder of radius $R=2$ nm and length $L=8$ nm attached to two hemispherical caps of radius $R=2$ nm in the extremes, giving a total length of $L_{\text{tot}}=12$ nm (see inset in Fig. 2). For comparison, we also study a spherical NC with roughly the same volume, i.e., $R=3.15$ nm. The material parameters are $m_e^*(\rho,z)=0.13$ inside the structure and 1 outside and $(\gamma_1,\gamma_2)=(1.66,0.41)$ inside and $(1.0, 0.0)$ outside.[25] The confinement potential of the outer media is set to $V_e^{\text{out}}=V_h^{\text{out}}=4$ eV. The dielectric constant is fixed at $\varepsilon(\mathbf{r})=9.2$ inside and we vary the outer value ε^{out} to simulate the effect of different surrounding media. For NRs, the ground state is assumed to be a light hole,[7,21] so the CI is built on a subspace of light-hole states. Conversely, for spherical NCs we use heavy holes.

I. ELECTRON-ELECTRON INTERACTION

We start by investigating the two-electron case. Figure 1(a) compares the electron-electron repulsion energy V_{ee} for the ground state of the NR and the NC as a function of the dielectric mismatch. As can be seen, the repulsion energy in the NR experiences a similar enhancement to that of the spherical NC. For a usual surrounding medium of $\varepsilon^{\text{out}}=2.0$, V_{ee} is over three times larger than the value one may expect neglecting the dielectric confinement. To quantify the amount of V_{ee} which is not captured by simple perturbational descriptions of the interaction, in the figure inset we depict the correlation energy defined as $E_{\text{corr}}=V_{\text{ee}}^0-V_{\text{ee}}$. Here V_{ee}^0 is the expectation value of the Coulomb repulsion for the dominant configuration in the CI expansion. At this point, we observe a first difference between NRs and NCs. In the absence of dielectric mismatch, E_{corr} is about twice larger for the NR. This is due to the weak confinement in the long axis direction. Furthermore, with increasing mismatch the ratio increases up to six, revealing much stronger correlation effects in NRs as compared to NCs.

Since the effect of correlations on the wave function is even more pronounced than that on the energies, in Fig. 1(b) we analyze the amount of configuration mixing experienced by the ground state, i.e., the weight of the CI expansion
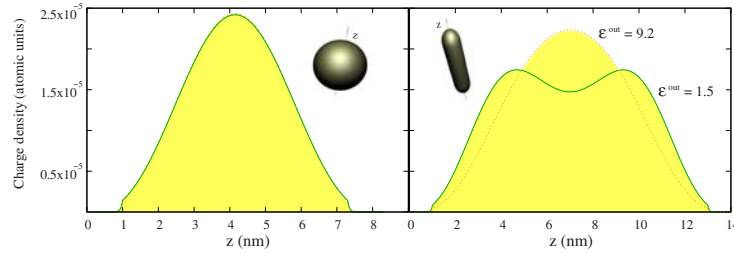
FIG. 2. (Color online) Two-electron ground-state charge density along the vertical axis of a NC (left) and a NR (right) with (solid line) and without (dotted line) dielectric confinement. The insets are schematics of the structures under study.
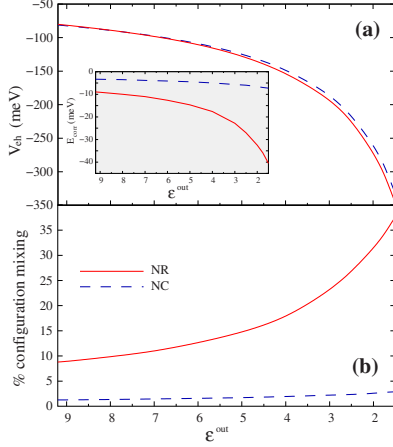
FIG. 3. (Color online) Same as Fig. 1, but for the exciton ground state.

FIG. 4. (Color online) (a) Recombination probability of the ground-state exciton as a function of the dielectric constant of the surrounding medium, in a NR (solid line) and a NC (dashed line) of the same volume. (b) Absorption spectrum of the NR under a weak electric field, in the absence and presence of dielectric confinement. The spectra are offset for clarity. The high-energy peak at $\varepsilon^{\mathrm{out}}=2.0$ arises from Coulomb correlations.

which does not come from the dominant Slater determinant. The different behavior of NCs and NRs is now striking. The configuration mixing is minor for the spherical dot,[13] but it becomes very large for dielectrically confined NRs.

The influence of the configuration mixing on the ground-state wave function is apparent in Fig. 2. In the figure, we represent the charge density of one electron along the vertical axis of the nanostructure after integrating over the coordinates of the second electron, for a spherical NC (left) and a NR (right). Solid and dotted lines are used for the cases with and without dielectric confinement. While the NC wave function remains essentially unaltered by the dielectric confinement, the NR wave function develops a valley in the center of the structure. This is a clear indication that Wigner localization is taking place in the NR, which will have direct implications for transport processes[26] and shell-filling spectroscopy.[27]

II. ELECTRON-HOLE INTERACTION

Next we investigate the effect of the dielectric confinement on the exciton ground state. The results summarized in Fig. 3 are qualitatively the same as in the two-electron case, but correlations are now even stronger because of the large mass of the holes. Thus, in Fig. 3(a) one can see that the dielectric confinement enhances the electron-hole attraction (binding) energy V_{eh} at a similar rate for NRs and NCs.[28] However the correlation energies are several times larger in the case of NRs (figure inset), for they undergo a sizable amplification with increasing dielectric mismatch. The effect of correlations is mostly felt through the wave function. As can be seen in Fig. 3(b), for a typical dielectric medium of

$\varepsilon^{\mathrm{out}}=2.0$, the exciton ground state in the spherical NC is essentially given by the dominant Hartree product (an electron and a hole in the lowest single-particle orbitals), which validates the perturbation treatment. By contrast, the NR ground state contains over 30% of excited configurations admixed through Coulomb correlations. Obviously, this strong mixing modifies the exciton wave function. This has important effects on the optical properties of the NR which are not captured by usual perturbational descriptions. In what follows, we illustrate some of these effects.

In large size quantum dots, it has been shown that correlations enhance the exciton luminescence.[29] We can show that this effect is also present in dielectrically confined NRs by calculating the electron-hole recombination probability, by means of the dipole approximation and a Fermi golden rule[30]

$$P_{\mathrm{gs}} \propto \left| \sum_i c_i^{\mathrm{gs}} \langle \phi_i^e | \phi_i^h \rangle \right|^2 \mathcal{P}^2. \qquad (3)$$

Here c_i^{gs} is the ground-state CI expansion coefficient corresponding to the Hartree product formed by the electron and hole spin orbitals ϕ_i^e and ϕ_i^h. $\mathcal{P}$ is the Kane matrix element. Figure 4(a) shows the exciton recombination probability in a NR and a NC as a function of the dielectric mismatch. As expected, the recombination probability in the NR is always larger than that in the NC.[16] In addition, with increasing dielectric mismatch, the luminescence of the NR increases up to 40%: a clear signature of the strong correlations affecting the wave function.

Correlated wave functions are more sensitive to environmental perturbations than strongly confined ones. A manifestation of this is shown next. We simulate the absorption spectrum of a NR $\mathcal{A}(E) = \sum_j P_j \delta(E - E_j)$, where E is the incident photon energy and P_j is the recombination probability of the jth exciton state, with energy E_j. The NR is subject to a moderate electric field of 50 kV/cm along the vertical direction, which breaks the parity symmetry, thus enabling optical transitions from the first-excited exciton state. Figures 4(b)

CLIMENTE *et al.*   PHYSICAL REVIEW B **79**, 161301(R) (2009)

compares the absorption spectrum without and with dielectric mismatch. In the absence of dielectric mismatch, when correlations are weaker, only the fundamental transition is visible. The first-excited transition is still negligible, as it involves the lowest single-electron orbital ($1s_e$), which is quasigerade, and the first-excited single-hole orbital ($2s_h$), which is quasiungerade. In the presence of dielectric mismatch a new transition appears. This transition corresponds to the first-excited exciton state because now the correlations lead to a strong mixing of the $1s_e 2s_h$ and $1s_e 1s_h$ configurations, the latter orbitals having a large overlap. A similar response may be originated by molecular dipoles in the vicinity of the rod, which suggests that dielectrically confined NRs are suited structures for sensing applications.

In conclusion, we have shown that the dielectric confinement of colloidal NRs leads to non-negligible configuration mixing effects, which are not captured by the usual single-particle or perturbational descriptions of Coulomb interac-

tions. The configuration mixing induces important changes in the few-body wave function, which have visible consequences on the optical and transport properties of NRs, including improved luminescence and sensitivity. Our results indicate that the optical properties of NRs may be engineered by controlling the regime of Coulomb interaction. Even though the calculations were carried out for a 12-nm-long CdSe NR, the findings apply also to different materials and correlations will be even more relevant for longer NRs.

*josep.planelles@qfa.uji.es

[1] X. Peng, L. Manna, W. Yang, J. Wickham, E. Scher, A. Kadavanich, and A. P. Alivisatos, Nature (London) **404**, 59 (2000).

[2] S. Kan, T. Mokari, E. Rothenberg, and U. Banin, Nature Mater. **2**, 155 (2003).

[3] U. Woggon, J. Appl. Phys. **101**, 081727 (2007), and references therein.

[4] H. Htoon, J. A. Hollingsworth, R. Dickerson, and V. I. Klimov, Phys. Rev. Lett. **91**, 227401 (2003).

[5] M. A. El-Sayed, Acc. Chem. Res. **37**, 326 (2004).

[6] D. Steiner, D. Katz, O. Millo, A. Aharoni, S. Kan, T. Mokari, and U. Banin, Nano Lett. **4**, 1073 (2004).

[7] D. Katz, T. Wizansky, O. Millo, E. Rothenberg, T. Mokari, and U. Banin, Phys. Rev. Lett. **89**, 086801 (2002).

[8] J. Hu, L. W. Wang, L. S. Li, W. Yang, and A. P. Alivisatos, J. Phys. Chem. B **106**, 2447 (2002).

[9] J. Li and L. W. Wang, Nano Lett. **3**, 101 (2003).

[10] J. Li and L. W. Wang, Nano Lett. **3**, 1357 (2003).

[11] L. E. Brus, J. Chem. Phys. **80**, 4403 (1984).

[12] V. A. Fonoberov, E. P. Pokatilov, and A. A. Balandin, Phys. Rev. B **66**, 085310 (2002).

[13] N. A. Hill and K. B. Whaley, Phys. Rev. Lett. **75**, 1130 (1995); A. Franceschetti and A. Zunger, *ibid.* **78**, 915 (1997).

[14] M. Lannoo, C. Delerue, and G. Allan, Phys. Rev. Lett. **74**, 3415 (1995).

[15] P. G. Bolcatto and C. R. Proetto, Phys. Rev. B **59**, 12487 (1999).

[16] A. Shabaev and Al. L. Efros, Nano Lett. **4**, 1821 (2004).

[17] L. V. Keldysh, Phys. Status Solidi A **164**, 3 (1997).

[18] G. Goldoni, F. Rossi, and E. Molinari, Phys. Rev. Lett. **80**, 4995 (1998).

[19] E. A. Muljarov, E. A. Zhukov, V. S. Dneprovskii, and Y. Masumoto, Phys. Rev. B **62**, 7420 (2000).

[20] In Eq. (1), we have considered that the mixing of heavy-hole and light-hole subbands is weak. For the low-lying states of the structures, we study that this can be shown to be true.

[21] P. C. Sercel and K. J. Vahala, Phys. Rev. B **44**, 5681 (1991).

[22] D. Boda, D. Gillespie, W. Nonner, D. Henderson, and B. Eisenberg, Phys. Rev. E **69**, 046702 (2004).

[23] For the NR, the CI basis is built from the 28 (12) lowest single-hole (electron) spin orbitals with $m_i = 0 (i = e, h)$, the eight (four) lowest with $m_i = \pm 1$, and the four lowest with $m_h = \pm 2$. For the NC, we use the eight (six) lowest spin orbitals with $m_i = 0$, the six (four) lowest with $m_e = \pm 1$, the four (two) lowest with $m_e = \pm 2$, and the two lowest with $m_h = \pm 3$.

[24] Electron-hole exchange and self-energy interactions are neglected as they do not influence the trends we report here. In particular, self-energy corrections consist roughly in a shift of the corresponding single-particle energy spectra, yielding minor effects on the Coulomb interactions. This is due to the nearly flat profile of the self-polarization potential in the medium with larger dielectric constant [see, e.g., L. Brus, J. Chem. Phys. **79**, 5566 (1983)], which here is the NR.

[25] U. E. H. Laheld and G. T. Einevoll, Phys. Rev. B **55**, 5184 (1997).

[26] J. S. Meyer and K. A. Matveev, J. Phys.: Condens. Matter **21**, 023203 (2009).

[27] L. Jdira, P. Liljeroth, E. Stoffels, D. Vanmaekelbergh, and S. Speller, Phys. Rev. B **73**, 115305 (2006).

[28] It is worth noting that our estimated enhancement of V_{eh} for the NR (265 meV at $\varepsilon^{out} = 1.75$) is in the range of experimental measurements ($\sim 240 – 300$ meV) (Ref. 7).

[29] S. Corni, M. Brasken, M. Lindberg, J. Olsen, and D. Sundholm, Phys. Rev. B **67**, 045313 (2003).

[30] L. Jacak, P. Hawrylak, and A. Wójs, *Quantum Dots* (Springer-Verlag, Berlin, 1998).

Correlation in narrow nanorods: a variational potential–configuration interaction scheme

J Planelles, J I Climente, M Royo and J L Movilla

Departament de Química-Física i Analítica, UJI, Box 224, E-12080 Castelló, Spain

E-mail: josep.planelles@qfa.uji.es

Abstract
Full configuration interaction calculations for two electrons in narrow semiconductor nanorods are carried out employing different orbital basis sets. It is shown that the usual configurations built from single-particle states cannot yield a correct singlet–triplet energetic order regardless of the basis size, as they miss the correlation energy. Mean-field optimized orbitals partially correct this drawback. A new approach is introduced, based on a simple variational procedure, which yields robust results.

(Some figures in this article are in colour only in the electronic version)

1. Introduction

Quantum dots (QDs) are artificial semiconductor structures with sizes a few tens of nanometers. They are often modeled as local perturbations of the periodic crystal field of the semiconductor surrounding matrix, using envelope function and effective mass approximations to describe their electronic structure [1, 2]. Within this approach the details of the unit cell are integrated out, so that only a macroscopic (or envelope) description of the system remains. Thus, the interaction between conduction electrons and atomic core electrons and nuclei is averaged as the interaction with a continuous polarizable medium. Likewise, Coulomb interaction between carriers is assumed to be screened by the dielectric constant of the QD bulk material [3]. The large value of the semiconductor dielectric constant coming into the Coulomb term (typically 10–14), along with the small value of the electron effective mass coming into the kinetic energy term, often lead to situations in which the separation between discrete single-particle (SP) levels exceeds by far the characteristic interaction energy between particles. As a consequence, SP descriptions of the many-body problem may be used, treating the Coulomb interaction between conduction electrons as a perturbation [4–6].

A better account of the two-particle interaction can be achieved through diagonalization of the many-body Hamiltonian in the basis set of non-interacting configurations.

This is the so-called full configuration interaction (FCI) method, which plays a central role in quantum chemistry [7]. FCI provides benchmark results for the ground state energy and wavefunction, as well as for the description of excited states, as it is inferred from the McDonald theorem [8]. The drawback of the approach is its computational cost, originating from its often slow convergence. The key for convergence is the selection of a suitable monoelectronic basis set. As showed by Löwdin and Shull [9], the basis of natural orbitals is the one which requires the fewest configurations to achieve a given accuracy in the energy. Natural orbitals are the orbitals that diagonalize the one-particle density matrix. Therefore, exact natural orbitals should be extracted from the FCI wavefunction. Alternatively, one may use single-particle (SP) orbitals, i.e. the eigenfunctions of the one-body operator coming into the many-body Hamiltonian. This approach is quite common in few-electron and excitonic QD calculations, where convergence problems do not usually arise [4, 5, 10].

In this paper, however, we identify a QD system where correlation energies are so strong that the basis choice becomes critical for overcoming slow convergence issues. Namely, we study narrow rod-shaped QDs (nanorods, NRs) [11, 12]. As recently shown, the large aspect ratio of these semiconductor structures is responsible for some remarkably strong Coulomb interactions [13–15]. Here we demonstrate that, even in the simplest case of two interacting electrons, the CI method based

on SP orbitals (SP-CI) fails to converge. Indeed, for long rods it predicts a triplet ground state, thus violating a fundamental theorem for two-body exact functions [16]. To solve this problem, we follow quantum chemistry CI methods and replace the regular SP orbitals by effective orbitals obtained through mean-field calculations, either Hartree–Fock (HF-CI) [7] or Kohn–Sham density functional theory (KS-CI) [17]. The suitability of using these mean-field optimized orbitals is discussed and compared with a new, simpler approach based on a two-fold variational procedure.

2. Theory

The Hamiltonian of interacting conduction electrons in a QD reads

$$\mathcal{H} = \sum_i T(i) + v^c(i) + \sum_{j<i} \frac{1}{\epsilon r_{ij}} = \sum_i h(i) + \sum_{j<i} g(i,j), \tag{1}$$

where $T = -\frac{1}{2m^*}\nabla^2$ is the kinetic energy operator, v^c the spatial confining potential, m^* the effective mass and ϵ the dielectric constant.

In order to carry out a CI calculation, one first has to select a given one-electron basis set $\{\phi_p\}_{p=1}^M$ and then build all possible N-body Salter determinants $\Phi_\alpha = \det\{\phi_1\phi_2\cdots\phi_N\}$ out of them. In a second step, the projection of Hamiltonian (1) onto the basis set of Slater determinants (or onto a subset of spin- and symmetry-adapted configurations) is carried out yielding matrix elements $\langle\Phi_\alpha|\mathcal{H}|\Phi_\beta\rangle$. The last step is the diagonalization.

For practical purposes the one-electron basis set is taken as orthogonal, although many-body approaches based on overlapping orbitals, as for example the generalized valence bond (GVB), have been successfully developed in quantum chemistry [7, 18]. A possible orbital choice is the SP states, i.e. the eigenfunctions of the one-electron Hamiltonian h. We must select a finite basis set. The natural choice is the M lowest-energy eigenvectors. This truncation of the basis set implies a projection of Hamiltonian (1) onto the corresponding FCI space yielding a model Hamiltonian that, in second quantization language, reads

$$H_{SP} = \sum_p^M \varepsilon_p a_p^+ a_p + \sum_{pqrs}^M g_{pqrs} a_p^+ a_q^+ a_r a_s, \tag{2}$$

where $\varepsilon_p = h_{pp}$ is the pth eigenvalue of h, g_{pqrs} is the two-electron integral and a_p^+, a_q the usual fermion creator/annihilator operators.

Alternatively, we may employ another M-dimensional orthogonal basis set $\{\chi_p\}_{p=1}^M$. In this case, Hamiltonian (1) turns into

$$H_X = \sum_{pq}^M h_{pq} a_p^+ a_q + \sum_{pqrs}^M g_{pqrs} a_p^+ a_q^+ a_r a_s, \tag{3}$$

where off-diagonal h_{pq} terms arise because χ_p is no longer an eigenfunction of h.

We may consider $\{\chi_p\}$ as related to a given $v^{mf}(r)$ potential operator which is added and subtracted to Hamiltonian (1),

$$\begin{aligned}
\mathcal{H} &= \sum_i h(i) + v^{mf}(i) - v^{mf}(i) + \sum_{j<i} g(i,j) \\
&= \sum_i \left(h(i) + v^{mf}(i) + \sum_{j<i} g(i,j) - v^{mf}(i) \right) \\
&= \sum_i f(i) + \sum_{j<i} \bar{g}(i,j).
\end{aligned} \tag{4}$$

Now we determine $\{\chi_p\}$ from the eigenvalue equation $f(r)\chi_p(r) = \bar{\varepsilon}_p \chi_p(r)$ and rewrite equation (3) as

$$H_X = \sum_p^M \bar{\varepsilon}_p a_p^+ a_p + \sum_{pqrs}^M \bar{g}_{pqrs} a_p^+ a_q^+ a_r a_s. \tag{5}$$

HF, DFT and, in general, any mean-field calculation are particular cases of this procedure. For example, in HF,

$$\bar{\varepsilon}_p = h_{pp} + \sum_q^M \left(\langle pq|\frac{1}{\epsilon r_{12}}|pq\rangle - \langle pq|\frac{1}{\epsilon r_{12}}|qp\rangle \right). \tag{6}$$

Note that $h_{pq} + v_{pq}^{mf} = \langle p|h + v^{mf}|q\rangle = \bar{\varepsilon}_p\langle p|q\rangle = \bar{\varepsilon}_p\delta_{pq}$.

Within the framework of this procedure, our approach to deal with strongly correlated regimes is the use of a variational potential, i.e. a potential depending on parameters that allow optimization of the orbital basis set in the CI process.

The advantage of adding a mean-field potential is that, contrary to the SP orbitals which disregard electron–electron interaction, HF orbitals include it somehow averaged in the Coulomb and exchange terms, and KS orbitals further account for some of the correlation through the corresponding functional. This has proved useful in describing many-electron QDs [19, 20]. In our approach, all terms in Hamiltonian (1) are treated on an equal footing to optimize the potential and hence the orbital basis set.

It is worth noting that the projected Hamiltonian (3) is not defined by the selected orbital basis set but rather by the linear space that it generates. Thus, for example, in [19], where HF spin orbitals of an N-electron system are expressed as a linear combination of a set of K SP states, a FCI expansion which employs either K-dimensional basis set yields identical result. The advantage of the strategy presented in [19] relies on a further truncation of the HF basis set.

3. Results and discussion

We carry out calculations for the lowest-lying singlet and triplet states of a two-electron semiconductor CdSe NR. The rod is composed of a cylinder of radius $R = 20$ Å and variable length L, attached to two hemispherical caps of the same radius R at the extremes. The material parameters are effective mass $m^* = 0.13$, dielectric constant $\epsilon = 9.2$ and confining potential $v^c = 4$ eV. The dominant electronic configurations for the studied singlet and triplet states are σ_1^2 and $\sigma_1\sigma_2$, respectively, where σ_1, σ_2 are the lowest-lying and first excited orbitals with zero z-component of the angular momentum ($M_z = 0$).

205

J. Phys.: Condens. Matter **21** (2009) 215801   J Planelles *et al*
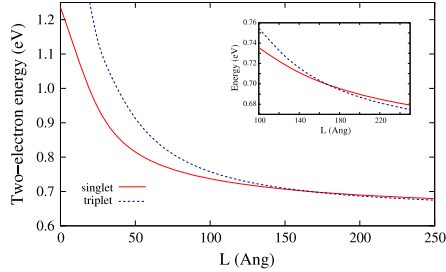
Figure 1. FCI calculations, employing a 1-6-1 SP basis set, of the singlet (solid line) and triplet (dashed line) states of a $R = 20$ Å two-electron semiconductor CdSe NR versus the length L. Inset: close-up of the large L region.

Figure 2. FCI singlet–triplet energy gap Δ_{TS}, corresponding to a CdSe $R = 20$ Å, $L = 200$ Å NR, calculated with a SP 1-n-1 basis set versus n. Inset: $\rho = 0$ profile of the FCI singlet (solid line) and triplet (dashed line) charge densities along the NR z-axis.

We have checked that, as expected, already in the case of a short NR, many σ ($M_z = 0$) SP states lie energetically below the first π ($M_z = \pm 1$) energy level, and that higher angular momentum states are much more excited. Then we employ a basis set 1-n-1 in the CI calculations, i.e. a basis set including the n lowest-lying σ and the lowest-lying degenerate pair of π orbitals, the last orbital pair making, in all studied cases, a very small contribution to the singlet and triplet CI wavefunctions.

Figure 1 shows a series of SP-CI calculations (basis set 1-6-1) of the singlet and triplet states of a $R = 20$ Å two-electron semiconductor CdSe NR versus L. At first glance, the results seem reasonable. At $L = 0$ (a sphere) the singlet state lies energetically far below the triplet state, and the contributions to the CI expansion of configurations other than the dominant one are extremely small. As L increases, the energetic singlet–triplet gap Δ_{TS} decreases, the contribution of excited configurations to the CI wavefunction increases and, in the large L limit, a singlet–triplet degeneration occurs. However, a closer view reveals that beyond $L = 170$ Å the triplet state becomes the ground state (see inset in figure 1). This fact is a violation of a known theorem, attributed to Wigner, stating that any general two-particle Hamiltonian including a symmetric and real potential energy operator has a singlet ground state [16]. Therefore, the result is qualitatively wrong. One may relate the failure to the truncation of the orbital basis set. In order to check it, we ran a series of SP-CI calculations of the singlet–triplet energy gap Δ_{TS} in an $L = 200$ Å NR versus the size n of the (1-n-1) basis set. The results, shown in figure 2, do not allow any finite n yielding the theoretically expected singlet ground state.

We now turn our attention to the wavefunction. The inset in figure 2 shows a profile of the FCI singlet (solid line) and triplet (dashed line) charge densities along the NR vertical axis. We can observe that the triplet and, to a lesser extent, the singlet state develop a valley in the electronic density profile around the rod center. The presence of this valley allows the interacting electrons to reduce the repulsion energy, hence stabilizing the states. This groove is already present in the independent-particle description of the triplet state (through the σ_2 orbital), but not in the singlet ground state, where it is a
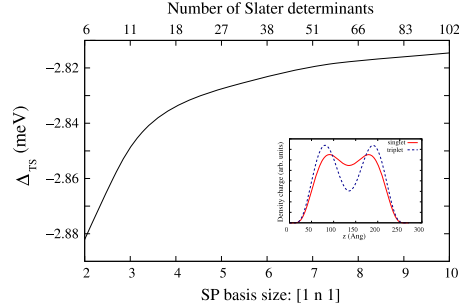
pure correlation effect [15]. In the case of a poor correlation description, the singlet valley is not deep enough and the triplet is more stable, leading to the triplet ground state predicted above.

Since the singlet state has gerade symmetry and only double excitations to ungerade orbitals may contribute to the formation of the central valley in the density profile of the singlet, we explore the possibility of carrying out a CI expansion using gerade orbitals with an in-built valley. A first attempt is to follow a recent approach proposed by Abolfath and Hawrylak of using HF orbitals [19]. However, the approach is useless in our case, because in this scheme HF orbitals are expanded in terms of a (large) SP basis set and, as shown in figure 2, even an extremely large (finite) SP basis set cannot prevent the singlet–triplet reversal. Note that gerade/ungerade HF orbitals would be linear combinations of gerade/ungerade SP orbitals. Therefore, no gerade HF orbital developing a valley can be obtained as a linear combination of SP orbitals. We then take a different approach and carry out numerical HF calculations, build a many-electron Hamiltonian (5) out of the M lowest-lying HF eigenvectors and repeat the calculations shown in figure 1 with this new orbital basis set. In particular, the results collected in figure 3 correspond to a 1-6-1 HF basis set. One can see that HF-CI outperforms SP-CI. Indeed, at $L = 170$ Å, HF-CI clearly predicts a singlet ground state. All the same, a singlet–triplet crossing is observed shortly after $L = 200$ Å, indicating that the basis set is still insufficient.

We investigate in some more detail the large L region. To this end, we consider a $L = 200$ Å NR, and carry out calculations employing a large basis set (1-10-1). In the first instance we run mean-field HF and KS (in the local density approximation) calculations. The corresponding mean-field potentials are represented in figure 4 left and center, respectively. We see that both have a similar shape, i.e. a profile versus z resembling a symmetric hill with the top at the rod center. In figure 4 (right) we show a simplified potential v^{tri}, composed of a triangle of height H along the NR z-axis. All
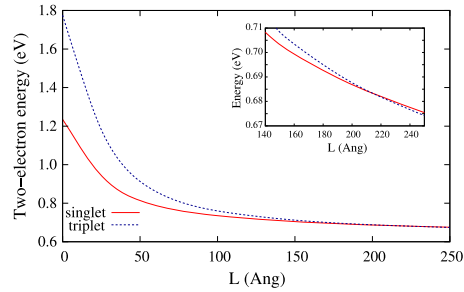
Figure 3. FCI calculations, employing a 1-6-1 HF basis set, of the singlet (solid line) and triplet (dashed line) states of a $R = 20$ Å two-electron semiconductor CdSe NR versus the length L. Inset: close-up of the large L region.
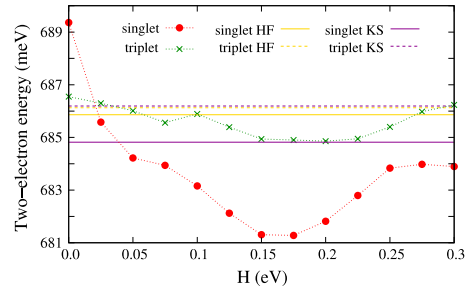
Figure 5. FCI optimization of the variational triangle-like $v^{\text{tri}}(H)$ potential versus its height H, in the case of a $R = 20$ Å, $L = 200$ Å CdSe NR, employing a 1-10-1 basis set. Singlet (dots) and triplet (crosses) energies are represented. Horizontal solid (singlet) and dashed (triplet) lines representing HF-FCI (dark lines) and KS-FCI (light lines) are also enclosed.

three potentials have a common feature: they destabilize the central region of the NR. In the case of HF and KS, the mean-field potentials are optimized in a self-consistent procedure. As far as the third potential is concerned, we optimized the height H of v^{tri} variationally, i.e. we perform FCI calculations with states obtained as eigenvectors of a modified SP Hamiltonian, which adds $v^{\text{tri}}(H)$ to the confining potential, and then select variationally the best H. This optimization is shown in figure 5 for a $n = 10$ basis set. We represent singlet and triplet FCI energies versus the triangle height H. For comparison, horizontal lines representing HF-FCI and KS-FCI are enclosed. Several relevant conclusions that may be drawn from this figure: (i) all three potentials recover the correct singlet/triplet energetic ordering; (ii) orbital optimization affects the singlet state far more than the triplet; (iii) from the variational principle and McDonald's theorem, we conclude that v^{KS} outperforms v^{HF} and the variational potential v^{tri} outperforms both v^{HF} and v^{KS}. The good performance of v^{KS} is remarkable in view of its typical failures in very-few-electron systems [21]. Also, we note that in this system HF-CI gives better results than the SP-CI scheme, contrary to the expectations of [19] for a small number of electrons. The singlet–triplet Δ_{TS} gap yielded by v^{HF}, v^{KS} and v^{tri} through the FCI calculations are 0.2, 1.4 and 3.5 meV, respectively.

As pointed out in section 1, the correlation energies in the QD system under study are so strong that the choice of
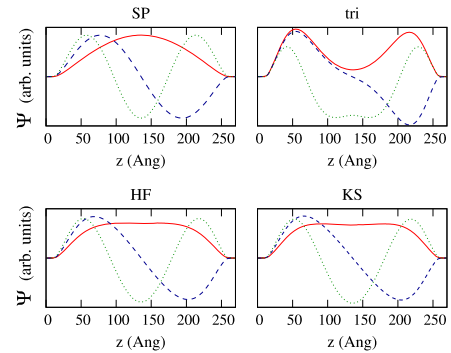
Figure 6. $\rho = 0$ z-profiles of the lowest-lying SP, HF, KS and variationally optimized (v^{tri}) orbitals in the NR investigated in figure 5. Solid, dashed and dotted lines are used for the lowest, first excited and second excited orbital, respectively.

a single-particle basis set becomes critical for a correct CI description. This is nicely shown in figure 6, where the $\rho = 0$ z-profiles of the orbitals with largest contribution
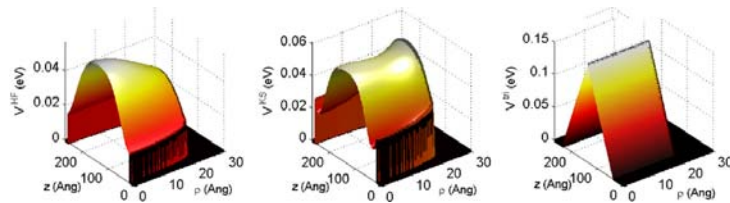
Figure 4. Mean-field HF (left), KS (center) and variationally optimized v^{tri} (right) potentials of a $R = 20$ Å, $L = 200$ Å two-electron CdSe NR.
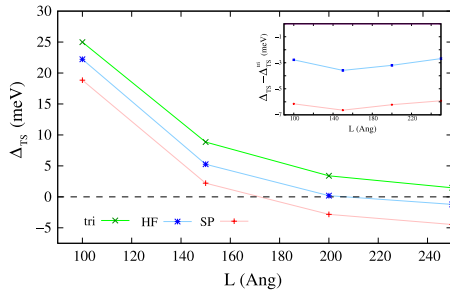
Figure 7. FCI singlet–triplet gap Δ_{TS} obtained with SP, v^{HF} and v^{tri} versus L of a $R = 20$ Å two-electron semiconductor CdSe NR. The inset shows the differences between the calculated SP and v^{HF} and the v^{tri} singlet–triplet gaps.

to the CI are illustrated. The lowest-lying (σ) SP orbital shows a prominent maximum at the NR center. Therefore, the *a priori* dominant σ^2 configuration of the lowest-lying two-body singlet state incorporates a strong Coulomb repulsion. Meanwhile, the same figure shows that HF and KS optimized orbitals present a central plateau instead. The observed plateau is the result of the mean-field optimization which, as pointed out in section 2, accounts for two-body interactions in an averaged way. In our approach, all terms in the many-body Hamiltonian are treated on an equal footing to optimize the orbital basis set and, as shown in figure 6, the result of the CI optimization yields a lowest-lying σ orbital with a valley at the NR center. Consequently, the σ^2 configuration already provides a qualitatively correct description of the central valley displayed by the two-body singlet ground state (see inset in figure 2). Similar arguments can be made for the low-lying excited orbitals, also shown in figure 6.

In the next step, in order to show the performance of our approach compared with standard mean-field calculations, we consider again the 1-6-1 basis set employed in figures 1 and 3, run calculations optimizing v^{tri} in the region 100 Å $\leqslant L \leqslant$ 250 Å, and compare the results yielded by v^{tri} with the SP-CI and HF-CI methods. The combined results are summarized in figure 7, where the FCI singlet–triplet gap Δ_{TS} obtained from SP, v^{HF} and v^{tri} versus L, is represented. One can see that only in the case of v^{tri} is the correct null asymptotic limit of the singlet–triplet gap obtained. In the inset, the difference between the calculated SP or HF gaps and the benchmark one (v^{tri}) is displayed. The inset shows that, within this region, the gap error is approximately constant for both approaches. It mainly comes from a deficient description of the singlet state (see figure 5).

To close this section we would like to note that the poorly correlated description of SP-CI is exclusive to NRs with a large aspect ratio. As a matter of fact, SP-CI calculations for a $R = 50$ Å, $L = 200$ Å (total length 300 Å) CdSe NR employing a 1-6-1 basis set yields the correct singlet–triplet order, contrary to the $R = 20$ Å NR we have analyzed in detail.

4. Conclusion

We have shown that the FCI correlation energy of two electrons in quasi-one-dimensional NRs calculated with the usual orbital basis set of numerical eigenfunctions of the one-electron operator h arising in the many-body Hamiltonian (SP-FCI scheme) leads to the wrong singlet–triplet energetic order. Irrespective of basis size, the correlation energy of the NR is very sensitive to the choice of orbitals. Thus, mean-field-CI approaches that somehow take into account an averaged electron–electron interaction in the orbital optimization can partially correct this drawback. A new CI scheme is proposed in which the mean-field potential is replaced by a simple triangular potential, with the triangle height as a variational parameter. The latter approach outperforms mean-field-CI schemes, yielding robust results.

References

[1] Bastard G 1988 *Wave Mechanics Applied to Semiconductor Heterostructures* (Les Ulis: Les Éditions de Physique)
[2] Singh J 2003 *Electronic and Optoelectronic Propoerties of Semiconductor Structures* (Cambridge: Cambridge University Press)
[3] Bányai L and Koch S W 1993 *Semiconductor Quantum Dots* (Singapore: Word Scientific)
[4] Jacak L, Hawrylak P and Wós A 1998 *Quantum Dots* (Berlin: Springer)
[5] Chakraborty T 1999 *Quantum Dots* (Amsterdam: Elsevier)
[6] Warburton R J, Miller M T, Dürr C S, Bödefeld C, Karrai K, Kotthaus J P, Medeiros-Ribeiro G, Petroff P M and Huant S 1998 *Phys. Rev.* B **58** 16221
[7] Szabo A and Ostlund N S 1989 *Modern Quantum Chemistry* (New York: McGraw-Hill)
[8] McDonald J K L 1933 *Phys. Rev.* **43** 830
[9] Löwdin P O and Shull H 1956 *Rev. Mod. Phys.* **101** 1730
[10] Wensauer A, Korkusinski M and Hawrylak P 2004 *Solid State Commun.* **130** 115
[11] Peng X, Manna L, Yang W, Wickham J, Scher E, Kadavanich A and Alivisatos A P 2000 *Nature* **404** 59
[12] Kan S, Mokari T, Rothenberg E and Banin U 2003 *Nat. Mater.* **2** 155
[13] Shabaev A and Efros Al L 2004 *Nano Lett.* **4** 1821
[14] Baskoutas S 2005 *Chem. Phys. Lett.* **404** 107
[15] Climente J I, Royo M, Movilla J L and Planelles J 2009 *Phys. Rev.* B **79** 161301(R)
[16] Lieb E and Mattis D 1962 *Phys. Rev.* **125** 164
[17] Bour P 2001 *Chem. Phys. Lett.* **345** 331
Grimme S and Waletzke M 1999 *J. Chem. Phys.* **111** 5645
[18] Goddard W A, Dunning T H, Hunt W J and Hay P J 1973 *Acc. Chem. Res.* **6** 368
[19] Abolfath R M and Hawrylak P 2006 *J. Chem. Phys.* **125** 034707
[20] Emperador A, Lipparini E and Pederiva F 2005 *Phys. Rev.* B **72** 033306
[21] Legrand C, Suraud E and Reinhard P G 2002 *J. Phys. B: At. Mol. Opt. Phys.* **35** 1115
Chwiej T, Bednarek S, Szafran C, Adamowski J and Peeters F M 2006 *Phys. Rev.* B **73** 075422

From quantum dots to quantum wires: Electronic structure of semiconductor nanorods

J. Planelles,[1,*] M. Royo,[1] A. Ballester,[1] and M. Pi[2]

[1]*Departament de Química Física i Analítica, Universitat Jaume I, P.O. Box 224, E-12080 Castelló, Spain*
[2]*Departament ECM, Facultat de Física and IN2UB, Universitat de Barcelona, E-08028 Barcelona, Spain*
(Received 28 May 2009; revised manuscript received 24 June 2009; published 28 July 2009)

The transition bridge between zero-dimensional quantum dots and one-dimensional quantum wires is explored theoretically by means of the construction of the addition energy spectra of nanorods with different lengths. Spin density-functional theory supplemented with full configuration interaction calculations are carried out. The addition energy spectra are qualitatively related to the single particle correlation diagram. The transition from charge-density waves to spin-density waves, characterizing the Wigner crystallization in the low density limit is shown.

I. INTRODUCTION

Nanorods (NRs) constitute the bridge between zero-dimensional quantum dots (QDs) and one-dimensional quantum wires (QWs). Investigations of the transition regime from QDs to QWs are of particular interest in the case of colloidal semiconductor nanocrystrals because size and shape control enables the synthesis of NRs with precise length and diameter,[1] so that by tuning the aspect ratio one can follow the transition from zero- to one-dimensional systems.

By changing the gate voltage attached to a nanocrystal, tunnel conductance and capacitance measures yield a peak every time the number of electrons in the QD increases by one. The spacing of peaks or addition spectrum, reflects differences between the ground states with different number of electrons. This shell filling is a neat manifestation of quantum-mechanical degeneracy. While for large dots containing many electrons, oscillations in the spectrum are periodic because the single-electron charging energy is determined classically by the total dot capacitance, for a dot containing few electrons both, quantum effects reflecting the symmetry of the confining potential and electron-electron interactions, lead to modifications of the oscillations so they are no longer periodic,[2] thus revealing the shell structure of the dot.

Tunneling spectra of single CdSe NRs of radii and lengths ranging between 1.8–3.2 and 11–60 nm, respectively, have been reported.[3] The spectra were measured with the tip at a distance avoiding charging effects. On the basis of a theoretical formalism for QWs, the observed peaks were assigned to low-lying conduction bands with azimultal angular momentum $m_z=0,1,2$, but no discretization of these bands originated from confinement was resolved. Similar InAs NR spectra with not well resolved conduction band states has also been published.[4] Not many experimental addition spectra of short NRs can be found in the literature. Long and wide Si NWs display a uniform peak height and width and equidistant spacing in the current vs gate voltage spectrum[5] while shorter thinner Si NRs show a more irregular spectra,[6] thus revealing a shell structure.

Theoretical understanding of QD addition spectra usually rely on isotropic and anisotropic harmonic confining potentials.[2,6,7] Thus, two-dimensional (2D) harmonic QDs has a 2, 4, 6, 8… degeneracy pattern yielding high peaks in the addition energy spectrum at $N=2,6,12,20…$ electrons,[8] this structure being partially destroyed by elliptical deformation of the QD.[9] On the other hand, the confining potential of a spherical colloidal nanocrystal, typically synthesized by wet chemistry methods, is better represented by a steplike hard wall potential,[10] which corresponds to the band gap difference between neighboring materials. This confining potential yields a 2, 6, 10… degeneracy pattern which shows up at $N=2,8,18…$ electrons. NRs are an elongated variant of colloidal QDs,[1] i.e., may be considered as a QD with a highly anisotropic confining potential, which is resposible for some remarkably strong Coulomb interactions.[11,12] Then, the transition from QD to NR is not only characterized by a symmetry change of the confining potential, but additionally by a transition from strong to weak confinent regime. Monitoring this change of symmetry and confining regime in the addition spectra is the aim of this work. We carry out local spin-density-functional theory calculations supplemented with full configuration interaction (FCI) computations. An interesting 2D model calculation, correlating the addition spectra of squared and rectangular boxes with the same area, shows the abovementioned double transition.[13] Our calculations, which correspond to a truly three-dimensional (3D) NR system of constant section and variable length, display a different addition energy pattern, as it corresponds to different confining potentials, but converges toward qualitative similar profiles in the limit of weak confining regime. In the low-density limit we also find a transition from charge-density waves (CDW) with $N/2$ peaks in the density profile vs the NR axis and preserved spin symmetry to spin-density waves (SDW) with N peaks (Wigner crystallization) and broken spin symmetry.[14] Further, the fully spin polarized state is reached.[15]

II. THEORY

Local spin density functional theory (LSDFT), which has given satisfactory results in the study of related structures,[8,13,18,19] is employed in the present work. Numerical integration of the Kohn-Sham equations is carried out. Details of the method followed are described in Ref. 8. The

exchange-correlation functional is taken as a sum of the Dirac exchange functional of a homogeneous electron gas and the correlation functional parametrized by Perdew and Zunger.[20] The electron effective mass and the dielectric constant, screening the electron-electron interaction, are assumed to be equal to that of the NR bulk material.[21] The confining potential is the same we used in a previous study of NRs,[22] namely, zero within the NR composed by a cylinder of radius R and variable length L, attached to two hemispherical caps of the same radius R, and V^{out} elsewhere. Some FCI calculations are carried out for $N=4,6,8$ electrons and $L=10$ nm, in order to confirm the density profiles obtained with LSDFT. As we will see, in these cases only $m_z=0$ orbitals come into play. Then, we select a basis set of orthogonalized floating spherical Gaussian functions. The original nonorthogonal spherical Gaussian functions $g(\mathbf{r})=e^{-\alpha(\mathbf{r}-\mathbf{R}_i)^2}$ are defined by the exponent α and the position $\mathbf{R}_i$ where they are centered. The exponent α is fitted variationally in a $L=0$ NR (sphere) calculation in which a single Gaussian function is employed. The floating Gaussian functions are centered along the NR axis, equally spaced, so that they saturate the space. The number of Gaussians is increased up to convergence in energy. The same density of Gaussian functions along the NR axis is employed in all calculations. Once the primitive Gaussian functions are established, orthonormalization yielding a new basis set which most closely resemble the original basis functions, i.e., a symmetric orthogonalization employing $S^{-1/2}$, the inverse of the original basis set metrics square root, is carried out.[23] With this orthonormal basis set, the many-body Hamiltonian reads in second quantization language,

$$H = \sum_{pq}^{M} h_{pq} a_p^+ a_q + \sum_{pqrs}^{M} g_{pqrs} a_p^+ a_q^+ a_r a_s, \qquad (1)$$

where a_p^+, a_q are fermion creator and annihilator operators, and h_{pq} and g_{pqrs} the one- and two-electron integrals. Except for the contribution of the potential energy coming from the confining potential to the single-electron integrals, which is calculated numerically, all integrals are computed analytically.[23]

In order to carry out FCI calculations, once the one-electron basis set $\{\phi_p\}_{p=1}^{M}$ is selected, we build all possible N-body Slater determinants $\Phi_\alpha=\det\{\phi_1\phi_2\ldots\phi_N\}$ out of them. In a second step, we project Hamiltonian (1) onto the basis set of Slater determinants yielding matrix elements $\langle\Phi_\alpha|H|\Phi_\beta\rangle$. Finally, we proceed with the diagonalization.

III. RESULTS AND DISCUSSION

We study the electronic structure of CdSe NRs. The geometry, described in the previous section, is defined by the NR radius, fixed to $R=2$ nm, and the length, which we range from $L=0$ up to $L=55$ nm. The material parameters employed are those of the bulk material,[24] namely, effective mass $m^*=0.13$ and dielectric constant $\varepsilon=9.2$. The height of the confining potential is set to $V^{out}=4$ eV.

In Fig. 1 we show the low-lying single particle noninteracting energy (sp) levels obtained within the effective mass
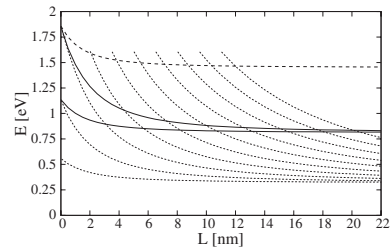
FIG. 1. Energy of the lowest NR sp noninteracting energy levels (eV) vs the NR length L (nm). Dotted, full and dashed lines correspond to orbitals with azimutal quantum number $m_z=0$, $m_z=\pm 1$, and $m_z=\pm 2$, respectively.

approach formalism. We represent sp energy vs NR length L. Dotted lines correspond to orbitals with $m_z=0$, full lines to $m_z=\pm 1$ and dashed lines to $m_z=\pm 2$. At $L=0$ we can see the typical spherical 1–3–5… degeneracy (2–6–10… including spin). As $L\neq 0$, the symmetry reduces from spherical to axial, with just one- and two-dimensional irreducible representations, i.e., with just nondegenerate and twofold degenerate orbitals (degeneration 2 and 4 including spin). In the figure one can also see how very excited $m_z=0$ orbitals at $L=0$ stabilize as L increases, converging toward the lowest conduction band of the infinite wire. This accumulation of $m_z=0$ states looks similar to the formation of Landau bands in the Fock-Darwin energy spectra vs magnetic field. Additionally, despite only two $m_z=\pm 1$ and one $m_z=\pm 2$ levels are included in Fig. 1, one can envisage the formation of the second conduction band and the bottom of the third one. These bands correspond to the ones observed in Ref. 3. Also, the figure allows us to determine degeneracy/quasidegeneracy vs L, which shows up as peak patterns in the addition energy spectra. Thus, one can foresee that for $L=0$ (sphere) the consecutive electron charging up to $N=20$ yields three strong peaks at 2, 8, and 18 electrons, while in the case of $L=20$ nm a featureless addition energy spectrum will be obtained. As can be seen in Fig. 2, these qualitative trends are fully confirmed by the LSDFT calculations, where exchange and correlation are included. In this figure we represent addition energies $\Delta_2(N)=E(N+1)-2E(N)+E(N-1)$, with $E(N)$ being the ground state total energy of the N-electron NR system, vs the number N of electrons for NRs of different length. From top to bottom, we represent $L=0$ up to $L=22$ nm in steps of $\Delta L=2$ nm. Addition energies are given in eV. However, in order to group all the results within a single figure, the different profiles have been offset 400 meV. For example, addition energies for $L=0$ should be subtracted by an amount of 4.4 eV.

As pointed out above, Fig. 2 qualitatively reproduces the degeneracy pattern observed in Fig. 1. Thus, for $L=0$, in addition to three main peaks at $N=2$, 8, and 18 electrons, which correspond to the filling of the three lowest shells, one can see secondary, less intense, peaks at $N=5$ and $N=13$ electrons, corresponding to half fillings. As shown in Fig. 1, as the NR gets longer, excited $m_z=0$ levels fall below the
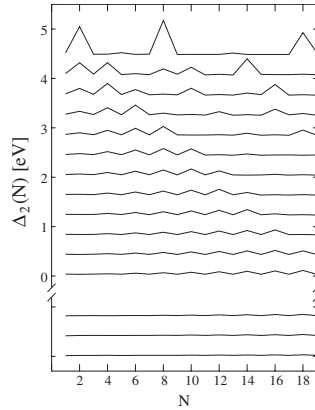
FIG. 2. Addition energy spectra (eV) for NR of increasing length L vs the number N of electrons. Increasingly larger NRs are represented from top to bottom, starting with $L=0$ (spherical QDs) up to $L=22$ nm NR, in steps $\Delta L=2$ nm. The different profiles have been offset 400 meV. The three almost flat profiles at the bottom correspond to the low-density NRs of length $L=40$, 45 and 55 nm.

low-lying $m_z=\pm 1$ one, and occupied orbitals become closer in energy, i.e., the density of states increases. This leads to a change in peak pattern and a general lowering of the addition energies (see Fig. 2). For long NR, e.g., $L=20$ nm, we also see in this figure that the spectrum starts almost flat at low N and wrinkles as this number increases. It is related to a growth in the energy gap between neighboring levels of the $m_z=0$ lowest band as we move toward higher energies, i.e., as we fill the NR with a larger number of electrons (see Fig. 1). For very large L we reach the Wigner crystallization limit and, as expected, an almost flat curve for all N (see bottom of Fig. 2). We will turn our attention to this limit later on in the paper.

Details of the addition spectra vs L can be understood with the help of Fig. 1. For example, as can be seen in this figure, if we fill with $N=18$ electrons an $L=2$ nm NR, we have the following electronic configuration: 0^2 0^2 1^4 0^2 1^4 2^4, where the exponents represent the number of electrons filling the orbital whose m_z-modulus is being powered. This configuration will show main peaks at $N=2,4,8,10,14,18$ electrons (filled shells) and secondary peaks at $N=6,12,16$ (half fillings). This result is confirmed in Fig. 2, although this figure also reveals that the peak at $N=18$ does not exist. Coming back to Fig. 1, one can see that at $L=2$ nm there is a quasidegeneration of the first $m_z=\pm 2$ and the fourth $m_z=0$ levels, so that instead of an electronic configuration 2^4 one may think of $(2,0)^4$, which does not yield a main peak in the addition energy spectrum at $N=18$.

As a main result of this set of calculations one may conclude that for CdSe NRs, with a shape ratio larger than 6, the addition energy spectra will become featureless. Since CdSe, with an effective mass of 0.13 and a dielectric constant of

9.2, has an effective Bohr radius of about 3.8 nm, one can foresee that semiconductor materials such as InAs, with effective Bohr radius about ten times larger, will display features revealing a given degeneracy pattern until much larger shape ratios.

We further explore the low-density limit. A comprehensive study on phase diagrams for interacting fermions in one-dimensional periodic potentials[25] brings a description of the electron system in terms of fields representing fluctuations in the spin and charge densities. The existence of localization and magnetic transitions in the low-density limit, have also been reported for infinite[26] and finite[27] wires defined by harmonic confinement potentials. In order to explore here the low-density limit of free standing NRs we calculate the LS-DFT ground state of long but finite NRs. The obtained results are summarized in Fig. 3, where total (full thick line), spin up (dashed line), and spin down (dotted line) density profiles vs the NR axis, for NR lengths $L=40$, 45, and 55 nm, and populations $N=4,6,8$ electrons, are represented. For the sake of comparison, results for a short $L=10$ nm NR are also enclosed. In this case, also the total density profile coming from FCI calculations (+) is shown. The reason of these FCI calculations is to confirm the observed concentration of total density distribution toward the ends of the NR. A similar behavior was already noticed in the model calculation of Ref. 13, in which LSDFT calculations were carried out, and contrast with the results in Ref. 27, where the total density is more pronounced at the center, due to the harmonic confinement employed in this last study. The same concentration of total density distribution toward the ends of the NR can also be seen in 16, where CI calculations of an effective one-dimensional (1D) model is performed. In this last calculation, the CI expansion employs the numerical sp eigenfunctions of the single-electron Hamiltonian. Provided the recently reported difficulties concerning CI calculations based on sp orbitals owing to a lack of saturation of the space along the axis of quasi-1D systems,[12] we have checked the obtained results with FCI calculations, as outlined in the previous section, which employ a basis set ensuring saturation along the NR axis. Comparison in Fig. 3 confirms the observed trend in the density profile of NR given by LSDFT calculations, which is probably related to the minimization of the electron-electron repulsion.

Figure 3 shows that for $L=40$ nm and $N=4$, 6, and 8, the so-called charge-density waves, with $N/2$ maxima in the density profile and same spin up and down density profiles (i.e., with preserved spin symmetry) appear. At $L=45$ nm, the more diluted $N=4$ electron system shows up another phase while less diluted, $N=6$ and 8 electron systems remain in the CDW phase. This phase, referred to as spin-density wave, shows N maxima in the density profile and broken spin symmetry.[14] This corresponds to a Wigner-like crystallization, in which the electrons behave like classical density charge arranged within the NR to avoid each other as much as possible. This phase transition, referred to as spin-Peierls transition, is paralleled by a pronounced increasing of the Fermi gap.[27] We also observe this opening. For example, for $N=6$, the ratio between the occupied bandwidth (energy difference between the lowest and highest occupied levels) and the Fermi gap (energy difference between the highest occu-
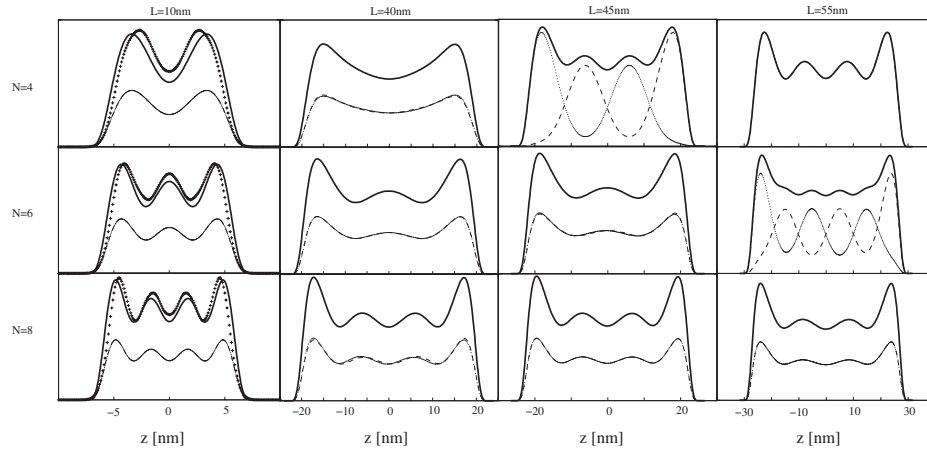
FIG. 3. Electron density profiles along the NR z axis, corresponding to NRs of different lengths L, populated with different number N of electrons. Columns from left to right cover the different lengths: L=10, 40, 45, and 55 nm, respectively. From top to bottom rows, increasing number N of electrons, N=4, 6, and 8. Total (full thick line), spin up (dashed line), and spin down (dotted line) density profiles are shown. For L=10 nm, FCI total density (+) is also enclosed. In those cases in which spin up and down density are equal, dashed and a dotted lines overlap and almost a full thin line profile results.

pied and lowest unoccupied levels) is 1.17 at L=45 nm (CDW phase) and 0.51 at L=55 nm (SDW phase). At L =55 nm the N=8 system still remains in the CDW one while the most diluted N=4 system undergoes a transition to a fully spin polarized state.[15]

IV. CONCLUDING REMARKS

We have investigated the electronic structure of semiconductor NRs. Most calculations employ LSDFT. A few FCI calculations supporting LSDFT results have been also performed. We study the transition from zero-dimensional QDs, with well defined energy levels, to one-dimensional QWs, with energy bands in one dimension. We monitor this transi-

tion with the addition energy spectrum which reveals changes in degeneracy and the increasing role of the electron-electron interactions as L increases. The obtained addition spectra are qualitatively related to the *sp* correlation diagram vs the NR length L. The limit of low-density is explored and the transition from CDW to SDW and, further, to the fully spin polarized phase is shown and discussed.

*josep.planelles@qfa.uji.es

[1] X. Peng, L. Manna, W. Yang, J. Wickham, E. Scher, A. Kadavanich, and A. P. Alivisatos, Nature (London) **404**, 59 (2000); S. Kan, T. Mokari, E. Rothenberg, and U. Banin, Nature Mater. **2**, 155 (2003).

[2] S. Tarucha, D. G. Austing, T. Honda, R. J. van der Hage, and L. P. Kouwenhoven, Phys. Rev. Lett. **77**, 3613 (1996).

[3] D. Katz, T. Wizansky, O. Millo, E. Rothenberg, T. Mokari, and Uri Banin, Phys. Rev. Lett. **89**, 086801 (2002).

[4] D. Steiner, D. Katz, O. Millo, A. Aharoni, S. Kan, T. Mokari, and U. Banin, Nano Lett. **4**, 1073 (2004).

[5] S. Huang, N. Fukata, M. Shimizu, T. Yamaguchi, T. Sekiguchi, and K. Ishibashi, Appl. Phys. Lett. **92**, 213110 (2008).

[6] K. H. Cho, Y. C. Jung, B. H. Hong, S. W. Hwang, J. H. Oh, D. Ahn, S. D. Suk, K. H. Yeo, D.-W. Kim, D. Park, and W.-S. Lee, Appl. Phys. Lett. **90**, 182102 (2007).

[7] S. M. Reimann and M. Manninen, Rev. Mod. Phys. **74**, 1283 (2002).

[8] M. Pi, A. Emperador, M. Barranco, and F. Garcias, Phys. Rev. B **63**, 115316 (2001).

[9] D. G. Austing, S. Sasaki, S. Tarucha, S. M. Reimann, M. Koskinen, and M. Manninen, Phys. Rev. B **60**, 11514 (1999).

[10] M. Pi, M. Royo, and J. Planelles, J. Appl. Phys. **100**, 073712 (2006); M. Royo, J. Planelles, and M. Pi, Phys. Rev. B **75**, 033302 (2007); J. Planelles, M. Royo, and M. Pi, J. Appl. Phys. **102**, 094304 (2007).

Dielectric confinement of excitons in type-I and type-II semiconductor nanorods

M. Royo, J.I. Climente, J.L. Movilla and J. Planelles

Departament de Química Física i Analítica, Universitat Jaume I, E-12080, Castelló, Spain

E-mail: `josep.planelles@qfa.uji.es`

Abstract. We theoretically study the effect of the dielectric environment on the exciton ground state of CdSe and CdTe/CdSe/CdTe nanorods. We show that insulating environments enhance the exciton recombination rate and blueshift the emission peak by tens of meV. These effects are particularly pronounced for type-II nanorods. In these structures, the dielectric confinement may even modify the spatial distribution of electron and hole charges. A critical electric field is required to separate electrons from holes, whose value increases with the insulating strength of the surroundings.

Dielectric confinement of excitons in type-I and type-II semiconductor nanorods   2

1. Introduction

Semiconductor nanocrystals are high-performance light emitters under intense investigation because of their applications in a wide range of fields, including lasing technology, quantum optics, solar energy capture and biomedicine [1]. Due to their nanoscopic size, the electronic structure of the carriers bound in these crystals is mainly determined by quantum confinement [2, 3]. For this reason, recent progress in size [4], shape [5] and composition [6] control of nanocrystals has boosted their technological prospects [7]. Nanorods (NR) or quantum rods are a clear example of this progress. Their elongated shape results in an anisotropic spatial confinement of carriers which is responsible for a series of improved optical properties relative to spherical quantum dots. These range from higher photoluminescence quantum efficiency [8] and faster carrier relaxation [9] to strongly polarized emission [10]. Furthermore, recent advances in vapor-liquid-solid methods have enabled the synthesis of layered semiconductor NRs [11, 12, 13, 14]. In these systems the heterogeneous composition allows the formation of band structures where electrons and holes are preferably located in different spatial regions, forming what is known as type-II quantum dots. Upon excitation, these systems develop a long-lived charge-separated state which makes them attractive for photovoltaic applications [13, 15].

Spatial confinement is not however the only source of quantum confinement in these structures. Nanocrystals are usually embedded in insulating materials, whose low dielectric constant adds a severe dielectric confinement. In spherical quantum dots, the strong isotropic confinement originates similar electron and hole charge distributions. As a result, the influence of dielectric confinement for excitons is weakened [16, 17], the main effect being an increase of the binding energy [18, 19]. One may wonder if this is also the case in NRs, where the presence of a weak confinement direction could lead to a different behavior. Indeed, several studies on quasi-one-dimensional nanostructures have suggested the dielectric mismatch between semiconductor materials and the environment as the driving mechanism to explain some experimental observations. For example, we can mention the large variation of the optical gap of CdSe NRs compared to the transport one [20], the effect on the excitonic energies observed in ZnS NRs [21] and type-II NRs [22], or the large magnitude of the polarization anisotropy on linear [23, 24, 25] and nonlinear [26] optical phenomena. Dielectric confinement has also been shown to affect the dynamics of the electron-hole separation in type-II heterostructured NRs [27] as well as the coupling between electrons and longitudinal optical phonons in CdSe NRs [28]. From the theory side, a few works have investigated excitons in dielectrically confined CdSe nanorods, but they neglected either the longitudinal confinement [29] or the self-interaction with the polarization charges [30].

In this work, we perform a theoretical study of the effects of the dielectric confinement on the excitonic properties of semiconductor NRs. We consider homogeneous CdSe NRs as well as recently synthesized linear CdTe/CdSe/CdTe heterostructured NRs subject to different dielectric environments. We use a fully 3D

effective-mass and envelope-function Hamiltonian which allows us to model sophisticated geometries. The contributions coming from the dielectric mismatch are accounted for using a numerical procedure, and the electron-hole correlations –which are important for long NRs– are treated by carrying full configuration interaction (FCI) calculations.

Our results show that in semiconductor NRs the dielectric confinement modifies the energy and intensity of the exciton photoluminescence. The influence is particularly important in type-II NRs, where the asymmetry between the electron and hole charge distribution enables strong dielectric mismatch effects. In this kind of structures, the electronic density shows a striking response to changes in the dielectric constant of the environment. In insulating environments, the enhanced electron-hole attraction moves the electron density from the center of the NR to the CdTe/CdSe interfaces. Last, we study the effect of longitudinal electric fields on the excitonic states of the NRs. Our results show that a threshold field is required to separate electrons from holes. The value of this critical field is strongly dependent on the dielectric constant of the environment.

2. Theory and computational details

In the effective mass approximation the exciton Hamiltonian can be expressed as

$$H = H_e^0(\mathbf{r}_e) + H_h^0(\mathbf{r}_h) + V_{eh}(\mathbf{r}_e, \mathbf{r}_h), \tag{1}$$

where $H_{e,h}^0(\mathbf{r}_{e,h})$ are single-particle Hamiltonians and $V_{eh}(\mathbf{r}_e, \mathbf{r}_h)$ is the electron-hole Coulomb interaction. To describe the single-particle spectra we assume the following Hamiltonian in cylindrical coordinates and atomic untis

$$H_i^0 = -\frac{1}{2m_i^*}\nabla_i^2 + V_i^c(\rho_i, z_i) + V^{sp}(\rho_i, z_i) - q_i F z_i. \tag{2}$$

Here $i = e, h$ is a subscript denoting electron or hole respectively, m_i is the effective mass that we assume to be constant in the whole system, $V_i^c(\rho_i, z_i)$ is the step-like spatial confining potential, and $V^{sp}(\rho_i, z_i)$ is the self-polarization potential arising from the interaction of each carrier with its own polarization charges, generated on the NR interface as a consequence of the dielectric constant mismatch with the environment. The last term of the Hamiltonian (2) describes the effect of an electric field F applied along the NR longitudinal axis, with q_i standing for the electric charge of the carrier.

Exciton energies and wave functions are obtained by means of FCI calculations, i.e., as the eigenvalues and eigenfunctions of the projection of Hamiltonian (1) onto the two-body basis set of all possible Hartree electron-hole products. Since the low-energy single-particle spectrum of large aspect ratio NRs only includes orbitals with zero azimuthal angular momentum [31] we use a single-particle basis set of 1s-gaussian functions

$$g_{i,x}(\mathbf{r}) = \exp\left[-\alpha_x(\mathbf{r} - \mathbf{R}_i)^2\right], \tag{3}$$

to obtain the exciton energies and wave functions. The exponents α_x (x = e, h for electron and hole, respectively) are fitted variationally in a sphere calculation where a

Dielectric confinement of excitons in type-I and type-II semiconductor nanorods   4

single gaussian function is employed. The gaussian functions are radially centered and equally spaced along the NR longitudinal axis, i.e., $\mathbf{R}_i = z_i\mathbf{k}$. We employ a large enough number of gaussian functions per nm of the NR axis to saturate the space and guarantee energy convergence ‡. Once the set of gaussian functions are obtained, we proceed to a symmetric orthogonalization in order to reach a set of orthonormal functions which most closely resemble the original basis set, both for electrons and holes. Then we build up all possible Hartree electron-hole products that expand the FCI space in which Hamiltonian (1) is projected.

In order to calculate the electron-hole interaction term (the electron-hole exchange is neglected as it does not influence the reported trends) of the FCI matrix elements

$$\langle\phi_i^{\mathrm{e}}\phi_j^{\mathrm{h}}|V_{\mathrm{eh}}|\phi_k^{\mathrm{e}}\phi_l^{\mathrm{h}}\rangle, \tag{4}$$

we first obtain an electron charge density $\eta(\mathbf{r}_{\mathrm{e}}) = \phi_i^{\mathrm{e}*}\phi_k^{\mathrm{e}}$ and then calculate the electrostatic potential that this charge distribution generates onto the hole. To calculate this potential in a medium with spatially inhomogeneous dielectric constant $\varepsilon(\mathbf{r})$, we rewrite the Poisson equation in terms of the source charges plus the induced polarization charges:

$$\nabla^2 V(\mathbf{r}_{\mathrm{h}}) = -4\pi\left[\eta(\mathbf{r}_{\mathrm{e}}) + \eta_{\mathrm{p}}(\mathbf{r}_{\mathrm{e}})\right]. \tag{5}$$

Here $\eta_{\mathrm{p}}(\mathbf{r}_{\mathrm{e}})$ is the polarization charge density, which we calculate with a method [34] equivalent to the *induced charge computation* one proposed by Boda et al. [35] The self-polarization potential appearing in the single-particle Hamiltonian (2) is calculated following a similar scheme but taking a point source charge and scaling the potential by a factor 0.5 due to the self-interaction nature of this term. We refer the reader to reference 32 for further details on the inclusion of these contributions.

In addition to energy and carrier density distribution, we calculate the ground state electron-hole recombination probability and electric dipole moment. For the first one, we use the dipole approximation and Fermi golden rule [36]

$$P \propto \left|\sum_{ij} c_{ij}\,\langle\phi_i^{\mathrm{e}}|\phi_j^{\mathrm{h}}\rangle\right|^2 p_0(T). \tag{6}$$

Here c_{ij} are the exciton ground state FCI expansion coefficients, ϕ_i^{e} and ϕ_j^{h} are symmetrically orthogonalized gaussian functions whose Hartree products constitute the basis set for the FCI expansion and $\langle\phi_i^{\mathrm{e}}|\phi_j^{\mathrm{h}}\rangle$ the corresponding overlap. Since we deal with large aspect ratio NRs in which the energy separation between the ground state and the low lying excited states is just a few meV, to compute the exciton ground state recombination probability we consider thermal population effects. To this end,

‡ A numerical basis set formed by the single-particle Hamiltonian eigenfunctions [30] would be better adapted to the spatial confinement and hence would yield lower exciton energies, closer to experimental values. [32, 33] However, we have chosen to use equidistant floating gaussians because, in contrast to the numerical eigenfunctions, they enable a uniform saturation along the NR as well as a continuously homogeneous description of the system, from the spherical limit to the extremely elongated one.

Dielectric confinement of excitons in type-I and type-II semiconductor nanorods 5

we assume the Boltzmann distribution $p_l(T) = N(g_l/g_0)\exp\left(-\Delta E_l/kT\right)$ for the exciton states occupation at temperature T, with g_l (g_0) as the degeneracy factor of the state l (ground state), ΔE_l the energy difference between the state l and the ground state, and k the Boltzmann constant. N is the normalization constant, which ensures that the sum of all exciton states population is equal to one. Finally, for simplicity, we omit the influence of local fields induced by the dielectric mismatch on the exciton-photon interaction. One can check that their influence in nanorods [29] is qualitatively the same as that resulting from the polarization charges we investigate.

On the other hand, we calculate the electric dipole moment as

$$\mu = \int [\rho^{\mathrm{h}} - \rho^{\mathrm{e}}]\, z \, dv, \tag{7}$$

where $\rho^{\mathrm{e,h}}$ are the electron and hole ground state densities.

3. Results and discussion

3.1. Type-I NRs

We start by studying homogeneous CdSe NRs of different lengths. The rods are composed of a cylinder with radius $R = 2$ nm and length L_{c}, attached to two hemispherical caps of radius $R = 2$ nm at the extremes, yielding a total length $L = 2R + L_{\mathrm{c}}$ (see figure 1 inset). CdSe material parameters are used [37]. Thus, electron and hole effective masses are $m_{\mathrm{e}}^* = 0.13$ and $m_{\mathrm{h}}^* = 0.4$. The latter corresponds to the longitudinal mass of a light-hole, since the hole ground state in long NRs is essentially a light-hole [20], For this system, the variational gaussian coefficients are $\alpha_{\mathrm{e}} = 0.0016$ and $\alpha_{\mathrm{h}} = 0.0020$. The dielectric constant inside the NR is fixed to $\varepsilon_{\mathrm{in}} = 9.2$, while outside $\varepsilon_{\mathrm{out}}$ is varied in a wide range, in order to simulate the effect of surrounding media with different insulating strength. Carriers are confined inside the NR by a typical potential barrier of 4 eV.

Figure 1(a) represents the exciton ground state energy as a function of the NR length L for embedding media of different insulating strength. For a given environment, we see that the exciton initially experiences a significant energy stabilization, and an asymptotic value is finally attained. This behavior, which has been observed in optical and tunneling gap measurements [20, 38], reflects the relaxation of the longitudinal spatial confinement. The asymptotic regime is usually identified with a quasi-1D system, where only radial confinement is present, and it explains the success of quasi-1D models in reproducing experimental observations [29].

A similar relaxation is observed in figure 1(b) for the exciton binding energy as the NR is elongated. The plot also reproduces the effect of the dielectric environment previously observed in spherical and cubic nanocrystals [18, 19], i.e., due to the polarization of the Coulomb interaction, low dielectric constant environments increase the electron-hole attraction, and hence, the binding energy.

Despite this gain in binding energy, figure 1(a) reveals that insulating environments blueshift the exciton energy by up to 50 meV [34]. This result is driven by the

Dielectric confinement of excitons in type-I and type-II semiconductor nanorods   6
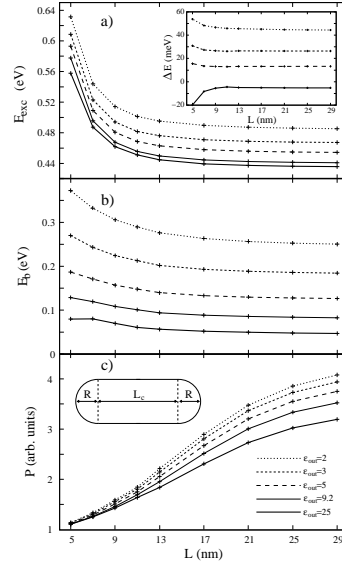
Figure 1. a) Exciton ground state energies (relative to the bulk CdSe gap), b) binding energies and c) recombination probabilities ($T = 30$ K) in homogeneous NRs with variable length L embedded in different dielectric media. Crosses correspond to calculations. Lines are guides to the eyes. Different line shapes correspond to different dielectric constants. The correspondence is shown in the bottom panel. Upper inset: Exciton energy differences between the cases with $\varepsilon_{\text{out}} \neq \varepsilon_{\text{in}}$ and the case $\varepsilon_{\text{out}} = \varepsilon_{\text{in}}$. Lower inset: schematic of the NR geometry.

self-polarization interaction and can be interpreted as follows. Due to the dielectric mismatch, the confined carriers induce polarization charges on the NR surface. When the NR is embedded in a medium of lower (higher) dielectric constant, $\varepsilon_{\text{in}} > \varepsilon_{\text{out}}$ ($\varepsilon_{\text{in}} < \varepsilon_{\text{out}}$), the sign of the induced charges is the same (opposite) as that of the source charges. This means that the self-interaction between source and induced charges, V^{sp}, is repulsive (attractive). Conversely, the electron-hole Coulomb polarization interaction is attractive (repulsive). While these two contributions tend to compensate each other [18, 19], the cancelation is not exact. In all the cases we study, the self-interaction term prevails. For insulating environments ($\varepsilon_{\text{in}} > \varepsilon_{\text{out}}$), this translates into a blueshifted exciton.

Note that the blueshift in figure 1(a) does not contradict the large reduction of

the optical gap observed experimentally in dielectrically confined NRs [20, 29]. This is because the optical gap was compared with the transport gap. Both gaps are subject to the self-interaction potential, but only the optical one includes electron-hole Coulomb polarization effects.

The inset in figure 1(a) shows the difference between the exciton energy with and without dielectric mismatch as a function of the NR length. The energy difference first decreases, and it becomes mostly insensitive to the length once the aspect ratio is larger than two. The initial decrease is due to the relaxation of the longitudinal (dielectric) confinement, and the plateau that follows suggests that the weaker confinement barely affects the balance between self-interaction and Coulomb polarization.

We next investigate the effect of the dielectric environment on the electron-hole recombination probability. The results obtained at $T = 30$ K are illustrated in figure 1(c). It follows from the figure that (i) the recombination probability increases with the NR length, (ii) the dielectric confinement enhances this probability and (iii) this enhancement is larger for long NRs. All these results can be rationalized in terms of the strong correlation regime induced by the softened spatial and the dielectric confinements [30]. In all cases, for long rods thermal population of excited states becomes important and the recombination probability saturates towards the quantum wire limit.

3.2. Type-II NRs

In this section we study heterogeneous NRs similar to those synthesized in references 13 and 22. The rods are composed of a central CdSe cylinder (core) of radius $R = 2$ nm and length L_c^{CdSe} attached to two external shells of CdTe. The shells in turn are formed by a hemispherical cap of radius $R = 2$ nm and a cylinder of length L_c^{CdTe} (see figure 2(c) inset). Bringing all the parts together yields two shells of length $L_s^{CdTe} = R + L_c^{CdTe}$ and a total NR length $L = 2L_s^{CdTe} + L_c^{CdSe}$. These heterostructured systems are known to display a type-II band alignment [12, 13, 14, 22], where electrons are preferably located in CdSe regions and holes in CdTe regions. To reproduce this situation, in our calculations we include a band offset in the interface between both materials. For electrons we take a band offset of 0.42 eV and for holes we take an inverse band offset of 0.57 eV [39]. Since the material parameters of CdSe and CdTe do not offer significant differences, we take CdSe effective mass and dielectric constant for the whole NR. Thus, we just consider the dielectric interface between the whole NR and the external matrix.

In figure 2(a) we show the exciton ground state energies for type-II NRs composed by a CdSe core of length $L_c^{CdSe} = 4$ nm and CdTe shells of increasing length L_s^{CdTe}. Different embbeding media are considered. As in the case of homogenous NRs, for a given environment the exciton experiences an initial energy stabilization and later it reaches an asymptotic value. Also, the same qualitative response to the dielectric environment is observed. However, the magnitude of the energy shifts originated by the dielectric confinement is now about twice that of type-I NRs, reaching values as large as

Dielectric confinement of excitons in type-I and type-II semiconductor nanorods 8
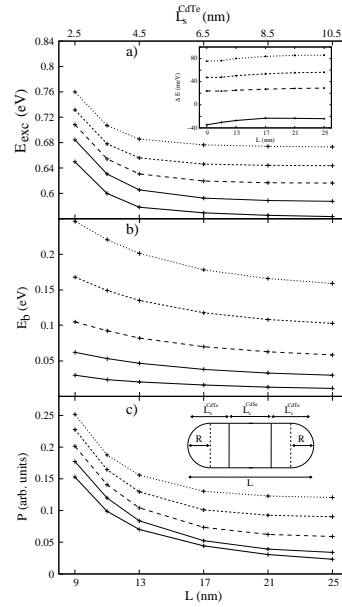
Figure 2. Same as figure 1 but for type-II NRs.

100 meV (see figure 2(a) inset). The reason is that the spatial separation of electron and hole charge distributions in type-II nanostructures weakens the Coulomb polarization term, as reflected in the smaller binding energies displayed in figure 2(b), but not the self-polarization. This leads to greatly enhanced dielectric mismatch effects.

At this point it is worth noting that the effect of the dielectric confinement predicted in figure 2(a) is consistent with the main trends reported in reference 22, where the photoluminescence spectra of similar CdTe/CdSe/CdTe NRs were compared for solvents with different dielectric constant. A blueshift of the exciton emission energy by tens of meV was observed under low dielectric constant environments (figure 7 in their work). This confirms the prevalence of the self-interaction potential over the electron-hole Coulomb one. The irregular differences between the energy shifts originated by the two low dielectric constant solvents of reference 22 are probably connected with microscopic effects, which are beyond our continuum model.

The inset in figure 2(a) shows the difference between the exciton energy with and

without dielectric mismatch as a function of the NR length. As in type-I NRs, the increasing anisotropy has a weak influence.

Figure 2(c) shows the electron-hole recombination probability of type-II NRs at $T = 30$ K. As can be observed, the probability is much smaller than in type-I NRs due to the charge separation, which was already noted in related experiments [12]. In addition, contrary to type-I NRs (figure 1(c)), the recombination probability now decreases with the NR lenght. This is because the length increase comes from longer CdTe shells, so that the hole lies further away from the electron, which leads to an additional reduction of the electron-hole overlap. The effect of the dielectric environment is also quite different from the homogeneous NR case. Insulating environments still enhance the recombination probability, but: (i) the enhancement does not vary with L, because the size increase of the CdTe shells does not entail an increase in the role of the electron-hole correlations, and (ii) the relative enhancement is many times larger. For example, at $L = 25$ nm the recombination probability for $\varepsilon_{\mathrm{out}} = 2$ is ~ 3.5 times that of $\varepsilon_{\mathrm{out}} = 9.2$, compared to ~ 1.2 times in type-I NRs. This is another manifestation of the important role of dielectric mismatch in type-II structures.
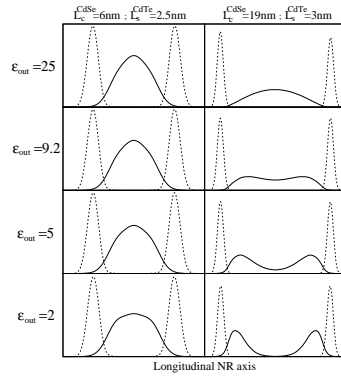
Figure 3. Electron (solid lines) and hole (dashed lines) densities along the longitudinal axis, for type-II NRs of $L_{\mathrm{c}}^{\mathrm{CdSe}} = 6$ nm and $L_{\mathrm{s}}^{\mathrm{CdTe}} = 2.5$ nm (left), and $L_{\mathrm{c}}^{\mathrm{CdSe}} = 19$ nm and $L_{\mathrm{s}}^{\mathrm{CdTe}} = 3$ nm (right). The dielectric constants of the surroundings are indicated on the left of each row.

Next we show that the strong influence of dielectric confinement in type-II NRs may even reshape the exciton wavefunction. Figure 3 illustrates the electron (solid line) and hole (dashed line) density profiles along the NR longitudinal axis. Left (right) panels correspond to NRs of dimensions $L_{\mathrm{c}}^{\mathrm{CdSe}} = 6$ nm and $L_{\mathrm{s}}^{\mathrm{CdTe}} = 2.5$ nm ($L_{\mathrm{c}}^{\mathrm{CdSe}} = 19$ nm and $L_{\mathrm{s}}^{\mathrm{CdTe}} = 3$ nm) embedded in media of different insulating strength. No noticeable

effects arise in the case of the shorter NR. By contrast, as the longer NR is embedded in strong insulating media, the electron moves from the rod center to the CdTe shells. For a strong enough dielectric mismatch, the electron density even develops a deep valley at the center of the NR (see e.g. $\varepsilon_{out} = 2$, bottom right panel in figure 3). The driving force of this behavior is the increase of the electron-hole interaction by means of the polarization charges. As the CdSe core is elongated, this attractive potential starts dominating over the longitudinal spatial potential felt by the electron, which is then dragged by the hole towards the material interface. This phenomenon is favored for long CdSe cores and short CdTe shells.

The electron localization near the external shells evidences a regime where the role of the longitudinal spatial confinement is taken over by the dielectric confinement. Moreover, important implications follow from this phenomenon, such as enhanced sensitivity of the exciton near the CdSe/CdTe interface and reduced coupling to impurities and defects in the center of the rod.

3.3. Electric field effect

In the last few years both theoretical [40] and experimental [41, 42] studies have pointed out interesting properties for technological devices arising from the application of an external electric field along the longitudinal direction of NRs. The electric field separates electrons from holes, thus reducing the radiative recombination probability. The rate at which this happens is known to be affected by the quantum confinement, which is related to the quantum confined Stark effect. Having observed the strong influence of dielectric confinement in NRs at zero field, we next probe how it modifies the exciton response to longitudinal electric fields.

In figure 4 we study the electric field effect over the exciton ground state energy (a), electron-hole recombination probability ($T = 30$ K) (b) and dipole moment (c), for a homogeneous CdSe NR of length $L = 25$ nm in different media. As can be seen, there is a critical electric field from which the system evolves in a different way. This is the field required to induce the electron-hole separation. The separation is reflected by a redshift of the exciton energy (figure 4(a)), a sudden reduction of the exciton recombination probability (figure 4(b)) and an abrupt increase of the dipole moment (figure 4(c)). The abrupt response to the electric field is consistent with the rapid switches observed in optical spectroscopy experiments [42].

Figure 4 proves that the dielectric confinement has important effects on the exciton response to electric fields. The critical field required to separate electrons from holes increases significantly with the insulating strength of the environment. This is due to the abovementioned modulation of the exciton binding energy.

We next illustrate the electric field effect on type-II NRs. Results are shown in figure 5 for a NR of $L_c^{CdSe} = 19$ nm and $L_s^{CdTe} = 3$ nm (total length $L = 25$ nm). The same trends as in homogeneous NRs are observed, but now, since the electron-hole interaction is weaker, smaller fields are required to separate both particles and
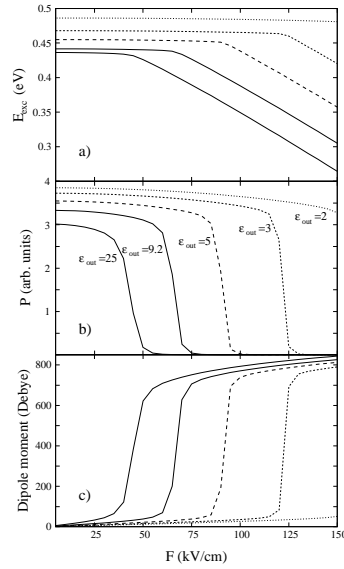
Figure 4. a) Exciton ground state energies (relative to the bulk CdSe gap), b) recombination probabilities ($T = 30$ K) and c) dipole moments of a $L = 25$ nm homogeneous NR vs. the applied electric field. The dielectric constants of the media are indicated by the lines in panel b).

this process takes place more gradually. In any case, the influence of the dielectric environment on the exciton response to electric fields is still felt, and it can increase the critical field value over an order of magnitude. The anomalous evolution observed at small fields in the recombination probability (figure 5(b)) is explained as follows. The electric field breaks the double-degeneracy of the hole states localized in the CdTe caps. Since in figure 5(b) we just show the ground state recombination probability, the initial increase comes from the thermal depopulation of the first excited state in favor of the ground state.

Finally, we focus our attention on the evolution of the exciton charge density under the influence of electric fields. In homogeneous NRs no noticeable effects arise. Electron and hole remain in the center of the rod until the field splits them up towards opposite NR ends (not shown). Conversely, type-II NRs display an interesting interplay between the electric field and Coulomb polarization effects, whose effect on the charge
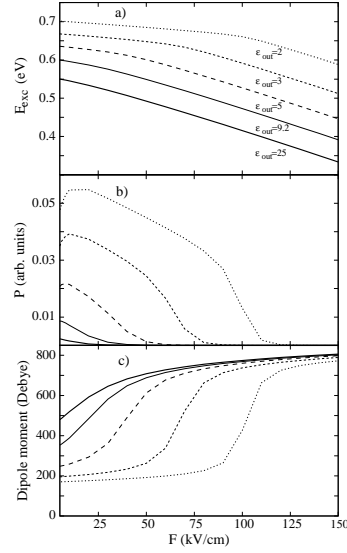
Figure 5. Same as figure 4 but for a type-II NR with $L_c^{CdSe} = 19$ nm and $L_s^{CdTe} = 3$ nm.

distribution is summarized in figure 6. A small electric field ($F = 20$ kV/cm) suffices to localize the hole in the CdTe shell near the negative electrode. The electron localization is however strongly dependent on the dielectric environment. In the absence of dielectric mismatch ($\varepsilon_{out} = 9.2$) it is centered, revealing a compensation between the electric field and electron-hole interactions. For $\varepsilon_{out} = 2$, Coulomb interaction dominates and the electron moves towards the hole (in spite of the electric field), and the opposite occurs for $\varepsilon_{out} = 25$. With increasing electric field ($F = 100$ kV/cm), the electron is forced to move towards the positive electrode, but this is still difficult if the environment is strongly insulating ($\varepsilon_{out} = 2$). Once again, this behavior comes from the modulation of the exciton binding energy by the dielectric confinement.

4. Conclusions

We have shown that the dielectric confinement has significant effects in the excitonic properites of semiconductor NRs. In type-I NRs, low dielectric constant environments blueshift the exciton photoluminescence peak by tens of meV, enhance electron-hole
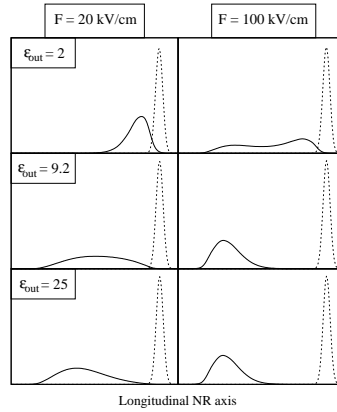
Figure 6. Electron (solid lines) and hole (dashed lines) densities along the longitudinal axis, for a type-II NR of $L_c^{CdSe} = 19$ nm and $L_s^{CdTe} = 3$nm subject to electric fields of 20 and 100 kV/cm. The dielectric constants of the different media are enclosed on the top-left corner of each row.

recombination rates and increase the electric field required to separate electrons from holes. The two latter effects are direct consequences of the enhanced correlation regime and exciton binding energy, while the former is a consequence of the exciton self-interaction with the induced polarization charges.

In type-II NRs, the same effects hold, but now greatly enhanced due to the asymmetric charge distribution of electrons and holes, which reduces the compensation between self-interaction and electron-hole Coulomb polarization. In these systems, a strong dielectric mismatch may move the electron charge density from the center of the core towards the heterostructure interface. This result has straightforward implications in the physical response of the NRs, and it shows that the dielectric confinement can be used -in addition to spatial confinement- to manipulate the shape and size of type-II excitons.

To experimentally confirm the electronic density localization trends reported here, we propose using wave function mapping techniques, such as near-field scanning optical microscopy [43]. Alternatively, the diamagnetic shift of NRs subject to transversal magnetic fields will discriminate excitons with an electron localized in the center or near the shells of the NR. We close by noting that the phenomena reported in this work are not exclusive of CdSe/CdTe NRs. They can be extended to rods made of different materials as long as the appropiate dielectric confinement regime is attained.

Dielectric confinement of excitons in type-I and type-II semiconductor nanorods 14

Acknowledgments

References

[1] Rogach A 2008 *Semiconductor Nanocrystal Quantum Dots* (Wien: Springer)
[2] El-Sayed M 2004 *Acc. Chem. Res* **37** 326–33
[3] Li J and Wang L 2003 *Nano lett.* **3** 1357–63
[4] Dabbousi B, Rodriguez-Viejo J, Mikulec F, Heine J, Mattoussi H, Ober R, Jensen K and Bawendi M 1997 *J. Phys. Chem. B* **101** 9463–75
[5] Manna L, Scher E and Alivisatos A 2000 *J. Am. Chem. Soc* **122** 12700–6
[6] Wang X, Ren X, Kahen K, Hahn M, Rajeswaran M, Maccagnano-Zacher S, Silcox J, Cragg G, Efros A and Krauss T 2009 *Nature* **459** 686–9
[7] Sanderson K 2009 *Nature* **459** 760
[8] Peng X, Manna L, Yang W, Wickham J, Scher E, Kadavanich A and Alivisatos A 2000 *Nature* **404** 59–61
[9] Mohamed M, Burda C and El-Sayed M 2001 *Nano Lett.* **1** 589–93
[10] Hu J, Li L, Yang W, Manna L, Wang L and Alivisatos A 2001 *Science* **292** 2060–3
[11] Milliron D, Hughes S, Cui Y, Manna L, Li J, Wang L and Alivisatos A 2004 *Nature* **430** 190–5
[12] Shieh F, Saunders A and Korgel B 2005 *J. Phys. Chem. B* **109** 8538–42
[13] Kumar S, Jones M, Lo S S and Scholes G D 2007 *Small* **3** 1633–9
[14] Saunders A, Koo B, Wang X, Shih C and Korgel B 2008 *ChemPhysChem* **9** 1158–63
[15] Klimov V, Ivanov S, Nanda J, Achermann M, Bezel I, McGuire J and Piryatinski A 2007 *Nature* **447** 441–6
[16] Lannoo M, Delerue C and Allan G 1995 *Phys. Rev. Lett.* **74** 3415–8
[17] Bolcatto P G and Proetto C R 1999 *Phys. Rev. B* **59** 12487–98
[18] Brus L E 1984 *J. Chem. Phys.* **80** 4403–9
[19] Fonoberov V A, Pokatilov E P and Balandin A A 2002 *Phys. Rev. B* **66** 085310–23
[20] Katz D, Wizansky T, Millo O, Rothenberg E, Mokari T and Banin U 2002 *Phys. Rev. Lett.* **89** 086801–5
[21] Mandal S K, Mandal A R, Das S and Bhattacharjee B 2007 *J. Appl. Phys.* **101** 114315–22
[22] Lo S S, Khan Y, Jones M and Scholes G D 2009 *J. Chem. Phys.* **131** 084714–24
[23] Wang J, Gudiksen M, Duan X, Cui Y and Lieber C 2001 *Science* **293** 1455–7
[24] Lan A, Giblin J, Protasenko V and Kuno M 2008 *Appl. Phys. Lett.* **92** 183110–3
[25] Wu K, Chu K, Chao C, Chen Y, Lai C, Kang C, Chen C and Chou P 2007 *Nano Lett.* **7** 1908–13
[26] Barzda V, Cisek R, Spencer T L, Philipose U, Ruda H E and Shik A 2008 *Appl. Phys. Lett.* **92** 113111–4
[27] Hewa-Kasakarage N N, El-Khoury P Z, Schmall N, Kirsanova M, Nemchinov A, Tarnovsky A N, Bezryadin A and Zamkov M 2009 *Appl. Phys. Lett.* **94** 133113–6
[28] Sun Z, Swart I, Delerue C, Vanmaekelbergh D and Liljeroth P 2009 *Phys. Rev. Lett.* **102** 196401–5
[29] Shabaev A and Efros A 2004 *Nano Lett.* **4** 1821–5
[30] Climente J I, Royo M, Movilla J L and Planelles J 2009 *Phys. Rev. B* **79** 161301–5
[31] Planelles J, Royo M, Ballester A and Pi M 2009 *Phys. Rev. B* **80** 045324–9
[32] Yu W, Qu L, Guo W and Peng X 2003 *Chem. Mater* **15** 2854–2860
[33] Li L, Hu J, Yang W and Alivisatos A 2001 *Nano Lett.* **1** 349–351
[34] Movilla J, Climente J and Planelles J 2010 *Comp. Phys. Commun.* **181** 92–8
[35] Boda D, Gillespie D, Nonner W, Henderson D and Eisenberg B 2004 *Phys. Rev. E* **69** 046702–12

Dielectric confinement of excitons in type-I and type-II semiconductor nanorods 15

[36] Jacak L, Hawrylak P and Wójs A 1998 *Quantum Dots* (Berlin: Springer-Verlag)
[37] Laheld U E H and Einevoll G T 1997 *Phys. Rev. B* **55** 5184–204
[38] Steiner D, Katz D, Millo O, Aharoni A, Kan S, Mokari T and Banin U 2004 *Nano Lett.* **4** 1073–7
[39] Lee H, Yoon S, Ahn J, Suh Y, Lee J, Lim H and Kim D 2009 *Sol. Energy Mater. Sol. Cells* **93** 779–82 17th International Photovoltaic Science and Engineering Conference
[40] Li X Z and Xia J B 2003 *Phys. Rev. B* **68** 165316–23
[41] Muller J, Lupton J, Lagoudakis P, Schindler F, Koeppe R, Rogach A, Feldmann J, Talapin D and Weller H 2005 *Nano Lett.* **5** 2044–9
[42] Rothenberg E, Kazes M, Shaviv E and Banin U 2005 *Nano lett.* **5** 1581–6
[43] Matsuda K, Saiki T, Nomura S, Mihara M, Aoyagi Y, Nair S and Takagahara T 2003 *Phys. Rev. Lett.* **91** 177401–5